Open Access Dissertations   Theses and Dissertations

8-2016

Experimental, theoretical and computational modeling of flow boiling, flow condensation and evaporating falling films

Chirag Rajan Kharangate
Purdue University

PURDUE UNIVERSITY
GRADUATE SCHOOL
Thesis/Dissertation Acceptance

This is to certify that the thesis/dissertation prepared

By CHIRAG RAJAN KHARANGATE

Entitled
EXPERIMENTAL, THEORETICAL AND COMPUTATIONAL MODELING OF FLOW BOILING, FLOW CONDENSATION AND EVAPORATING FALLING FILMS

For the degree of Doctor of Philosophy

Is approved by the final examining committee:

ISSAM A. MUDAWAR
Chair

AMY M. MARCONNET

LIANG PAN

STEVEN H. COLLICOTT

To the best of my knowledge and as understood by the student in the Thesis/Dissertation Agreement, Publication Delay, and Certification Disclaimer (Graduate School Form 32), this thesis/dissertation adheres to the provisions of Purdue University's "Policy of Integrity in Research" and the use of copyright material.

Approved by Major Professor(s): ISSAM A. MUDAWAR

Approved by: JAY P. GORE   7/19/2016
             Head of the Departmental Graduate Program   Date

EXPERIMENTAL, THEORETICAL AND COMPUTATIONAL MODELING OF FLOW

BOILING, FLOW CONDENSATION AND EVAPORATING FALLING FILMS

A Dissertation

Submitted to the Faculty

of

Purdue University

by

Chirag Rajan Kharangate

In Partial Fulfillment of the

Requirements for the Degree

of

Doctor of Philosophy

August 2016

Purdue University

West Lafayette, Indiana

ACKNOWLEDGEMENTS

I would like to express sincere gratitude towards my advisor Dr. Issam Mudawar, for his constant motivation, enthusiasm and support throughout my tenure at Purdue. With his expertise in the field of two-phase flows, I could not have asked for a better advisor and mentor for my doctoral work. His thorough involvement in my research from day one and constant flow of ideas were truly inspiring. I am also grateful for the support and involvement of my advisory committee members Dr. Steven Collicott, Dr. Amy Marconnet, and Dr. Liang Pan.

I also extend my sincere thanks to the following members at the NASA Glenn Research Center: Dr. Mohammad Hasan, Dr. Henry Nahra, Nancy Hall, and Jeffrey Mackey. Additionally, I would also like to thank the members of the Boiling and Two-Phase Flow Laboratory who have helped both in the lab and outside. I want to acknowledge Lucas, Hyoungsoon, Ilchung, Nikhin, Sung-Min, Seunghyun, Devahdhanush, and Vishwanath.

Finally, and most importantly, I would like to thank my wife Jagruti Tembe for her immense love and understanding over the last many years. As my best friend, she has been extremely supportive throughout this process. I also want to express deepest gratitude toward my parents, Rajan Kharangate and Sima Kharangate, for the dedication and the countless sacrifices they made to ensure that I got an excellent education. I owe everthing I am today to my family.

TABLE OF CONTENTS

LIST OF TABLES

LIST OF FIGURES

NOMENCLATURE

Symbol

A channel flow area

A_b bubble surface area

A_i interfacial area

A_k flow area for phase k

A^+ constant in eddy diffusivity model

b ratio of wetting front length to wavelength

c wave speed; parameter in Eq. (A.18a); wave speed

C color function

C_{PF} phase-field parameter

Δc mesh (cell) size

$C_{f,i}$ interfacial friction factor

c_i imaginary component of wave speed

c_p specific heat at constant pressure

c_r real component of wave speed

c_v specific heat at constant volume

CHF critical heat flux, q''_m

d distance of liquid-vapor interface from wall

D_d departure diameter during nucleate boiling

D hydraulic diameter of flow channel; bubble diameter

D_k hydraulic diameter for phase k

E specific internal energy [J/kg]

$e_{i,j}$ strain rate tensor

F force

F_ψ fractional function

F_ω level set function between liquid and solid

Fo_{bi} Fourier number based on initial bubble diameter

f friction factor

Symbol

G	mass velocity
g	gravity
g_e	Earth's gravity
g_n	component of gravity normal to heater wall
h	cell width or grid spacing; heat transfer coefficient
$\bar{h}$	average heat transfer coefficient
h_E	heat transfer coefficient for evaporative heating, $q_w'' / (T_w - T_{sat})$
h_E^*	dimensionless heat transfer coefficient for evaporative heating, $h_E v_f^{2/3} / (k_f g^{1/3})$
h_i	interfacial heat transfer coefficient
h_{fg}	latent heat of vaporization
H	Heaviside function; height of flow channel's cross-section; domain height
H_a	heated wall a
H_b	heated wall b
I	turbulence intensity; Indicator function
J	Jacobian
Ja	Jacob number
k	thermal conductivity; turbulent kinetic energy; wave number
K	Von-Karman constant
Ka	Kapitza number, $\mu_f^4 g / (\rho_f \sigma^3)$
k_c	critical wave number
L	length; length of heated portion of falling-film test section; condensation length used in computational model; length of domain
L_d	development length of flow channel
L_e	exit length of flow channel
L_h	heated length of flow channel
Δl	normal distance between superheated liquid cell and interface
l_0	characteristic length, $l_0 = \sqrt{\sigma / g(\rho_f - \rho_g)}$
l_s	length scale
M	molecular weight
$\dot{m}$	mass transfer rate [kg/m^{2}s]
MAE	mean absolute error
Mo	Morton number
$\vec{n}$	unit vector normal to interface

Symbol

N	number of data points
Nu	Nusselt number
p	pressure
P_i	interfacial perimeter
p_{in}	pressure at inlet to heated portion of channel
Δp	pressure drop across heated portion of channel
Pr	Prandtl number
$Pr_{f,T}$	turbulent Prandtl number
P_w	wall friction perimeter
q''	heat flux
q_i''	heat flux across interface
$\bar{q}_m''$	critical heat flux (CHF)
$\bar{q}_w''$	average wall heat flux
Q	energy source term [W/m^3]; volume flow rate
Q_f	energy source term based on liquid fraction f based on total enthalpy
R	universal gas constant (8.314 J/mol.K); radius of domain
R_0	radius of dry region below bubble in micro-region
R_1	radial location of interface at $y = h/2$
R_{gas}	gas constant
R_1, R_2	radii of curvature at free interface
Re	Reynolds number
r	radial coordinate
r_c	mobility factor [s^{-1}]
r_i	mass transfer intensity factor [s^{-1}]
$r_{i,m}$	modified mass transfer intensity factor [K^{-1}s^{-1}]
S	volumetric mass source in continuity equation [kg/m^{3}s]
T	temperature
t	time
t_d	bubble growth time period during nucleate boiling
t_i	unit tangential vector on free interface
T_{in}	temperature at inlet to heated portion of channel
T_{out}	temperature at outlet from heated portion of channel
T_{sat}	saturation temperature
$\Delta T_{sub,in}$	inlet subcooling, $T_{sat} - T_{in}$

Symbol

ΔT_{sub}	inlet subcooling, $\Delta T_{sub} = T_{sat} - T_{in}$
$\Delta T_{sub,out}$	outlet subcooling, $T_{sat} - T_{out}$
ΔT_w	wall superheat, $\Delta T_w = T_w - T_{sat}$
$T_{w,avg}$	spatial average of wall temperatures
u	velocity
U	mean inlet liquid velocity
ΔU	phase velocity difference between heated wall vapor layer and liquid layer
u	local x-direction velocity
$\vec{u}$	velocity vector
$\vec{u}_{front}$	velocity of front
u^*	friction velocity, $\sqrt{\tau_w / \rho_f}$
V	volume
$\vec{v}_f$	liquid velocity normal to liquid-vapor interface
W	width of flow channel and heated walls; width of domain
x	flow quality; x-coordinate; dimensionless parameter in Fig. A.2
x_e	thermodynamic equilibrium quality
$\vec{x}_{front}$	position of front
x_{water}	mole fraction of water
y	y-coordinate; coordinate perpendicular to heated wall; distance perpendicular to the wall
y^+	dimensionless distance perpendicular to the wall, $y u^* / v_f$
z	axial coordinate; z-coordinate
z_0	axial coordinate where $U_g = U_f$; axial location where $x_e = 1$
z^*	axial location for determining vapor layer thickness and critical wavelength in *Interfacial Lift-off Model*

Greek Symbols

α	volume fraction
α_a	volume fraction of air
γ	accommodation coefficient in Schrage model
Γ	mass flow rate per unit film width
δ	mean thickness of vapor layer; thickness of liquid micro-layer
δ_i	initial assumed liquid film thickness
δ_a	mean thickness of vapor layer generated along heated wall H_a
δ_b	mean thickness of vapor layer generated along heated wall H_b

Symbol

δ_l	liquid film thickness
δ_0	liquid film thickness at R_0
δ_s	Dirac delta function
ε	heat utility ratio; dissipation rate of turbulent kinetic energy; liquid layer thickness; transformed coordinate
ε_h	eddy heat diffusivity
ε_m	eddy momentum diffusivity
η	interfacial perturbation; transformed coordinate
η_0	amplitude of interfacial perturbation
θ	flow orientation angle
λ	interfacial wavelength
λ_{d2}	2-D most dangerous wavelength
λ_{d3}	3-D most dangerous wavelength
$\lambda_{d,KH}$	most dangerous Kelvin-Helmholtz instability wavelength
λ_c	critical wavelength
κ	curvature given by Eq. (A.18b)
κ_m	diffusion parameter
μ	dynamic viscosity
v	kinematic viscosity
ρ	density
ρ''	modified density
σ	surface tension
τ	shear stress; time period ($L/U_{g,in}$)
τ_i	interfacial shear stress
τ_w	wall shear stress
φ_e	kinetic mobility
φ	chemical potential
φ	contact angle
Ψ	radiation heat flux
ψ	level set function

Superscripts

$-$	time average
$\rightarrow$	vector
'	fluctuating component

Symbol

+	dimensionless
*	dimensionless

Subscripts

a	vapor layer generated along heated wall H_a
avg	average
b	vapor layer generated along heated wall H_b; bubble
c	condensation; critical; liquid layer in separated flow model
crit	critical
d	developing; middle vapor core in separated flow model
e	evaporation; Earth; exit; equilibrium
eff	effective
exp	experimental
f	liquid; bulk liquid; frictional
fc	saturated liquid in liquid layer *c*
g	vapor
ga	saturated vapor generated along heated wall H_a
gb	saturated vapor generated along heated wall H_b
gd	saturated vapor in middle vapor core *d*
h	heated wall; hydraulic
H	sensible heating
i	initial; interfacial; thermocouple location; direction index
j	direction index; interfacial cell
in	inlet to heated or cooled portion of channel
k	phase *k*, *k* = *fc, ga, gb* or *gd*
m	mean; wall identifier (*a* for heater H_a or *b* for heater H_b)
n	thermocouple location along heated wall; normal to heated wall
out	outlet from heated portion of channel
pred	predicted
s	surface
sat	saturated
sub	subcooling
T	turbulent
unsat	unsaturated

Symbol

vol	volume
w	heated wall; wall; wetting front
wall	wall

ABSTRACT

Kharangate, Chirag Rajan, Ph.D., Purdue University, August 2016. Experimental, Theoretical and Computational Modeling of Flow Boiling, Flow Condensation and Evaporating Falling Films. Major Professor: Dr. Issam Mudawar, School of Mechanical Engineering.

The transition from single-phase to two-phase thermal systems in future space vehicles demands a thorough understanding of phase change methods in reduced gravity, including microgravity. In this study, phase change methods like flow boiling, flow condensation and evaporative falling-films are investigated experimentally, theoretically and computationally.

The experimental part of the study consists of an investigation of the influence of inlet subcooling and two-phase inlet on flow boiling heat transfer and critical heat flux in a horizontal 2.5-mm wide by 5-mm high rectangular channel in different orientations with respect to Earth gravity using FC-72 as working fluid. High-speed video imaging is used to identify dominant interfacial characteristics for different combinations of inlet conditions and heating configurations. Gravity is shown having a dominant influence on interfacial behavior at low mass velocities, while inertia dwarfs gravity effects at high mass velocities. CHF variation between different orientations with respect to Earth gravity is large for low mass velocities and diminishes for high mass velocities.

In the theoretical part of the study, a consolidated investigation of the complex trends of flow boiling CHF in a rectangular channel in both microgravity and for different orientations in Earth gravity are performed. Separate theoretical models are constructed to investigate subcooled inlet flows and saturated two-phase inlet flows. It is shown that the *Interfacial Lift-off Model* provides good predictions of CHF data for both gravitational environments, both single-sided and double-sided heating, and both subcooled and saturated inlet conditions.

In the computational part of the study, CFD models are constructed for two separate phase change configurations. First, turbulent, free-falling liquid films subjected to evaporative heating, and second, annular flow condensation in vertical upflow configuration. Implemented in FLUENT, the models are used to predict variations of various flow and thermal parameters and compare the results with available experimental data. Energy transfer at the two-phase interface are implemented successfully with the aid of appropriate phase change models. For both phase change configurations, the CFD model was able to capture complex flow behavior observed in experiments and predict heat transfer coefficients with reasonable accuracy. Also included in this part is a comprehensive review of literature on computational modeling of various boiling and condensation applications. This part of the study is laying the groundwork for future implementation of CFD models in capturing more complicated flow boiling and CHF phenomena.

CHAPTER 1. INTRODUCTION

1.1 Flow Boiling

1.1.1 Flow Boiling Critical Heat Flux (CHF)

For decades, single-phase thermal management systems have been used to remove heat from temperature sensitive devices in a broad variety of applications. However, as heat fluxes from devices began to escalate, interest has shifted to two-phase thermal management. Examples of these systems include electronic data centers, hybrid vehicle power electronics, avionics, and laser and microwave directed energy systems [1]. The shift to two-phase thermal management is rooted in the ability of these systems to offer orders of magnitude enhancement in heat transfer performance compared to single-phase counterparts. This enhancement is the result of utilization of the coolant's sensible and latent heat content rather than sensible heat alone. With a firm commitment to utilize two-phase thermal management, interest quickly shifted to selecting a suitable two-phase cooling configuration. Simplicity of design and operation, and low cost rendered pool-boiling-based thermosyphons as the primary thermal management solutions for many applications [2,3]. Where pool boiling failed to meet cooling targets, interest shifted to channel flow boiling, including the use of mini/micro-channels, to take advantage of fluid motion to enhance cooling performance [4-6]. And when channel flow boiling could not handle cooling needs, thermal designer engineers opted for more aggressive cooling

schemes, including jet-impingement [7,8] and spray cooling [9-11]. Recently, there have been efforts to further enhance cooling performance by combining the benefits of different phase-change cooling schemes using hybrid cooling configurations such as micro-channel/jet-impingement cooling [12].

Regardless of which two-phase cooling scheme is selected for a given application, it is essential to maintain nucleate boiling by allowing liquid to replenish the surface of the heat dissipating device to replace the vapor generated by evaporation. The concern here is that intense vapor nucleation, growth and coalescence at high fluxes might culminate in formation of an insulating vapor layer on the surface, which may interrupt bulk liquid access to it. This process is the foundation for occurrence of critical heat flux (CHF), which signals unsteady rise in surface temperature to levels that may cause device overheating or even physical burnout. This is precisely why CHF constitutes the most important design limit for any two-phase thermal management system [13].

1.1.2 Application of Flow Boiling in Future Space Systems

Future manned space missions are expected to increase in scope, size and duration. Associated with these increases will be a commensurate increase in vehicle power as well as rate of rejection of waste heat. These trends are also expected to have a profound adverse impact on the vehicle's size and weight. To tackle these issues, Fission Power Systems (FPSs), which feature both very high power and very low mass to power ratios, have been recommended for long-duration manned missions using a Rankine power cycle [14,15]. This technology involves many complex flow boiling and condensation processes. Additional reductions in vehicle size and weight are possible by replacing present single-

phase Thermal Control Systems (TCSs) with two-phase counterparts [14]. These systems play a vital role in life support in a space vehicle by controlling the temperature and humidity of the internal environment. They are comprised of three subsystems that tackle (1) *heat acquisition* from heat-dissipating sources, (2) *heat transport* from the sources, and (3) *heat rejection* to the outside environment. In most space vehicles, including space shuttles, these tasks have been tackled by a single-phase (liquid only) TCS. The two-phase TCS designs now being projected for use on future vehicles greatly decrease size and weight by capitalizing upon the orders-of-magnitude enhancement in flow boiling and condensation heat transfer coefficients compared to those possible with a single-phase TCS.

The transition to two-phase technologies requires a thorough understanding of two-phase flow and both flow boiling and condensation heat transfer in reduced gravity, especially microgravity. Reduced gravity can be simulated in a number of platforms, including above ground Drop Towers or below ground Drop Shafts, Sounding Rockets and Parabolic Flight Aircraft [14,15]. The latter has been especially populer for their ability to provide 15 – 30 s of microgravity, perform multiple tests in a single flight, and ability to accommodate larger experiment packages and permit direct interaction of the operator with the experimental package; they can also simulate both Lunar and Martian gravities. The International Space Station (ISS) provides an ideal environment for microgravity two-phase flow and heat transfer experiments, providing long test durations, operator access, and both automatic and remote control capabilities. Unforuately ISS experiments are both very expensive and require many years of development and safety certification.

The vast majority of published works concerning two-phase flow and heat transfer comes from parabolic flight experiments. These include a number of adiabatic two-phase flow studies, such as those of Dukler *et al.* [16], Colin *et al.* [17], Reinarts [18], Bousman *et al.* [19,20], and Choi e*t al.* [21] that were aimed at understanding the influence of microgravity on two-phase flow patterns as well as the transitions between different flow patterns. Parabolic flight flow boiling studies include flow patterns in both subcooled and saturated flow boiling by Misawa [22], impact of bubble detachment and coalescence on flow pattern development by Saito *et al.* [23] and Ohta *et al.* [24], flow boiling frictional pressure drop in flow boiling by Brutin *et al.* [25], and subcooled flow boiling heat transfer and CHF by Ma and Chung [26]. More recently, a collaborative effort between the Purdue University Boiling and Two-Phase Flow Laboratory (PU-BTPFL) and NASA Glenn Research Center has been focussed mostly on flow boiling CHF. Findings from this specific effort will be discussed later in this paper.

Aside from the high-cost microgravity platforms, researchers often capitalize upon the relative simplicity and low cost of testing in Earth gravity. The effects of reduced gravity on flow boiling are simulated by tilting the flow channel relative to Earth gravity. This yields a reduced component of gravity perpendicular to the heated wall. But a primary limitation with these tests is the inability to isolate the influence of this gravity component and simultaneously eliminate the component of gravity along the direction of fluid flow. Nonetheless, this testing approach is widely used to amass large data bases and video records in pursuit of a mechanistic model for the influence of gravity on both pool boiling [27] and flow boiling CHF; the latter will be discussed in detail in the present paper. Investigators at PU-BTPFL have adopted this testing approach to complement parabolic

flight tests in an attempt to acquire a comprehensive understanding of the influence of gravity on flow boiling CHF.

1.1.3 Single–Sided and Double-Sided Heating in a Rectangular Channel

Of the different boiling schemes, channel flow boiling has received the most attention for space applications because of its simplicity and suitability to thermal management of multiple heat sources. Most prior reduced gravity flow boiling studies have been concentrated on CHF measurement [24,26], particularly in rectangular flow channels that are heated along one side [28,29]. The key reason for relying on single-sided heating is to isolate the effects of reduced or Earth gravity perpendicular to, and parallel to the heated wall.

Figures 1.1(a) and 1.1(b) depict flow boiling near CHF at low flow velocities in a horizontal rectangular heated channel with heated top wall and bottom wall, respectively, at 1 g_e. These figures illustrate fundamental differences in liquid-vapor interfacial behavior between these two orientations. Top wall heating is shown accumulating vapor against the top wall, culminating in the formation of a thick insulating layer and fairly low CHF. Bottom wall heating benefits form gravity aiding in both vapor removal from the heated wall, and liquid replenishment to the wall. Flow boiling in a horizontal channel that is heated on both top and bottom walls (*i.e.,* double-sided heating) is far more complex, as gravity simultaneously plays a negative role along the top wall, and a positive role along the bottom wall. This behavior is depicted in Fig. 1.1(c), where the flow boiling behaviors for separately heated top wall, Fig. 1.1(a), and bottom wall, Fig. 1.1(b) are more or less superimposed in the same channel. A recent study by Konishi *et al.* [30,31] involving flow
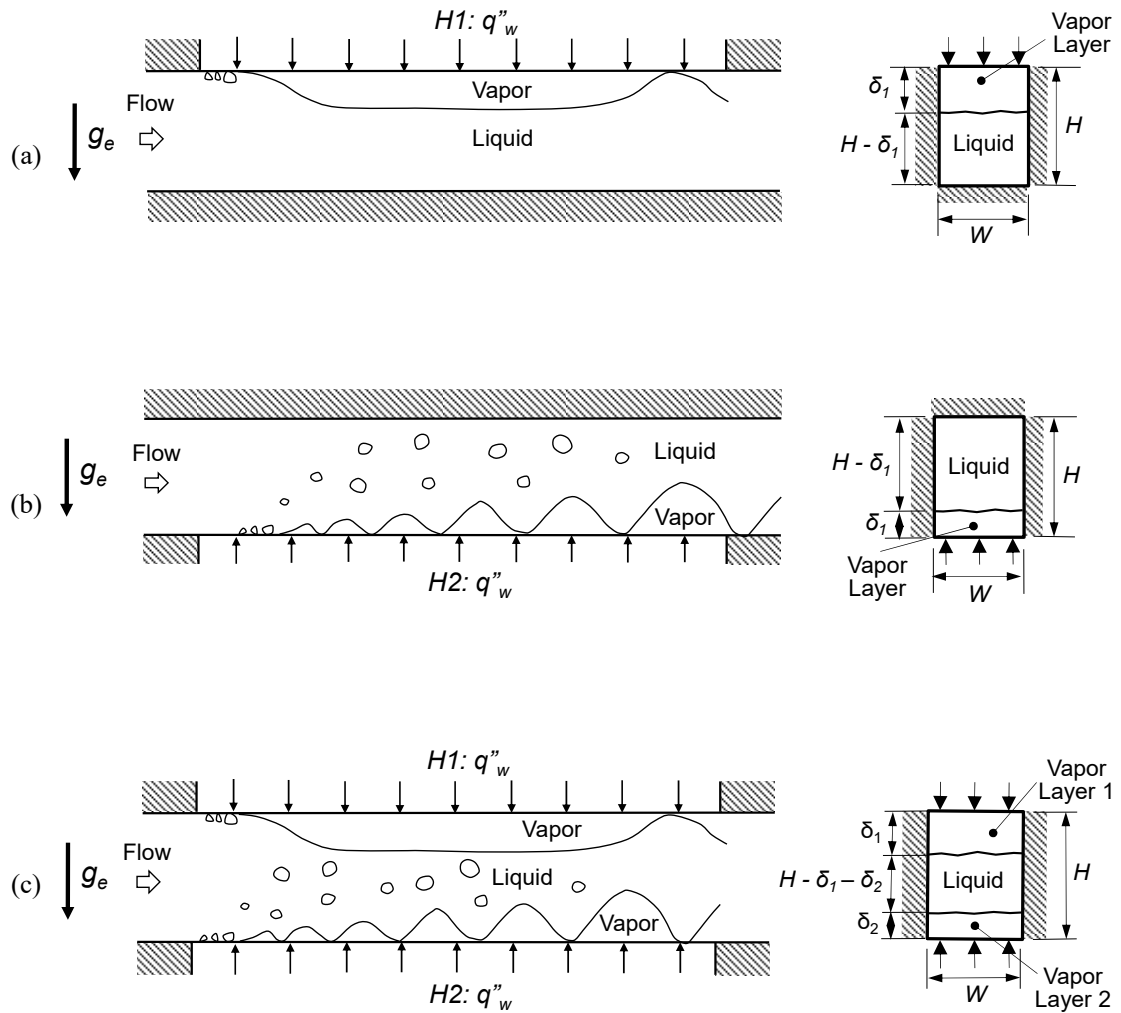
Fig. 1.1: Depiction of horizontal flow boiling near CHF for a rectangular channel with (a) top wall heating, (b) bottom wall heating, and (c) double-sided heating.

boiling of FC-72 in the microgravity environment of parabolic flight showed double-sided heating provides higher CHF values in comparison with single-sided heating for velocities ranging from 0.1 to 1.9 m/s.

1.1.4 <u>Effects of Inlet Subcooling and Heat Utility Ratio</u>

Flow boiling heat transfer and CHF are highly dependent on fluid state at the inlet to the flow channel. Three types of inlet conditions are possible: highly subcooled liquid, slightly subcooled liquid, and saturated liquid-vapor mixture. High inlet subcooling enhances CHF appreciably by enabling the coolant to absorb a considerable portion of the wall heat flux in the form of sensible heat instead of by latent heat alone. Strong support for the merits of subcooled inlet conditions over two-phase inlet conditions comes from a number of studies involving single-sided heating in both microgravity [28-31] and Earth gravity [32-35].

To understand the effects of subcooling on flow boiling CHF, it crucial to quantify the influence of *heat utility ratio*, defined as the ratio of CHF associated with both sensible and latent heat to that with latent heat alone. This is perhaps one of the most challenging endeavors in two-phase heat transfer literature, despite many previous correlative attempts [36-40], where subcooled flow boiling was described as a superposition of single phase forced convection and pool boiling. More recently, Zhang *et al.* [28] combined experimental results from their own experiments and those of Sturgis and Mudawar [32,33] to develop an empirical correlation for the heat utility ratio.

1.1.5 <u>Predictive Flow Boiling CHF Models</u>

Like most two-phase phenomena, researchers rely heavily on empirical correlations to predict flow boiling CHF. However, correlations are valid for specific fluids and limited ranges of operating and flow parameters, and there is great uncertainty when attempting to determine CHF for other fluids or beyond the validity range of individual parameters [41-44].

Very few theoretically based, mechanistic models have been constructed for flow boiling CHF, and these models are intended mostly for vertical upflow. As discussed in a recent review article by Konishi *et al.* [45] and depicted schematically in Fig.1.2(a), these models are based on four competing mechanisms: *Boundary Layer Separation*, *Bubble Crowding*, *Sublayer Dryout* and *Interfacial Lift-off*. Postulated by Kutateladze and Leont've [46], the *Boundary Layer Separation Model* is based on analogy between vapor production and gas injection from a permeable wall into a turbulent boundary layer. In the same manner a turbulent boundary layer is separated when the injection velocity exceeds a threshold value, CHF is postulated to occur when the rate of vapor production perpendicular to the wall is increased to a level that greatly decreases the bulk liquid velocity near the wall, causing liquid stagnation at the wall and preventing adequate liquid replenishment of the wall. Proposed by Weisman and Pei [47], the *Bubble Crowding Model* is described by formation of a dense bubbly layer close to the wall at CHF, which renders turbulent fluctuations in the bulk liquid flow, which they postulated as the main source of liquid replenishment, too weak to penetrate the bubbly layer and reach the wall. Lee and Mudawar [48] proposed the *Sublayer Dryout Model*, which states that CHF will occur when the enthalpy of bulk liquid supplied to liquid sublayers that are trapped beneath

(a)

(b)
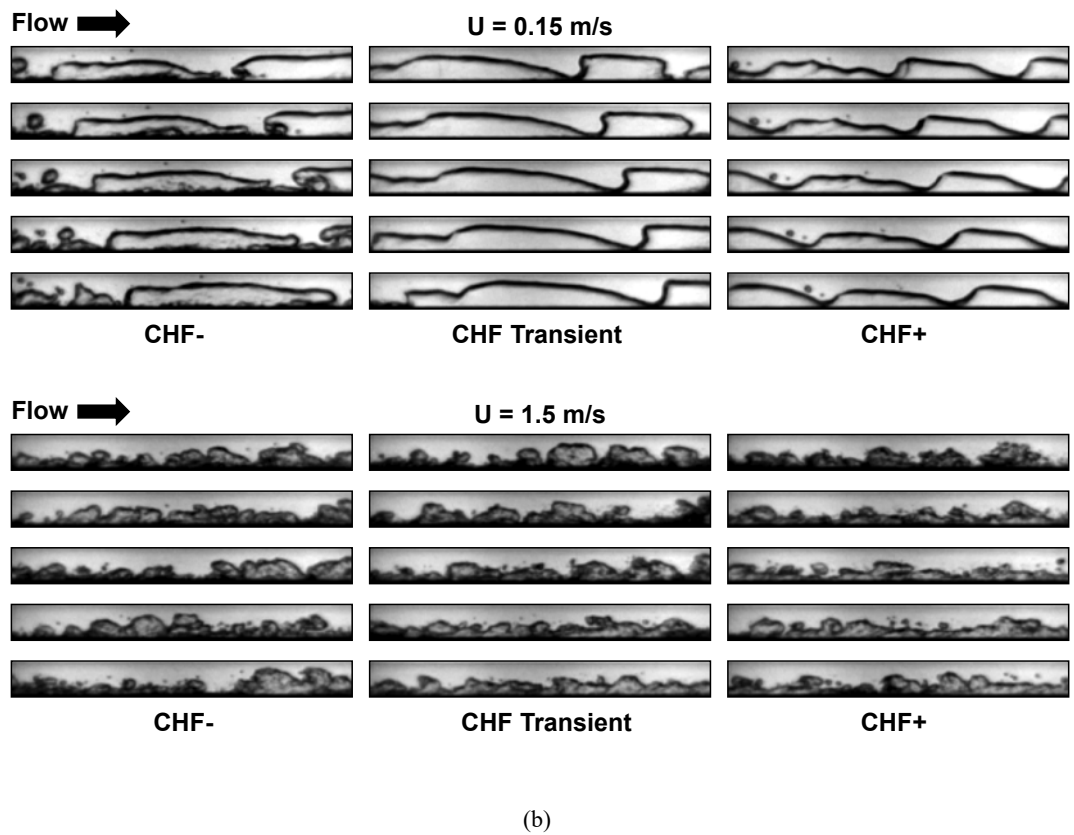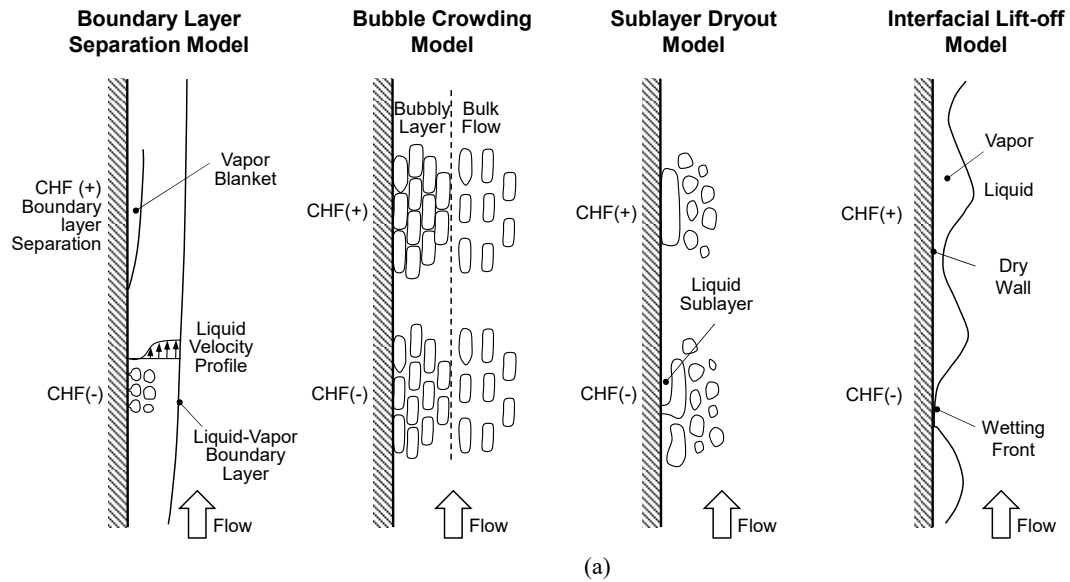
Fig. 1.2: (a) Trigger mechanisms for flow boiling CHF according to different models. (b) CHF transient in microgravity for FC-72 at $U = 0.15$ m/s ($\Delta T_{sub,out} = 3.0°C$) and $U = 1.50$ m/s ($\Delta T_{sub,out} = 3.8°C$). Adapted from [45].

large vapor blankets at the wall falls short of dissipating the heat supplied at the wall. Galloway and Mudawar [49,50] proposed the *Interfacial Lift-off Model* based on detailed high-speed video records of interfacial features of flow boiling in a flow channel associated with CHF occurrence. Prior to CHF, vapor bubbles were observed to coalesce into a wavy vapor layer that propagated along the heated wall while allowing liquid contact with the wall in wetting fronts corresponding to the wave troughs. At CHF, intense vapor momentum in these wetting fronts caused the interface in the troughs to be lifted from the wall, extinguishing any further liquid access.

1.1.6 <u>Influence of Fluid Flow and Heated Wall Orientations on CHF</u>

Aside from enabling the study of reduced gravity influence on flow boiling, experiments performed by tilting the flow channel relative to Earth gravity also provide the flexibility of one-sided or two-sided wall heating. While these two wall heating configurations can greatly complicate the influence of gravity on CHF, they also provide the opportunity for a more detailed mechanistic assessment of this influence. This assessment is a key objective of the present study.

Single-sided heating is borne out of the need to simulate cooling of electronic or power sources using flow boiling in a rectangular channel [51,52]. Using similar single-sided heating, Zhang *et al.* [53] studied the influence of flow orientation on CHF for subcooled inlet conditions. Using FC-72 as working fluid, they showed that the influence of orientation, and therefore gravity, on CHF diminishes monotonically with increasing flow velocity, becoming virtually independent of orientation above a threshold of 1.5 m/s. Similar trends were measured by Konishi *et al.*[54] for two-phase inlet conditions, $x_{e,in} \geq 0$.

Originally proposed by Galloway and Mudawar [49,50], the *Interfacial Lift-off Model* has been validated in several studies that were performed in both Earth gravity [53-55] and microgravity [56,30-31] over a wide range of operating conditions using both CHF data and high-speed video. Shown in Fig. 1.2(b) are images of the wavy vapor layer captured by Zhang *et al*. [56] before, during, and shortly after CHF for single-sided heating of FC-72 in microgravity at inlet liquid velocities of $U = 0.15$ and 1.5 m/s. These images depict the wavy vapor layer development prior to wetting front dryout that accompanies CHF occurrence.

1.2 Falling Films

Free-falling liquid films are found in a variety of industries, including chemical, pharmaceutical, and power generation. These films provide high heat transfer coefficients while capitalizing on gravity to achieve liquid motion. Heat exchangers utilizing falling films rely on either sensible or evaporative heating of the film. With sensible heating, the heat absorbed from the wall gradually increases the mean liquid temperature in the flow direction. On the other hand, evaporative heating is achieved once the film's interface reaches saturation temperature. Evaporating liquid films in practical applications are typically turbulent and capitalize upon the added mixing provided by interfacial waves to achieve very attractive heat transfer performance.

Most of the published falling-film studies concern laminar and turbulent fluid flow in adiabatic films. And, while studies concerning heat transfer to films are relatively sparse, far more data are available for sensible heating than evaporation. Table 1.1 provides the

Table 1.1: Heat transfer coefficient correlations for falling films.

Author(s)	Correlation	Range
Sensible heating		
Wilke [57]	$h_H^* = 2.07 Re^{-1/3}$	$Re < 2460 Pr_f^{-0.646}$
	$h_H^* = 0.0323 Re^{1/5} Pr_f^{0.344}$	$2460 Pr_f^{-0.646} < Re < 1600$
	$h_H^* = 0.00102 Re^{2/3} Pr_f^{0.344}$	$1600 < Re < 3200$
	$h_H^* = 0.00871 Re^{2/5} Pr_f^{0.344}$	$3200 < Re$
		$5.4 < Pr_f < 210$
Gimbutis [58]	$h_H^* = \left(0.165 Re^{0.16} - 0.4\right) Pr_f^{0.34} \left(\frac{Pr_f}{Pr_{f,w}}\right)^{0.25}$	$2800 \leqslant Re \leqslant 70{,}000$
		$4.3 < Pr_f < 8.4$
Shmerler and Mudawar [59]	$h_H^* = 0.0106 Re^{0.3} Pr_f^{0.63}$	$2500 \leqslant Re \leqslant 39{,}500$
		$2.55 < Pr_f < 6.87$
Al-Najem et al. [60]	$h_H^* = 6.832 \times 10^{-4} \left(Re^{0.4829} Pr_f^{0.93717} - \frac{21{,}817.84}{Re}\right)$	$4000 \leqslant Re \leqslant 20{,}000$
		$1.8 < Pr_f < 4.4$
Ye et al. [61]	$h_H^* = 0.00462 Re^{0.429} Pr_f^{1/3}$	$800 \leqslant Re \leqslant 7000$
		$2.55 < Pr_f < 7.2$
Evaporative heating		
Chun and Seban [62]	$h_E^* = 0.0038 Re^{0.4} Pr_f^{0.65}$	$320 \leqslant Re \leqslant 21{,}000$
		$1.77 < Pr_f < 5.7$
Shmerler and Mudawar [63]	$h_E^* = 0.0038 Re^{0.35} Pr_f^{0.95}$	$4990 < Re < 37{,}620$
		$1.75 < Pr_f < 5.42$

summary of popular falling-film correlations for both sensible heating and evaporative heating derived from measurements by different researchers. For evaporative films, early works include a study by Struve [64], who presented heat transfer data for R11. Chun and Seban [62] performed fairly extensive measurements of evaporating water films and recommended heat transfer coefficient correlations for both laminar and turbulent films. Fujita and Ueda [65] also performed evaporative heating experiments with water at 1 atmosphere and compared their data to Chun and Seban correlations. Shmerler and Mudawar [63] performed experiments with turbulent free-falling water films and recommended an alternative correlation for the heat transfer coefficient.

1.3 Flow Condensation

The vast majority of recent studies concerning two-phase thermal management have been focused on heat acquisition through evaporation or boiling, while the number of studies addressing heat rejection by condensation is relatively small. And most of the published condensation studies concern vertical downflow, a flow orientation that provides fairly stable condensate film motion aided by gravity. This configuration was explored in great detail by Park *et al.* [66] both experimentally and theoretically. However, because of volume and packaging constraints, it is impractical to design condensers utilizing the vertical downflow orientation alone. Most condensers adopt a serpentine design, with flow often alternating between vertical downflow and vertical upflow. Therefore, understanding vertical upflow condensation is crucial for the design of condensers used in two-phase thermal management systems.

Vertical upflow condensation is substantially more complicated than vertical downflow because of the opposing influences of vapor shear and gravity on the motion of the condensate film. As indicated in [67], several distinct flow regimes are encountered in vertical upflow condensation. At low inlet flow rates, the liquid film is driven downwards by gravity as the upward vapor shear is too weak to influence the film's motion; this flow behavior is categorized as the *falling film* regime. Increasing the flow rate causes the flow to transition to an *oscillating film* regime, corresponding to the liquid film alternating between upflow and downflow. A further increase in flow rate results in *flooding*, where vapor shear becomes strong enough to just balance the weight of the liquid film, causing the film to begin its ascent. Further flow rate increases cause the vapor shear to overcome garvity effects and the liquid film to flow upwards; this behavior is categorized as the *climbing film* regime.

1.4 Computational Methods for Phase Change Processes

Developing two-phase heat transfer facilities and performing experiments using different fluids and over broad ranges of operating parameters in order to measure heat transfer parameters is a very costly endeavor. This explains the present growing interest in utilizing computational methods to determine the same parameters. Use of computational tools to predict fluid flow and heat transfer in phase change system has been the subject of intense study only during the past two decades. Researchers have suggested different interfacial models to predict mass, momentum and heat transfer in phase change systems. Three main types of phase change models have been widely used for this purpose.

Early works conducted in the 1990's were based on the sharp interface model, which uses the Rankine-Hugoniot jump condition [68] for energy conservation at the interface. Micro-scale mass transfer is neglected and the liquid-vapor interface is maintained at saturation temperature. This allows mass transfer rate to be determined from energy conservation at the interface according to the relation

$$q_i^{"} = -k\nabla T_i . \vec{n} = \dot{m} h_{fg},$$ (1.1)

where $\dot{m}$ [kg/m^{2}s] is the mass flux due to phase change at the interface. The volumetric mass source term, S [kg/m^{3}s], for the individual phases is determined from

$$S_g = -S_f = \dot{m}|\nabla \alpha_g| = \frac{k(\nabla \alpha . \nabla T)}{h_{fg}},$$ (1.2)

where k_{eff} is the effective thermal conductivity determined from the volume fractions and thermal conductivities of the liquid and vapor. In effect, this model uses all energy crossing the interface for mass transfer.

The second popular approach is based on a model by Schrage [69], which in turn is based on the Hertz-Knudsen equation [70] that allows for interfacial jump in temperature and pressure, where $T_{sat}(p_f) = T_f \neq T_{sat}(p_g) = T_g$. The net mass flux across the interface, $\dot{m}$ [kg/m^{2}s], is determined by the difference between liquid to vapor and vapor to liquid mass fluxes,

$$\dot{m} = \frac{2}{2-\gamma_c}\sqrt{\frac{M}{2\pi R}}\left[\gamma_c \frac{p_g}{\sqrt{T_g}} - \gamma_e \frac{p_f}{\sqrt{T_f}}\right],$$ (1.3)

where $R = 8.314$ J/mol.K is universal gas constant, γ the fraction of molecules transferred from one phase to the other during phase change, and $1-\gamma$ the fraction of molecules reflected at the interface. The subscripts c and e in Eq. (1.3) refer to condensation and

evaporation, respectively, and $\gamma_e = 1$ and $\gamma_c = 1$ represent complete evaporation and complete condensation, respectively [71]. Many investigators use equal values of γ_c and γ_e by setting $\gamma_c = \gamma_e = \gamma$ in phase change simulations, and refer to γ as the "accommodation coefficient." Tanasawa [72] simplified Eq. (1.3) by setting the interfacial temperature equal to T_{sat}, and assuming the heat flux is linearly dependent on temperature jump between the interface and the vapor. For evaporation, their modified model is expressed as

$$\dot{m} = \frac{2}{2-\gamma_c}\sqrt{\frac{M}{2\pi R}}\frac{\rho_g h_{fg}\left(T-T_{sat}\right)}{T_{sat}^{3/2}},\tag{1.4}$$

where T_{sat} is based on local pressure, p, and the volumetric mass source term is determined from

$$S_g = -S_f = \dot{m}\left|\nabla\alpha_g\right|.\tag{1.5}$$

This model is applicable only to the liquid-vapor interface, and has been used mostly to tackle evaporating and condensing films, and film boiling.

The third popular approach is based on a phase change model proposed by Lee [73]. This model has been widely used in condensation studies, but is applicable to both condensation and boiling. The Lee model is based on the assumption that mass is transferred at a constant pressure and a quasi thermo-equilibrium state, and obtained from the relations

$$S_g = -S_f = r_i\,\alpha_g\,\rho_g\,\frac{\left(T-T_{sat}\right)}{T_{sat}}\ \text{for condensation } (T < T_{sat})\tag{1.6a}$$

and
$$S_g = -S_f = r_i\,\alpha_f\,\rho_f\,\frac{\left(T-T_{sat}\right)}{T_{sat}}\ \text{for evaporation } (T > T_{sat}),\tag{1.6b}$$

where r_i is an empirical coefficient called the "mass-transfer intensity factor," and has the units of s^{-1}. This model is the least physical of the three models but has the simplest form. Equations (1.6a) and Eq. (1.6b) reveal that this model relies on some form of weighting factor to determine mass transfer. It is important to note that the Lee model does not set physical limits on the coefficient r_i. With this model, phase change is defined both at the liquid-vapor interface and the phase being changed, *i.e.,* liquid phase for boiling and vapor phase for condensation.

The Appendix A reviews the large pool of articles addressing computational simulations of boiling and condensation. This includes (1) popular two-phase computational schemes and key differences between schemes, (2) surface tension modeling in conjunction with different schemes, (3) different approaches to predicting interfacial mass, momentum and energy transfer, and (4) boiling and condensation articles involving comparison of predictions of computational schemes with experiments and correlations. This review also provides key recommendations for improving predictive capabilities of computational schemes.

1.5 Objective of Study

The present study is a part of a NASA project that was initiated in 2012 with the ultimate goal of developing the Flow Boiling and Condensation Experiment (FBCE) for the International Space Station (ISS). Main objectives of this study are:

1. Address the combined complex effects of (i) inlet thermodynamic state (highly subcooled, slightly subcooled or saturated), (ii) mass velocity, and (iii) heating configuration (top wall heating, bottom wall heating and double-sided heating) on both

local and spatially averaged heat transfer coefficient and CHF for different orientations in Earth gravity. High-speed video imaging is used to capture dominant interfacial patterns for the different combinations of inlet conditions, mass velocity and heating configuration.

2. Model, for all flow orientations, the complex influence of Earth gravity components perpendicular to the heated wall and parallel to the direction of fluid flow on CHF for FC-72 in a rectangular channel with single-sided and double-sided heating. Separate models will be developed for both subcooled inlet flow and saturated two-phase inlet flow. It will be shown how the *Interfacial Lift-off Model* possesses both the flexibility and rigor to predict the effects of flow velocity and wall heating in both Earth gravity and microgravity.

3. Develop computational models for evaporating turbulent free-falling liquid films and annular flow condensation. An appropriate phase change model will be adapted to predict the fluid flow and heat transfer characteristics for each of those situations. The predictive accuracy of the model will be assessed against experimental data corresponding to a broad range of Reynolds numbers. Another objective of this study is to help lay a foundation for future computational modeling of more complicated boiling processes.

CHAPTER 2. EXPERIMENTAL METHODS

2.1 <u>Flow Boiling Module and Heated Wall Construction</u>

A highly instrumented flow boiling module is designed for the present experiments. This exact design is planned to be used in the future for experiments on the International Space Station. As shown in Figs. 2.1(a) and (b), the flow boiling module designed for this study consists mainly of three transparent polycarbonate plastic (Lexan) plates. A 2.5-mm wide and 5.0-mm high rectangular flow channel is milled into the middle Lexan plate as depicted in Fig. 2.1(c). Slots are milled into the top and bottom Lexan plates to accommodate two 15.5-mm wide, 114.6-mm long and 1.04-mm thick oxygen-free copper heating slabs. O-ring seals are fitted into shallow grooves in the Lexan plates to guard against leaks. The three Lexan plates are sandwiched together between two aluminum support plates. The flow channel features an inlet honeycomb flow straightener followed by an entry length upstream of the heated walls 100 times the hydraulic diameter to ensure fully developed flow. Pressure is measured at the channel inlet, just upstream and just downstream of the copper slabs. Fluid temperature is measured by type-E thermocouples inserted in the channel inlet and exit. Figure 2.1(c) shows important dimensions of the flow channel.

The two copper slabs are used as heating walls for the flow channel. Figures 2.1(d) and 2.1(e) depict the detailed construction and instrumentation of the walls, respectively.
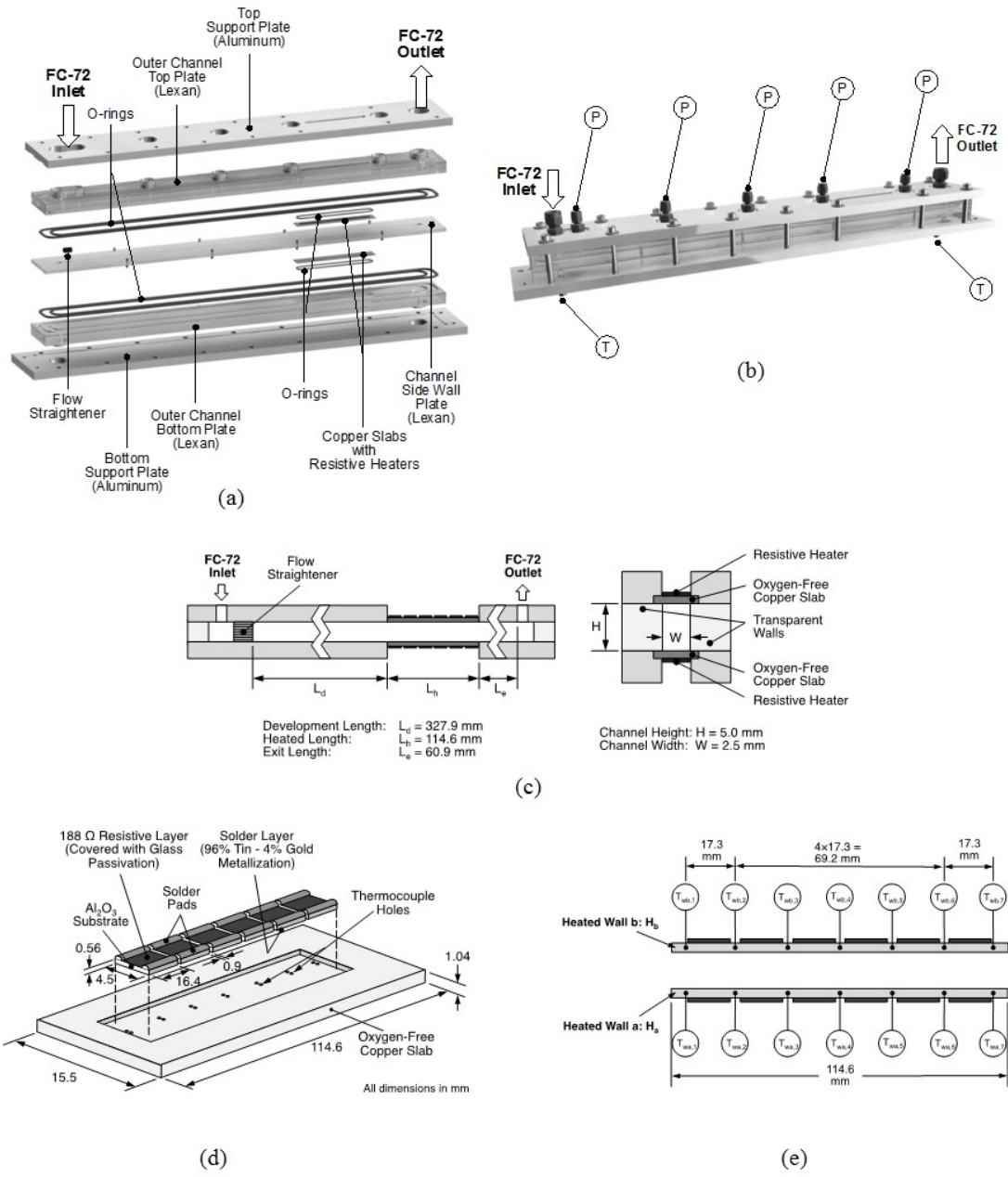
Fig. 2.1: (a) Exploded view of flow boiling module. (b) Assembled view of flow boiling module. (c) Key dimensions of flow channel. (d) Construction of heated walls and thick-film resistors. (e) Thermocouple layout in two heated walls.

Six 188-Ω, 4.5-mm wide, and 16.4-mm long thick-film resistors are soldered to the back of each copper slab. The resistors are connected electrically in parallel and powered by a variable voltage source to produce uniform heat flux along each wall. A previous study by Zhang *et al.* [56] showed that a minimum 'asymptotic wall thickness' is necessary to ensure that the measured CHF is both wall thickness independent and representative of real heat exchanger surfaces. For FC-72, they showed that the minimum thickness for a copper surface is 0.40 mm. Using a much larger thickness also has the disadvantage of delaying the attainment of steady state after supplying electrical power to the resistors. Hence, a copper slab thickness of 1.04 mm is adopted in the present study. Each copper slab features two parallel sets of seven shallow holes that are drilled between the resistors for insertion of type-E thermocouples. One set is used to make temperature measurements while the second set is used to trigger an electric relay and cut off power supply to the resistors once CHF is detected. Figure 2.1(e) shows axial positions of the measurement thermocouples. The thermocouples are designated as $T_{wm,n}$, where m represents the heated wall (b for top heated wall H_b or a for bottom heated wall H_a), and n the axial thermocouple location.

2.2 Two-Phase Loop

Depicted in Fig. 2.2, the two-phase loop is constructed to supply FC-72 to the flow boiling module at a prescribed flow rate, pressure and either temperature for subcooled inlet or thermodynamic equilibrium quality for saturated two-phase inlet. The FC-72 is deaerated in a separate degassing facility before being supplied to the flow loop. It is circulated within the loop with the aid of a magnetically coupled gear pump, downstream
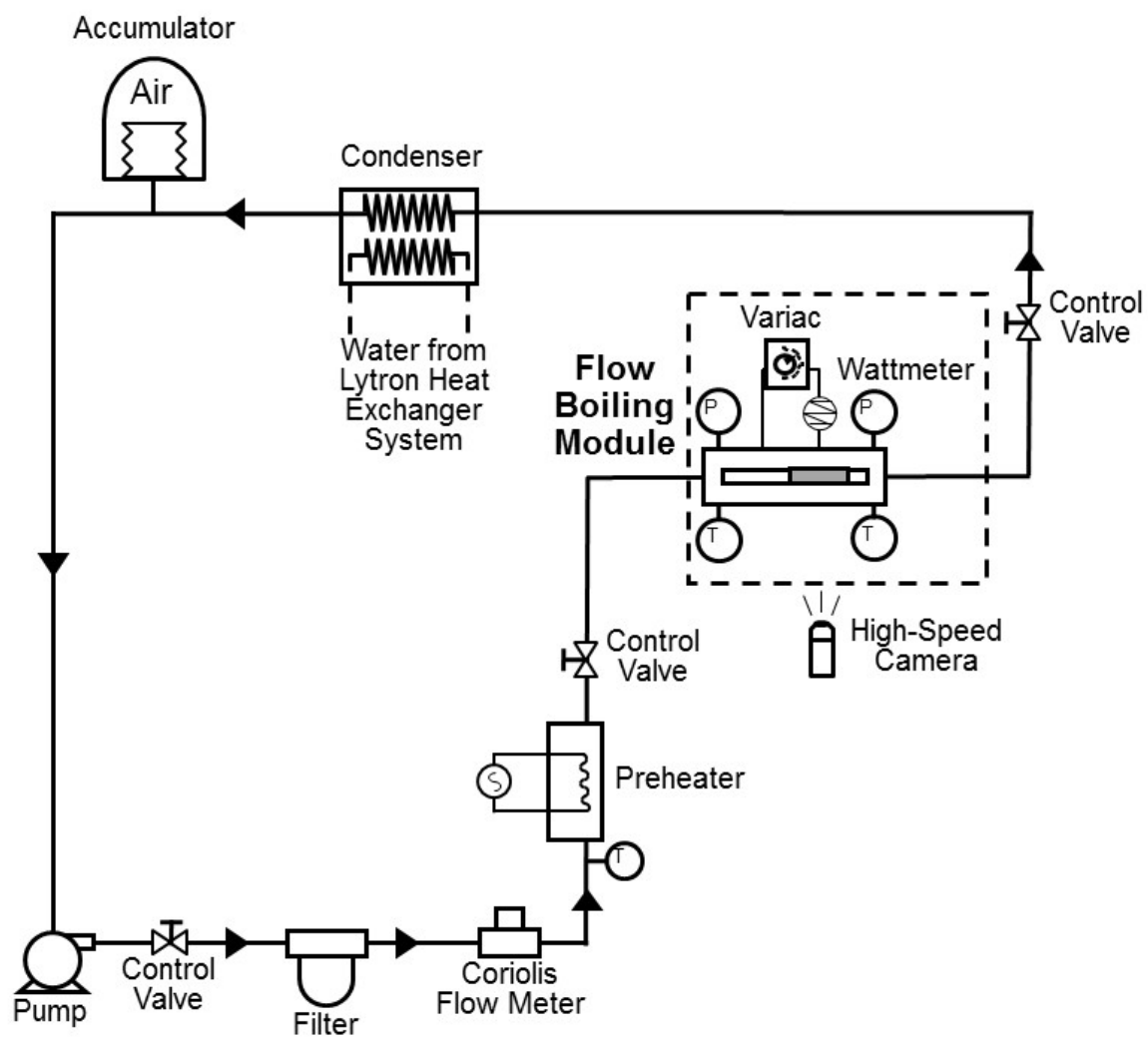
Fig. 2.2: Schematic diagram of the flow loop.

of which are a filter, Coriolis flow meter, electric pre-heater, and the flow boiling module. Exiting the module, the two-phase mixture passes through a water-cooled condenser to return the fluid to liquid state. An air-pressurized accumulator is situated between the condenser and pump, serving the dual purpose of setting a low pressure reference junction and compensating for any volume expansion or contraction (due to temperature changes or vapor production/collapse) throughout the loop. The entire flow boiling facility, including the flow loop components, data acquisition system, power and instrumentation cabinets, and high-speed camera, are mounted onto an optical table.

2.3 Flow Visualization Techniques

A high-speed camera-link imaging system utilizing a full 10-tap camera-link camera, ATX computer and PCI-Express frame grabber is used to capture the two-phase interfacial features along the heated portion of the flow channel. A fixed frame rate of 2000 frames per second (fps) and pixel resolution of 2040 x 174 are used to capture the entire heated length for each test run. Each video image sequence consists of 3000 frames, or 1.5 s of flow visualization data per test run. Illumination is provided from the back of the flow channel by an array of LEDs, with a light shaping diffuser (LSD) situated between the LEDs and the channel to distribute the light uniformly over the flow channel.

The imaging system is operated using commercial-off-the-shelf (COTS) imaging software provided by the frame grabber company to set the imaging parameters, including the area of interest, exposure time and frame rate. The imaging system is manually triggered to acquire and store the 3000-frame image sequence once the flow boiling achieves steady state. Since each image is 2040 pixel elements x 174 pixel elements x 1

byte, the image occupies approximately 355,960 bytes of memory. At 2000 fps, the image data transfer rate from the camera through the frame grabber and into the host random access memory (RAM) is approximately 710 MB/s. Due to the data bandwidth limitations of the solid-state hard drives (~500 Mb/s write speed), image sequences are first buffered to the host RAM before they are saved to a solid-state hard drive for archiving and post-acquisition analysis purposes.

2.4 Operating Conditions, Procedure, and Measurement Uncertainty

The operating conditions for the study are as follows: FC-72 inlet mass velocity of $G =$ 183.5 – 3211.6 kg/m^{2}s, inlet temperature of $T_{in} = 28.4 – 81.3°C$ (for subcooled flow: inlet subooling of $\Delta T_{sub,in} = 3.3 – 31°C$ and for saturated flow: inlet equilibrium quality of $x_{e,in} =$ 0.00 – 0.69), and inlet pressure of $p_{in} = 97.1 – 191.8$ kPa (14.1– 27.8 psi).

For every experiment, an initial waiting period is required to achieve steady state at the inlet to the flow boiling module. Thereafter, data measurements are saved using a Labview program in conjunction with an NI SCXI-1000 data acquisition system. Power to the specific flow boiling heated wall(s) (H_a or H_b or both) is then turned on depending on the prescribed heating configuration for the test. The power is increased in small increments, followed by a waiting period after each increment to achieve steady state, after which the high-speed camera system is triggered to record flow visualization data. The next power increment is then applied and measurements repeated in the same manner. Over the course of a single experiment, the mass flow rate is maintained constant by adjusting pump speed following every power increment.   The heated wall relay is set to automatically cut off

power supply to the resistors once any of the wall temperatures exceed 130°C, indicating CHF.

Fluid and heated wall temperatures throughout the facility are measured with type-E thermocouples having an accuracy of ±0.5°C. STS absolute pressure transducers having an accuracy of ±0.05% are used to measure pressure at several locations along the flow boiling module and the flow loop. The Coriolis flow meter has an accuracy of ±0.1%. The wall heat input is measured with an accuracy of ±0.5 W, and the uncertainty in heat transfer coefficient measurement is ±8%.

CHAPTER 3. FLOW BOILING EXPERIMENTAL RESULTS

3.1 Flow Visualization Results

Figures 3.1(a)-(f) show individual images of flow boiling along the entire heated portion of the channel for top wall heating, top and bottom wall heating, and bottom wall heating for heat fluxes up to CHF and three different inlet flow conditions: 24.5 – 25.6°C subcooling (highly subcooled), 3.3 – 5.1°C subcooled (slightly subcooled), and inlet equilibrium quality of 0.03 – 0.18 (saturated), corresponding to two different mass velocities. Figures 3.1(a) and (b) show images for $G = 408.6 – 469.8$ kg/m²s ($U = 0.25 – 0.29$ m/s) and $G = 1592.5 – 1601.3$ kg/m²s ($U = 0.98 – 0.99$ m/s), respectively, for the highly subcooled cases. For top wall heating and the lower velocity, Fig. 3.1(a) shows a wavy vapor layer along the heated wall, with liquid appearing to reach the wall in the wave troughs. Weak flow inertia allows buoyancy to stratify the vapor along the upper wall. For bottom wall heating, Fig. 3.1(a) shows both discrete and larger coalescent bubbles emanating from the heated wall and projecting towards the opposite wall in the absence of strong flow inertia. This causes bulk liquid to flow downwards, uninterrupted, to compensate for the released vapor, which explains the higher CHF for the bottom heated wall (31.8 W/cm²) compared to the top heated wall (26.3 W/cm²). For double-sided heating, the top wavy vapor layer appears to interrupt the bubble formation, coalescence and liquid return along the bottom wall, which is manifest in a
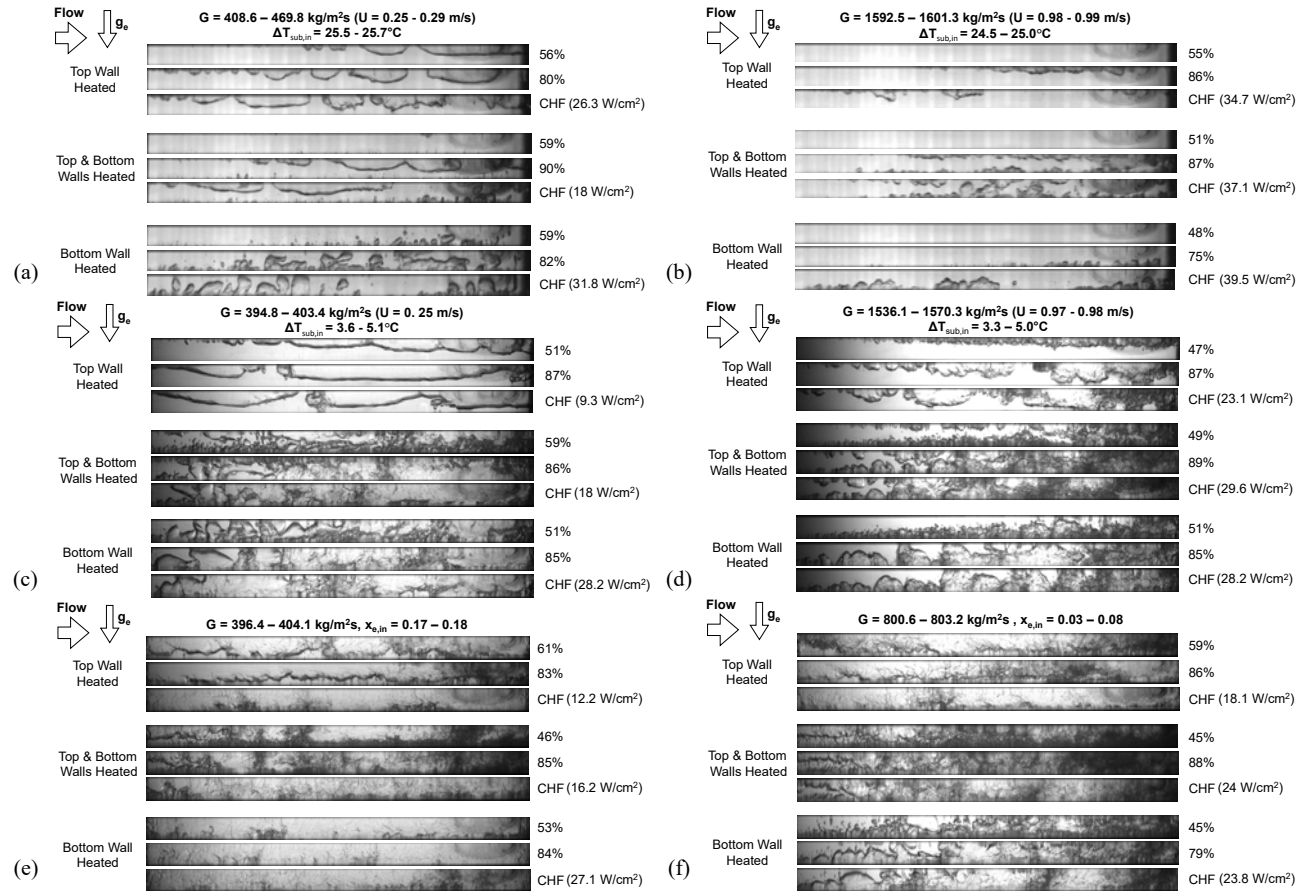
Fig. 3.1: Variations of interfacial behavior with increasing heat flux for top wall heating, double-sided heating, and bottom wall heating for (a) $G = 408.6 – 469.8$ kg/m²s and $\Delta T_{sub,in} = 25.5 – 25.7$°C, (b) $G = 1592.5 – 1601.3$ kg/m²s and $\Delta T_{sub,in} = 24.5 – 25.0$°C, (c) $G = 394.8 – 403.4$ kg/m²s and $\Delta T_{sub,in} = 3.6 - 5.1$°C, (d) $G = 1536.1 – 1570.3$ kg/m²s and $\Delta T_{sub,in} = 3.3 – 5.0$°C, (e) $G = 396.4 – 404.1$ kg/m²s and $x_{e,in} = 0.17 – 0.18$, and (f) $G = 800.6 – 803.2$ kg/m²s and $x_{e,in} = 0.03 - 0.08$.

CHF value (18 W/cm^2) smaller than that for both top and bottom wall heating. Overall, gravity appears to play a dominant role for this low inertia case.

Figure 3.1(b) shows images for similarly high inlet subcooling (24.5 – 25°C) but higher mass velocity of G = 1592.5 – 1601.3 kg/m^{2}s (U = 0.98 – 0.99 m/s). Here, higher inertia appears to (i) move boiling activity downstream and (ii) greatly reduce the thickness of the vapor layer along the top heated wall. For bottom wall heating, increased inertia compared to Fig. 3.1(a) confines boiling activity to the bottom wall. For double-sided heating, the flow appears to combine the vapor behaviors of the top wall and bottom wall heating in the absence of appreciable interaction of top and bottom wall vapor layers. Overall, higher inertia appears to negate much of the gravity-dominated behavior captured in Fig. 3.1(a), which helps explain why CHF values for all three heating configurations are close to one another. Another important outcome of the combination of higher inertia and high subcooling, which is manifest by confinement of vapor activity to the respective heated walls, is the likelihood of high inequilibrium across the channel, with the liquid saturated near the heated wall and potentially highly subcooled in the core.

Figures 3.1(c) and 3.1(d) show images of the flow for G = 394.8 – 403.4 kg/m^{2}s (U = 0.25 m/s) and G = 1536.1 – 1570.3 kg/m^{2}s (U = 0.97 – 0.98 m/s), respectively, for low subcooling cases with $\Delta T_{sub,in}$ = 3.3 – 5.1°C. For top wall heating and U = 0.25 m/s, Fig. 3.1(c) shows a wavy vapor layer developing along the top wall and growing in both thickness and wavelength with increasing heat flux. Notice how the downstream of the two wave trough regions, where the liquid contacts the wall, is virtually eliminated at CHF. For bottom wall heating, the influence of gravity is quite apparent, as vapor generated along the bottom wall quickly detaches and moves towards the top wall while being replaced by

a downflow of liquid towards the lower wall. While this behavior is also observed in Fig. 3.1(a) for higher subcooling, the low subcooling in Fig. 3.1(c) is shown allowing greater vapor production as well as vapor mixing with the bulk liquid, and an appreciable increase in CHF for bottom wall heating compared to top wall heating. High vapor production is also shown inducing significant vapor-liquid mixing in Fig. 3.1(c) for the double-sided heating. CHF is greatly enhanced with double-sided heating in comparison to top and bottom wall heating because of axial flow acceleration resulting from the increased void fraction. Figure 3.1(d) shows flow behavior for $U = 0.97 – 0.98$ m/s, where inertia appears to dwarf gravity effects, resulting in more or less similar wavy vapor layer behavior for both top wall heating and bottom wall heating, and the double-sided heating combining vapor behaviors of the two walls when heated separately. Another effect of the inertia dominated flow is a narrower range of CHF values for the three wall heating configurations compared to Fig. 3.1(c).

Figures 3.1(e) and 3.1(f) show images of the flow for $G = 396.4 – 404.1$ kg/m^{2}s and $G = 800.6 – 803.2$ kg/m^{2}s, respectively, for inlet quality ranging from $0.03 – 0.18$. With a positive inlet quality, vapor is observed entering the heated portion of the flow channel. For top wall heating at $G = 396.4 – 404.1$ kg/m^{2}s, Fig. 3.1(e) shows a very thick wavy vapor layer, consisting of both the incoming vapor and the vapor generated by heating, propagating along the top wall. The thickness of the vapor layer increases with increasing heat flux until the vapor appears to engulf the entire cross-section at CHF. For bottom wall heating, high flow acceleration resulting from the large void fraction confines vapor activity to the bottom wall. This implies that the dominant role of gravity observed in Figs. 3.1(a) and 3.1(c) is greatly compromised with saturated inlet conditions. For double-sided

heating, a three-layer separated flow is established with wavy vapor layers covering both top and bottom walls, and a middle liquid layer in between. Notice that the top wall vapor layer is much thicker than the bottom wall vapor layer. This can be explained by buoyancy effects accumulating both incoming and generated vapor towards the top wall. Figure 3.1(f) shows flow behavior for $G = 800.6 - 803.2$ kg/m^{2}s and $x_{e,in} = 0.03 - 0.08$. A lower inlet quality for this case compared to Fig. 3.1(e) is shown reducing the amount of incoming vapor. There is also better symmetry in wavy vapor layer development along the top heated and bottom heated walls because of the high mass velocity. Additionally, high inertia helps achieve closer CHF values for the three wall heating configurations in Fig. 3.1(f) compared to those in Fig. 3.1(e).

Figure 3.2 shows 15 sequential images of the flow spaced 1.5 ms apart at 74-86% CHF for top wall heating (with only H_b on), for $G = 400.3 - 1597.2$ kg/m^{2}s ($U = 0.25 - 0.98$ m/s) and three types of inlet conditions: highly subcooled, slightly subcooled, and saturated. For high inlet subcooling of $\Delta T_{sub,in} = 25.6°C$ and $U = 0.29$ m/s, bubble nucleation commences downstream of the inlet, and the bubbles coalesce into a wavy vapor layer. Increasing the velocity to $U = 0.98$ m/s for the same high subcooling greatly reduces the thickness of the vapor layer. For low inlet subcooling of $\Delta T_{sub,in} = 3.6°C$, bubbles are seen nucleating closer to the inlet and coalescing into a thick wavy vapor layer. Increasing the velocity to $U = 0.98$ m/s for similarly small inlet subcooling decreases the wavelength of the vapor layer while increasing the number of wetting fronts in between. For saturated inlet conditions with $x_{e,in} = 0.08 - 0.17$, the vapor layer is initiated at the inlet where it is

G = 469.8 kg/m²s (U = 0.29 m/s), $\Delta T_{sub,in}$ = 25.6°C
80% CHF (CHF = 26.3 W/cm²)

G = 1597.2 kg/m²s (U = 0.98 m/s), $\Delta T_{sub,in}$ = 24.9°C
86% CHF (CHF = 34.7 W/cm²)

g$_e$

Flow

G = 403.4 kg/m²s (U = 0.25 m/s), $\Delta T_{sub,in}$ = 3.6°C
74% CHF (CHF = 9.3 W/cm²)

G = 1570.3 kg/m²s (U = 0.98 m/s), $\Delta T_{sub,in}$ = 3.3°C
79% CHF (CHF = 23.1 W/cm²)

G = 400.3 kg/m²s, $x_{e,in}$ = 0.18, 77% CHF (CHF = 12.2 W/cm²)

G = 803.2 kg/m²s, $x_{e,in}$ = 0.08, 76% CHF (CHF = 18.1 W/cm²)
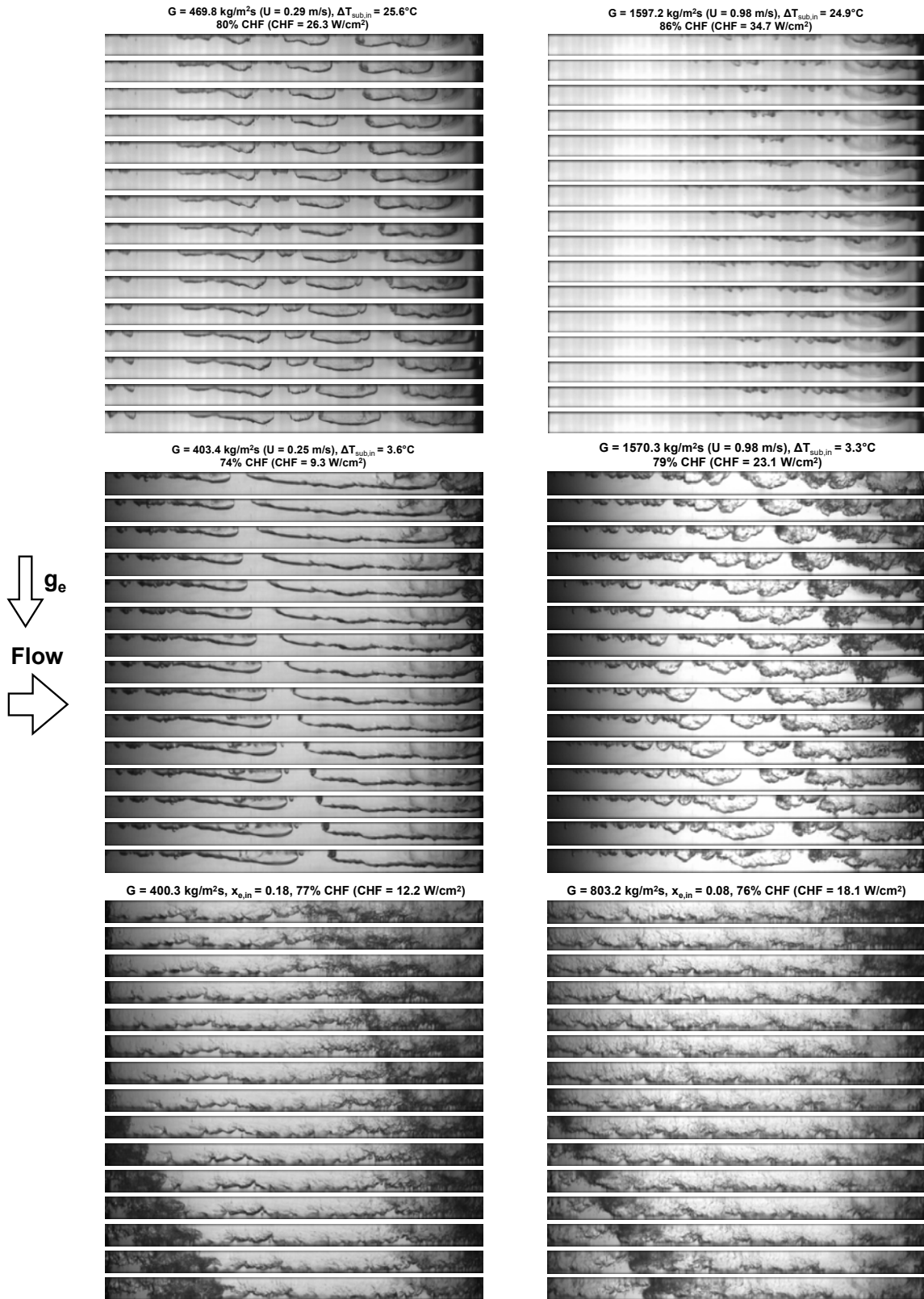
Fig. 3.2: Sequential high-speed video images from top wall heating experiments for different mass velocities, inlet subcoolings, and inlet qualities.

fed by the incoming vapor. The combination of incoming vapor and the vapor generated due to heating results in a comparatively very thick vapor layer along the top heated wall.

Figure 3.3 shows 15 sequential images of the flow spaced 1.5 ms apart at 75-85% CHF for bottom wall heating (with only H_a on) for $G = 396.4 - 1601.3$ kg/m²s ($U = 0.25 - 0.99$ m/s) and three types of inlet conditions: highly subcooled, slightly subcooled, and saturated. For high inlet subcooling of $\Delta T_{sub,in} = 25.5°C$ and $U = 0.25$ m/s, small vapor bubbles are seen forming upstream and both growing and coalescing as they propagate along the bottom wall. Relatively weak inertia allows gravity to draw the vapor across the channel towards the top wall. Some of these bubbles are seen to condense in the highly subcooled liquid. For a similar subcooling and a higher velocity of $U = 0.99$ m/s, the vapor formation is pushed farther downstream and the vapor layer is much thinner and, because of the high inertia, well confined to the lower wall. For low inlet subcooling of $\Delta T_{sub,in} = 5.1°C$ and $U = 0.25$ m/s, a thick vapor layer is seen forming along the bottom wall growing in thickness while approaching the top wall. Increasing the velocity to $U = 0.98$ m/s for a similarly low inlet subcooling increases the importance of inertia relative to buoyancy, which is manifest by a lesser tendency of the bottom wall's vapor layer to reach the top wall. For saturated inlet conditions with $x_{e,in} = 0.03 - 0.18$, the flow is comprised of three layers at the inlet as described by Kharangate *et al.* [34], with a very thin top layer of incoming vapor, a middle liquid layer and the newly generated vapor layer along the bottom wall. This behavior is less discernible downstream because of the high vapor void fraction.

G = 408.6 kg/m²s (U = 0.25 m/s), ΔT$_{sub,in}$ = 25.5°C
82% CHF (CHF = 31.8 W/cm²)

G = 1601.3 kg/m²s (U = 0.99 m/s), ΔT$_{sub,in}$ = 24.5°C
75% CHF (CHF = 39.5 W/cm²)

g$_e$

Flow

G = 400.5 kg/m²s (U = 0.25 m/s), ΔT$_{sub,in}$ = 5.1°C
85% CHF (CHF = 28.2 W/cm²)

G = 1567.4 kg/m²s (U = 0.98 m/s), ΔT$_{sub,in}$ = 3.8°C
75% CHF (CHF = 28.2 W/cm²)

G = 396.4 kg/m²s, x$_{e,in}$ = 0.18, 77% CHF (CHF = 27.1 W/cm²)

G = 802.0 kg/m²s, x$_{e,in}$ = 0.03, 79% CHF (CHF = 23.8 W/cm²)
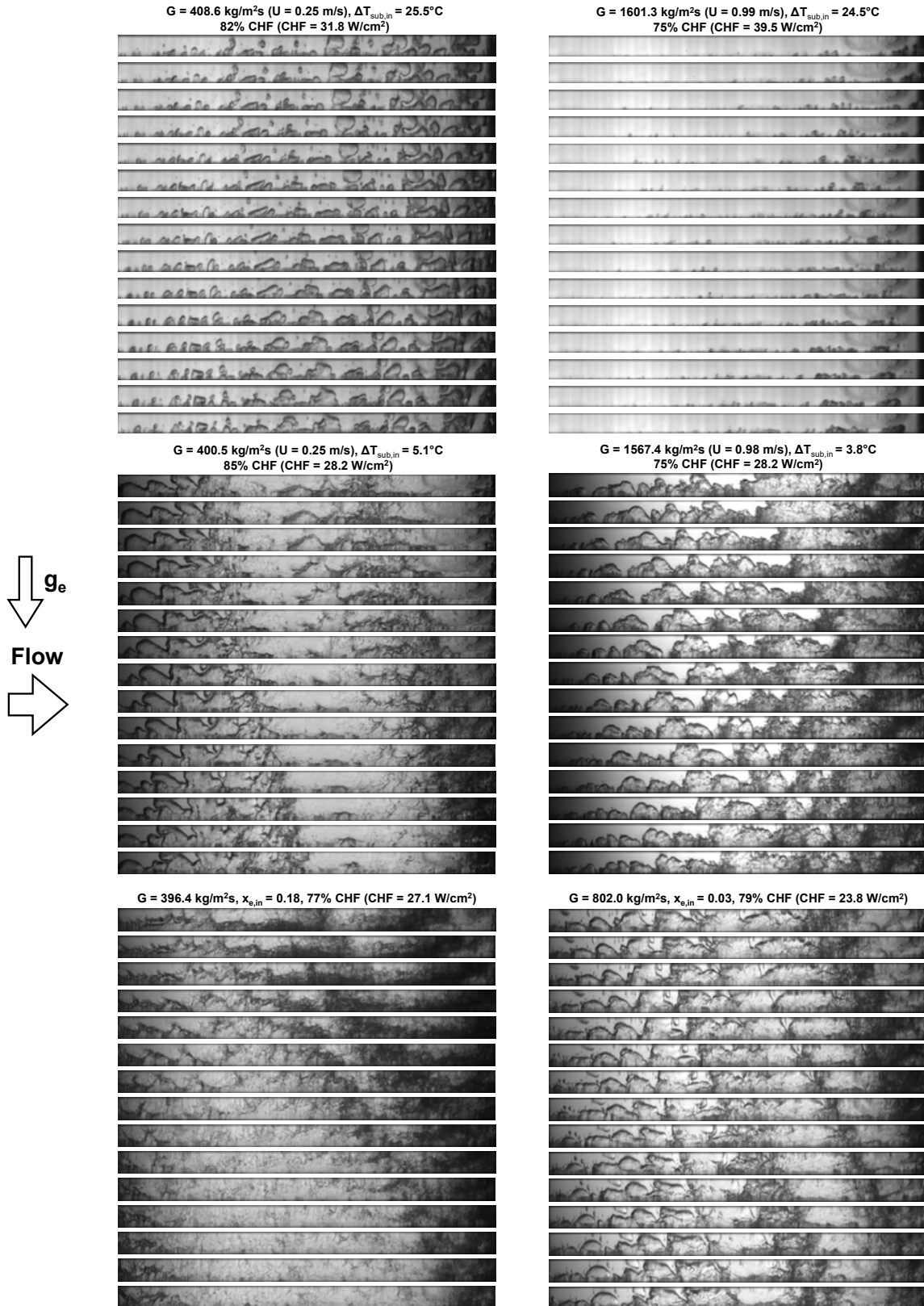
Fig. 3.3: Sequential high-speed video images from bottom wall heating experiments for different mass velocities, inlet subcoolings and inlet qualities.

Figure 3.4 shows 15 sequential images spaced 1.5 ms apart at 75-83% CHF for double-sided heating (with H_a and H_b simultaneously turned on) for $G = 394.8 - 1592.5$ kg/m²s ($U = 0.25 - 0.98$ m/s) and the three types of inlet conditions: highly subcooled, slightly subcooled, and saturated. For high inlet subcooling of $\Delta T_{sub,in} = 25.6°C$ and $U = 0.25$ m/s, there are clear differences in vapor formation along the top and bottom walls. For the bottom wall, small bubbles are generated along the bottom wall, which, because of relatively strong gravity effects at this low velocity, travel across towards the top wall where they accumulate into the top walls' wavy vapor layer. Increasing the velocity to $U = 0.98$ m/s for the same high inlet subcooling strengthens inertia relative to gravity, which is manifest by thinner vapor layers and lessened vapor accumulation along the top wall. For low inlet subcooling of $\Delta T_{sub,in} = 4.9°C$ and $U = 0.25$ m/s, the flow appears to combine the vapor layer behaviors exhibited by the two walls when heated separately as shown in Figs. 3.2 and 3.3 for similar inlet conditions. Increasing the velocity to $U = 0.97$ m/s for a similarly low inlet subcooling results in wavy vapor layers along the top and bottom walls exhibiting a wavy 'meshing' behavior, where the wave peak from one of the heated walls grows towards the trough (wetting front) between two wave peaks on the opposite wall, which is reminiscent of gear meshing as discussed by Konishi *et al.* [30,31] for flow boiling in microgravity at $U = 0.1 - 1.9$ m/s. For saturated inlet conditions with $x_{e,in} = 0.07 - 0.17$, vapor enters the heated portion of the channel attached to the top wall. This causes large differences between the thicknesses of the top and bottom layers, especially for the lower mass velocity of $G = 404.1$ kg/m²s.

G = 408.6 kg/m²s (U = 0.25 m/s), ΔT$_{sub,in}$ = 25.7°C
83% CHF (CHF = 18 W/cm²)

G = 1592.5 kg/m²s (U = 0.98 m/s), ΔT$_{sub,in}$ = 25.0°C
81% CHF (CHF = 37.1 W/cm²)

g$_e$

Flow

G = 394.8 kg/m²s (U = 0.25 m/s), ΔT$_{sub,in}$ = 4.9°C
76% CHF (CHF = 18 W/cm²)

G = 1536.1 kg/m²s (U = 0.97 m/s), ΔT$_{sub,in}$ = 5.0°C
81% CHF (CHF = 29.6 W/cm²)

G = 404.1 kg/m²s, x$_{e,in}$ = 0.17, 75% CHF (CHF = 16.2 W/cm²)

G = 800.6 kg/m²s, x$_{e,in}$ = 0.07, 79% CHF (CHF = 24 W/cm²)
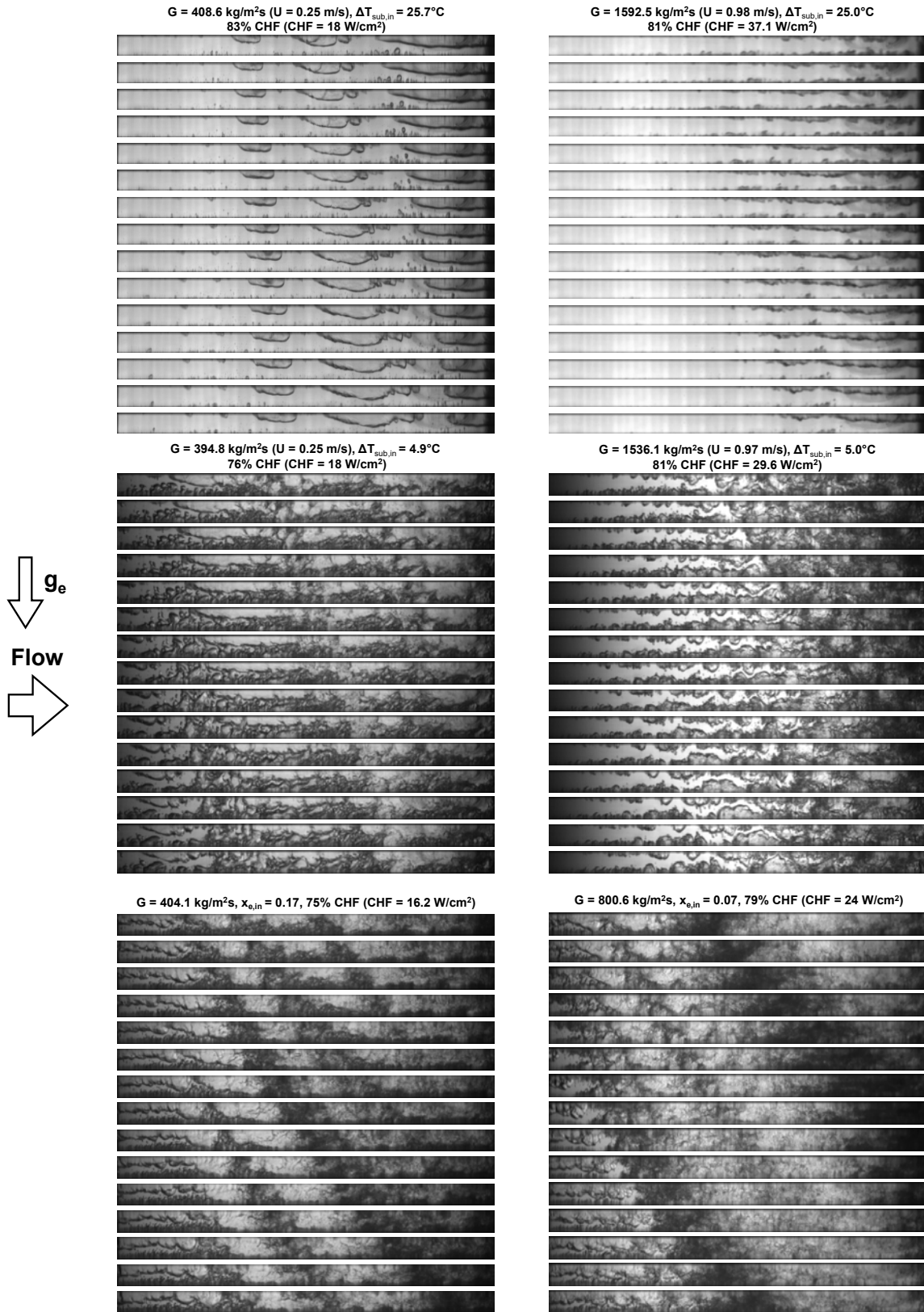
Fig. 3.4: Sequential high-speed video images from double-sided heating experiments for different mass velocities, inlet subcoolings, and inlet qualities.

3.2 <u>Experimental Results</u>

3.2.1 <u>CHF Trends</u>

Figure 3.5(a) shows the variation of CHF with mass velocity for top wall heating, bottom wall heating, and double-sided heating configurations and the three inlet conditions of highly subcooled ($\Delta T_{sub,in} = 24.5 - 31°C$), slightly subcooled ($\Delta T_{sub,in} = 3.3 - 7.7°C$), and saturated ($x_{e,in} = 0.03 - 0.18$).

For the low subcooling and saturated inlet cases, CHF for $G < 800$ kg/m²s is lowest for top wall heating due to vapor accumulation along the top wall by the relatively strong buoyancy effects as observed in Figs. 3.1(c) and 3.1(e). Also for $G < 800$ kg/m²s, bottom wall heating is shown to yield the highest CHF because of the strong buoyancy effects that assist vapor removal from the bottom heated wall towards the top unheated wall and increase mixing as well as bulk liquid access to the bottom heated wall. For the low subcooling and saturated inlet cases, double-sided heating yields CHF values for $G < 800$ kg/m²s that are in between those for top wall heating and bottom wall heating. The double-sided configuration could be viewed as a superposition of the two other heating configurations. For low inlet subcooling ($\Delta T_{sub,in} = 3.3 - 7.7°C$) and $G > 1600$ kg/m²s, double-sided heating outperforms the other two configuration. As shown earlier in Fig. 3.1(d), this inertia dominated range tends to confine vapor during double-sided heating to the individual walls, while also capitalizing on the heat transfer enhancement resulting from greater axial flow acceleration compared to individually heated walls. Notice also for low inlet subcooling that CHF values for all three heating configurations converge around $G = 3200$ kg/m²s, where the vapor layers become quite thin and axial acceleration quite low. For saturated inlet ($x_{e,in} = 0.03 - 0.18$), CHF values for all three heating configs.
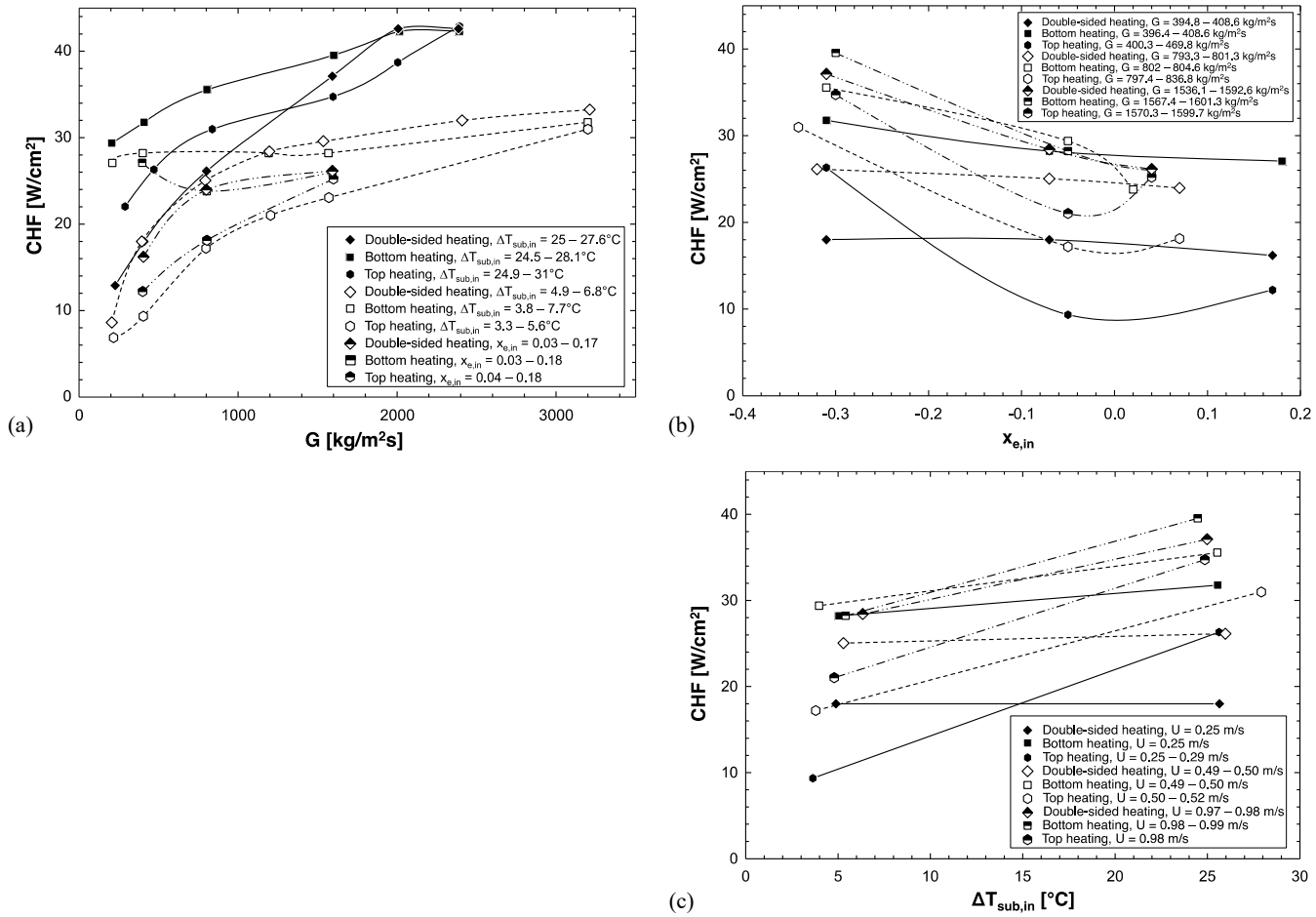
Fig. 3.5: Variations of CHF with (a) mass velocity, (b) inlet quality, and (c) inlet subcooling for top wall heating, bottom wall heating and double-sided heating.

converge around 1600 kg/m^{2}s. With respect to the high inlet subcooling ($\Delta T_{sub,in} = 24.5 - 31°C$) cases, Fig. 3.5(a) also shows that bottom wall heating outperforms the other heating configurations for lower mass velocities, in this case $G < 1600$ kg/m^{2}s. However, unlike the low subcooling and saturated inlet cases, CHF for double-sided heating is lower than for top wall heating for $G < 1600$ kg/m^{2}s. This behavior can be explained by examining Fig. 3.1(a), which shows double-sided heating allowing vapor generated from the bottom wall to accumulate along the top wall, resulting in further thickening of the top wall vapor layer. Convergence of CHF values for the three heating configurations for the high subcooling cases occurs around $G = 2400$ kg/m^{2}s. Overall, it is worth noting that flow acceleration is low for high subcooling, which may explain some of the differences in CHF trends between high subcooling cases on one hand and both low subcooling and saturated cases on the other.

Figure 3.5(b) shows the variation of CHF with inlet equilibrium quality, $x_{e,in}$, for top wall heating, bottom wall heating, and double-sided heating configurations, and mass velocities of $G = 394.6 - 469.8$ kg/m^{2}s, $793.3 - 836.8$ kg/m^{2}s and $1536.1 - 1601.3$ kg/m^{2}s. In the subcooled region where $x_{e,in} < 0$, CHF is seen to decrease monotonically with increasing $x_{e,in}$, (*i.e.,* decreasing inlet subcooling). Bottom heating and double-sided heating show CHF continuing to decrease with increasing $x_{e,in}$ for $x_{e,in} > 0$, which is to be expected since reduced liquid content decreases the energy required to trigger CHF. However, top wall heating does not follow this trend and CHF increases with increasing $x_{e,in}$ for $x_{e,in} > 0$. This reversal in trend relative to the two other heating configurations can be explained by the high positive $x_{e,in}$ values producing appreciable flow acceleration,

which increase inertia compared to gravity effects, eliminating the detrimental effects of vapor accumulation along the top wall.

Figure 3.5(c) shows the variation of CHF with inlet subcooling for only the highly subcooled and slightly subcooled cases. CHF increases monotonically with increasing subcooling for all cases because of the need to overcome the liquid's increasing sensible heat deficiency prior to evaporation. CHF variations among the three different heating configurations for a given velocity are consistent with those of CHF versus $x_{e,in}$ for $x_{e,in} <$ 0 in Fig. 3.5(b).

3.2.2 Flow Boiling Curves

As shown earlier in Fig. 2.1(e), the heated walls are fitted each with seven thermocouples for wall temperature measurements. The temperatures are designated as $T_{w1,n}$ and $T_{w2,n}$, where 1 and 2 refer to top heated wall H_b and bottom heated wall H_a, respectively, and n thermocouple axial location along the respective heated wall. Figures 3.6(a) – 3.6(c) show boiling curves for $G = 394.8 – 1601.3$ kg/m^{2}s ($U = 0.25 – 0.99$ m/s) for top wall heating, bottom wall heating, and double-sided heating, respectively, for highly subcooled, slightly subcooled and saturated inlet conditions. The wall heat flux, q''_w, is plotted against the difference between average wall temperature, $T_{w,avg}$, and inlet saturation temperature, $T_{sat,in}$. All curves exhibit trends observed in a typical boiling curve, with the slope increasing as the flow transitions from single phase to nucleate boiling, then decreasing sharply just before CHF. However, the transition points differ for different inlet conditions and heating configurations. For top wall heating and high inlet subcooling of $\Delta T_{sub,in} = 24.9 – 25.6°C$, Fig. 3.6(a) shows increasing G from 469.8 to 1597.2 kg/m^{2}s shifts
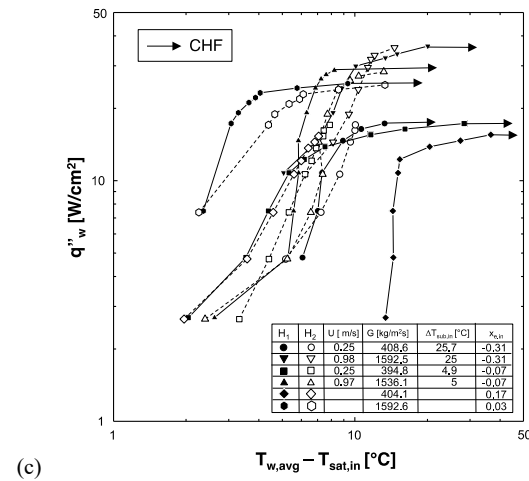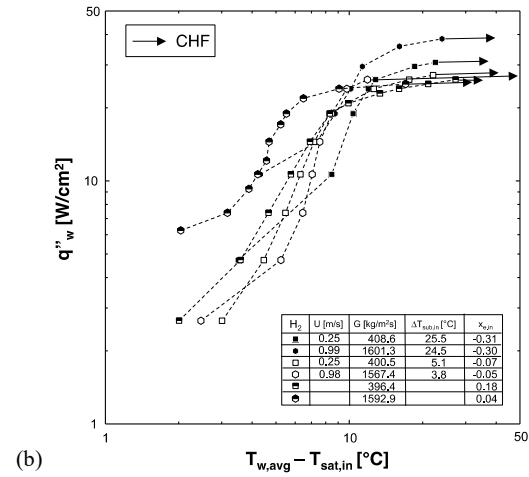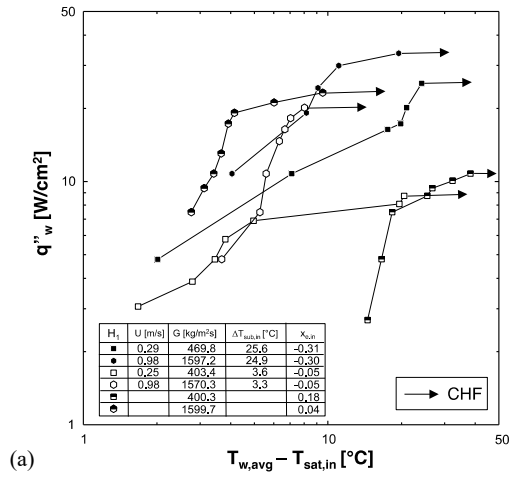
Fig. 3.6: Boiling curves for different mass velocities, inlet subcoolings, and inlet qualities for (a) top wall heating, (b) bottom wall heating, and (c) double-sided heating.

the entire boiling curve upwards. An even more profound upward shift in the boiling curve is achieved with increasing G for both low inlet subcooling of $\Delta T_{sub,in} = 3.3 - 3.6°C$ and saturated inlet with $x_{e,in} = 0.04 - 0.18$. Increased sensitivity to G with low subcooling and saturated inlet conditions reflects the strong negative influence of gravity in the form of substantial thickening of the vapor layer along the top wall for low G, compared to a more inertia dominated flow thinning the same vapor layer for high G. For bottom wall heating, Fig. 3.6(b) shows overall trends similar to those for top wall heating, with the main difference that the overall influence of G is abated compared to Fig. 3.6(a), especially for the low subcooling and saturated inlet conditions. For double-sided heating, Fig. 3.6(c), where the flow is influenced by vapor layer development along both walls, the effect of G is exacerbated as for top wall heating, Fig. 3.6(a). This effect is most pronounced for the saturated inlet cases with $x_{e,in} = 0.03 - 0.17$. Another observation in Fig. 3.6(c) is that the boiling curves for the individual walls in the double-sided configuration are more or less reflective of trends of same walls in single-sided heating configurations, Figs. 3.6(a) and 3.6(b). A notable difference for double-sided heating versus both top wall and bottom wall heating is a steeper slope in the nucleate boiling region, which, as discussed earlier, is a reflection of greater flow acceleration with double-sided heating.

3.2.3 Heated Wall Temperatures

Figures 3.7(a) – 3.7(c) show temporal records of the heated wall temperatures for $G = 1536.1 - 1601.3$ kg/m^{2}s for top wall heating, bottom wall heating, and double-sided heating during the CHF transient for highly subcooled ($\Delta T_{sub,in} = 24.5 - 25°C$), slightly subcooled
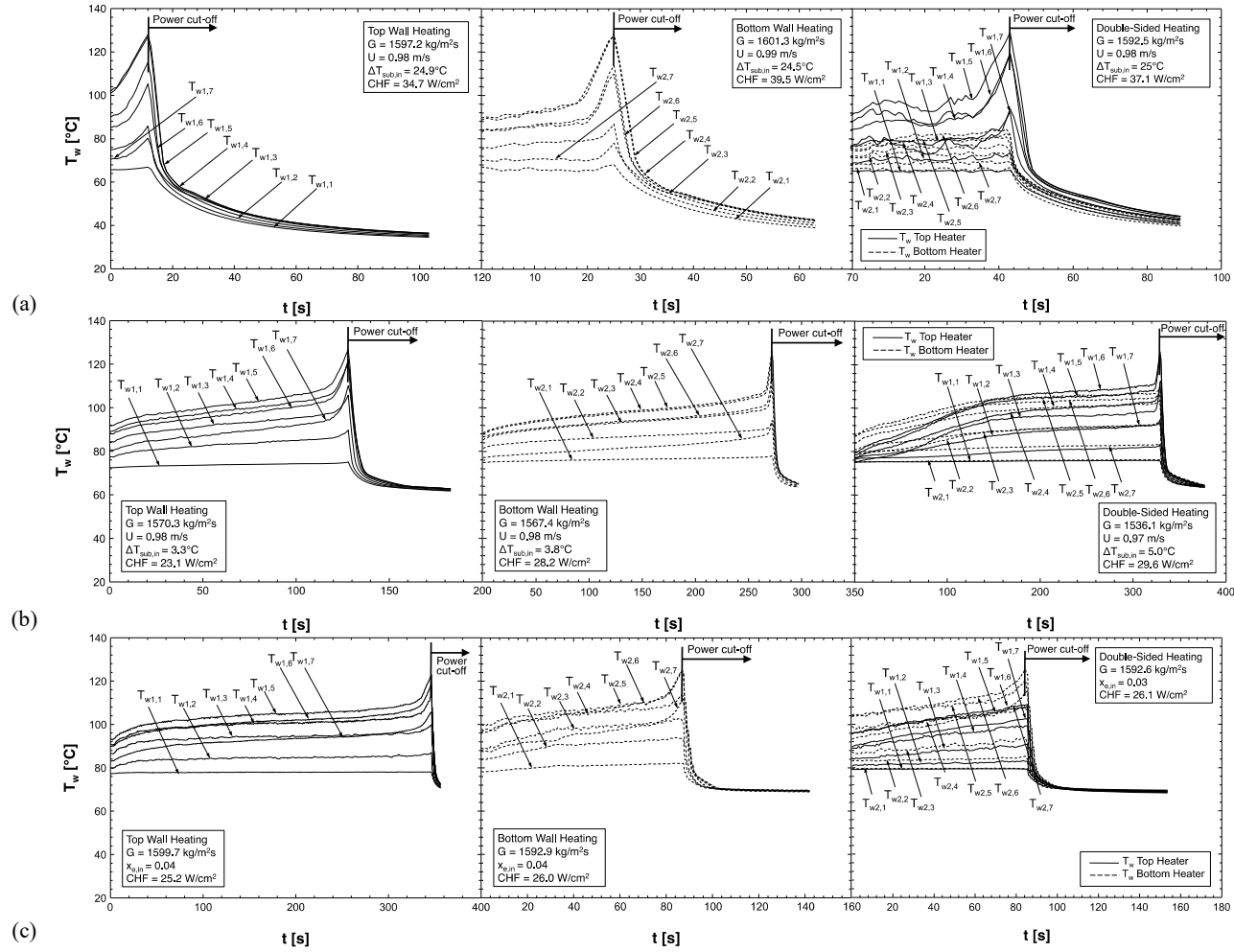
Fig. 3.7: Temporal records of wall thermocouples during CHF transient for different mass velocities and top wall heating, bottom wall heating, and double-sided heating for (a) $\Delta T_{sub,in}$ = 24.5 – 25°C, (b) $\Delta T_{sub,in}$ = 3.3 – 5.0°C, and (c) $x_{e,in}$ = 0.03 – 0.04.

($\Delta T_{sub,in} = 3.3 - 5.0°C$), and saturated ($x_{e,in} = 0.03 - 0.04$) inlet conditions, respectively. The x-axis in these plots indicates the time in seconds starting the instant the last heat flux increment that culminated in CHF is initiated. As discussed earlier, power input to the heaters is automatically cut off once any of the relay thermocouples exceeds 130°C. A common trend observed for most cases and all three heating configurations is temperatures increasing from the leading edge of the heated wall ($T_{w1,1}$, $T_{w2,1}$) to a maximum immediately downstream from the middle ($T_{w1,5}$ or $T_{w1,6}$, $T_{w2,5}$ or $T_{w2,6}$), before decreasing again towards the exit ($T_{w1,7}$, $T_{w2,7}$). This can be explained by the fact that flow acceleration and increased vapor layer thickness counter act to give the heat transfer trends observed. Figure 3.7(a) shows CHF is triggered over a much shorter time span for high inlet subcooling of $\Delta T_{sub,in}$ = 24.5 – 25°C compared to both slightly subcooled inlet, Fig. 3.7(b), and saturated inlet, Fig. 3.7(c).

3.2.4 Heat Transfer Coefficients

The local heat transfer coefficient at a thermocouple location along a heated wall is obtained from the relation

$$h_{m,n} = \frac{q''_w}{\left(T_{wm,n} - T_f\right)},$$ (3.1)

where q''_w is the wall heat flux, $T_{wm,n}$ the wall temperature measured along heated wall m ($m = a$ for H_a and b for H_b), n the thermocouple location, and T_f the bulk fluid temperature. For double-sided heating, the bulk fluid temperatures for the subcooled and saturated regions are given, respectively, by

$$T_{f,n+1} = T_{f,n} + \frac{\left(q''_{w1} + q''_{w2}\right)W\Delta z}{\dot{m}c_{p,f}} \quad \text{for } x_e < 0$$ (3.2a)

and
$$T_f = T_{sat} \quad \text{for} \;\; 0 \le x_e \le 1. \tag{3.2b}$$

The above equations are also used for single-sided heating by setting $q''_{w1} = 0$ for bottom wall heating, or $q''_{w2} = 0$ for top wall heating. A single value of the heat transfer coefficient is determined for each thermocouple location, and the values for all thermocouples along a heated wall are then spatially averaged to determine h_{avg}.

Figures 3.8(a) – 3.8(c) show the variations of h_{avg} with q''_w for $G = 394.8 – 1601.3$ kg/m^{2}s and $\Delta T_{sub,in} = 0 – 25.6°C$ and $x_{e,in} = $ -0.31 – 0.18, for top wall heating, bottom wall heating, and double-sided heating, respectively. For top wall heating, Fig. 3.8(a) shows h_{avg} increases with increasing G for each set of inlet conditions. For $\Delta T_{sub,in} = 24.9 – 25.6°C$, the variation of h_{avg} with q''_w is rather subdued. For $\Delta T_{sub,in} = 3.3 – 3.6°C$ and $x_{e,in} = 0.04 – 0.18$, h_{avg} increases to a peak value, and then decreases until CHF is reached. For $x_{e,in} = 0.04 – 0.18$, h_{avg} is substantially higher than for $\Delta T_{sub,in} = 24.9 – 25.6°C$. This difference can be explained by the highly subcooled flow inhibiting bubble nucleation along the heated length, which compromises heat transfer effectiveness. Figures 3.8(b) and 3.8(c) show fairly similar trends of h_{avg} versus q''_w for bottom heating and double-sided heating, respectively. Overall, Figs. 3.8(a) - 3.8(c) show that the influence of G on h_{avg} is relatively small for highly subcooled inlet, more significant for slightly subcooled inlet, and quite substantial for saturated inlet. For top wall heating and double-sided heating, the influence of G on h_{avg} is apparent for both slightly subcooled and saturated inlet cases, while for bottom heating, this influence is limited to saturated inlet cases only. The variations of h_{avg} with q''_w for double-sided heating in Fig. 3.8(c) bare some similarity
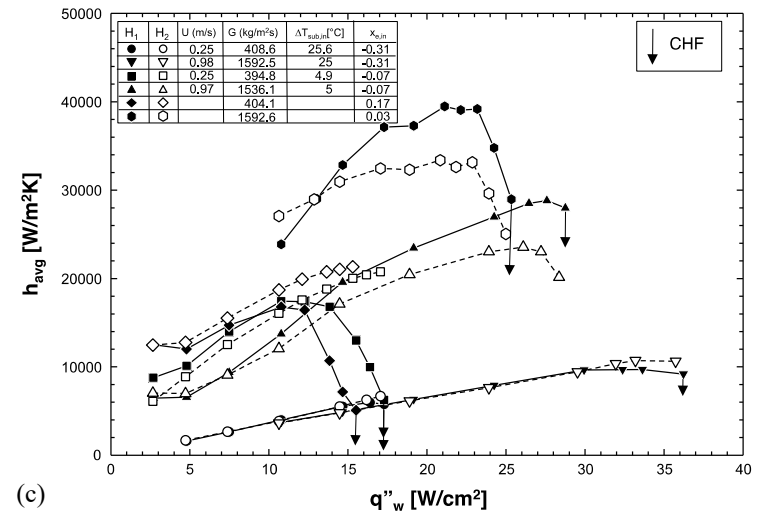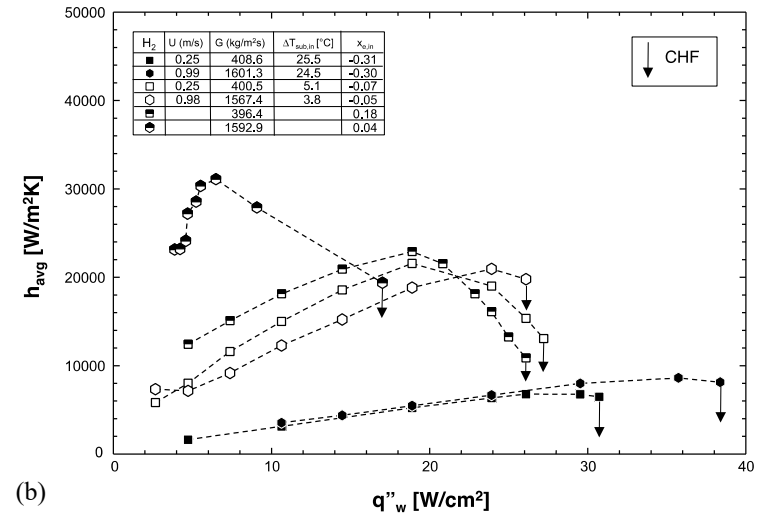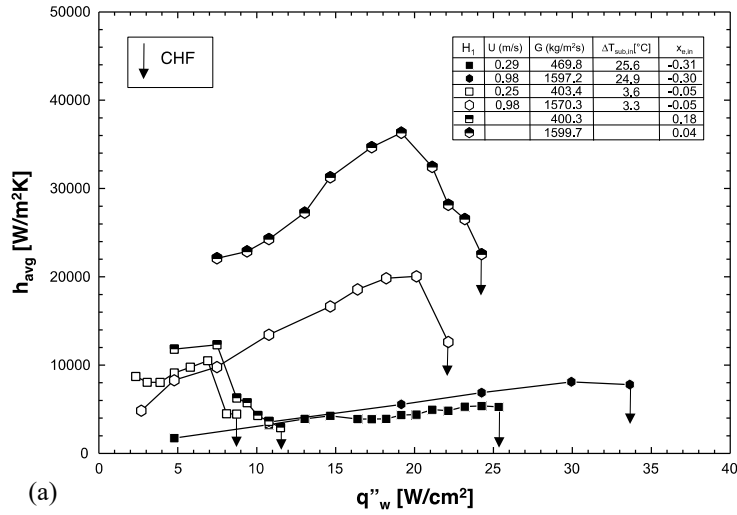
Fig. 3.8: Variations of average heat transfer coefficient with wall heat flux for different inlet mass velocities, inlet subcoolings, and inlet qualities for (a) top wall heating, (b) bottom wall heating, and (c) double-sided heating.

Table in (a):

H_1	U (m/s)	G (kg/m²s)	$\Delta T_{sub,in}$ [°C]	$x_{e,in}$
■	0.29	469.8	25.6	-0.31
●	0.98	1597.2	24.9	-0.30
□	0.25	403.4	3.6	-0.05
○	0.98	1570.3	3.3	-0.05
▣		400.3		0.18
◐		1599.7		0.04

Table in (b):

H_2	U (m/s)	G (kg/m²s)	$\Delta T_{sub,in}$ [°C]	$x_{e,in}$
■	0.25	408.6	25.5	-0.31
●	0.99	1601.3	24.5	-0.30
□	0.25	400.5	5.1	-0.07
○	0.98	1567.4	3.8	-0.05
▣		396.4		0.18
◐		1592.9		0.04

Table in (c):

H_1	H_2	U (m/s)	G (kg/m²s)	$\Delta T_{sub,in}$ [°C]	$x_{e,in}$
●	○	0.25	408.6	25.6	-0.31
▼	▽	0.98	1592.5	25	-0.31
■	□	0.25	394.8	4.9	-0.07
▲	△	0.97	1536.1	5	-0.07
◆	◇		404.1		0.17
●	○		1592.6		0.03

(a)   (b)   (c)

to the variations of respective individually heated top wall, Fig. 3.8(a), and bottom wall, Fig. 3.8(b), though overall heat transfer performance is higher than for single-sided heating. Comparing these trends with those for CHF in Figs. 3.5(a) – 3.5(c) show that increasing subcooling enhances CHF but decreases h_{avg} significantly.

Thus far, double-sided heating appears to combine the effects of single-sided heating configurations. To further explore this trend, it is useful to examine the axial variations of the local heat transfer coefficient, h, for the double-sided heating. Figures 3.9(a) – 3.9(c) show these variations for $G = 1536.3 – 1592.6$ kg/m²s for high subcooled inlet ($\Delta T_{sub,in} = 25°C$), slightly subcooled inlet ($\Delta T_{sub,in} = 5.0°C$), and saturated inlet ($x_{e,in} = 0.03$), respectively. For $\Delta T_{sub,in} = 25°C$, Fig. 3.9(a) shows the variation of h with z is rather flat, but shifted upwards with increasing q''_w. For $\Delta T_{sub,in} = 5°C$, Fig. 3.9(b) shows a similarly flat variation of h with z for low heat fluxes. And while there is an upwards shift with increasing q''_w, there are appreciable axial variations in h for high heat fluxes, especially close to CHF. These spatial variations are the result of wavy vapor layer formation and development along the channel.

For saturated inlet with $x_{e,in} = 0.03$, Fig. 3.9(c) shows variations of h with z for heat fluxes ranging from 50% CHF to 96% CHF. Here, h is highest at the inlet to the heated portion of the channel and decreases appreciably with z before increasing again downstream. The upstream decrease is apparently the result of appreciable thickening of the incoming vapor layers along both walls due to vapor generation by heating. However, h begins to increase downstream due to intensified flow acceleration brought about by the vapor production. Figure 3.9(c) also shows h increasing with increasing q''_w up to 73% CHF, because of the benefits of added flow acceleration, and decreasing as CHF is
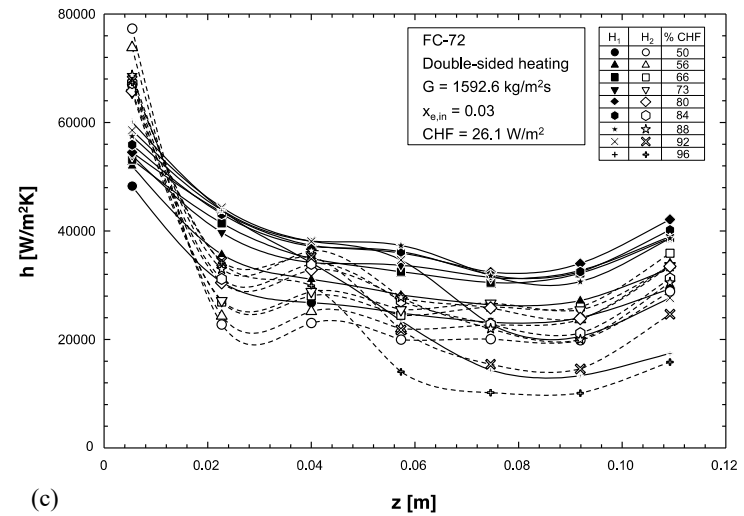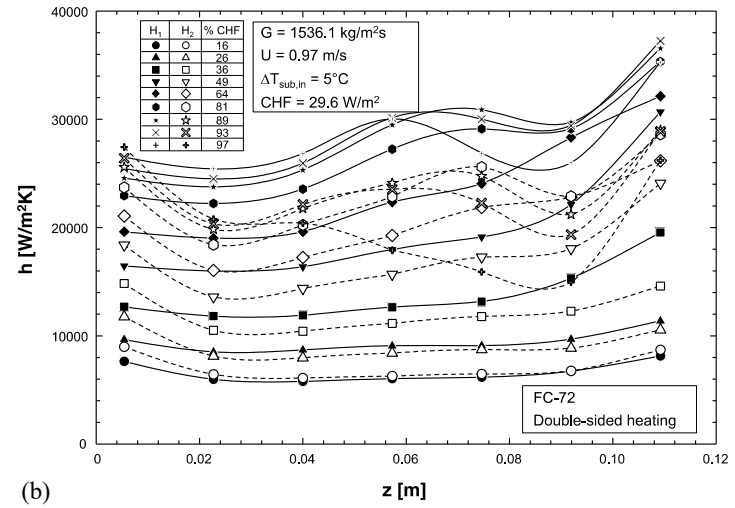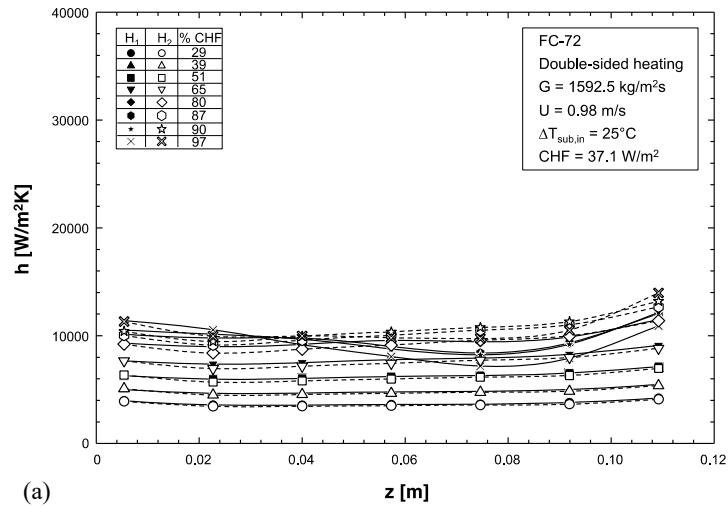
Fig. 3.9: Variations of local heat transfer coefficient along the channel for double-sided heating with increasing heat flux for G = 1536.1 – 1592.6 kg/m^{2}s and (a) $\Delta T_{sub,in}$ = 25°C, (b) $\Delta T_{sub,in}$ = 5°C, and (c) $x_{e,in}$ = 0.03.

approached as the detrimental effects of thicker insulating vapor layers begin to outweigh the merits of acceleration.

Figures 3.10(a) – 3.10(c) show the variations of h with z for double-sided heating and different mass velocities for high subcooled inlet ($\Delta T_{sub,in}$ = 25 – 27.4°C), slightly subcooled inlet ($\Delta T_{sub,in}$ = 4.9 – 6.7°C), and saturated inlet ($x_{e,in}$ = 0.03 – 0.17), respectively. The values of wall heat flux in these figures correspond to those that yield peak h_{avg} values as depicted earlier in Figs. 3.8(a) – 3.8(c). In Fig. 3.10(a), the variation of h with z for $\Delta T_{sub,in}$ = 25 – 27.4°C is rather flat and shifted upwards with increasing G. For $\Delta T_{sub,in}$ = 4.9 – 6.7°C, Fig. 3.10(b) shows h values increase appreciably compared to those in Fig. 3.10(a), but the axial variations are more complex, reflecting the aforementioned effects of both vapor layer development and flow acceleration. For $x_{e,in}$ = 0.03 – 0.17, Fig. 3.10(c) shows improvement in overall heat transfer performance, with the highest h occurring at the upstream edge, and downstream variations reflecting both vapor layer development and flow acceleration effects. One notable trend in Fig. 3.10(c) is the significant difference in heat transfer performance between the top and bottom heating walls at the leading edge for G = 404.1 kg/m²s. This trend can be attributed to the combined effects of incoming vapor and strong buoyancy accumulating vapor mostly against the top wall for this low mass velocity. Figs. 3.10(a) and 3.10(c) show that heat 2.04 m/s) are quite close. This apparent anomaly can be explained as follows. For low inlet subcooling, there is a trade-off when comparing heat transfer results for different mass velocities at the same wall heat flux, where a lower velocity yields higher vapor void, especially downstream, offsetting the benefits of higher velocity. The absence of this anomaly for $\Delta T_{sub,in}$ = 25 – 27.4°C,

H_1	H_2	U [m/s]	G [kg/m²s]	% CHF
●	○	0.25	408.6	95
▼	▽	0.98	1592.5	90
■	□	1.47	2386.3	94

FC-72
Double-Sided Heating
$\Delta T_{sub,in} = 25 - 27.4°C$

(a)

H_1	H_2	U [m/s]	G [kg/m²s]	% CHF
●	○	0.25	394.8	76
▼	▽	0.97	1536.1	89
■	□	2.04	3211.6	86

FC-72
Double-Sided Heating
$\Delta T_{sub,in} = 4.9 - 6.7°C$

(b)

H_1	H_2	G [kg/m²s]	% CHF
●	○	404.1	75
▼	▽	800.6	79
■	□	1592.6	80

FC-72
Double-Sided Heating
$x_{e,in} = 0.03 - 0.17$
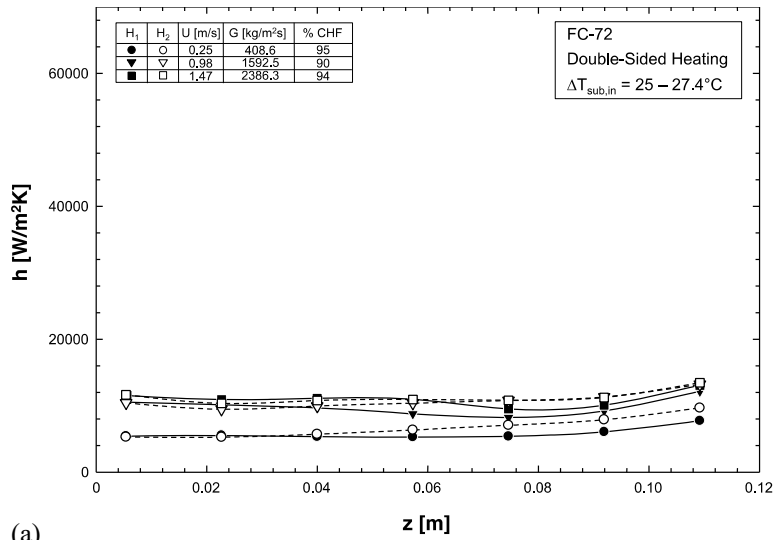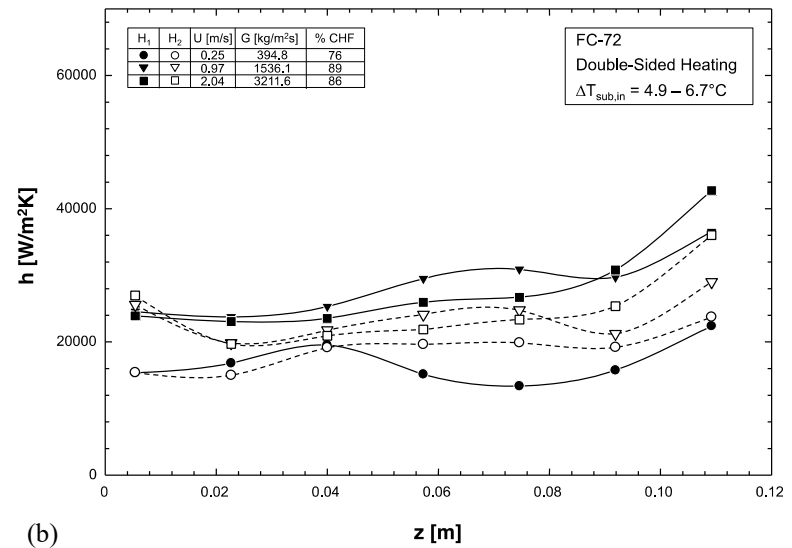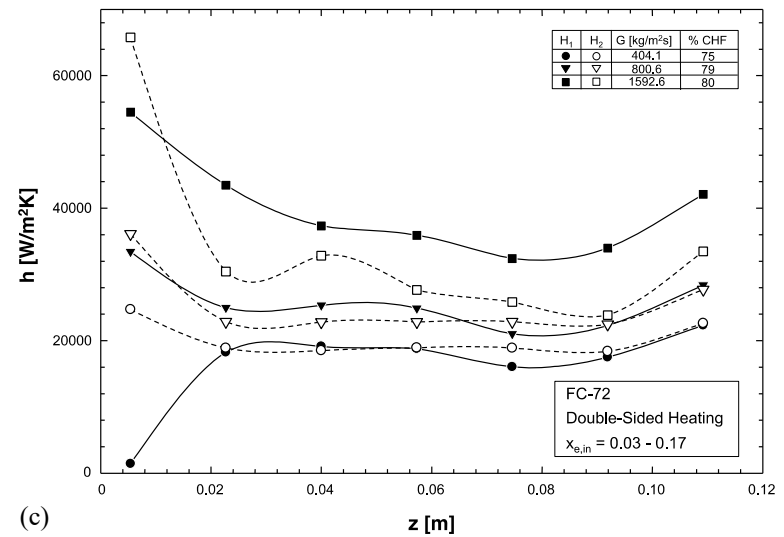
(c)

Fig. 3.10: Variations of local heat transfer coefficient along the channel for double-sided heating and different mass velocities for (a) $\Delta T_{sub,in} = 25 - 27.4°C$, (b) $\Delta T_{sub,in} = 4.9 - 6.7°C$, and (c) $x_{e,in} = 0.03 - 0.17$.

Fig. 3.10(a), and $x_{e,in} = 0.03 - 0.17$, Fig. 3.10(c), points to the complexity of assessing the combined influence of inlet quality and mass velocity on heat transfer and CHF.

3.2.5 Effects of Subcooling on CHF

A series of prior studies by Galloway and Mudawar [49,50], and Sturgis and Mudawar [32,33] have culminated in a theoretical *Interfacial Lift-off Model* for flow boiling CHF corresponding to zero subcooling that yields

$$CHF_{sat} = b \rho_g h_{fg} \left[\left(\frac{4\pi\sigma\delta}{\rho_g b \lambda_c^2} \sin(\pi b) \right) \Big|_{z^*} \right]^{1/2}, \tag{3.3}$$

where b, δ and λ_c, are, respectively, the ratio of wetting front length to wavelength, mean vapor layer thickness, and critical wavelength, all determined at axial location z^* (extent of upstream wetting front) using a two-phase slip flow model. The same model was later proven by Zhang *et al.* to be highly effective at predicting CHF for different flow orientation relative to Earth gravity [53] as well as for flow boiling in microgravity [56]. Zhang *et al.* [28] later extended this model to highly subcooled conditions according to

$$CHF_{sub} = \frac{b}{\varepsilon} \rho_g (h_{fg} + c_{pf} \Delta T_{sub,out}) \left[\left(\frac{4\pi\sigma\delta}{\rho_g b \lambda_c^2} \sin(\pi b) \right) \Big|_{z^*} \right]^{1/2}, \tag{3.4}$$

where $\Delta T_{sub,out}$ is the outlet subcooling, and ε the heat utility ratio. Two key criteria concerning the magnitude of this parameter are $0 \leq \varepsilon \leq 1$ for subcooled flow, and $\varepsilon = 1$ for saturated flow. Zhang *et al.* [28] developed the following empirical relation for ε

$$\varepsilon = 1 - 0.00285 \frac{\rho_f}{\rho_g} \frac{c_{p,f} \Delta T_{sub,out}}{h_{fg}} \left(\frac{\rho_f U^2 D}{\sigma} \right)^{0.2}, \tag{3.5}$$

where D is the channel's hydraulic diameter.

Figure 3.11(a) shows the variation of heat utility ratio according to Eq. (3.5) for $U =$ 0.25, 0.5, 1 and 1.5 m/s, and a saturation pressure of 150 kPa. The heat utility ratio has a value of $\varepsilon = 1$ for $\Delta T_{sub,out} = 0$, and decreases with increasing subcooling. From Eq. (3.4), it is evident that CHF increases with decreasing ε, *i.e.,* with increasing subcooling. Figure 3.11(a) shows a 20 – 45% decrease in ε at 30°C subcooling, depending on flow velocity. This behavior is consistent with the trend of CHF increasing monotonically with increasing subcooling (albeit inlet rather than outlet) captured in Fig.3.5(c) for the present data. Another important trend that is manifest in Fig.3.11(a) is the steepening of negative slope of ε, or positive slope for CHF, with increasing velocity, a trend also captured in Fig. 3.5(c) for bottom wall heating and double-sided heating, but not top wall heating. This is a reflection of the fact that the influence of heat utility ratio on CHF according to Eqs. (3.4) and (3.5) is intended to account for the effects of subcooling and velocity but not gravity [28]. For top wall heating, CHF is highly influenced by gravity for low velocity and inertia for high velocity, which leads to a less than monotonic variation of CHF versus velocity.

Dividing the expression for CHF for subcooled outlet conditions, Eq. (3.4), by the expression for zero outlet subcooling, Eq. (3.3), and substituting the expression for ε, Eq. (3.5), yields the dimensionless relation

$$\frac{CHF_{sub}}{CHF_{sat}} = \frac{\left[1 + \dfrac{c_{p,f}\, \Delta T_{sub,out}}{h_{fg}} \right]}{1 - 0.00285 \dfrac{\rho_f}{\rho_g} \dfrac{c_{p,f}\, \Delta T_{sub,out}}{h_{fg}} \left(\dfrac{\rho_f U^2 D}{\sigma} \right)^{0.2}}. \qquad (3.6)$$

(a)

(b)
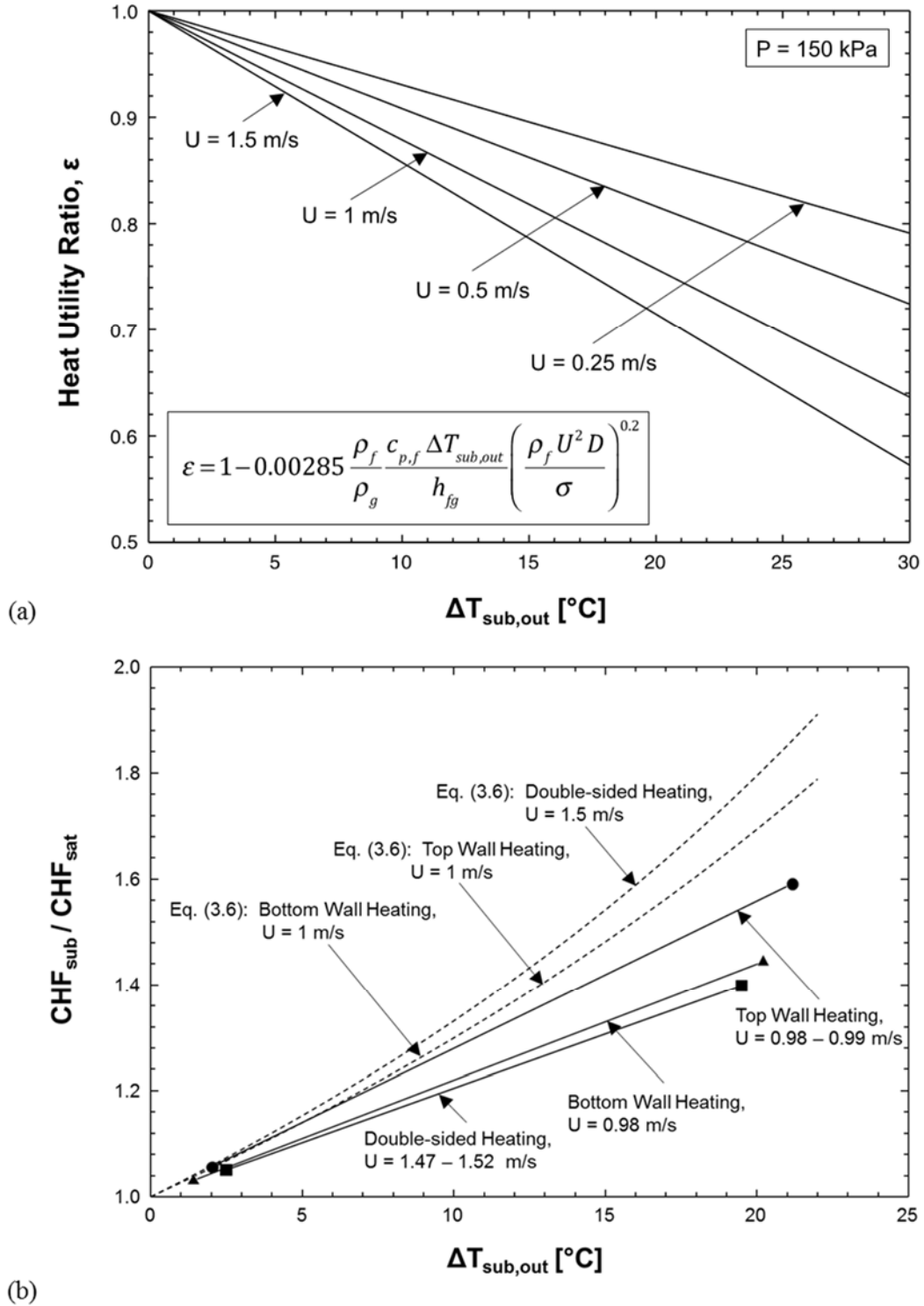
Fig. 3.11: (a) Variation of heat utility ratio with outlet subcooling for $U = 0.25 - 1.5$ m/s, and (b) Comparison of CHF ratio of subcooled outlet to saturated outlet with experimental data.

Using pairs of inlet subcooling conditions with the same flow velocity for each of the three heating configurations, Fig. 3.11(b) compares the measured CHF ratio for subcooled flow to saturated flow at the exit with predictions according to Eq. (3.6). Note that the curves for top wall heating and bottom wall heating in Fig. 3.11(b) overlap. Overall, the measured trends are similar to those predicted by Eq. (3.6), however, the predictions show measureable divergence from the data that increases with increasing subcooling. Better predictions are achieved with top wall heating compared to both bottom wall and double-sided heating.

Future studies with more extensive data may both refine this comparison and yield more accurate correlations that are heating configuration dependent. These endeavors must take advantage of sophisticated instrumentation methods to measure local liquid velocity [74] as well as interface location and temperature distribution across the channel [75].

3.3 Conclusions

This section explored the influence of inlet subcooling and two-phase inlet on flow boiling and CHF in a rectangular channel for top wall heating, bottom wall heating and double-sided heating configurations. FC-72 was used as a working fluid with three inlet conditions: highly subcooled liquid ($\Delta T_{sub,in}$ = 24.5 – 31°C), slightly subcooled liquid ($\Delta T_{sub,in}$ = 3.3 – 7.7°C), and saturated two-phase mixture ($x_{e,in}$ = 0.03 – 0.18) for mass velocities of G = 205.1 – 3211.6 kg/m²s. High-speed video imaging was also used to identify dominant interfacial characteristics for different combinations of inlet conditions and heating configurations. Key findings from the study are as follows.

(1) Overall, gravity plays a dominant role on interfacial behavior for low mass velocities around 400 kg/m²s. This role is manifest in vapor removal from the bottom wall and vapor accumulation along the top wall. For mass velocities around 1600 kg/m²s, inertia takes over, leading to formation of similar wavy vapor layers along the top and bottom walls when heated individually, and to double-sided heating appearing as a superposition of vapor layer behaviors observed in the single-sided heating configurations.

(2) Highly subcooled inlet produces a wavy vapor layer along the top wall for low mass velocities compared to thin vapor layers confined to the heated walls at high mass velocities. For slightly subcooled inlet, a higher rate of vapor generation is observed with distinct wavy vapor layers generated along the heated walls. Saturated two-phase inlet results in a complicated flow pattern due to interaction of vapor entering the channel with the vapor generation by heating.

(3) The average heat transfer coefficient increases with increasing heat flux to a peak value before degrading as CHF is approached. Heat transfer is improved significantly as inlet conditions are changed from highly subcooled to slightly subcooled to saturated.

(4) Overall, CHF increases considerably with increasing inlet subcooling. Bottom wall heating provides the best performance for gravity-dominated low velocity conditions, while double-sided heating outperforms both top wall and bottom wall heating for inertia-dominated high velocity conditions.

(5) Despite some divergence between predicted and measured CHF values at high subcooling, heat utility ratio provides an effective means for assessing the influence of inlet subcooling on CHF.

CHAPTER 4. EXTENSIVE INVESTIGATION OF FLOW BOILING

EXPERIMENTAL RESULTS FOR TWO-PHASE SATURATED INLET

CONDITIONS

4.1 Flow Visualization Results

4.1.1 Flow Orientation Nomenclature

Figures 4.1(a) and 4.1(b) illustrate the four flow orientations examined in this study for single-sided and double-sided heating, respectively. For all these orientations, the flow is shown entering from the center and radiating outwards. Three directions are tested: horizontal flow ($\theta = 0°$ and 180°), vertical upflow ($\theta = 90°$), and vertical downflow ($\theta = 270°$). For horizontal flow, two different orientations are tested for single-sided heating: upward-facing heated wall ($\theta = 0°$) and downward-facing heated wall ($\theta = 180°$). For horizontal flow with double-sided heating, the orientations $\theta = 0°$ and $\theta = 180°$ are identical due to symmetry, so only $\theta = 0°$ is tested.

Flow visualization at high mass velocities and high inlet qualities did not provide clear video images of the flow because high vapor shear at these conditions greatly reduced the thicknesses of the individual liquid and vapor layers adjacent to the heated wall, rendering identification of any near-wall effects quite elusive. Therefore, flow visualization results from only the low flow rate and low inlet quality tests are presented in this study.
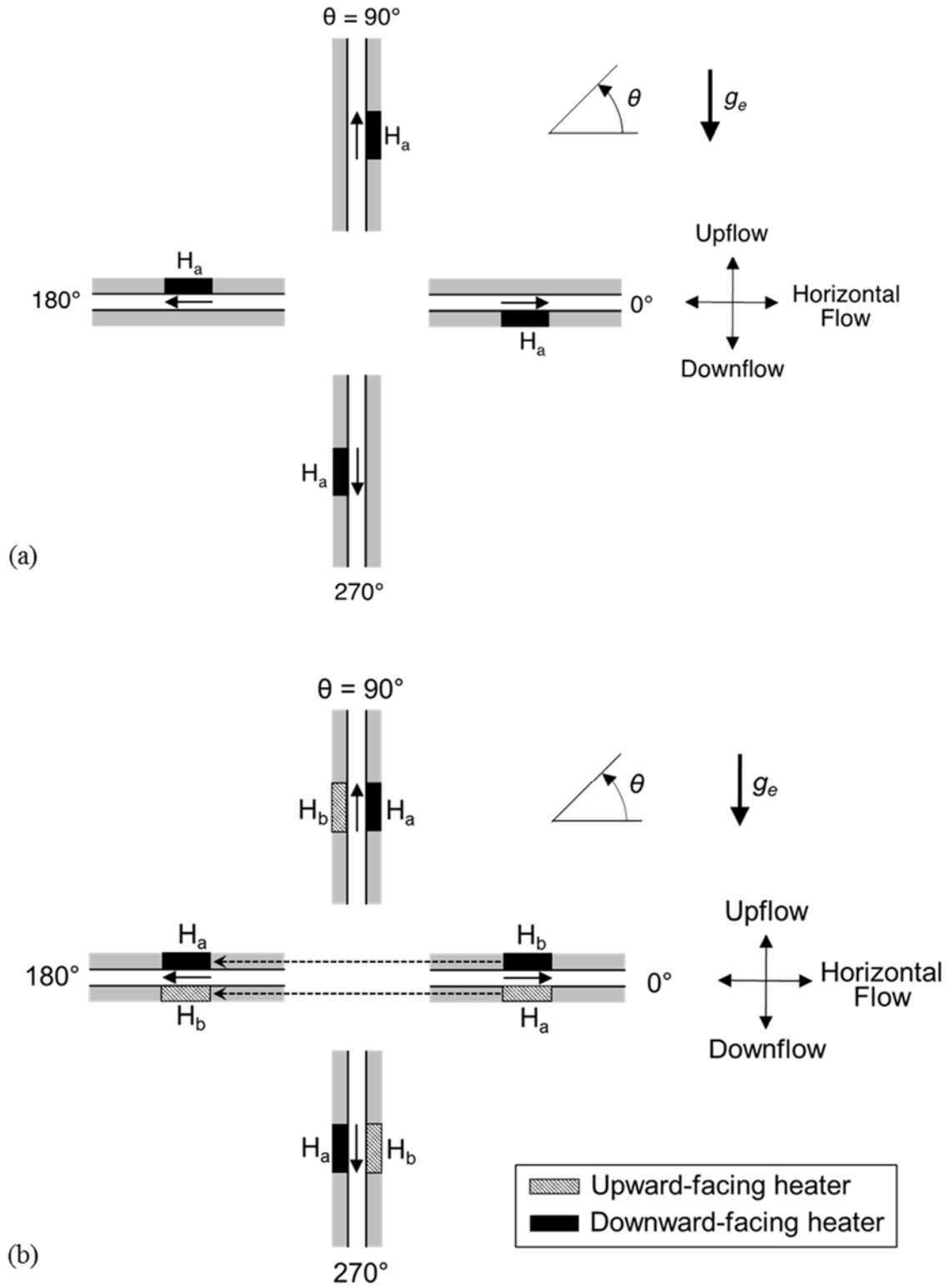
Fig. 4.1: Flow orientation and heater nomenclature for (a) single-sided heating and (b) double-sided heating in Earth gravity.

4.1.2 Flow Visualization Results for Horizontal Flow

Using the schematics in Fig. 4.2(a) as guide, individual images of flow boiling along the entire heated portion of the channel are provided in Figs. 4.2(b) – 4.2(g) for horizontal flow with top wall heating, top and bottom wall heating, and bottom wall heating, and increasing heat flux (up to 91% CHF), at mass velocities of $G = 192.5 – 420.0$ kg/m²s with qualities at the inlet to the heated portion ranging from $x_{e,in} = 0.00$ to 0.25. At $G = 199.5 – 217.9$ kg/m²s and $x_{e,in} = 0.00 – 0.02$, Fig. 4.2(b), top wall heating shows vapor generated along the top wall combining with incoming elongated vapor bubbles, further increasing vapor accumulation along the heated wall. Top and bottom wall heating show similar behavior along the top wall, with small bubbles from the bottom wall migrating across the channel toward the top wall. For bottom wall heating, relatively large vapor bubbles generated along the bottom wall are seen mixing with the incoming vapor, especially when the heat flux is increased. It is important to note that, for bottom wall heating, the heat flux values, including CHF, are substantially greater for bottom wall heating than the two other heating configurations. This behavior is caused by buoyancy aiding vapor removal from the bottom wall and wall replenishment with liquid, as described in Chapter 3 for a wide range of inlet conditions including $x_e > 0$. Similar interfacial behavior is observed for all three heated wall configurations for $x_{e,in} = 0.07 – 0.10$, Fig. 4.2(c). But as inlet quality is increased to $x_{e,in} = 0.16 – 0.21$ for fairly similar mass velocities, Fig. 4.2(d), the incoming vapor flow exhibits longer vapor bubbles and shorter liquid slugs. A further increase in inlet quality to $x_{e,in} = 0.22 – 0.25$, also at about the same mass velocity, Fig. 4.2(e), triggers liquid-vapor stratification along the entire channel, and heating along any or both walls causes the generated vapor to combine with the incoming stratified vapor. Figures 4.2(f)
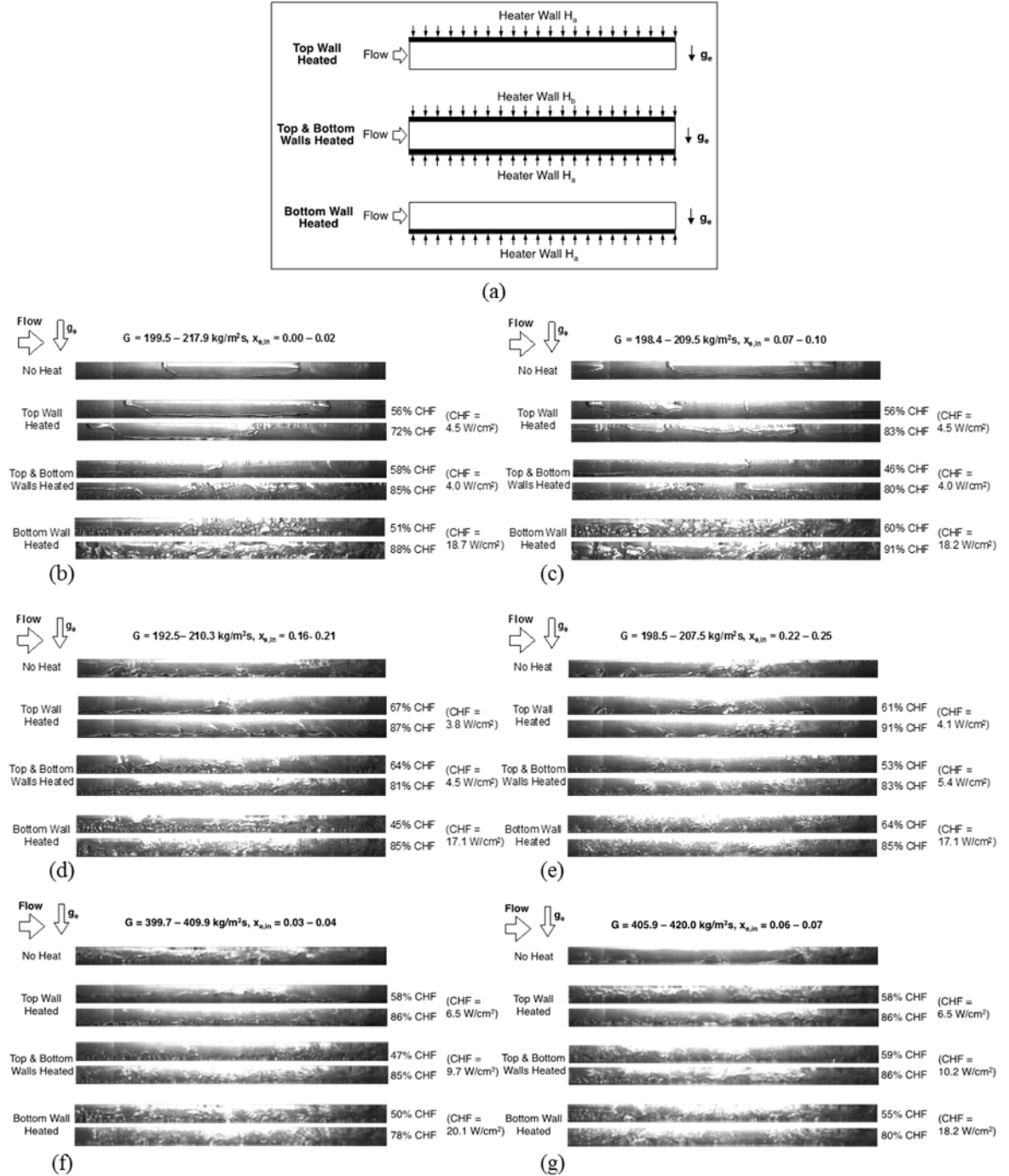
Fig. 4.2: (a) Heated wall configurations for horizontal flow, and corresponding variations of interfacial behavior with increasing heat flux for (b) $G = 199.5 – 217.9$ kg/m^{2}s and $x_{e,in} = 0.00 – 0.02$, (c) $G = 198.4 – 209.5$ kg/m^{2}s and $x_{e,in} = 0.07 – 0.10$, (d) $G = 192.5– 210.3$ kg/m^{2}s and $x_{e,in} = 0.16- 0.21$, (e) $G = 198.5 – 207.5$ kg/m^{2}s and $x_{e,in} = 0.22 – 0.25$, (f) $G = 399.7 – 409.9$ kg/m^{2}s and $x_{e,in} = 0.03 – 0.04$, and (g) $G = 405.9 – 420.0$ kg/m^{2}s and $x_{e,in} = 0.06 – 0.07$.

and 4.2(g) show images corresponding to higher mass velocity in the range of $G = 399.7 -$ 420.0 kg/m²s. While the boiling behavior is not significantly different from that observed at the lower velocities in Figs. 4.2(b) – 4.2(e), there are signs of inertia sweeping interfacial features along the channel with greater intensity.

4.1.3 Flow Visualization Results for Vertical Upflow

The schematics in Fig. 4.3(a) serve as guide for the two heating configurations associated with vertical upflow. Figures 4.3(b) – 4.3(e) shows individual images of flow boiling along the entire heated portion of the channel for vertical upflow with single-sided and double-sided heating for mass velocities in the range of $G = 210.6$ to 236.3 kg/m²s and two heat fluxes, with the inlet quality gradually increased from $x_e = 0.00 - 0.02$, Fig. 4.3(b), to $x_{e,in} = 0.17 - 0.19$, Fig. 4.3(e). Both single-sided and double-sided heating configurations show bubbles nucleating along the heated wall(s), with the increasing heat flux yielding larger coalescent vapor masses along the channel. The increase in inlet quality is shown culminating in elongated vapor bubbles entering the channel, which are shown growing and being distorted by the vapor generated along the heated wall(s). Figure 4.3(f) shows similar interfacial behavior for the higher mass velocity of $G = 406.1 - 409.0$ kg/m²s. Overall, the main difference between vertical upflow and horizontal flow is a tendency for vapor in the former to flow symmetrically along the channel with no apparent bias towards either wall, while the vapor in horizontal flow has a clear tendency to stratify towards the top wall.
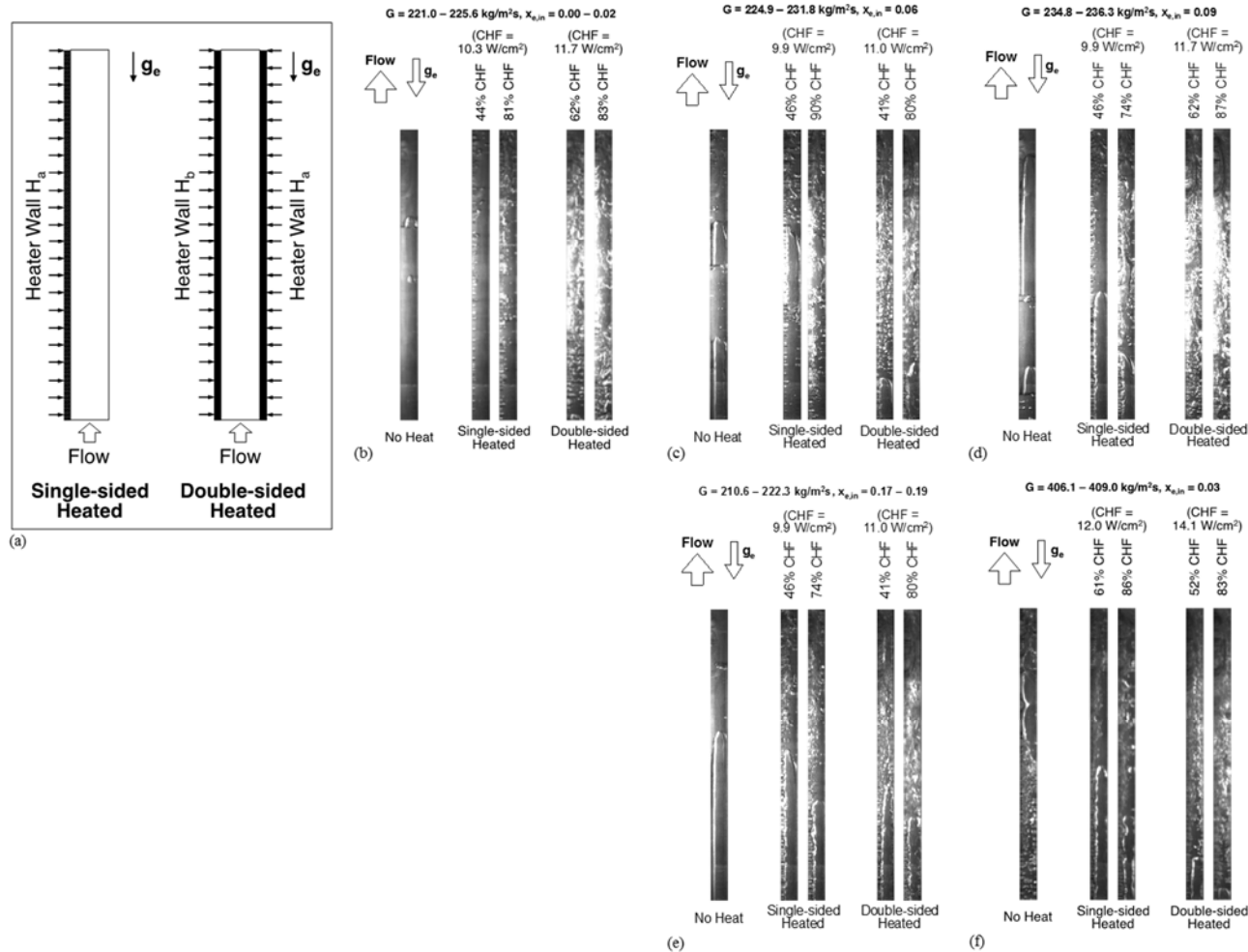
Fig. 4.3: (a) Heated wall configurations for vertical upflow, and corresponding variations of interfacial behavior with increasing heat flux for (b) $G = 221.0 - 225.6$ kg/m^{2}s and $x_{e,in} = 0.00 - 0.02$, (c) $G = 224.9 - 231.8$ kg/m^{2}s and $x_{e,in} = 0.06$, (d) $G = 234.8 - 236.3$ kg/m^{2}s and $x_{e,in} = 0.09$, (e) $G = 210.6 - 222.3$ kg/m^{2}s and $x_{e,in} = 0.17 - 0.19$, and (f) $G = 406.1 - 409.0$ kg/m^{2}s and $x_{e,in} = 0.03$.

4.1.4 <u>Flow Visualization Results for Vertical Downflow</u>

Figure 4.4(a) serves as guide for the two heating configurations used in conjunction with vertical downflow. Figures 4.4(b) and 4.4(c) show individual images of flow boiling along the entire heated portion of the channel for vertical downflow with single-sided and double-sided heating at mass velocities in the range of $G = 205.2 – 217.9$ kg/m²s and two heat fluxes, the main difference being a relatively low quality of $x_{e,in} = 0.01 – 0.03$ in Fig. 4.4(b), compared to a higher quality of $x_{e,in} = 0.09$ in Fig. 4.4(c). Both inlet quality ranges exhibit vapor coalescence in the heated portion of the channel into a large bubble. Figures 4.4(d) and 4.4(e) show images for a higher mass velocity range of $G = 405.4 – 422.0$ kg/m²s, with $x_e = 0.04 – 0.05$ and $0.07 – 0.08$, respectively. With no heating, vapor is seen forming a large vapor bubble marred by many ripples along the vapor-liquid interface, which are caused by buoyancy acting opposite (upwards) to the main downflow direction. Increasing the heat flux for both heated wall configurations is reflected in increased vapor void along the heated portion of the channel.

4.2 <u>Experimental Results</u>

4.2.1 <u>Flow Boiling Curves</u>

4.2.1.1 <u>Flow Boiling Curves for Horizontal Flow</u>

Figures 4.5(a) shows flow boiling curves for horizontal flow with single-sided heating and different combinations of mass velocity and inlet quality. The boiling data are presented as variations of wall heat flux, q''_w, with the difference between average wall temperature, $T_{w,avg}$, and inlet saturation temperature, $T_{sat,in}$. The data exhibit typical flow boiling curve trends with the slope increasing appreciably around the region of initial
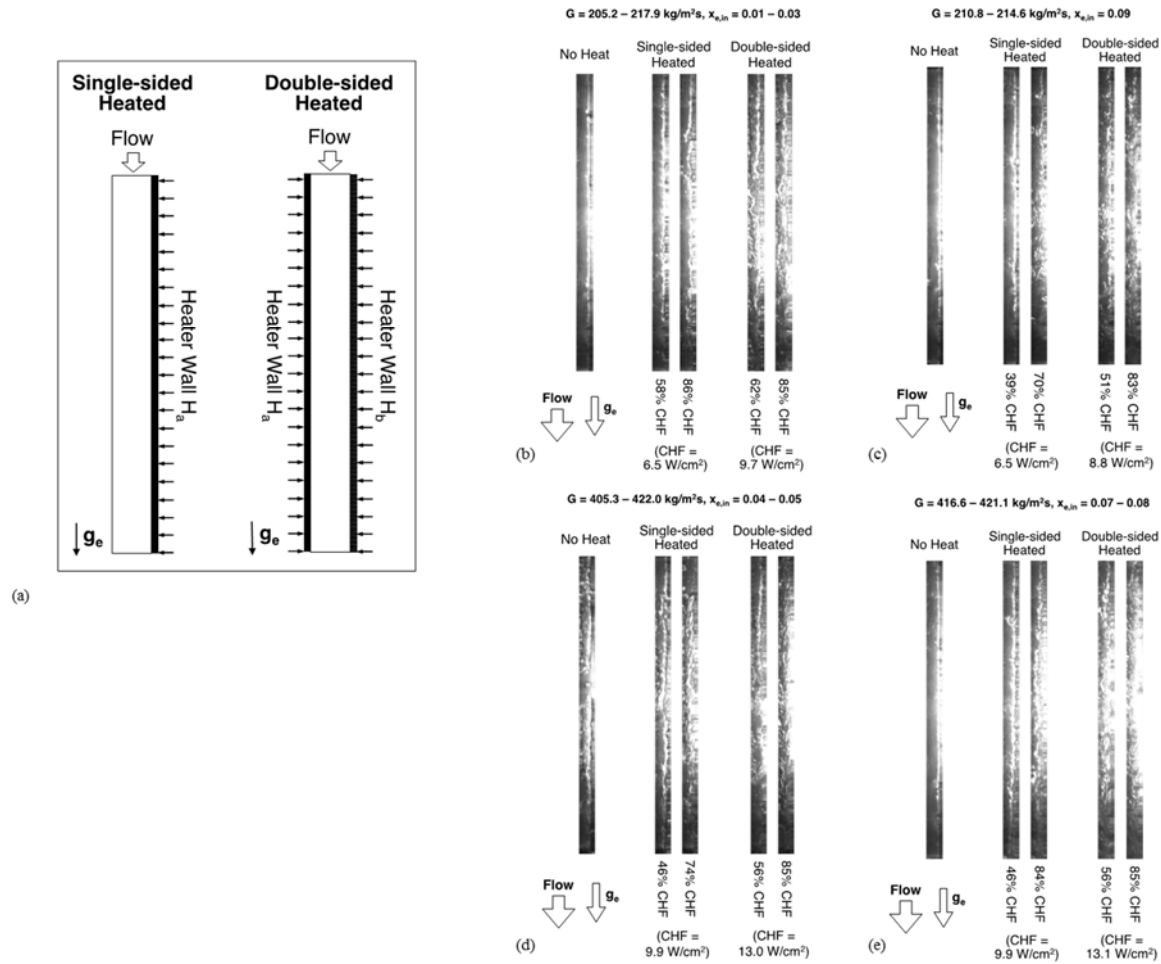
Fig. 4.4: (a) Heated wall configurations for vertical downflow, and corresponding variations of interfacial behavior with increasing heat flux for (b) $G = 205.2 - 217.9$ kg/m²s and $x_{e,in} = 0.01 - 0.03$, (c) $G = 210.8 - 214.6$ kg/m²s and $x_{e,in} = 0.09$, (d) $G = 405.3 - 422.0$ kg/m²s and $x_{e,in} = 0.04 - 0.05$, and (e) $G = 416.6 - 421.1$ kg/m²s and $x_{e,in} = 0.07 - 0.08$.
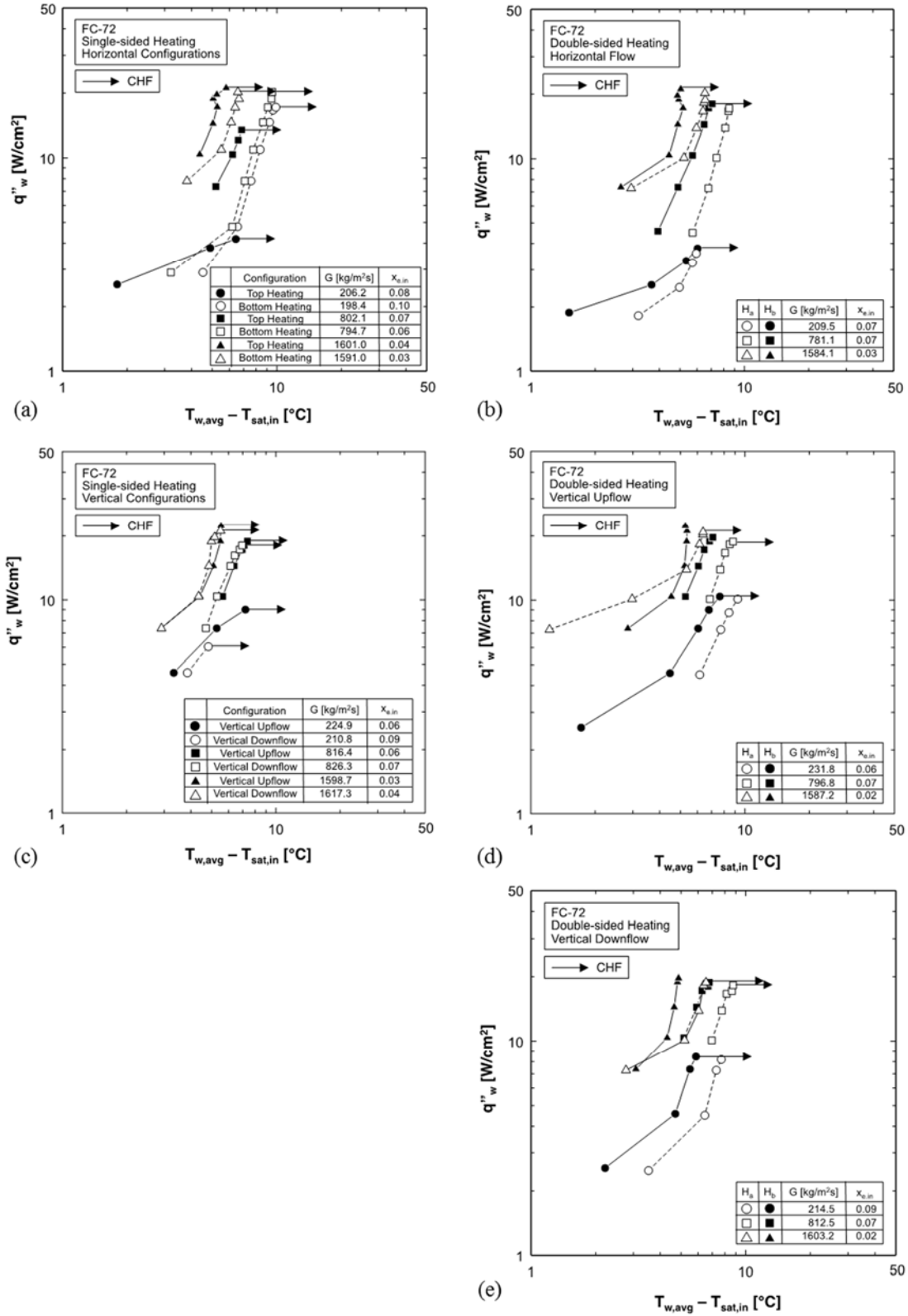
Fig. 4.5: Boiling curves for different inlet mass velocities for (a) single-sided heated horizontal flow, (b) double-sided heated horizontal flow, (c) single-sided heated vertical upflow and downflow, (d) double-sided heated vertical upflow, and (e) double-sided heated vertical downflow.

bubble nucleation, and the wall temperature increasing sharply in an unsteady manner at CHF. Increasing the mass velocity is shown shifting the boiling curve to the left, indicating an enhancement in the heat transfer coefficient, as well as increasing CHF. Notice the large differences in heat transfer data for bottom wall heating compared to top wall heating, especially for the lowest mass velocities of $G = 198.4 – 206.2$ kg/m^{2}s. The top wall heating is shown yielding far more inferior heat transfer performance, which can be explained by the appreciable vapor stratification along the top wall as shown earlier in Fig. 4.2(c). Increasing the mass velocity in Fig. 4.5(a) is reflected by the top wall heating and bottom wall heating acquiring fairly equal slope, and the differences in heat transfer performance decreasing because of the increasing magnitude of flow inertia compared to buoyancy.

Figure 4.5(b) shows flow boiling curves for horizontal flow with double-sided heating. While the top wall shows slightly higher heat transfer performance and triggers CHF consistently for all mass velocities, there is closer agreement in heat transfer data between the two heated walls for each mass velocity compared to those in Fig. 4.5(a). This trend can be explained by the two heated walls increasing void fraction, thereby increasing flow acceleration and better combating buoyancy effects compared to a single heated wall.

4.2.1.2 Flow Boiling Curves for Vertical Upflow

Figure 4.5(c) shows flow boiling curves for both vertical upflow and vertical downflow with single-sided heating and different combinations of mass velocity and inlet quality. For vertical upflow, there is a monotonic enhancement in heat transfer performance and CHF with increasing mass velocity. A similar trend is observed in Fig. 4.5(d), which shows boiling curves for vertical upflow with double-sided heating. Because of symmetry, there

is some randomness regarding which of the two walls provides the better performance in two-sided heating.

4.2.1.3 Flow Boiling Curves for Vertical Downflow

The boiling data for vertical downflow with single-sided heating is shown on Fig. 4.5(c), which reflects the same trends as those for vertical upflow with single-sided heating. This lack of differences between vertical upflow and vertical downflow is attributed to the saturated inlet conditions producing a central elongated vapor core that grows along the heated portion of the channel due to vapor production, while pushing liquid against both the heated and insulated walls, as observed in Fig. 4.3(c) for vertical upflow and Fig. 4.4(c) for vertical downflow. One major exception is a large difference in CHF for the lowest mass velocity, which can be explained by buoyancy playing a more significant role at low velocity compared to flow inertia. Figure 4.5(e) shows general trends for double-sided vertical downflow resemble those for single-sided heating. Because of similarity in both the flow and heating boundaries, there is randomness as to which of the two walls provides the better performance.

4.2.2 Heat Transfer Coefficient

4.2.2.1 Average Heat Transfer Coefficient

In this study, the FC-72 enters the channel as a saturated two-phase mixture at T_{sat}, and this temperature is maintained along the entire heated portion of the channel. The local heat transfer coefficient at each thermocouple location along the heated wall is defined as

$h_{m,n} = q''_w / \left(T_{wm,n} - T_{sat} \right)$, where q''_w is the wall heat flux, $T_{wm,n}$ the wall temperature

measured along heated wall m ($m = a$ for H_a and b for H_b), and n the thermocouple location. The local heat transfer coefficient values are then spatially averaged to obtain h_{avg}.

Figures 4.6(a) and 4.6(b) show variations of h_{avg} with wall heat flux for horizontal flow with single-sided heating and inlet qualities ranging from $x_{e,in} = 0.03$ to 0.63 for two ranges of mass velocity, $G = 387.0 - 419.0$ kg/m²s and $G = 784.4 - 804.0$ kg/m²s, respectively. Overall, these figures show h_{avg} increasing monotonically with increasing wall heat flux. For the lower mass velocity range, Fig. 4.6(a) shows inlet quality having a measurable influence on h_{avg} for top wall heating, but a much weaker influence for bottom wall heating. The heat transfer performance for top wall heating at the highest inlet quality of $x_{e,in} = 0.63$ is especially intriguing. Its behavior is drastically different in comparison with top wall heating with at an inlet quality of $x_{e,in} = 0.31$. Two effects are acting together as we increase the inlet quality of the incoming fluid. These two effects are increase in fluid and vapor velocity due to flow acceleration and increase in vapor quality of the fluid. The increase in quality causes a scarcity of liquid in the incoming flow, and therefore a very thin, high velocity film is formed along the top wall, resulting in a very high h_{avg} value at low wall fluxes. But as the heat flux increases, partial dryout in the same liquid film drastically compromises h_{avg}, also paving the way for early CHF occurrence. Figure 4.6(b) shows that increasing mass velocity provides better agreement between top wall and bottom wall heating, presumably because of increased flow inertia compared to buoyancy.
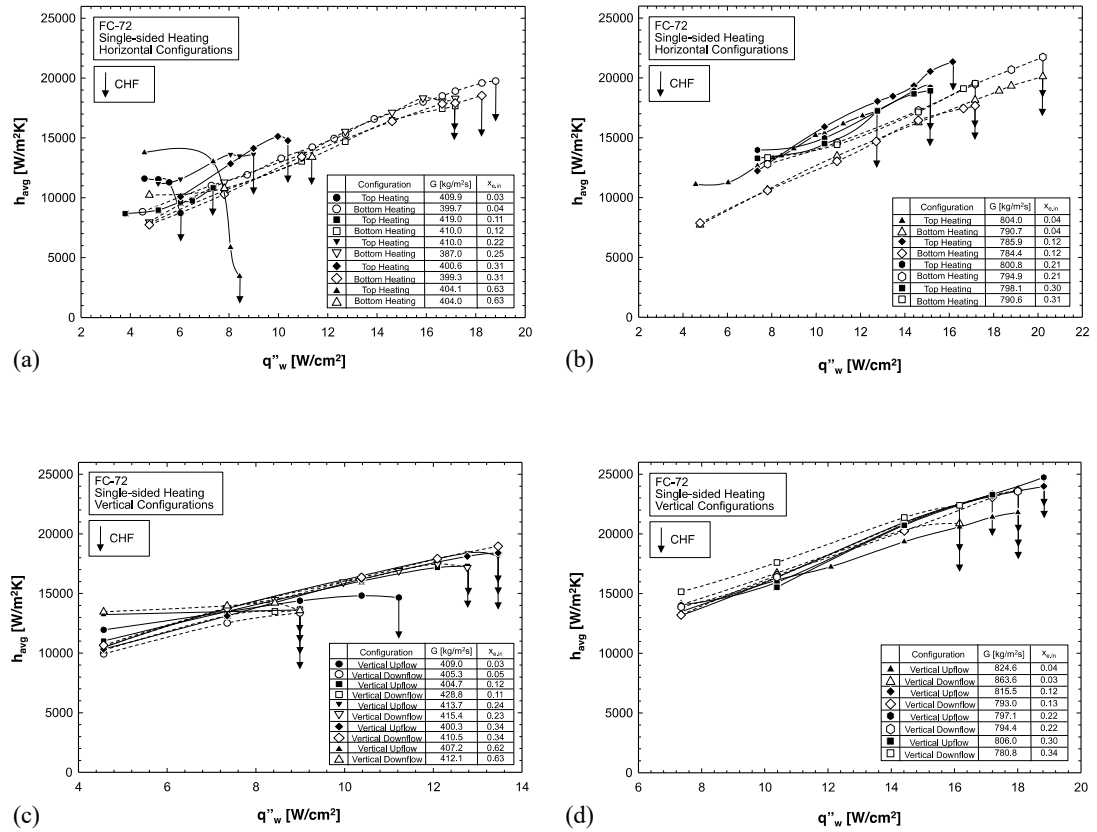
Fig. 4.6: Variations of average heat transfer coefficient with wall heat flux for single-sided heating with different inlet qualities for (a) horizontal configurations with G = 387.0 – 419.0 kg/m^{2}s, (b) horizontal configurations with G = 784.4 – 804.0 kg/m^{2}s, (c) vertical configurations with G = 400.3 – 428.8 kg/m^{2}s, and (d) vertical configurations with G = 780.8 – 863.6 kg/m^{2}s.

Figures 4.6(c) and 4.6(d) show h_{avg} results for vertical upflow and vertical downflow with single-sided heating with qualities in the range of $x_{e,in} = 0.03 - 0.63$ and two ranges of mass velocity, $G = 400.3 - 428.8$ kg/m²s and $G = 780.8 - 863.6$ kg/m²s, respectively. For the lower mass velocity range, Fig. 4.6(c) shows far closer agreement in h_{avg} between vertical upflow and vertical downflow than horizontal flow, Fig. 4.6(a), proving these operating conditions correspond to flows dominated by inertia. With even stronger inertia for $G = 780.8 - 863.6$ kg/m²s, Fig.4.6(d) shows even closer agreement between vertical upflow and vertical downflow.

Figures 4.7(a) and 4.7(b) show variations of h_{avg} with wall heat flux for horizontal flow with double-sided heating and inlet qualities from $x_{e,in} = 0.03$ to 0.63 for two ranges of mass velocity, $G = 393.3 - 404.5$ kg/m²s and $G = 777.4 - 786.4$ kg/m²s, respectively. Figures 4.7(c) and 4.7(d) show h_{avg} variations for vertical upflow with double-sided heating and inlet qualities from $x_{e,in} = 0.03$ to 0.61 for $G = 391.7 - 409.0$ kg/m²s and $G = 786.4 - 809.1$ kg/m²s, respectively. Similarly, Figs. 4.7(e) and 4.7(f) shows h_{avg} plots for vertical downflow with double-sided heating and inlet qualities from $x_{e,in} = 0.03$ to 0.61 for $G = 394.9 - 427.3$ kg/m²s and $G = 782.1 - 844.7$ kg/m²s, respectively. Overall, all these double-sided heating plots show heat transfer performance improving with increasing heat flux before suddenly declining at CHF. They also show the increase in mass velocity increasing the slope of h_{avg} versus wall heat flux. Figures 4.7(a) – 4.7(f) also show only minor differences in h_{avg} values between different orientations. Overall, these trends point to double-sided heating aiding vapor production and, therefore, flow acceleration, rendering
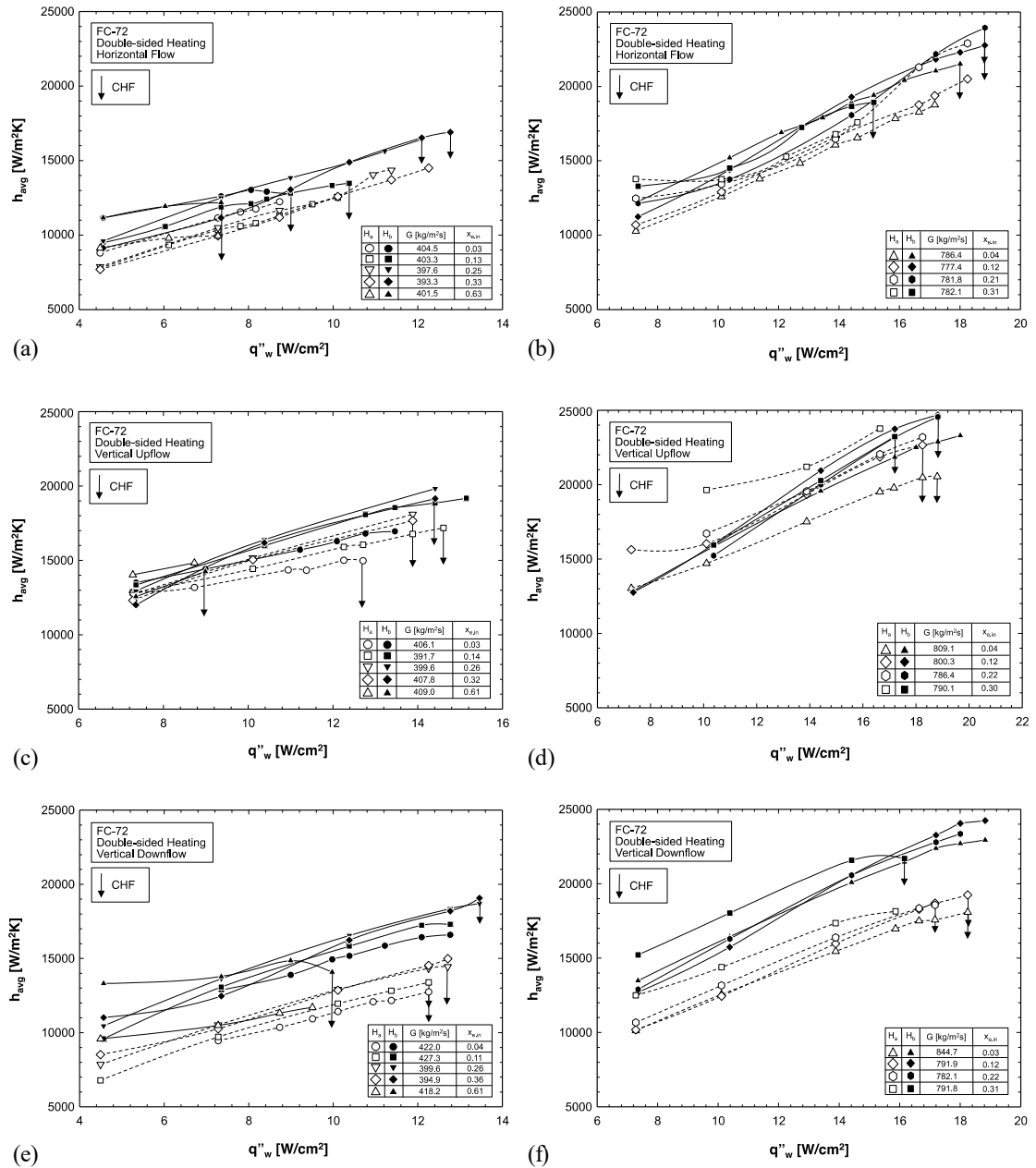
Fig. 4.7: Variations of average heat transfer coefficient with wall heat flux for double-sided heating with different inlet qualities for (a) horizontal flow with G = 393.3 – 404.5 kg/m²s, (b) horizontal flow with G = 777.4 – 786.4 kg/m²s, (c) vertical upflow with G = 391.7 – 409.0 kg/m²s, (d) vertical upflow with G = 786.4 – 809.1 kg/m²s, (e) vertical downflow with G = 394.9 – 427.3 kg/m²s, and (f) vertical downflow with G = 782.1 – 844.7 kg/m²s.

inertia more effective at combating gravity effects. It is important to also see that there are some variations in heat transfer between the walls. The slight differences in resistance between the two heaters is responsible for variation in heat flux input and therefore the average heat transfer coefficients between the two walls. Physically, the two walls in vertical upflow and vertical downflow configurations, are supposed to be symmetric and hence should give similar heat transfer coefficient performance. In most cases, slight differences between the walls with the top wall outperforming the bottom wall in heat transfer is observed. But in some cases like in both Fig. 4.7(c) and 4.7(d), at higher qualities we see that top and bottom wall performances might switch. This behavior is due to uncertainty in heat transfer measurement and not related to any physical phenomenon.

4.2.2.2 <u>Local Heat Transfer Coefficient Results</u>

Figures 4.8(a), 4.8(b) and 4.8(c) show variations of the local heat transfer coefficient, h, with distance, z, along the heated length for horizontal double-sided heating with $G =$ 387.6 - 417.7 kg/m^{2}s and different wall heat fluxes, with inlet qualities of $x_{e,in} = 0.06, 0.25,$ and 0.63, respectively. These figures show h increases monotonically with increasing heat flux at each thermocouple location. There is an appreciable decline in h in the inlet region, followed by a rather flat variation in the middle region, and a large increase in the exit region. The decrease in the inlet region is attributed to thermal boundary layer development, while the downstream increase is most likely the result of appreciable flow acceleration towards the exit. It is difficult to quantify the effect of flow acceleration just by looking at the local heat transfer variation. But, acceleration in flow is expected in flow
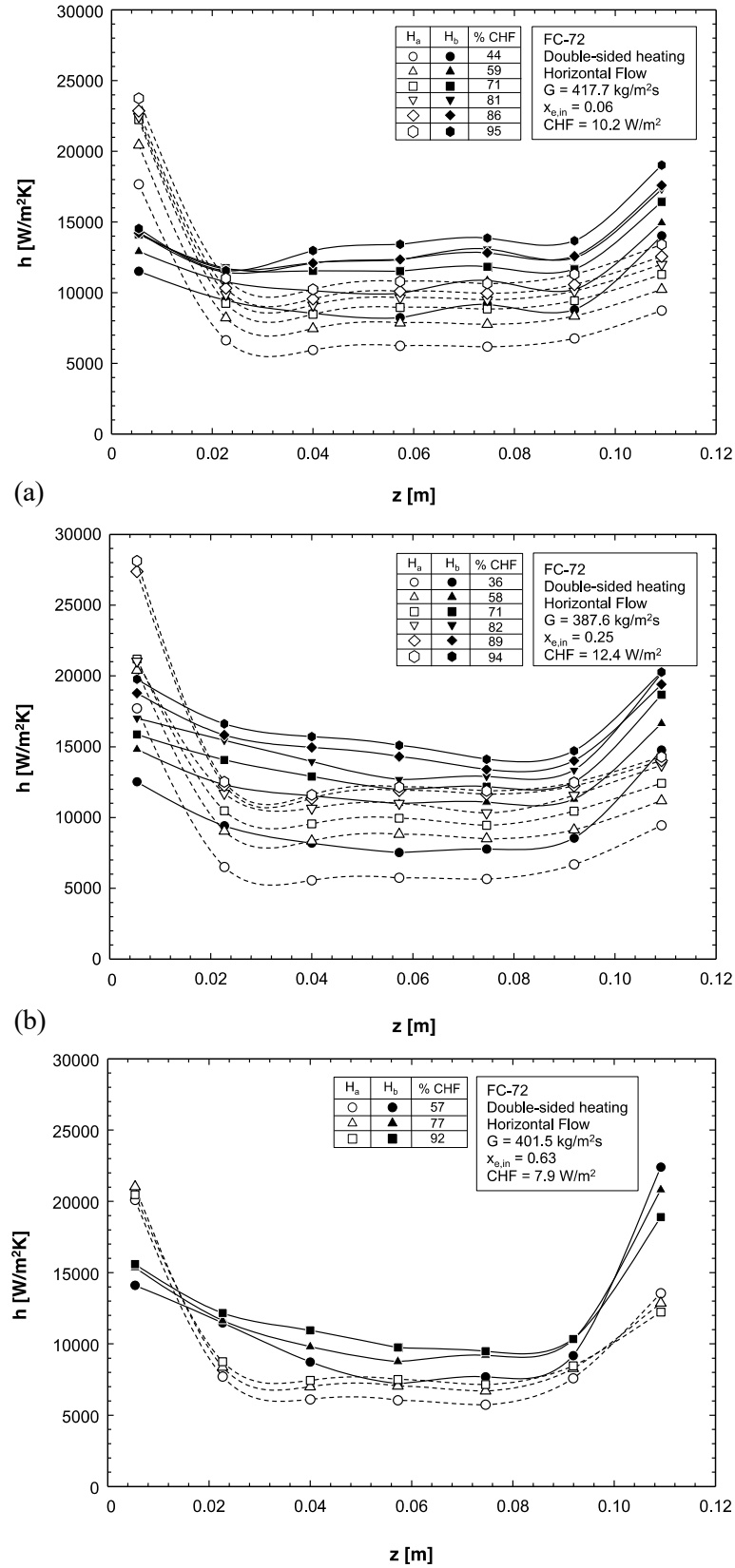
Fig. 4.8: Variations of local heat transfer coefficient along heated length of the channel for double-sided heating in horizontal orientation with increasing heat flux for $G = 387.6 - 417.7$ kg/m^{2}s and (a) $x_{e,in} = 0.06$, (b) $x_{e,in} = 0.25$, and (c) $x_{e,in} = 0.63$.

boiling configurations when there is an increase in heat flux and increase in inlet flow quality. Firstly, for each configuration, local variations show that increase in heat flux shifts curves up which can be attributed to flow acceleration. Secondly, between the three plots, increase in inlet quality also shows that at a higher quality a higher increase is observed in the exit region, which can also be attributed to flow acceleration. Overall, the three different inlet qualities show fairly similar performances.

4.2.2.3 Influence of Orientation on Heat Transfer Coefficient

A key objective of the present study is to assess the influence of gravity for different operating conditions. This is best achieved by comparing heat transfer results for the different flow orientations. Shown in Figs. 4.9(a), 4.9(b), and 4.9(c) are polar plots for peak h_{avg} (obtained from Figs. 4.6(a) – 4.6(d)) for single-sided heating over a broad range of mass velocity, and inlet qualities of $x_{e,in}$ = 0.04 – 0.10, 0.14 – 0.22 and 0.30 – 0.36, respectively. For the lowest x_e range, Fig. 4.9(a) shows drastic differences in peak h_{avg} for horizontal bottom wall heating ($\theta = 0°$) compared to top wall heating ($\theta = 180°$) for the two lowest mass velocities. These differences are attributed to the stratification to the heated wall for $\theta = 0°$, and compromise both for $\theta = 180°$. These differences diminish with increasing mass velocity. Notice that peak h_{avg} values for vertical upflow ($\theta = 90°$) and vertical downflow ($\theta = 270°$) are about equal for the entire range of mass velocities, and values for all four orientations ($\theta = 0°, 90°, 180°,$ and $270°$) are about equal above G = 794.7 - 826.3 kg/m²s, indicating inertia around this mass velocity range is effective at

73
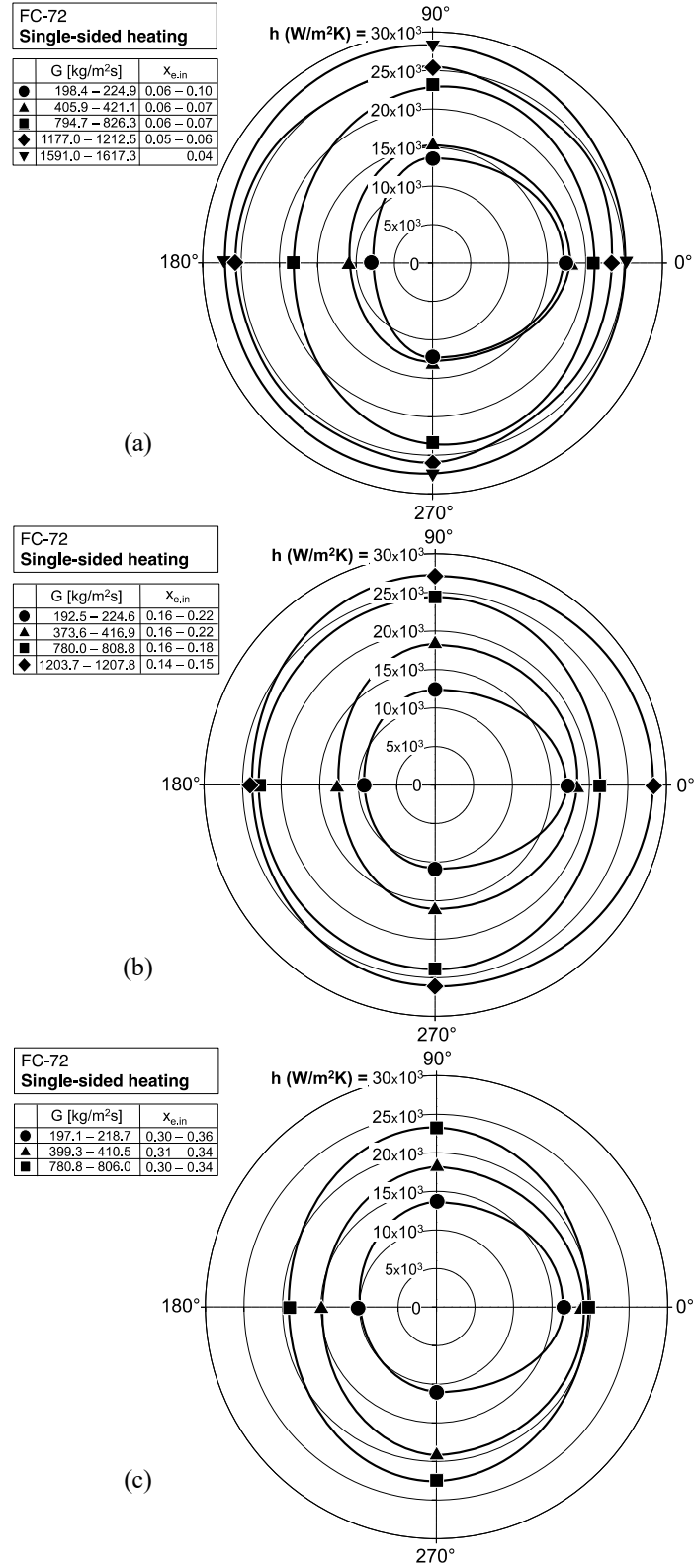
Fig. 4.9: Polar plots showing variations of peak heat transfer coefficient with orientation relative to Earth gravity for single-sided heating and different mass velocities, with (a) $x_{e,in}$ = 0.04-0.10, (b) $x_{e,in}$ = 0.14-0.22, and (c) $x_{e,in}$ = 0.30-0.36.

negating any gravity effects. Fairly similar trends can be seen in Figs. 4.9(b) and 4.9(c) corresponding to $x_{e,in}$ = 0.14 – 0.22 and 0.30 – 0.36, respectively. Therefore, for single-sided heating, the ability to negate gravity effects is determined mostly by mass velocity rather than inlet quality.

Figures 4.10(a), 4.10(b), and 4.10(c) show polar plots for peak h_{avg} for double-sided heating over a broad range of mass velocity, and inlet qualities of $x_{e,in}$ = 0.02 – 0.09, 0.13 – 0.19, and 0.30 – 0.36, respectively. A major fundamental feature of these plots is symmetry around the vertical axis. All three figures show fairly similar trends relative to mass velocity, with values for the lowest mass velocity range of G = 200.9 - 235.9 kg/m²s showing the greatest variations relative to orientation. Notice for these low mass velocities how vertical upflow (θ = 90°) and vertical downflow (θ = 270°) yield fairly equal peak h_{avg} values, which are significantly greater than those for horizontal flow (θ = 0° and 180°). The two horizontal orientations are quite unique in that they simultaneously combine heat transfer enhancement for the bottom heated wall and relatively poor heat transfer along the top heated wall. The polar trends in Figs. 4.10(a) – 4.10(c) for the lowest G range suggest bottom heated wall enhancement is too weak to compensate for the poor performance of the top heated wall. All three quality ranges show the influence of orientation on peak h_{avg} greatly diminishing with increasing G. Additionally, peak h_{avg} values begin to converge for all orientations at $x_{e,in}$ = 0.02 – 0.09, Fig. 4.10(a), and 0.13 – 0.19, Fig. 4.10(b), around the same range of G = 781.1 - 812.5 kg/m²s. However, the highest inlet qualities of $x_{e,in}$ = 0.30 – 0.36, Fig. 4.10(c), reduce the influence of orientation for the lowest mass velocity range of G = 200.9 – 214.6 kg/m²s compared to the two lower quality ranges, presumably
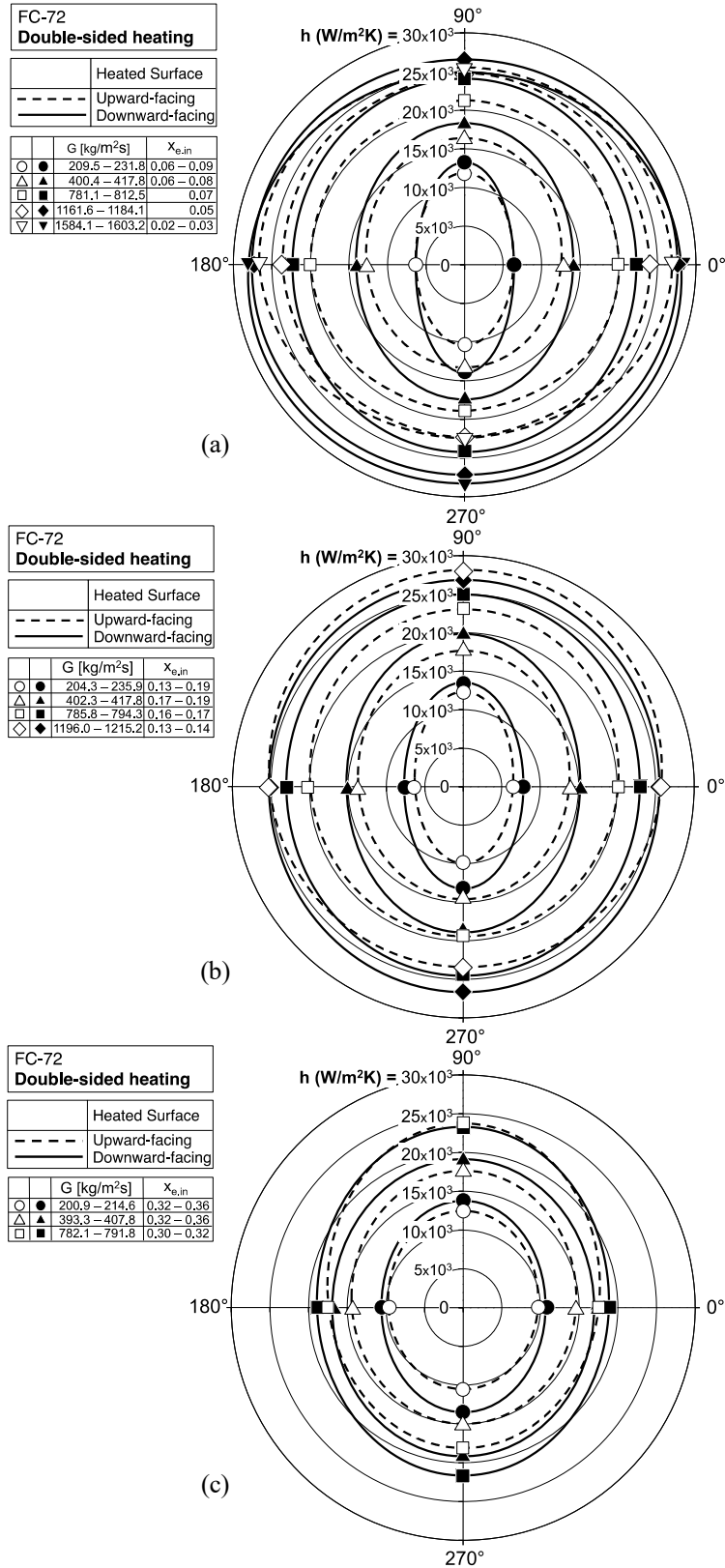
Fig. 4.10: Polar plots showing variations of peak heat transfer coefficient with orientation relative to Earth gravity for double-sided heating and different mass velocities for (a) $x_{e,in}$ = 0.02-0.09, (b) $x_{e,in}$ = 0.13-0.19, and (c) $x_{e,in}$ = 0.30-0.36.

because of the higher flow acceleration provided by higher inlet quality. But equally interesting is how the highest inlet qualities of $x_{e,in} = 0.30 – 0.36$ preserve a rather weak influence of orientation for other mass velocities. Overall, Figs. 4.10(a) – 4.10(c) prove that orientation effects are dictated mostly by mass velocity and, to a far lesser extent, by inlet quality.

4.2.3 <u>Pressure Drop</u>

As indicated earlier, fluid pressure in the flow boiling module is measured at the module's inlet and outlet, as well as at several locations along the flow channel. These include one pressure measurement just upstream, and another just downstream of the heated wall. Those two measurements are used to measure pressure drop, Δp, across the heated portion of the channel. To determine the influences of mass velocity, inlet quality, heating configuration, and orientation, the pressure drop values are compared for equal values of wall heat flux. Figures 4.11(a), 4.11(b), and 4.11(c) show polar plots of Δp for single-sided heating configurations over a broad range of mass velocity and inlet qualities of $x_{e,in} = 0.04 – 0.07$, $0.19 – 0.25$, and $0.40 – 0.45$, respectively. For the lowest quality range of $x_{e,in} = 0.06 – 0.07$, Fig. 4.11(a) shows the lowest mass velocity ranges of $G = 405.9$ - 421.1 and 794.7 – 826.3 kg/m²s yielding higher Δp for vertical upflow ($\theta = 90°$) and vertical downflow ($\theta = 270°$) than the two horizontal flows ($\theta = 0°$ and 180°). Equally intriguing is that the two vertical flows show fairly equal Δp, even though the direction of gravity is reversed. Additionally, the two horizontal flows show equal Δp despite the opposite orientations of the heated walls. The fairly equal Δp values for vertical upflow and vertical downflow can be explained by the relative contributions of individual

FC-72
Single-sided heating

	G [kg/m²s]	$x_{e,in}$	q''_w [W/cm²]
●	405.9 – 421.1	0.06 – 0.07	6.0 – 7.3
▲	794.7 – 826.3	0.06 – 0.07	10.3 – 10.9
■	1177.0 – 1212.5	0.05 – 0.06	18.3 – 18.7
◆	1591.0 – 1617.3	0.04	19.6 – 21.0

(a)

FC-72
Single-sided heating

	G [kg/m²s]	$x_{e,in}$	q''_w [W/cm²]
●	387.0 – 415.4	0.19 – 0.25	7.3 – 7.7
▲	794.4 – 800.8	0.22 – 0.25	17.1
■	1191.5 – 1209.1	0.19 – 0.20	18.7

(b)

FC-72
Single-sided heating

	G [kg/m²s]	$x_{e,in}$	q''_w [W/cm²]
●	396.7 – 418.6	0.42 – 0.45	10.3 – 10.9
▲	786.6 – 800.5	0.40 – 0.44	10.3 – 10.9

(c)
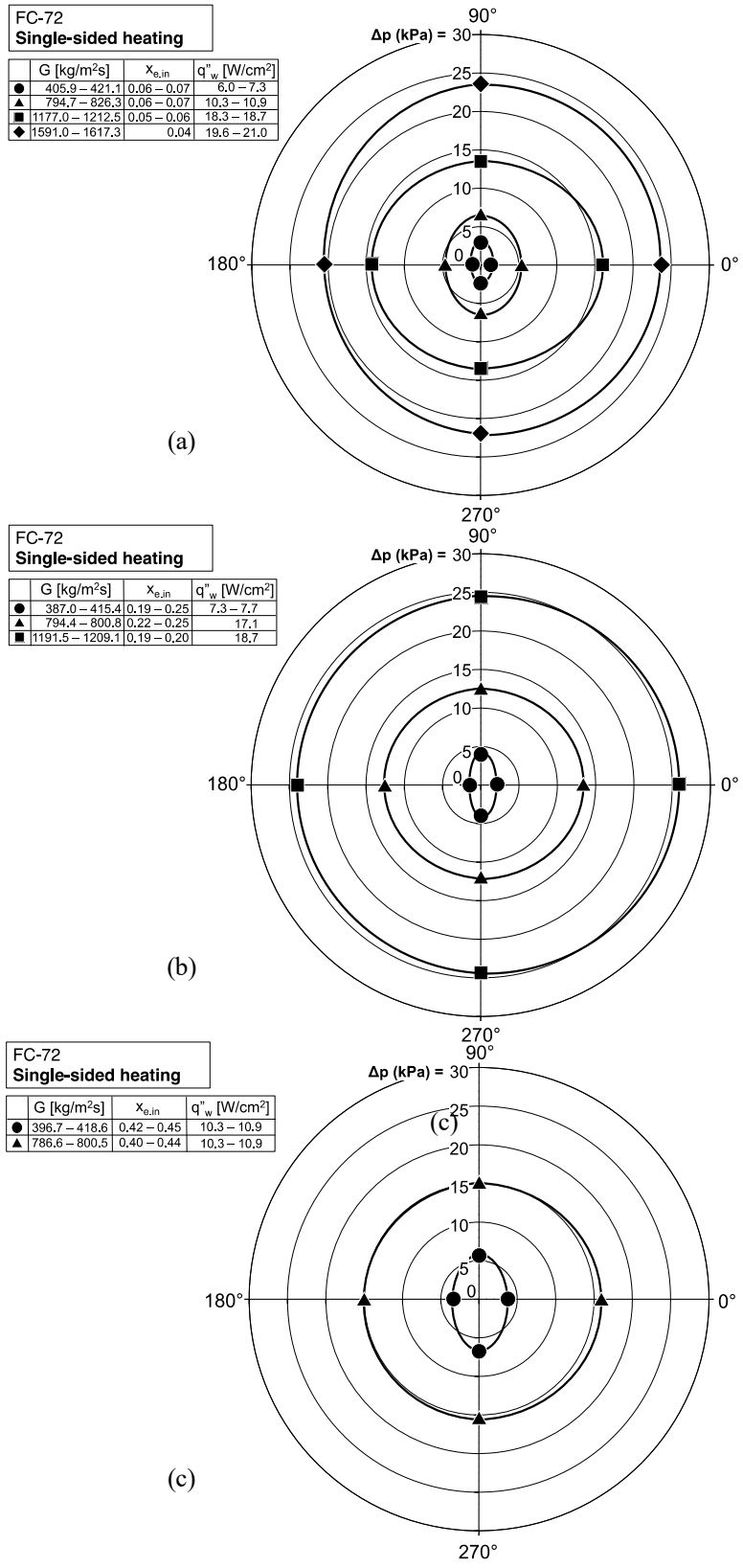
Fig. 4.11: Polar plots showing variations of pressure drop across heated portion of channel with orientation relative to Earth gravity for single-sided heating and different mass velocities for (a) $x_{e,in}$ = 0.04-0.07, (b) $x_{e,in}$ = 0.19-0.25, and (c) $x_{e,in}$ = 0.40-0.45.

components of Δp. Two-phase pressure drop is comprised of three components, friction, acceleration and gravitation, and the influence of orientation is reflected in the magnitude of the gravitational component, which is approximately proportional to the product of mean two-phase mixture density, Earth gravity, and length of heated portion of the channel. Given the large void fraction associated with these two orientations as discussed earlier in conjunction with the flow visualization results, the two-phase mixture density is quite small, rendering the contribution of the entire gravitational component negligible. The larger values for Δp for vertical upflow and vertical downflow compared to the two horizontal orientations can be explained by higher accelerational pressure drop for the vertical orientations. Notice how the influence of orientation on Δp decreases with increasing G. For the two higher inlet quality ranges of $x_{e,in} = 0.19 - 0.25$ and $0.40 - 0.45$, Figs. 4.11(b) and 4.11(c), respectively, show Δp values converge for all orientations around $G = 786.6 - 800.8$ kg/m^{2}s, compared to a higher mass velocity of $G = 1177.0 - 1212.5$ kg/m^{2}s for the lowest quality range of $x_{e,in} = 0.04 - 0.07$ as shown in Fig. 4.11(a). Overall, Figs. 4.11(a) – 4.11(c) prove that orientation effects are dictated mostly by mass velocity and, to a lesser extent, by inlet quality.

Figures 4.12(a), 4.12(b), and 4.12(c) show polar plots for Δp for double-sided heating over a broad range of mass velocity at inlet qualities of $x_{e,in} = 0.02 - 0.08$, $0.18 - 0.26$, and $0.39 - 0.43$, respectively. A fundamental feature of these plots is symmetry around the vertical axis. For the lowest quality range, Fig. 4.12(a) shows that Δp values at $G = 400.4 - 417.8$ kg/m^{2}s for vertical upflow ($\theta = 90°$) and vertical downflow ($\theta = 270°$) are greater than for the two horizontal orientations, and the influence of orientation diminishes with
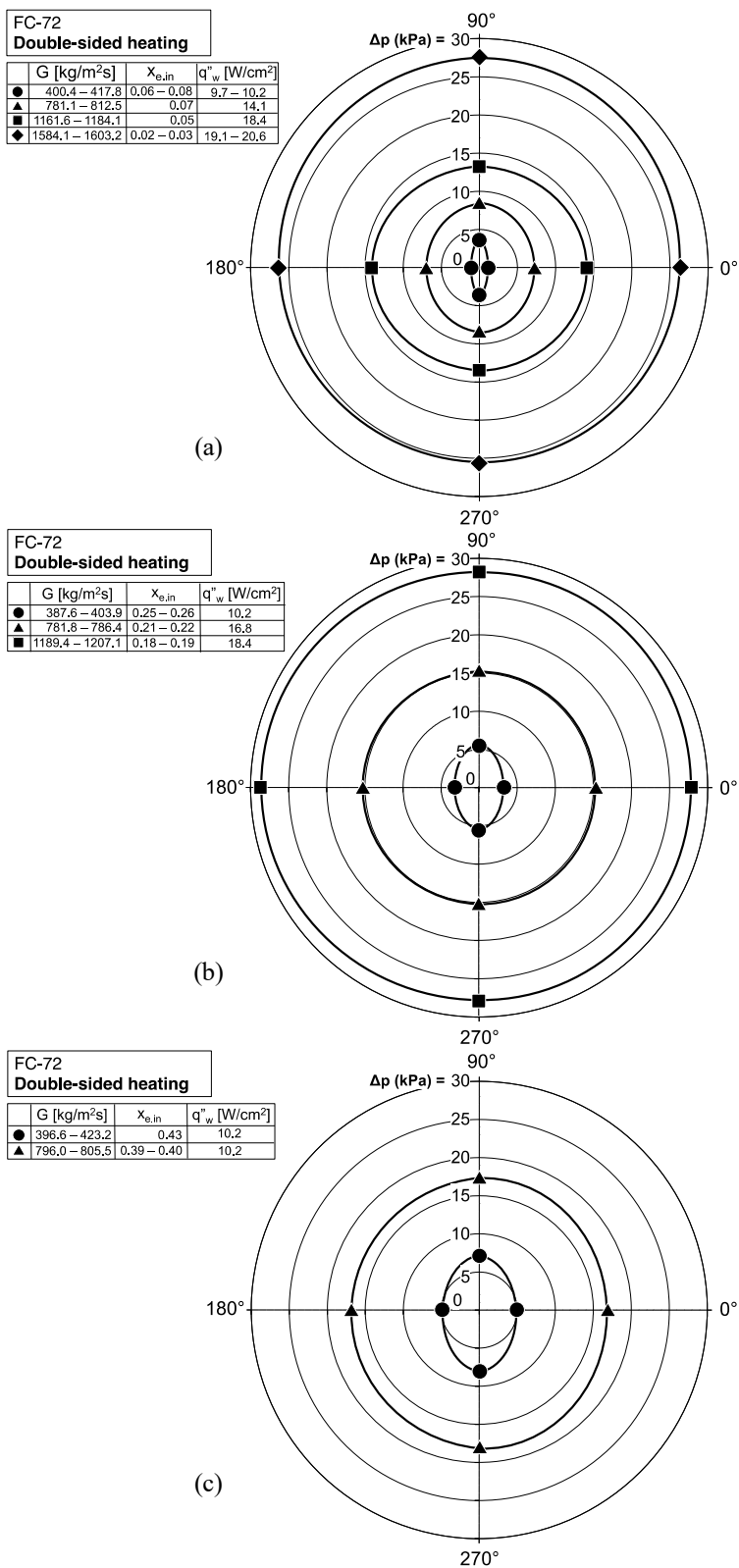
Fig. 4.12: Polar plots showing pressure drop across heated portion of channel with orientation relative to Earth gravity for double-sided heating and different mass velocities for (a) $x_{e,in}$ = 0.02-0.08, (b) $x_{e,in}$ = 0.18-0.26, and (c) $x_{e,in}$ = 0.39-0.43.

increasing G. While this trend is similar to that for single-sided heating, Fig. 4.11(a), two-sided heating decreases the influence of orientation for $G = 781.1 - 812.5$ kg/m²s. The polar plots for the double-sided heating at $x_{e,in} = 0.18 - 0.26$, Fig. 4.12(b), and $x_{e,in} = 0.39 - 0.43$, Fig. 4.12(c), exhibit similar trends, with the influence of orientation becoming quite small starting around $G = 781.8 - 805.5$ kg/m²s. Once again, these trends prove that orientation effects are dictated mostly by mass velocity rather than inlet quality.

Comparing the Δp results for double-sided heating, Figs. 4.12(a), 4.12(b), and 4.12(c), to those for single-sided heating, Figs. 4.11(a), 4.11(b), and 4.11(c), reveals that, for identical values of G, $x_{e,in}$ and wall heat flux, Δp is generally higher for two-sided heating. This tend can be explained by the nearly twice the amount of vapor produced with double-sided heating.

4.2.4 CHF Results

4.2.4.1 Orientation Effects on CHF

Figures 4.13(a)-4.13(d) show polar plots of CHF for single-sided heating over a range of mass velocities at inlet qualities of $x_{e,in} = 0.00 - 0.05$, $0.07 - 0.15$, $0.19 - 0.25$, and $0.62 - 0.69$, respectively. For the lowest inlet quality range of $x_{e,in} = 0.00 - 0.05$, Fig. 4.13(a) shows CHF values for the lowest mass velocity of $G = 197.1 - 226.5$ kg/m²s are lowest for top-wall heating ($\theta = 180°$) due to vapor stratification along the heated wall, while vertical upflow ($\theta = 90°$) and vertical downflow ($\theta = 270°$) show better performances, a trend shared with heat transfer coefficients and pressure drops in sections 4.2.2 and 4.2.3. The CHF for vertical upflow shows slightly higher values in comparison to vertical downflow.
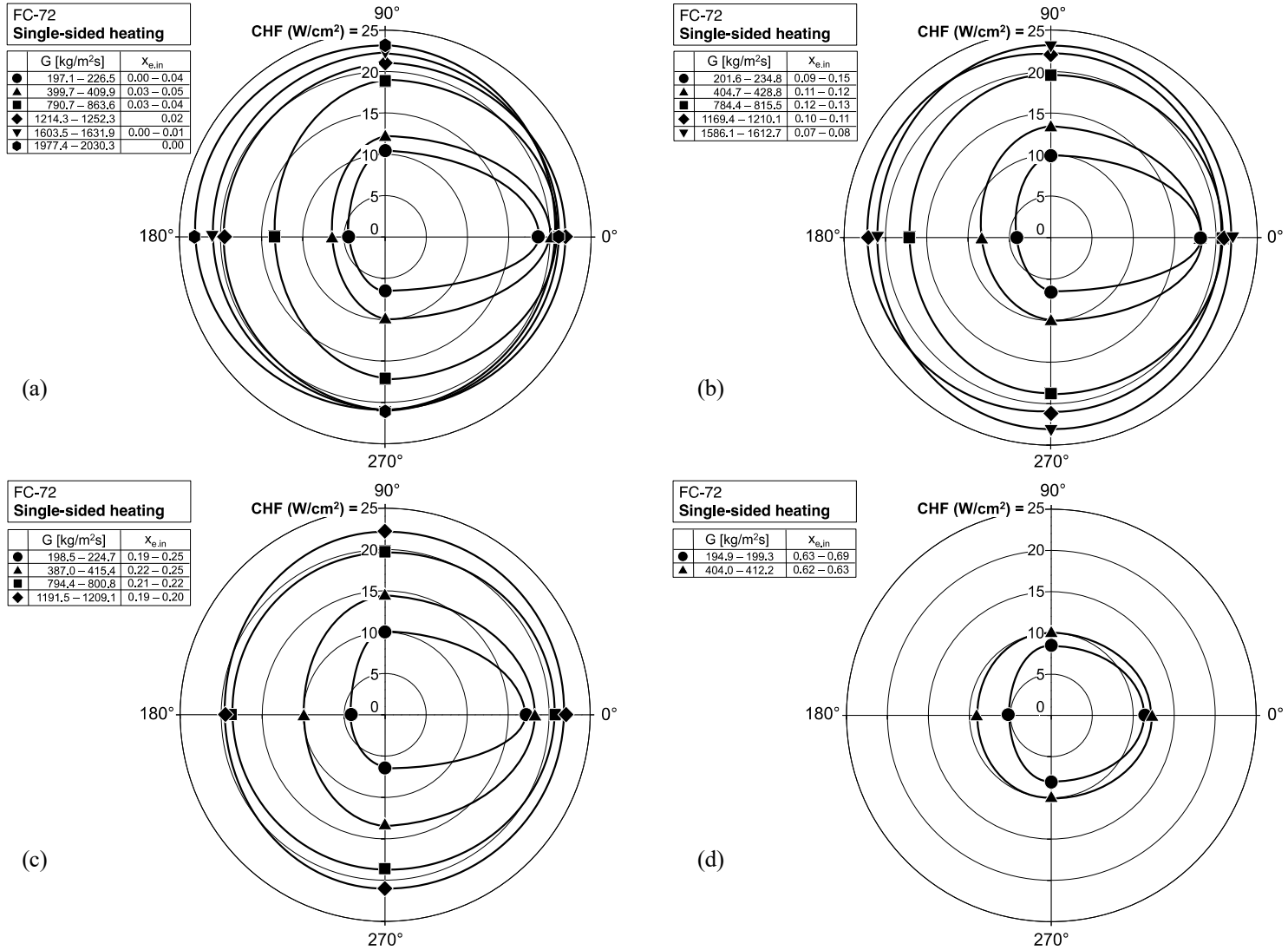
Fig. 4.13: Polar plots showing variations of CHF with orientation relative to Earth gravity for single-sided heating and different mass velocities with (a) $x_{e,in}$ = 0.00-0.05, (b) $x_{e,in}$ = 0.07-0.15, (c) $x_{e,in}$ = 0.19-0.25, and (d) $x_{e,in}$ = 0.62-0.69.

This is due to flow direction assisting vapor removal while the opposite being true for vertical downflow. The effect is not a significant factor even at low mass velocities as incoming vapor due to saturated conditions increases inertial forces in comparison to gravity. Horizontal flow with bottom-wall heating ($\theta = 0°$) shows the best performance, which can be attributed to strong buoyancy effects aiding vapor removal from, and liquid replenishment of the heated wall. For the same low quality range of $x_{e,in} = 0.02$, Fig. 4.13(a) shows increasing mass velocity to $G = 1214.3 - 1252.3$ kg/m^{2}s completely negates the influence of orientation and therefore body force. Figures 4.13(b), 4.13(c), and 4.13(d) show the mass velocities at which the effects of orientation on CHF are completely negated at $x_{e,in} = 0.07 - 0.15$, $0.19 - 0.25$, and $0.62 - 0.69$ are $G = 784.4 - 815.5$, $794.4 - 800.8$, and $400.4 - 412.2$ kg/m^{2}s, respectively. Therefore, increasing inlet quality decreases the mass velocity required for inertia to overcome gravity effects. This can be explained by higher $x_{e,in}$ increasing liquid and vapor velocities and, therefore, flow inertia upstream of the heated portion of the channel.

Figures 4.14(a)- 4.14(d) show polar plots of CHF for double-sided heating over a range of mass velocities at inlet qualities of $x_{e,in} = 0.00 - 0.04$, $0.06 - 0.14$, $0.18 - 0.26$, and $0.61 - 0.68$, respectively. Notice that, because of double-sided heating, CHF values are symmetrical around the vertical axis. For example, horizontal flows at $\theta = 0°$ and $180°$ both include top-wall and bottom-wall heating, rendering the two orientations identical. For $x_{e,in} = 0.00 - 0.02$ and $G = 217.9 - 221.0$ kg/m^{2}s, Fig. 4.14(a) shows vertical upflow ($\theta = 90°$) and vertical downflow ($\theta = 270°$) greatly outperforming the horizontal orientations ($\theta = 0°$ and $180°$). The relatively inferior performances of the horizontal orientations can

FC-72
Double-sided heating

	G [kg/m²s]	$x_{e,in}$
●	217.9 – 221.0	0.00 – 0.02
▲	404.5 – 422.0	0.03 – 0.04
■	786.4 – 844.7	0.03 – 0.04
◆	1204.5 – 1219.3	0.01
▼	1582.8 – 1623.1	0.00
●	1963.4 – 1999.6	0.00
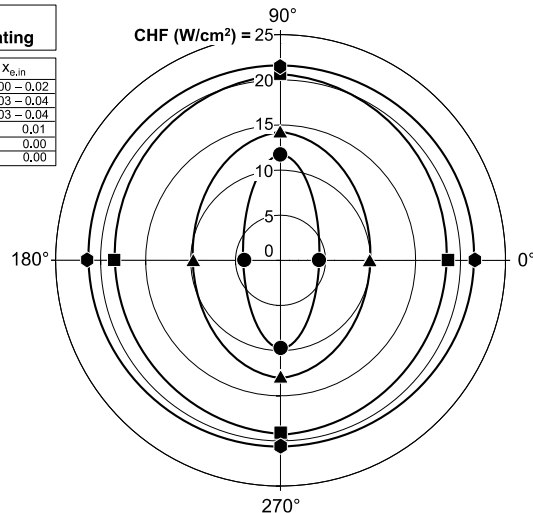
FC-72
Double-sided heating

	G [kg/m²s]	$x_{e,in}$
●	208.2 – 236.3	0.09 – 0.13
▲	391.7 – 427.3	0.11 – 0.14
■	777.4 – 800.3	0.12
◆	1154.7 – 1203.5	0.09 – 0.10
▼	1579.6 – 1604.5	0.06 – 0.07
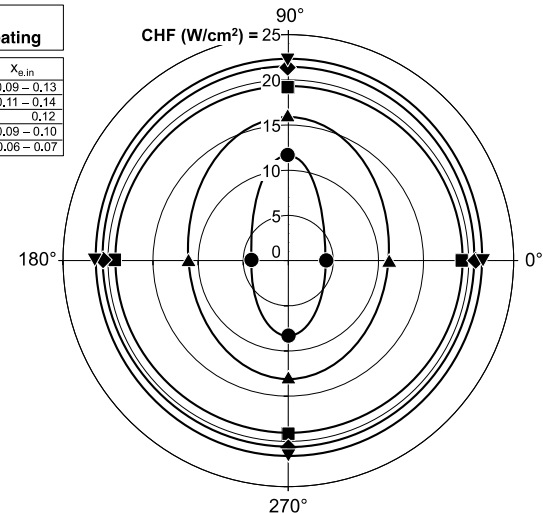
FC-72
Double-sided heating

	G [kg/m²s]	$x_{e,in}$
●	202.0 – 214.4	0.23 – 0.25
▲	387.6 – 403.9	0.25 – 0.26
■	781.8 – 786.4	0.21 – 0.22
◆	1189.4 – 1207.1	0.18 – 0.19
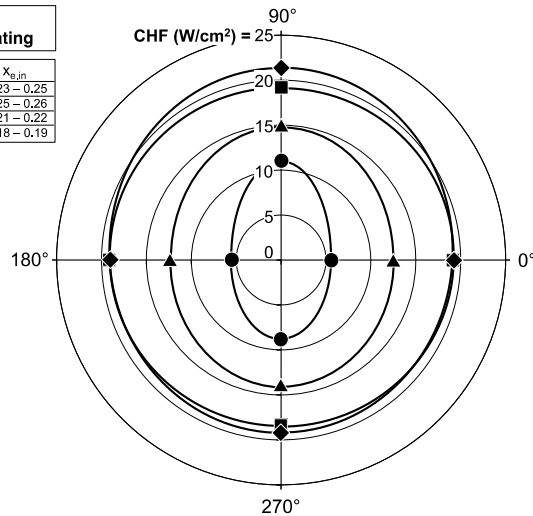
FC-72
Double-sided heating

	G [kg/m²s]	$x_{e,in}$
●	197.1 – 201.0	0.63 – 0.68
▲	401.5 – 418.2	0.61 – 0.63
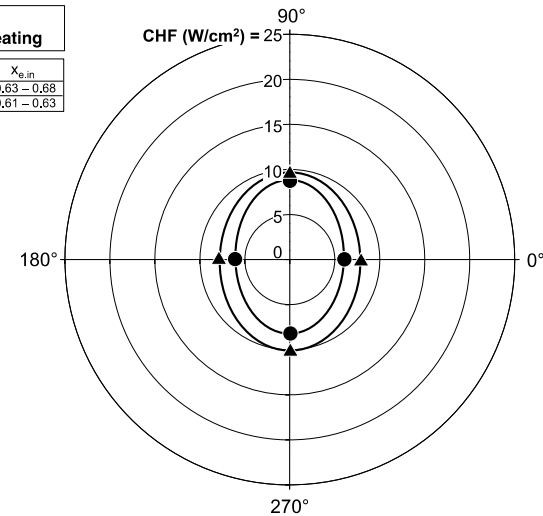
(a) (b) (c) (d)

Fig. 4.14: Polar plots showing variations of CHF with orientation relative to Earth gravity for double-sided heating and different mass velocities for (a) $x_{e,in}$ = 0.00-0.04, (b) $x_{e,in}$ = 0.06-0.14, (c) $x_{e,in}$ = 0.18-0.26, and (d) $x_{e,in}$ = 0.61-0.68.

be explained by their reliance on both top-wall and bottom-wall heating, which compromises their overall performance by vapor stratification along the top wall. The mass velocities at which the effects of orientation on CHF are fully negated for $x_{e,in} = 0.00$ – 0.04, 0.06 – 0.14, 0.18 – 0.26, and 0.61 – 0.68 are G = 786.4 - 844.5, 777.4 - 800.3, 387.6 - 403.9, and 401.5 - 418.2 kg/m²s, respectively. Like the trend for single-sided heating, Figs. 4.13(a) – 4.13(d), the results in Figs. 4.14(a) – 4.14(d) for double-sided heating show increasing $x_{e,in}$ decreases the mass velocity required for inertia to overcome gravity. Here, again, the higher $x_{e,in}$ is believed to increase the velocities of both vapor and liquid at the inlet, which increases flow inertia upstream of the heated portion of the channel. But the main difference between single-sided and double-sided results is the increased flow acceleration and inertia with double sided heating, where vapor is generated along both walls. This difference is reflected in a lower mass velocity range of G = 786.4 - 844.7 kg/m²s corresponding to full negation of orientation effects at $x_{e,in}$ = 0.00 – 0.04, Fig. 4.14(a), compared to G = 1214.3 – 1252.3 kg/m²s for $x_{e,in}$ = 0.02, Fig. 4.13(a).

4.2.4.2 <u>Inlet Quality Effects on CHF</u>

Figures 4.15(a)-4.15(c) show variations of CHF for double-sided heating with $x_{e,in}$ over a range of mass velocities for horizontal flow (θ = 0 and 180°), vertical upflow (θ = 90°) and vertical downflow (θ = 270°), respectively. For all three orientations, CHF for a fixed $x_{e,in}$ is shown increasing monotonically with increasing G. A very interesting trend for all three orientations at low mass velocities is CHF first increases with increasing $x_{e,in}$, reaches peak value, and decreases thereafter. The initial increase can be explained by the increased
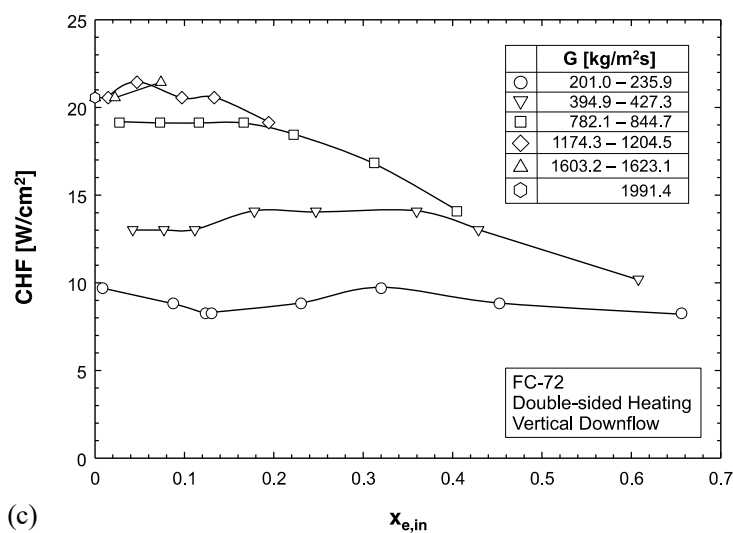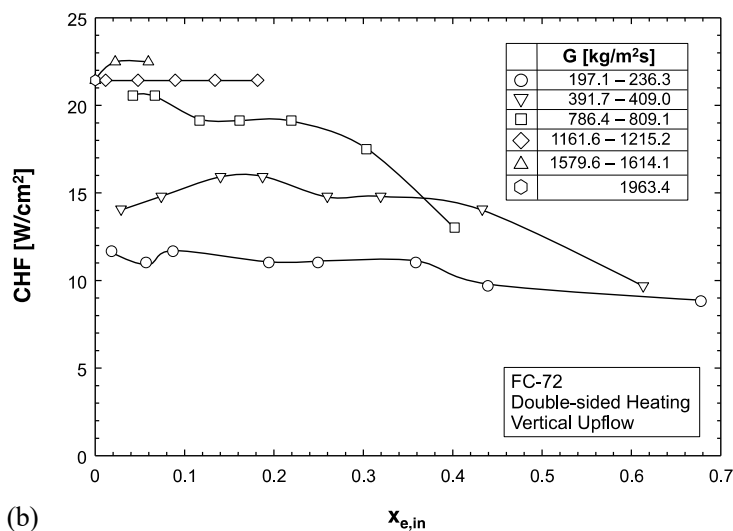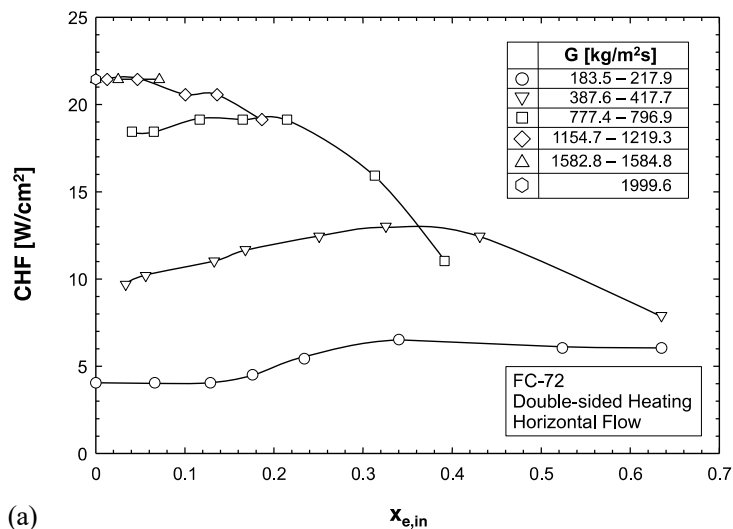
Fig. 4.15: Variations of CHF for double-sided heating with inlet quality for different mass velocities in (a) horizontal flow, (b) vertical upflow, and (c) vertical downflow.

$x_{e,in}$ increasing inlet velocities of both the liquid and vapor. Downstream from the peak value, the benefits of those increases are counterbalanced by an appreciable increase in vapor volume and corresponding scarcity of liquid along the channel. For horizontal flow ($\theta = 0$ and 180°), Fig. 4.15(a) shows peak CHF values for $G = 183.5$ - 217.9 and 387.6 - 417.7 kg/m²s are achieved around $x_{e,in} = 0.35$. The inlet quality corresponding to peak value decreases to around $x_{e,in} = 0.15$ for 777.4 – 796.9 kg/m²s, and $x_{e,in} = 0$ for all higher mass velocities. For vertical upflow ($\theta = 90°$), Fig.4.15(b) shows CHF variations with $x_{e,in}$ for different mass velocities are less pronounced than those for horizontal flow. It is difficult to assign a value for $x_{e,in}$ corresponding to peak CHF for the lowest mass velocity range of $G = 197.1 – 236.3$ kg/m²s. However, peak CHF is achieved around $x_{e,in} = 0.15$ for $G = 391.7 – 409.0$ kg/m²s, and close to $x_{e,in} = 0$ for $G = 786.4 – 809.1$ kg/m²s, and CHF variations with $x_{e,in}$ are similar to those for vertical upflow, Fig. 4.15(c), with some variations in $x_{e,in}$ values corresponding to peak CHF.

4.3 Conclusions

This section explored flow boiling of FC-72 along a rectangular channel with one wall or two opposite walls heated. Experiments were performed in three channel orientations: horizontal, vertical upflow, and vertical downflow over broad ranges of mass velocity, inlet quality and wall heat flux, aided by high-speed video capture of interfacial features. This study focused on the influence of gravity, and therefore orientation, on interfacial behavior during flow boiling, boiling curve, local and average heat transfer coefficients, and pressure drop and CHF results. Key findings from this part are as follows:

(1) For horizontal flow, the effects of gravity are reflected in appreciable stratification across the channel. For the bottom heated wall, gravity aids vapor removal from, and liquid return to the bottom wall.   On the other hand, gravity leads to vapor accumulation along the top heated wall. For vertical upflow and vertical downflow, with both single-sided and double-sided heating, there is far better symmetry in vapor formation along the channel, with no apparent bias towards either wall.

(2) Gravity has a strong influence on the boiling curve for horizontal flow at low mass velocities, but differences in heat transfer performance between bottom wall and top wall heating decrease with increasing mass velocity. On the other hand, there are only minor differences in boiling performance between vertical upflow and vertical downflow.

(3) For all orientations, the local heat transfer coefficient shows an appreciable decline in the inlet region, followed by a rather flat variation in the middle region, and a large increase in the exit region. The decrease in the inlet region is attributed to thermal boundary layer development, while the downstream increase is most likely the result of appreciable flow acceleration towards the exit.

(4) For horizontal flows, large differences in peak heat transfer coefficient are observed between top wall and bottom wall heating for low mass velocities because of the aforementioned stratification phenomenon.   On the other hand, peak heat transfer coefficient values are about equal for all orientations above $G \cong 800$ kg/m^{2}s, proving inertia around this mass velocity is effective at negating any orientation effects. Overall, gravity effects are governed mostly by mass velocity and, to a far lesser extent, by inlet quality.

(5) Pressure drops at low mass velocities are fairly equal for vertical upflow and vertical downflow, but greater than for horizontal flows. However, equal pressure drop is achieved for all orientations above $G \cong 800$ kg/m²s for all inlet qualities excepting the case with single-sided heating and low quality of $x_{e,in} = 0.04 – 0.07$, for which the transition mass velocity is $G \cong 1200$ kg/m²s.

(6) For both single-sided heating and double-sided heating, mass velocity and inlet quality decreases the influence of orientation on CHF, with identical CHF values achieved at high mass velocities irrespective of orientation. Also, increasing inlet quality serves to decrease the mass velocity required for inertia to negate gravity effects.

(7) For double-sided heating and low mass velocities, all three orientations show CHF first increases with increasing quality, reaches peak value, and decreases thereafter. Higher mass velocities exhibit peak CHF value for inlet quality values close to zero. CHF variations with quality are more pronounced for the horizontal orientation compared to vertical upflow and vertical downflow.

CHAPTER 5. CRITICAL HEAT FLUX MODEL FOR SUBCOOLED INLET FLOW

5.1 Interfacial Lift-off Model

Figure 5.1(a) illustrates the interfacial complexity resulting from wall heating configuration (top-wall heating, bottom-wall heating, double-sided heating) for horizontal flow in Earth gravity. Clearly, more complex flow regimes are encountered in other orientations, and it is the goal of this section to utilize the *Interfacial Lift-off Model* to explore the influence of flow orientation, flow velocity and heating configuration on interfacial instability, as well as to predict CHF.

5.1.1 Single-Sided Heating

Zhang *et al*. [53] developed a control-volume-based separated flow model for single-sided heating. As subcooled liquid enters the heated section of the channel, a vapor film begins to form near the leading edge. Due to phase change occurring along the channel, the vapor layer grows monotonically in thickness in the axial direction. The model is based on slip flow assumptions, *i.e.*, uniform velocity in the liquid and vapor layers, while allowing for velocity differences between the two layers. The separated flow model also assumes pressure is uniform across the flow area. This model is used to determine the

(a)

(b)
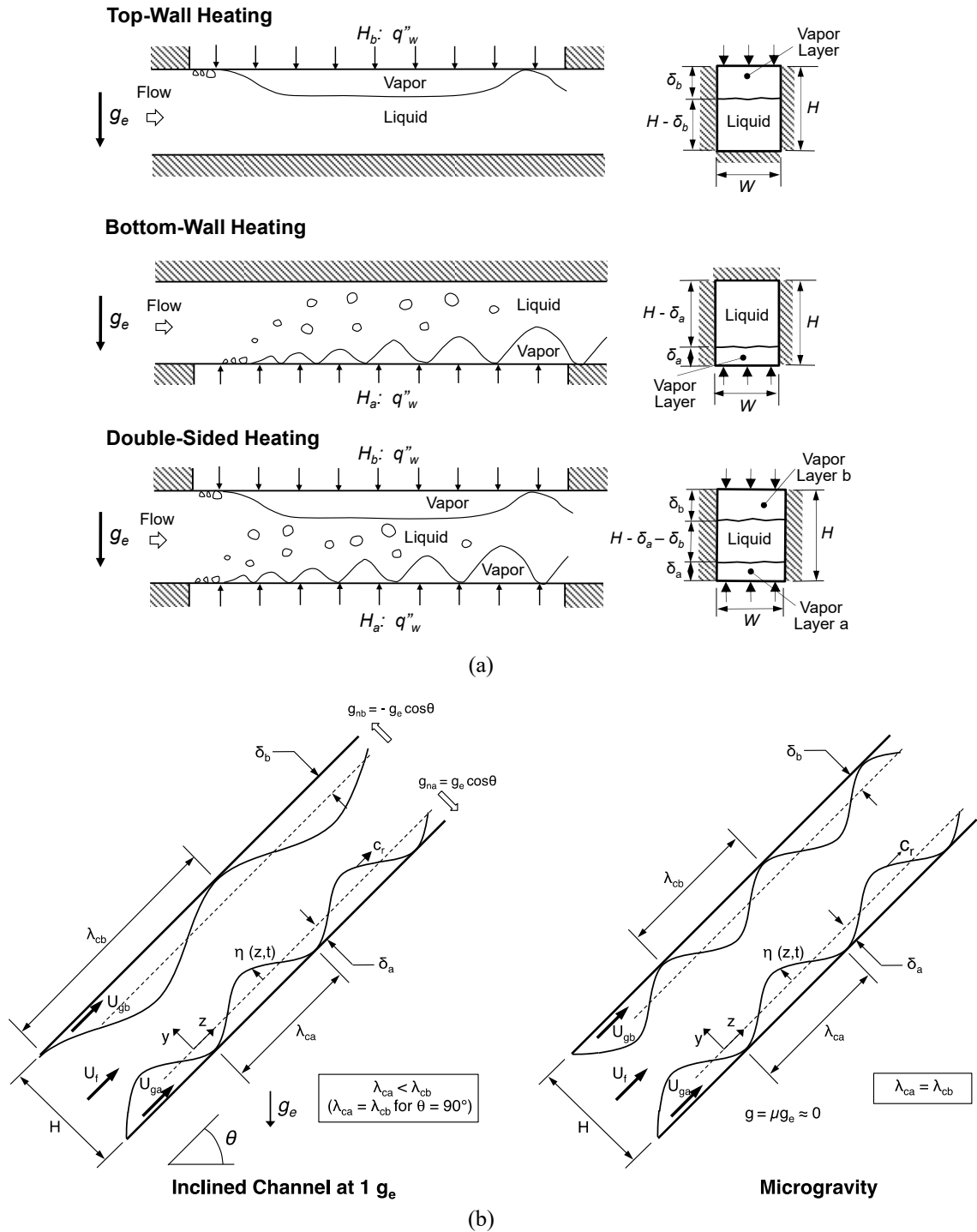
Fig. 5.1: (a) Depiction of horizontal flow boiling near CHF for a rectangular channel with top-wall heating, bottom-wall heating, and double-sided heating. (b) Hydrodynamic instability of wavy vapor layers along heated walls of double-sided heated channel at CHF- for inclined channel in Earth gravity and for microgravity.

variations of mean velocities and thicknesses of the liquid and vapor layers along the channel. These parameters are used to determine the critical wavelength for instability of the vapor layer. For an unstable interface along heated wall H_a, the critical wavelength, λ_{ca}, is given by

$$k_{ca} = \frac{2\pi}{\lambda_{ca}} = \frac{\rho_{fa}'' \rho_{ga}'' \left(U_{ga} - U_f\right)^2}{2\sigma\left(\rho_{fa}'' + \rho_{ga}''\right)} + \sqrt{\left[\frac{\rho_{fa}'' \rho_{ga}'' \left(U_{ga} - U_f\right)^2}{2\sigma\left(\rho_{fa}'' + \rho_{ga}''\right)}\right]^2 + \frac{\left(\rho_f - \rho_g\right)g_{na}}{\sigma}}, \quad (5.1)$$

where ρ_{fa}'', ρ_{ga}'', U_f, U_{ga} and g_{na} are the modified liquid density, modified vapor density, mean velocity of the liquid layer, mean velocity of the wavy vapor layer, and component of gravity normal to the heated wall; the latter given by

$$g_{na} = g_e \cos\theta. \quad (5.2)$$

Using the *Interfacial Lift-off Model*, Zhang *et al.* [53] determined CHF according to the relation

$$CHF = q_m'' = \frac{\rho_g}{\varepsilon}\left(c_{p,f}\,\Delta T_{sub,in} + h_{fg}\right)\left[\frac{4\pi\sigma b\sin\left(b\pi\right)}{\rho_g}\right]^{1/2} \frac{\delta_a^{1/2}}{\lambda_{ca}}\Bigg|_{z_a^*}, \quad (5.3)$$

where b, ε, δ_a and z_a^* are the ratio of wetting front length to critical wavelength, heat utility ratio, mean vapor layer thickness along heated wall H_a, and axial location where vapor layer thickness and critical wavelength are determined. CHF for horizontal flow with bottom-wall and top-wall heating is calculated by setting $\theta = 0$ and 180°, espectively. The key equations for the CHF model for single-sided heating are provided in Tables 5.1 and 5.2.

Table 5.1: Summary of separated flow model and *Interfacial Lift-off Model* relations for single-sided heating (Zhang *et al.* [53]).

Momentum conservation:

$$G^2 \frac{d}{dz}\left[\frac{(1-x_a)^2}{\rho_f(1-\alpha_a)}\right] = -(1-\alpha_a)\frac{dp}{dz} - \frac{\tau_{w,f} P_{w,f}}{A} + \frac{\tau_{ia} P_{ia}}{A} - \rho_f(1-\alpha_a)g\sin\theta$$

$$G^2 \frac{d}{dz}\left[\frac{x_a^2}{\rho_g\alpha_a}\right] = -\alpha_a\frac{dp}{dz} - \frac{\tau_{w,ga} P_{w,ga}}{A} - \frac{\tau_{ia} P_{ia}}{A} - \rho_g\alpha_a g\sin\theta$$

Energy conservation:

$$\frac{dx_a}{dz} = \frac{q''_w W}{\dot{m}\left(c_{p,f}\, \Delta T_{sub,in} + h_{fg}\right)}$$

Critical wavelength:

$$k_{ca} = \frac{2\pi}{\lambda_{ca}} = \frac{\rho''_{fa} \rho''_{ga}\left(U_{ga} - U_f\right)^2}{2\sigma\left(\rho''_{fa} + \rho''_{ga}\right)} + \sqrt{\left[\frac{\rho''_{fa} \rho''_{ga}\left(U_{ga} - U_f\right)^2}{2\sigma\left(\rho''_{fa} + \rho''_{ga}\right)}\right]^2 + \frac{\left(\rho_f - \rho_g\right)g_{na}}{\sigma}}$$

where the modified densities are given by

$$\rho''_{ga} = \rho_g \coth\left(\frac{2\pi}{\lambda_{ca}}\delta_a\right) \text{ and } \rho''_{fa} = \rho_f \coth\left(\frac{2\pi}{\lambda_{ca}}(H - \delta_a)\right)$$

Critical heat flux (CHF):

$$CHF = \frac{\rho_g}{\varepsilon}\left(c_{p,f}\, \Delta T_{sub,in} + h_{fg}\right)\left[\frac{4\pi\sigma b\sin(b\pi)}{\rho_g}\right]^{1/2} \frac{\delta_a^{1/2}}{\lambda_{ca}}\bigg|_{z_a^*}$$

where $z_a^* = z_{0a} + \lambda_{ca}\left(z_a^*\right)$

Table 5.2: Summary of relations used in conjunction with the separated flow model and *Interfacial Lift-off Model* for single-sided wall heating (Zhang *et al.* [53]) and double-sided wall heating (Konishi *et al.* [31]).

Single-sided heating quality relation for vapor layer:

$$x_a = \frac{\rho_g U_{ga} \alpha_a}{G}$$

Double-sided heating quality relations for individual vapor layers:

$$x_a = \frac{\rho_g U_{ga} \alpha_a}{G} \text{ and } x_b = \frac{\rho_g U_{gb} \alpha_b}{G}$$

Wall shear stress relations:

$$\tau_{w,k} = \frac{1}{2} \rho_k U_k^2 f_k$$

$$f_k = C_1 + \frac{C_2}{Re_{D_k}^{1/C_3}} = C_1 + \frac{C_2}{\left(\frac{\rho_k U_k D_k}{\mu_k}\right)^{1/C_3}}$$

where $k = f$, ga or gb. $C_1 = 0$, $C_2 = 16$ and $C_3 = 1$ for laminar flow ($Re_{D_k} \leq 2100$), $C_1 = 0.0054$, $C_2 = 2.3 \times 10^{-8}$ and $C_3 = -2/3$ for transitional flow ($2100 < Re_{D_k} \leq 4000$), and $C_1 = 0.00128$, $C_2 = 0.1143$ and $C_3 = 3.2154$ for turbulent flow ($Re_{D_k} > 4000$), where $D_k = 4 A_k / P_k$

Interfacial shear stress relations:

$$\tau_{ia} = \frac{C_{f,ia}}{2} \rho_g \left(U_{ga} - U_f\right)^2 \text{ and } \tau_{ib} = \frac{C_{f,ib}}{2} \rho_g \left(U_{gb} - U_f\right)^2$$

$$\text{where } C_{f,ia} = C_{f,ib} = 0.5$$

Heat utility ratio:

$$\varepsilon = 1 - 0.00285 \frac{\rho_f}{\rho_g} \frac{c_{p,f} \Delta T_{sub,out}}{h_{fg}} \left(\frac{\rho_f U^2 D}{\sigma}\right)^{0.2}$$

5.1.2 Double-Sided Heating

Konishi *et al.* [31] extended the model by Zhang *et al.* [53] to double-sided heating for subcooled inlet conditions. As subcooled liquid enters the heated section of the channel, two vapor layers begin to form at the leading edges of both heated walls surrounding a middle liquid layer. Using slip flow assumptions similar to those adopted for single-sided heating, momentum and energy conservation relations are used to determine mean velocities and thicknesses for the three layers. Critical wavelength is calculated using the same relation as for single-sided heating, the major difference being gravity components perpendicular to the heated wall. In Earth gravity, the gravity components normal to the upward-facing heated wall and downward-facing heated wall are expressed, respectively, as

$$g_{na} = g_e \cos\theta \qquad (5.4a)$$

and
$$g_{nb} = g_e \cos(\theta + \pi) = -g_e \cos\theta. \qquad (5.4b)$$

The differences in critical wavelength between the upward-facing and downward-facing walls are illustrated in Fig. 5.1(b). In Earth gravity, the normal component tends to stabilize the interface along the downward-facing wall and destabilize the interface along the upward-facing wall. This causes CHF for the upward-facing wall to be larger than for the downward-facing wall. The differences in CHF decrease monotonically with increasing inlet velocity as inertia tends to overcome body force effects, ultimately leading to convergence of CHF values for the two heated wall orientations. For microgravity, identical interfacial behavior is encountered on both walls, which leads to equal CHF values regardless of inlet velocity. The key equations of the model for double-sided heating

are summarized in Table 5.3. Table 5.2 provides relations used in conjunction with the separated flow model and the *Interfacial Lift-off Model* to predict CHF for both single-sided and double-sided heating.

5.2 Model Results and Discussions

5.2.1 Seperated Flow Model Predictions

Figures 5.2(a) – 5.2(d) show predictions of the separated flow model for horizontal double-sided heating in Earth gravity with $U = 1.0$ m/s, $p_{in} = 150$ kPa, $\Delta T_{sub,in} = 3°C$, and $q''_w = 30$ W/cm². Figure 5.2(a) shows variations of thicknesses of the separated layers along the heated section of the channel. The two vapor layers are shown beginning to form at the leading edges and grow monotonically along the heated walls on the expense of a gradually consumed middle liquid layer. The phase layer thicknesses are needed to calculate the modified phase densities, ρ''_f and ρ''_g, in the relation for critical wavelength, Eq. (5.1). Another parameter that is important to calculating the critical wavelength is phase velocity difference. Figure 5.2(b) shows the variations of the phase velocities and velocity difference between the vapor layers and middle liquid layer. The liquid layer is faster than the two vapor layers at $z = 0$, but is quickly overtaken by the vapor layers over a short distance from the leading edges of the heated walls. The distance where the vapor layers overtake the liquid layer is $z = z_o$, which is an important parameter in the *Interfacial Lift-off Model*. Figures 5.2(c) and 5.2(d) show predictions of pressure and quality, respectively, along the heated section of the channel. Notice that the equilibrium quality starts with a negative value at $z = 0$ because of the subcooled inlet conditions but becomes positive downstream along the heated section.

Table 5.3: Summary of separated flow model and *Interfacial Lift-off Model* relations for double-sided heating (Konishi *et al.* [31]).

Momentum conservation:

$$G^2 \frac{d}{dz}\left[\frac{\left(1-x_a-x_b\right)^2}{\rho_f\left(1-\alpha_a-\alpha_b\right)}\right] = -\left(1-\alpha_a-\alpha_b\right)\frac{dp}{dz} - \frac{\tau_{w,f}\, P_{w,f}}{A} \pm \frac{\tau_{ia}\, P_{ia}}{A} \pm \frac{\tau_{ib}\, P_{ib}}{A} - \rho_f\left(1-\alpha_a-\alpha_b\right)g\sin\theta$$

$$G^2 \frac{d}{dz}\left[\frac{x_a^2}{\rho_g\alpha_a}\right] = -\alpha_a \frac{dp}{dz} - \frac{\tau_{w,ga}\, P_{w,ga}}{A} \mp \frac{\tau_{ia}\, P_{ia}}{A} - \rho_g\alpha_a\, g\sin\theta$$

$$G^2 \frac{d}{dz}\left[\frac{x_b^2}{\rho_g\alpha_b}\right] = -\alpha_b \frac{dp}{dz} - \frac{\tau_{w,gb}\, P_{w,gb}}{A} \mp \frac{\tau_{ib}\, P_{ib}}{A} - \rho_g\alpha_b\, g\sin\theta$$

Energy conservation:

$$\frac{dx_a}{dz} = \frac{dx_b}{dz} = \frac{q_w''\, W}{\dot{m}\left(c_{p,f}\,\Delta T_{sub,in} + h_{fg}\right)}$$

Critical wavelength:

$$k_{cm} = \frac{2\pi}{\lambda_{cm}} = \frac{\rho_{fm}''\,\rho_{gm}''\left(U_{gm}-U_f\right)^2}{2\sigma\left(\rho_{fm}''+\rho_{gm}''\right)} + \sqrt{\left[\frac{\rho_{fm}''\,\rho_{gm}''\left(U_{gm}-U_f\right)^2}{2\sigma\left(\rho_{fm}''+\rho_{gm}''\right)}\right]^2 + \frac{\left(\rho_f-\rho_g\right)g_{nm}}{\sigma}}$$

where the modified densities are given by

$$\rho_{gm}'' = \rho_g \coth\left(\frac{2\pi}{\lambda_{cm}}\delta_m\right) \quad\text{and}\quad \rho_{fm}'' = \rho_f \coth\left(\frac{2\pi}{\lambda_{cm}}(H-\delta_a-\delta_b)\right)$$

$m = a$ for heater H_a and $m = b$ for heater H_b

Critical heat flux (CHF):

$$CHF = \frac{\rho_g}{\varepsilon}\left(c_{p,f}\,\Delta T_{sub,in} + h_{fg}\right)\left[\frac{4\pi\sigma\, b\sin\left(b\pi\right)}{\rho_g}\right]^{1/2} \left.\frac{\delta_m^{1/2}}{\lambda_{cm}}\right|_{z_m^*}$$

where $z_m^* = z_{0m} + \lambda_{cm}\left(z_m^*\right)$

Fig. 5.2: Separated flow model predictions of (a) phase layer thicknesses, (b) phase velocities, (c) pressure, and (d) quality.

The results from the separated flow model are used to compute CHF. Because the heated walls face opposite orientations of the perpendicular component of Earth gravity, two different CHF values are determined, one for each heated wall. Even though the model predicts two CHF values, only the lower of the two is physically relevant since, in the actual experiments, power input to both heated walls is cut off once CHF is detected in either wall.

5.2.2 CHF Predictions

To assess the effectiveness of the *Interfacial Lift-off Model*, predictions are compared to experimental data for single-sided and double-sided heating in both Earth gravity and microgravity. Figure 5.3(a) compares CHF predictions to experimental horizontal flow data for single-sided and double-sided heating in Earth gravity for slightly subcooled inlet conditions. The model predicts a stable interface below $U = 1.0$ and 0.5 m/s for top-wall heating and double-sided heating configurations, respectively, and an unstable interface for bottom-wall single-sided heating. A stable interface, which will be discussed later in this study, corresponds to low CHF values beyond the validity range of the *Interfacial Lift-off Model*. The experimental results showed that bottom-wall heating below $U = 0.5$ m/s yields conditions resembling pool boiling that are dominated by gravity, and for which the wavy vapor layer is not observed. The velocity ranges associated with a stable interface ($U \leq 1.0$ m/s for top-wall heating and $U \leq 0.5$ m/s for double-sided heating) and pool boiling behavior ($U \leq 0.5$ m/s for bottom-wall heating) impose lower limits for validity of the *Interfacial Lift-off Model*, as indicated in Fig. 5.3(a). Above these velocity limits, the
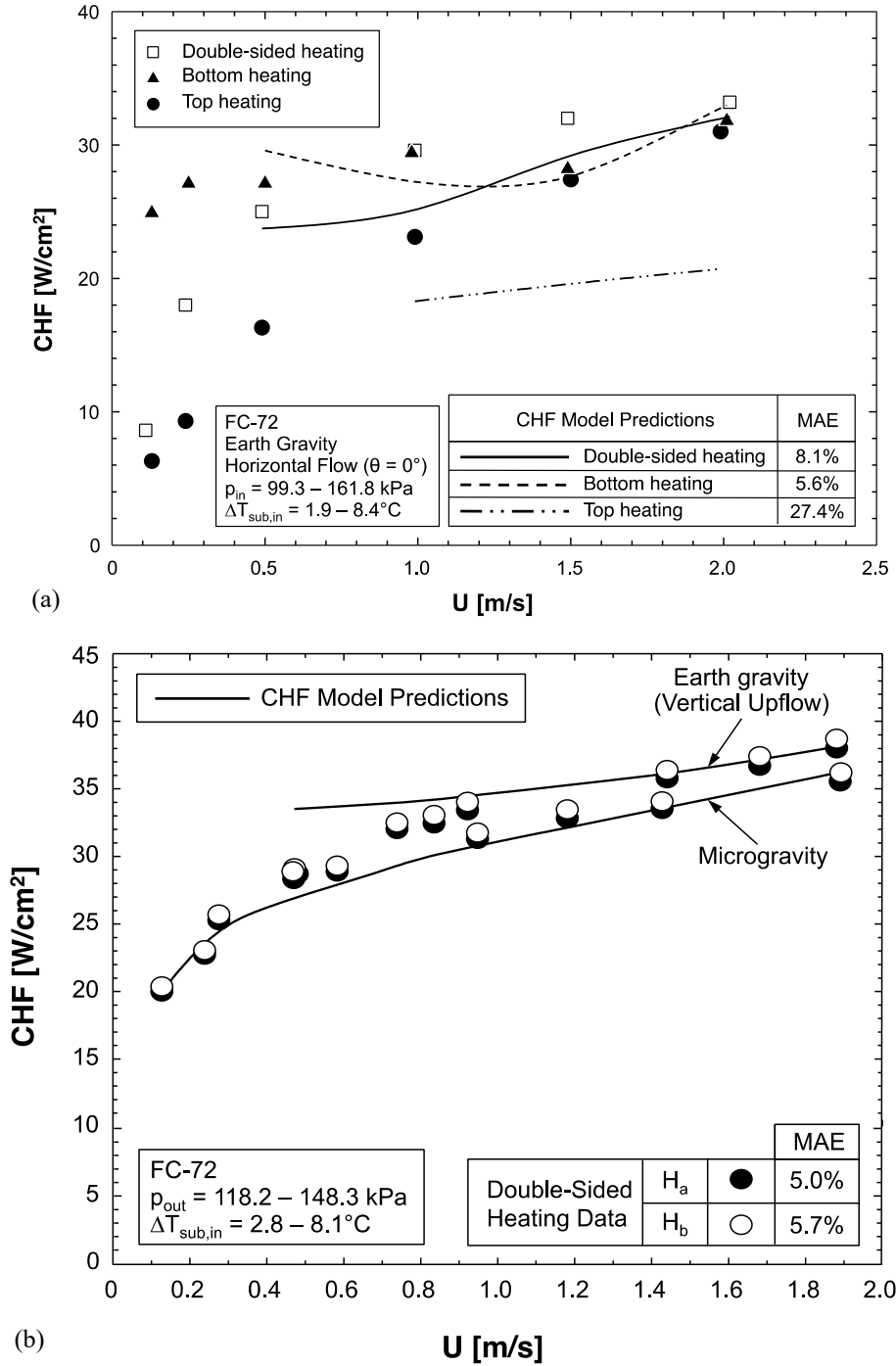
Fig. 5.3: Comparison of *Interfacial Lift-off Model* predictions to CHF data for (a) horizontal top-wall, bottom-wall and double-sided heating in Earth gravity, and (b) double-sided heating in microgravity and vertical upflow in Earth gravity. Figure (b) has been adapted from [31].

predictive accuracy of the model is accessed using mean absolute error (MAE), which is defined as,

$$MAE = \frac{1}{N} \sum \left| \frac{CHF_{pred} - CHF_{exp}}{CHF_{exp}} \right|. \tag{5.5}$$

For bottom-wall heating and double-sided heating, Fig. 5.3(a) shows good model predictions both in magnitude and trend, evidences by MAEs of 5.6% and 8.1%, respectively. For bottom-wall heating, the model predicts a transition from gravity-dominated to inertia-dominated flow, with the slope of CHF versus U changing from negative to positive around 1.5 m/s. For top-wall heating, the model is able to capture the trend of CHF increasing with increasing U, albeit with a higher MAE of 27.4%. In a previous study by Konishi *et al*. [31], good agreement was demonstrated between the model predictions and experimental results for double–sided heating in both microgravity and vertical upflow in Earth gravity, as shown in Fig. 5.3(b). In summary, Figs. 5.3(a) and 5.3(b) demonstrate the effectiveness of the *Interfacial lift-off Model* in modeling both single-sided and double-sided heating in both Earth gravity and microgravity.

5.2.3 Liquid-Vapor Interfacial Behavior

Figures 5.4(a) and 5.4(b) show the eight flow orientations that are examined for single-sided and double-sided heating in Earth gravity. For all these orientations, the flow enters from the center and radiates outwards. The orientation angle dictates whether the channel is incurring *upflow* or *downflow* relative to Earth gravity, while the placement of
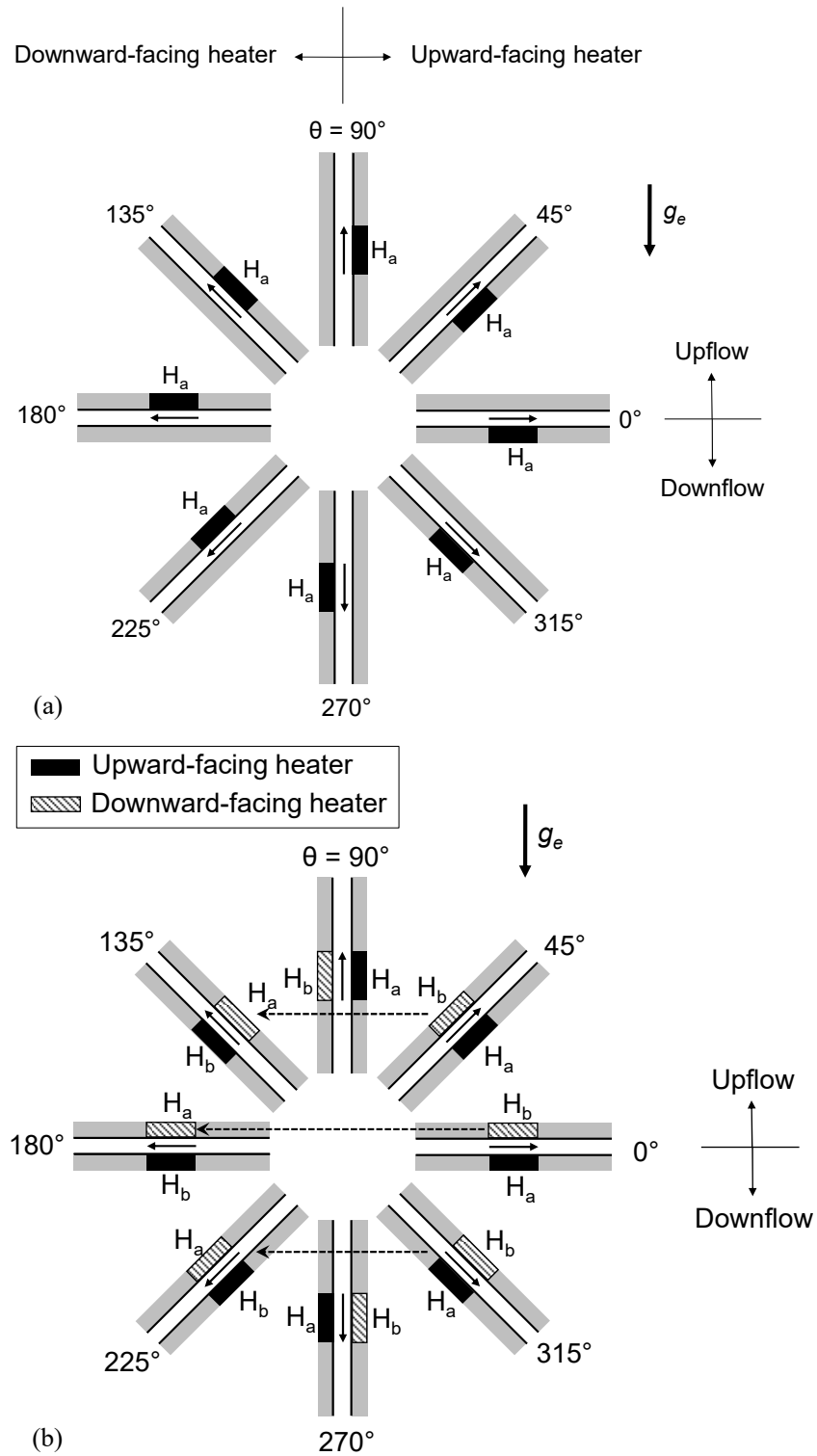
Fig. 5.4: Flow orientation and heater nomenclature for (a) single-sided heating and (b) double-sided heating in Earth gravity.

the heated wall decides if the wall is *upward-facing* or *downward-facing*. Due to symmetry, double-sided heating in Earth gravity requires the flow channel to span only half a full circle ($\theta = 0$ - 360°) from vertical upflow to vertical downflow to cover all orientations. But for consistency between single-sided and double-sided heating configurations, results are presented below for the entire range of $\theta = 0$ - 360°. Figures 5.4(a) and 5.4(b) indicate the locations of the heated walls H_a and H_b. For double-sided heating, Fig. 5.4(b) also indicates where H_a and H_b are either upward-facing or downward-facing.

As indicated earlier, Zhang *et al*. [53] performed extensive studies on the effects of orientation on interfacial behavior and CHF for single-sided heating in Earth gravity. They compared interfacial behavior at CHF- for $\Delta T_{sub,out} = 3°C$ for flow velocities between $U = 0.1$ and 1.5 m/s. Large variations of interfacial behavior were observed with different orientation at 0.1 m/s, which should have a profound influence on CHF mechanism and magnitude. For $U = 1.5$ m/s, a significant increase in inertia yielded virtually identical wavy vapor layer interfacial behavior over the entire range of orientations. In the experimental results from this study we observed the same wavy vapor layer behavior for both single-sided and double-sided heating in horizontal flow in Earth gravity for $U \geq 1$ m/s. In another study, Konishi *et al*. [30] observed the same wavy vapor layer behavior in microgravity for $0.1 < U < 1.9$ m/s.

5.2.4 <u>Effect of Orientation on Critical Wavelength</u>

The interfacial behavior captured with high-speed video and the CHF predictions provide ample support of the validity of the *Interfacial Lift-off Model*. Predicted results

hereafter are obtained using the *Interfacial Lift-off Model* for FC-72 for near-saturated inlet conditions, $\Delta T_{sub,in} = 3°C$, and an inlet pressure of $p_{in} = 100$ kPa. As discussed earlier, the critical wavelength is a key parameter of the *Interfacial Lift-off Model*. It is calculated using Eq. (5.1) by utilizing the liquid and vapor layer thicknesses and velocities predicted using the separated flow model. Several of the flow visualization studies discussed earlier have confirmed the existence of a wavy vapor layer along the heated wall, with contact of the bulk liquid with the wall maintained at CHF- only in wetting fronts corresponding to the wave troughs. Clearly, hydrodynamic instability of the liquid-vapor interface is crucial to formation of both the wavy vapor layer and the wetting fronts.

An iterative procedure discussed in detail by Konishi *et al.* [31] is adopted to calculate CHF. In this procedure, an input heat flux to the heated walls is assumed, which is used to calculate the key output parameters of the separated flow model. These parameters are then used to calculate the critical wavelength and CHF using equations provided in Table 5.1 and 5.3 for single-sided and double-sided heating, respectively. Bisection method is used to achieve convergence between the assumed heat flux and computed CHF.

In this section, this iterative procedure is used to determine the variations of critical wavelength corresponding to the convergent CHF value with orientation and velocity in Earth gravity, and with velocity in microgravity. These variations are then used to gain insight into the influence of critical wavelength on CHF trends. Figures 5.5(a) and 5.5(b) show, for different velocities, the variation of critical wavelength, λ_{ca}, for heated wall H_a
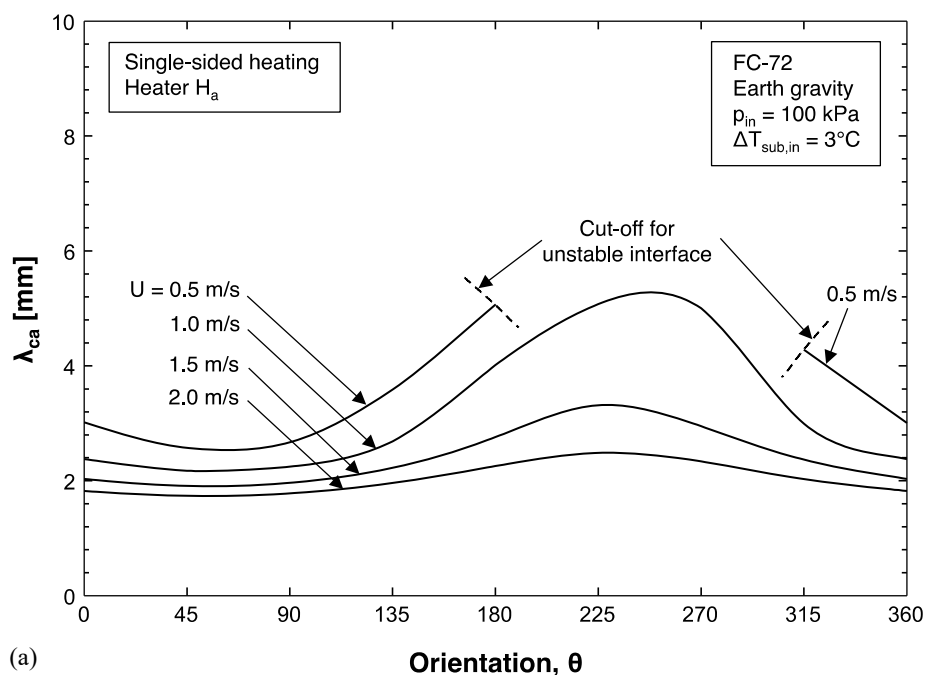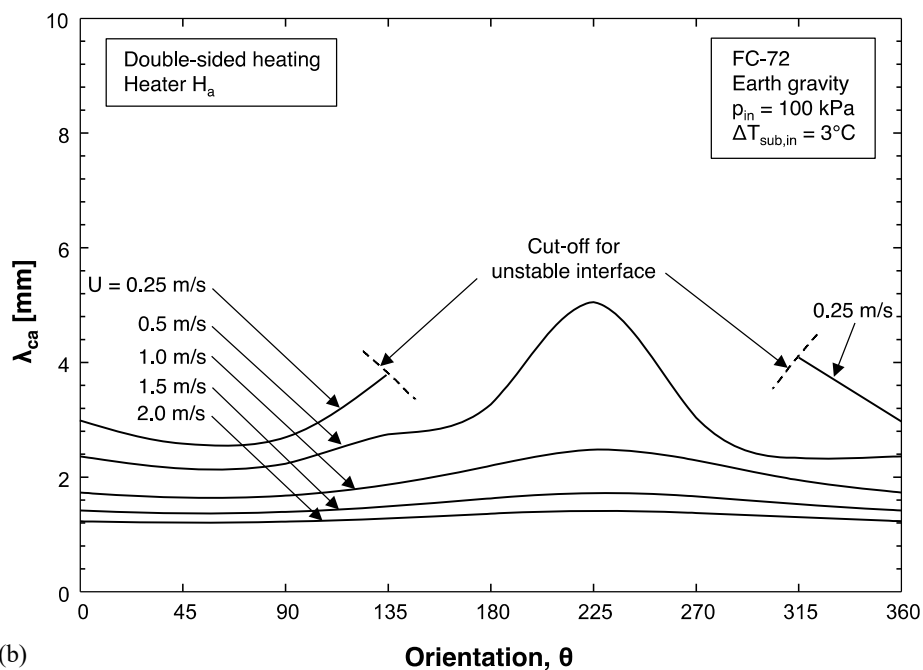
Fig. 5.5: Variation of predicted critical wavelength with orientation relative to Earth gravity for (a) single-sided heating and (b) double-sided heating.

with orientation relative to Earth gravity for single-sided and double-sided heating, respectively. Notice in Fig. 5.5(a) the existence of a region between $\theta = 180°$ and $270°$ for $U = 0.5$ m/s, where the interface is stable; this is where the *Interfacial Lift-off Model* is invalid. Increasing the velocity to $U = 1$ m/s, the interface becomes unstable and the critical wavelength is predicted over the entire range of orientations. Increasing the velocity further, λ_{ca} exhibits little variation with orientation. This can be explained mathematically by examining the two terms under the radical in Eq. (5.1), which account for inertia and gravity effects. High velocity allows inertia to dwarf gravity effects, and the second term becomes negligible, leading to convergence of λ_{ca} values for a given velocity regardless of orientation. Figure 5.5(a) also shows that λ_{ca} decreases with increasing velocity, which implies wetting fronts become more remote from one another with decreasing velocity, a behavior that is confirmed experimentally in this study.

Fig. 5.5(b) shows similar trends for double-sided heating. One significant difference is that, while a stable orientation region is predicted with single-sided heating at $U = 0.5$ m/s, this region is nonexistent for double-sided heating at 0.5 m/s, but is encountered at a lower velocity of 0.25 m/s. These differences can be attributed to double-sided heating producing more vapor and resulting in higher flow acceleration, which causes inertia to dwarf gravity effects at lower velocities than for single-sided heating.

5.2.5 Effects of Orientation on CHF

Figure 5.6(a) shows, for a range of velocities, a polar plot of CHF predictions with orientation relative to Earth gravity for single-sided heating. Notice how the influence of
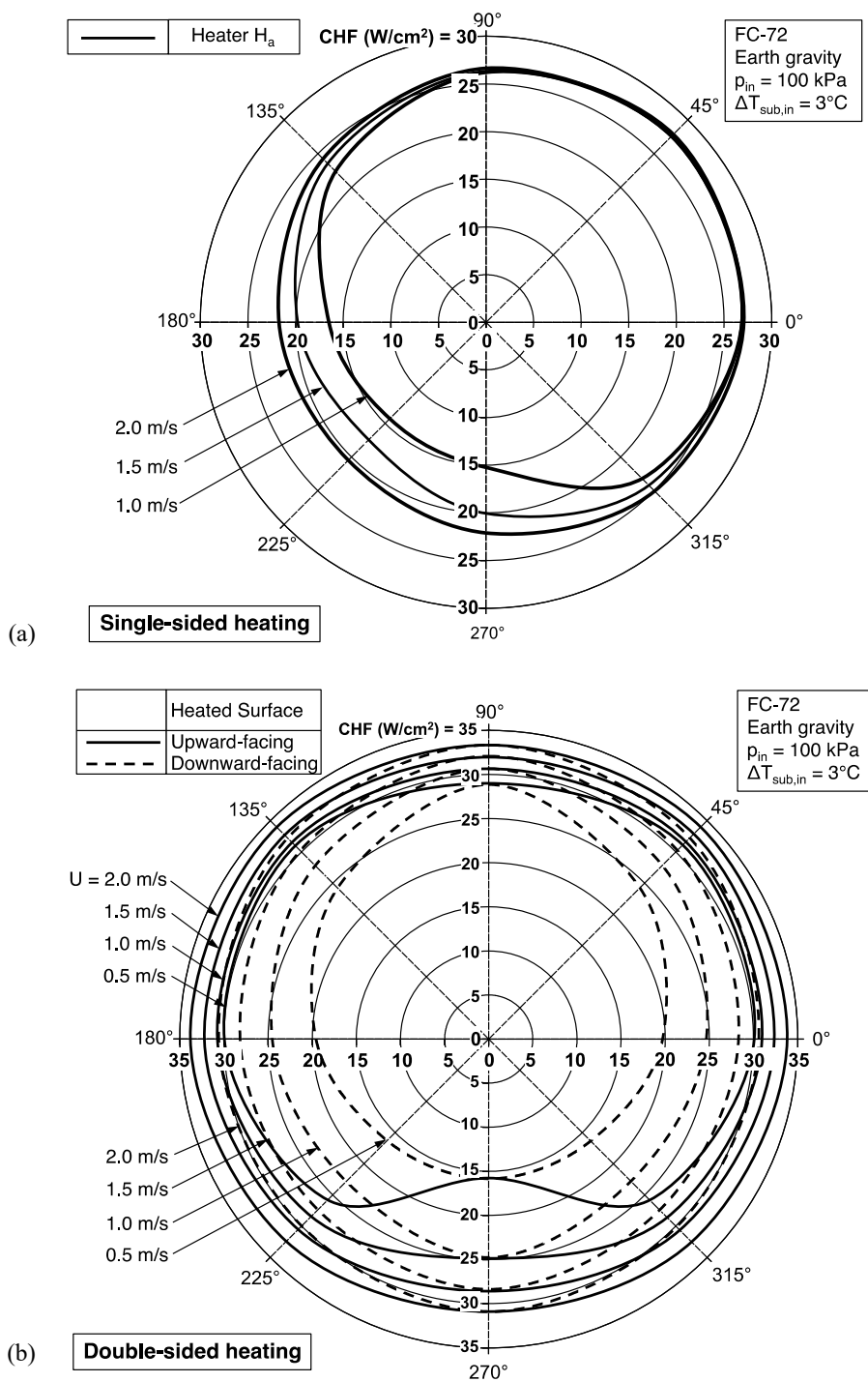
Fig. 5.6: Polar plots of predicted CHF with orientation relative to Earth gravity for different inlet velocities for (a) single-sided heating and (b) double-sided heating.

orientation is more pronounced for lower velocities and gradually abates with increasing velocity. The lowest CHF values in this figure correspond to $\theta = 225°$, which is consistent with experimental results [53,54] that showed this orientation to yield the worst CHF performance. Overall, CHF values are both highest and less sensitive to orientation for upflow and upward-facing heated wall orientations ($\theta = 0 - 90°$), and both significantly smaller and very sensitive to orientation for downflow and downward-facing heated wall orientations ($\theta = 0 - 90°$); the influence of orientation, especially for the latter range, is shown diminishing with increasing velocity.

Figure 5.6(b) shows CHF polar plots for double-sided heating in Earth gravity. CHF predictions are shown for both upward-facing and downward-facing heated walls for all orientations. Recall that, during the experiments, power to the heated walls is cut off once either wall reaches CHF. But the *Interfacial Lift-off Model* is used here to predict CHF for both heated walls, which is useful to understanding the differences in underlying physical mechanisms between the two wall orientations. With reference to the flow orientation nomenclature, Fig. 5.6(b) distinguishes CHF for upward-facing and downward-facing heated walls using solid and dashed line, respectively. Notice how, as shown earlier in Fig. 5.4(b), a heated wall that is upward-facing for $\theta = 45, 0$, and 315° becomes downward-facing for $\theta = 135, 180$ and 225°, and visa versa, which explains the symmetry in Fig. 5.6(b). Each double-sided heating orientation includes two heated walls that are subjected to opposite gravity components, and CHF is lower for a downward-facing wall than one upward-facing. This behavior is explained by buoyancy tending to remove vapor away from the upward-facing wall and towards the downward-facing wall, and decreasing liquid access to the latter. Increasing velocity is shown increasing CHF for both upward-facing

and downward-facing walls, and the difference between the two wall orientations also decreases with increasing velocity, ultimately leading to convergence of CHF values for both wall orientations at high velocities.

Figures 5.7(a) and 5.7(b) show alternative representations of CHF predictions over the entire range of orientations in Earth gravity, as well as in micro-gravity for single-sided heating and double-sided heating, respectively. For microgravity, orientation effects are inconsequential and CHF values are shown falling between the maxima and minima for Earth gravity. This is an important finding since it implies that performing terrestrial experiments for the entire range of orientations will provide a CHF range that encompasses that for microgravity at the same velocity. Moreover, CHF value for microgravity at a given velocity is close to the mean for all terrestrial orientations, and the microgravity and mean terrestrial values converge with increasing velocity. For double-sided heating, Fig. 5.7(b) shows the predicted CHF for microgravity and for heated walls H_a and H_b as well as minimum of the two for Earth gravity; the minimum is the value anticipated in actual experiments since power input to both walls is cut off once CHF is detected in either wall.

It is also useful to examine the influences of velocity and orientation on important parameters of *Interfacial Lift-off Model*. These parameters are examined with respect to heated wall H_a during double-sided heating to demarcate the influences of gravity on both flow orientation and heated wall orientation. Figures 5.8(a) shows the variation of CHF with inlet velocity. It shows CHF increases with increasing U, with orientations in the range
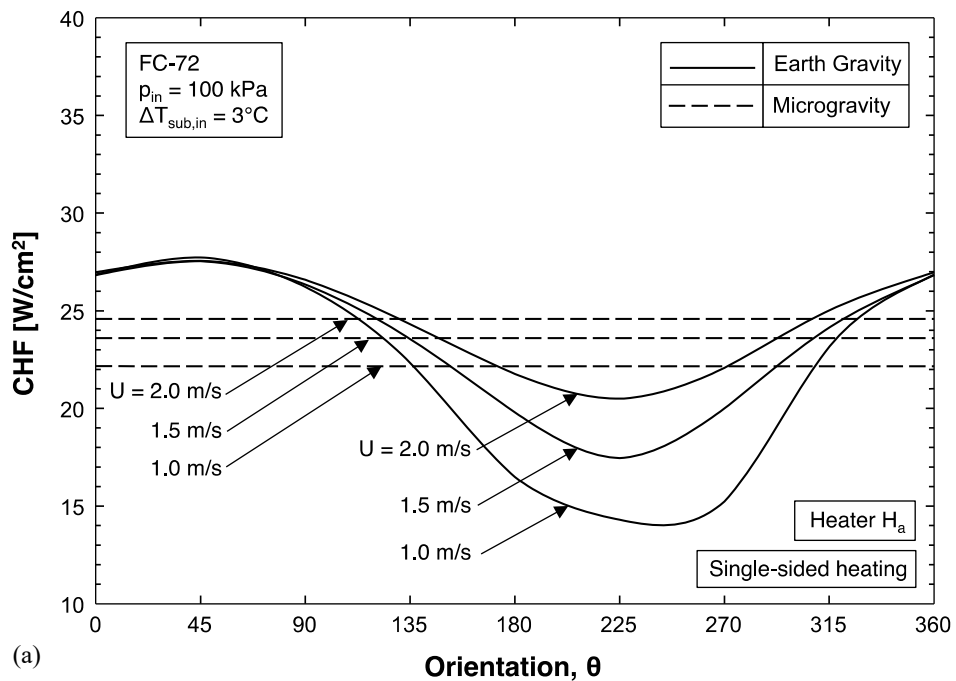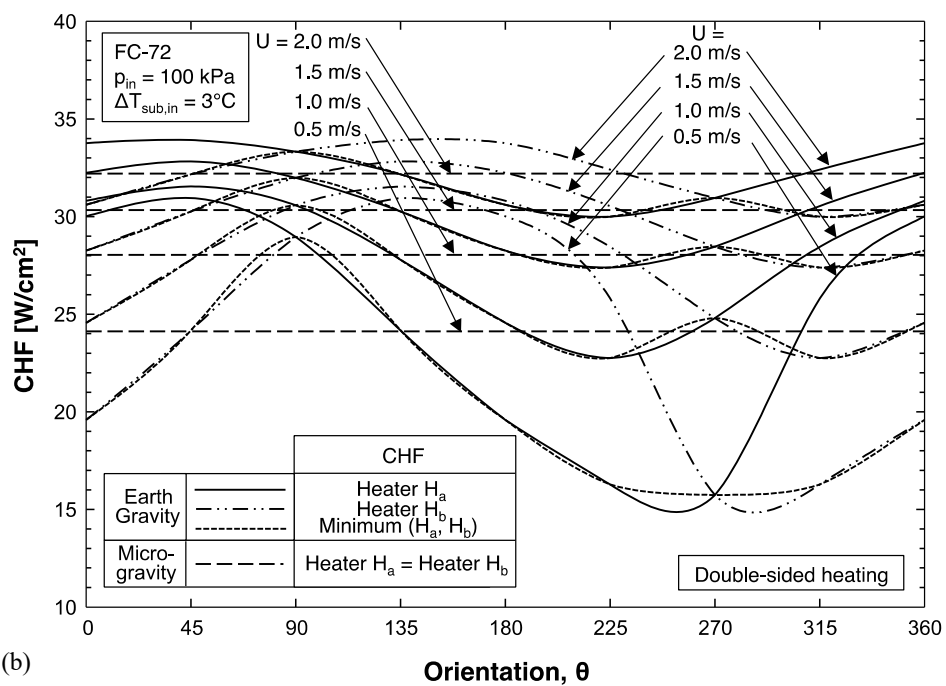
Fig. 5.7: Variation of predicted CHF with orientation in Earth gravity and microgravity for (a) single-sided heating and (b) double-sided heating.
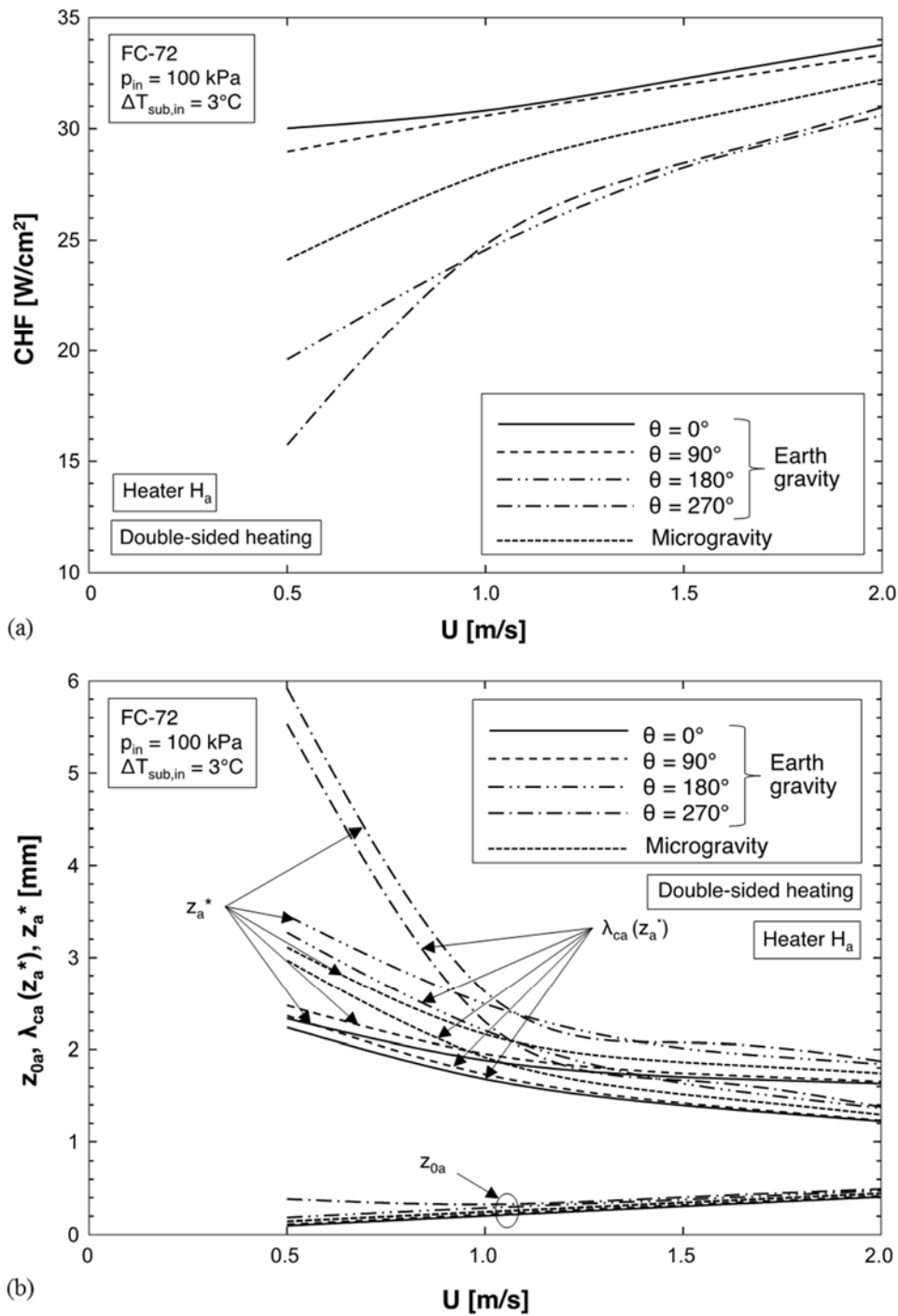
Fig. 5.8: Variations of (a) CHF and (b) z_{0a}, $\lambda_{ca}(z_a^*)$ and z_a^* versus inlet velocity for heater wall H_a in double-sided heating in Earth gravity and microgravity.

of $\theta = 0 - 90°$ clearly out-performing $\theta = 180 - 270°$. This confirms what was stated earlier, that upflow with upward-facing heated wall orientations out-performs downflow with doward-facing orientations, but CHF values tend to converge with increasing U. CHF values for microgravity fall midway between the maxima and minima for Earth gravity.

Figure 5.8(b) shows variations of computed values for other parameters of the *Interfacial Lift-off Model* with U. They include streamwise distance, z_{0a}, where $U_g = U_f$, extent of continuous upstream wetting region, z_a^*, and critical wavelength, $\lambda_{ca}(z_a^*)$. z_{0a} is both quite small and increases very slowly with increasing U, proving that the vapor velocity surpasses the liquid velocity very close to the upstream edge of the heated wall. Both z_a^* and $\lambda_{ca}(z_a^*)$ are shown decreasing with increasing U. These two parameters are highest at $\theta = 270°$, followed by 180, 90 and 0°. Like CHF, the magnitudes of both parameters for different orientations tend to converge with increasing U. Here too, the parameters for microgravity fall midway between the maxima and minima for different orientations in Earth gravity. Overall, Figs. 5.8(a) and 5.8(b) point to the need to increase velocity above ~ 1.5 m/s to negate the influence of orientation in Earth gravity.

These findings clearly demonstrate the effectiveness of the *Interfacial Lift-off Model* in describing interfacial behavior at CHF- as well as the trigger event for CHF for both Earth gravity and microgravity. Further validation of the model may benefit from future experiments involving detailed tracking of the vapor-liquid interface as well as local, instantaneous velocity measurements as discussed in refs. [74] and [75].

5.3 Conclusions

This section is a consolidated investigation of the diverse and complex trends associated with flow boiling CHF in a rectangular channel in microgravity and for different orientations in Earth gravity. Several previous databases for FC-72 corresponding to slightly subcooled inlet conditions are used to assess the accuracy of the *Interfacial Lift-off Model* in capturing the CHF trends for both single-sided and double-sided wall heating. Key findings from the study are as follows.

(1) The *Interfacial Lift-off Model* shows good accuracy in predicting experimental CHF data for both Earth gravity and microgravity with both single-sided and double-sided wall heating.

(2) For Earth gravity, CHF mechanism is highly sensitive to flow orientation at very low velocities, but is consistent with the wavy vapor layer depiction of the *Interfacial Lift-off Model* at higher velocities. The model predicts a stable vapor-liquid interface for flow orientations between $\theta = 180$ and $270°$ for $U < 0.5$ m/s for single-sided wall heating, and $U < 1$ m/s for double-sided heating. A wavy liquid-vapor interface is predicted for all other orientations and velocities, the critical wavelength for which decreases with increasing velocity and become independent of orientation above ~ 1.5 m/s.

(3) For single-sided heating in Earth gravity, predicted CHF values for upflow with an upward-facing heated wall ($\theta = 0 - 90°$) are greater than those for downflow with a downward-facing wall ($\theta = 180 - 270°$). For double-sided heating, lower CHF is predicted for downward-facing than upward-facing walls.

(4) CHF values for microgravity fall about midway between the maxima and minima for Earth gravity. This is an important finding since it implies that, for a given inlet velocity,

performing terrestrial experiments over the entire range of orientations will provide a range that encompasses CHF for microgravity.

(5) Overall, the *Interfacial Lift-off Model* shows that the values of CHF and key interfacial parameters for all orientations in Earth gravity and for microgravity converge together above ~ 1.5 m/s, where inertia begins to effectively negate gravity effects.

CHAPTER 6. CRITICAL HEAT FLUX MODEL FOR SATURATED TWO-PHASE

INLET FLOW

6.1 <u>Separated Flow Model</u>

A separated flow model is constructed to predict key flow variables necessary for development of a mechanistic CHF model. For the saturated inlet conditions ($x_{e,in} > 0$) of the present study, the FC-72 is supplied to the heated portion of the channel as a vapor-liquid mixture. Excepting horizontal flows at low mass velocities, where the inlet mixture is stratified, the fluid for most operating conditions and orientations enters the channel fully separated with a liquid layer covering the entire perimeter, surrounding a central vapor core. Recently, Konishi *et al.* [54] and Kharangate *et al.* [35] provided the framework for a separated flow model with those same inlet conditions, but for only single-sided heating. In the present model, which is intended for single-sided and double-sided heating, a similar framework is adopted, using slip flow assumptions, *i.e.,* with flat velocity profiles for the individual liquid and vapor layers, but different velocities between the phases, and uniform pressure across the flow area. As shown in Figs. 6.1(a) and 6.1(b) for single-sided and double-sided heating, respectively, identical inlet flow patterns are assumed, with a liquid layer with uniform thickness ε_{in} surrounding a central vapor core with inlet void fraction α_{in}. This void fraction is determined by applying momentum conservation to differential
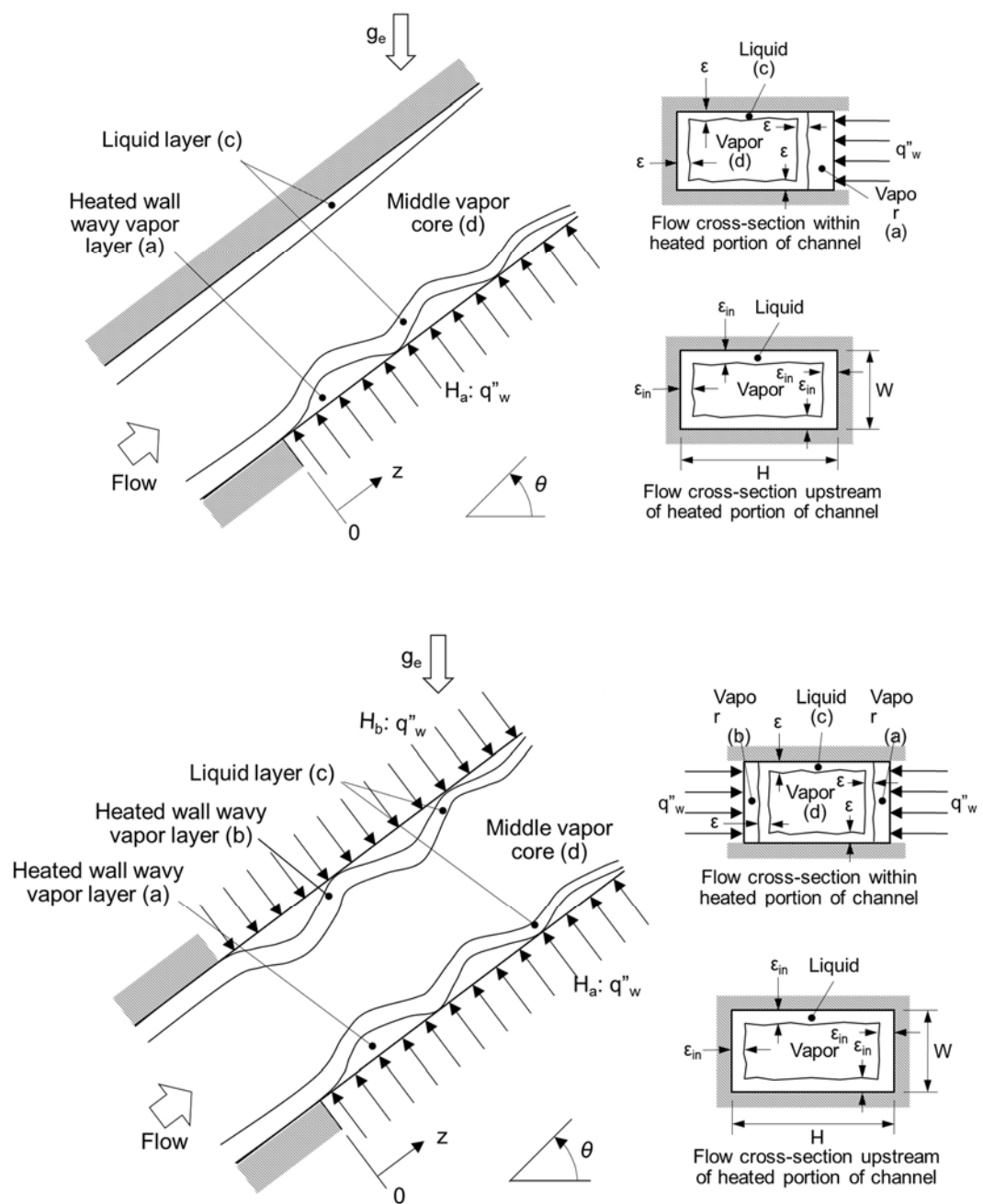
Fig. 6.1: Schematics of different layers in (a) single-sided heating and (b) double-sided heating configurations.

control volumes of vapor and liquid of axial length Δz in the adiabatic region upstream of the heated portion of the channel, which yields the following relations,

$$G^2 \frac{d}{dz}\left[\frac{x_{e,in}^2}{\rho_g \alpha_{in}}\right] = -\alpha_{in}\frac{dp}{dz} - \frac{\tau_i P_i}{A} - \rho_g \alpha_{in} g_e \sin\theta \qquad (6.1)$$

and $\quad G^2 \frac{d}{dz}\left[\frac{(1-x_{e,in})^2}{\rho_f(1-\alpha_{in})}\right] = -(1-\alpha_{in})\frac{dp}{dz} - \frac{\tau_{w,f} P_{w,f}}{A} \pm \frac{\tau_i P_i}{A} - \rho_f(1-\alpha_{in})g_e \sin\theta, (6.2)$

where p, $\tau_{w,f}$, τ_i, A, $P_{w,f}$ and P_i are the pressure, wall shear stress, interfacial shear stress between the liquid and vapor layers, cross-sectional area of the channel, wall perimeter, and interfacial perimeter. The $\pm$ sign in Eq. (6.2) takes into account variations in shear stress direction depending on the relative velocities of the liquid and vapor layers. The inlet liquid layer thickness, ε_{in}, is related to α_{in} by the relation

$$\alpha_{in} = \frac{(H - 2\varepsilon_{in})(W - 2\varepsilon_{in})}{H\,W}. \qquad (6.3)$$

For the heated portion of the channel, a new vapor layer is initiated along the heated wall as shown in Fig. 6.1(a) for single-sided heating and Fig. 6.1(b) for double-sided heating. The present separated flow model assumes the liquid layer continues to maintain uniform thickness, ε, on all four sides of the channel's perimeter. For single-sided heating, Fig. 6.1(a) shows the flow consisting of three layers: vapor layer (*a*) generated along the heated wall, liquid layer (*c*), and vapor core (*d*). For double-sided heating, Fig. 6.1(b) shows the flow consisting of four layers: vapor layer (*a*) along heated wall H_a, vapor layer (*b*) along heated wall H_b, liquid layer (*c*), and central vapor core (*d*). The model assumes the heat supplied at the wall is consumed entirely by vapor formation in layer (*a*) for single-

sided heating, or layers (*a*) and (*b*) for double-sided heating. In other words, phase change between the liquid layer and vapor core is neglected, which is justified by the fact that these two layers enter the flow at the same saturation temperature. Therefore, the mass of the central vapor core is conserved, *i.e.,* $x_d = x_{e,in}$. The present separated flow model deviates from the model in [35] in the treatment of the liquid layer, where only the portion of the liquid layer adjacent to the heated wall(s) was allowed to change phase. With this assumption, the previous model constrained the ability of liquid along the insulated walls from feeding the near-wall liquid and compensating for the evaporated liquid. Besides, the assumption in the previous model was observed to lead to divergence in the numerical solution. The present model is therefore modified to employ the aforementioned assumption of a circumferentially uniform liquid layer thickness.

Tables 6.1 and 6.2 provide summaries of momentum and energy conservation equations for the heated portion of the channel for single-sided and double-sided heating, respectively. Table 6.3 provides additional relations that are used in conjunction with the conservation equations in Table 6.1 and Table 6.2 to calculate key flow parameters.

Figures 6.2(a) – 6.2(d) show predictions of the separated flow model for horizontal double-sided heating in Earth gravity for phase layer thicknesses, phase layer velocities, pressure, and quality, respectively, along the heated portion of the channel with $G = 800$ kg/m²s, $p_{in} = 150$ kPa, $x_{e,in} = 0.05$, and $q''_w = 20$ W/cm². Figure 6.2(a) shows the vapor layers generated along the heated walls grow axially in thickness along the channel. The liquid layers are shown thinning gradually due to both loss of mass by evaporation and axially increasing shear forces.   The central vapor core also grows smaller because of the

Table 6.1: Summary of separated flow model relations for single-sided heating.

Momentum conservation:

$$G^2 \frac{d}{dz}\left[\frac{x_a^2}{\rho_g \alpha_a}\right] = -\alpha_a \frac{dp}{dz} - \frac{\tau_{w,ga} P_{w,ga}}{A} \quad \frac{\tau_{iac} P_{iac}}{A} - \rho_g \alpha_a g_e \sin\theta$$

$$G^2 \frac{d}{dz}\left[\frac{x_d^2}{\rho_g \alpha_d}\right] = -\alpha_d \frac{dp}{dz} \quad \frac{\tau_{idc} P_{idc}}{A} - \rho_g \alpha_d g_e \sin\theta$$

$$G^2 \frac{d}{dz}\left[\frac{(1-x_a-x_d)^2}{\rho_f (1-\alpha_a-\alpha_d)}\right] = -(1-\alpha_a-\alpha_d)\frac{dp}{dz} - \frac{\tau_{w,fc} P_{w,fc}}{A} \pm \frac{\tau_{iac} P_{iac}}{A} \pm \frac{\tau_{idc} P_{idc}}{A} - \rho_f (1-\alpha_a-\alpha_d) g_e \sin\theta$$

Energy conservation:

$$\frac{dx_a}{dz} = \frac{q''_{wa} W}{\dot{m} h_{fg}}$$

$$\frac{dx_d}{dz} = 0$$

Table 6.2: Summary of separated flow model relations for double-sided heating.

Momentum conservation:

$$G^2 \frac{d}{dz}\left[\frac{x_a^2}{\rho_g \alpha_a}\right] = -\alpha_a \frac{dp}{dz} - \frac{\tau_{w,ga} P_{w,ga}}{A} \quad \frac{\tau_{iac} P_{iac}}{A} - \rho_g \alpha_a g_e \sin\theta$$

$$G^2 \frac{d}{dz}\left[\frac{x_b^2}{\rho_g \alpha_b}\right] = -\alpha_b \frac{dp}{dz} - \frac{\tau_{w,gb} P_{w,gb}}{A} \quad \frac{\tau_{ibc} P_{ibc}}{A} - \rho_g \alpha_b g_e \sin\theta$$

$$G^2 \frac{d}{dz}\left[\frac{x_d^2}{\rho_g \alpha_d}\right] = -\alpha_d \frac{dp}{dz} \quad \frac{\tau_{idc} P_{idc}}{A} - \rho_g \alpha_d g_e \sin\theta$$

$$G^2 \frac{d}{dz}\left[\frac{\left(1 - x_a - x_b - x_d\right)^2}{\rho_f \left(1 - \alpha_a - \alpha_b - \alpha_d\right)}\right] = -\left(1 - \alpha_a - \alpha_b - \alpha_d\right)\frac{dp}{dz} - \frac{\tau_{w,fc} P_{w,fc}}{A} \pm \frac{\tau_{iac} P_{iac}}{A} \pm \frac{\tau_{ibc} P_{ibc}}{A} \pm \frac{\tau_{idc} P_{idc}}{A} - \rho_f \left(1 - \alpha_a - \alpha_b - \alpha_d\right)g_e \sin\theta$$

Energy conservation:

$$\frac{dx_a}{dz} = \frac{q''_{wa} W}{\dot{m} h_{fg}}$$

$$\frac{dx_b}{dz} = \frac{q''_{wb} W}{\dot{m} h_{fg}}$$

$$\frac{dx_d}{dz} = 0$$

Table 6.3: Summary of relations used in conjunction with the separated flow model and Interfacial Lift-off Model.

Single-sided heating quality relations for vapor layers:

$$x_a = \frac{\rho_g U_{ga} \alpha_a}{G} \text{ and } x_d = x_{e,in}$$

Double-sided heating quality relations for vapor layers:

$$x_a = \frac{\rho_g U_{ga} \alpha_a}{G}, \; x_b = \frac{\rho_g U_{gb} \alpha_b}{G} \text{ and } x_d = x_{e,in}$$

Wall shear stress relations:

$$\tau_{w,k} = \frac{1}{2} \rho_k U_k^2 f_k$$

$$f_k = C_1 + \frac{C_2}{\text{Re}_{D_k}^{1/C_3}} = C_1 + \frac{C_2}{\left(\frac{\rho_k U_k D_k}{\mu_k} \right)^{1/C_3}}$$

where $k = fc, ga, gb$ or gd. $C_1 = 0$, $C_2 = 16$ and $C_3 = 1$ for laminar flow ($\text{Re}_{D_k} \leq 2100$), $C_1 = 0.0054$, $C_2 = 2.3 \times 10^{-8}$ and $C_3 = -2/3$ for transitional flow ($2100 < \text{Re}_{D_k} \leq 4000$), and $C_1 = 0.00128$, $C_2 = 0.1143$ and $C_3 = 3.2154$ for turbulent flow ($\text{Re}_{D_k} > 4000$) [76], where $D_k = 4 A_k / P_k$

Interfacial shear stress relations:

$$\tau_{iac} = \frac{C_{f,iac}}{2} \rho_g \left(U_{ga} - U_{fc} \right)^2, \; \tau_{ibc} = \frac{C_{f,ibc}}{2} \rho_g \left(U_{gb} - U_{fc} \right)^2 \text{ and } \tau_{idc} = \frac{C_{f,idc}}{2} \rho_g \left(U_{gd} - U_{fc} \right)^2$$

$$\text{where } C_{f,iac} = C_{f,ibc} = C_{f,idc} = 0.5 \; [50]$$
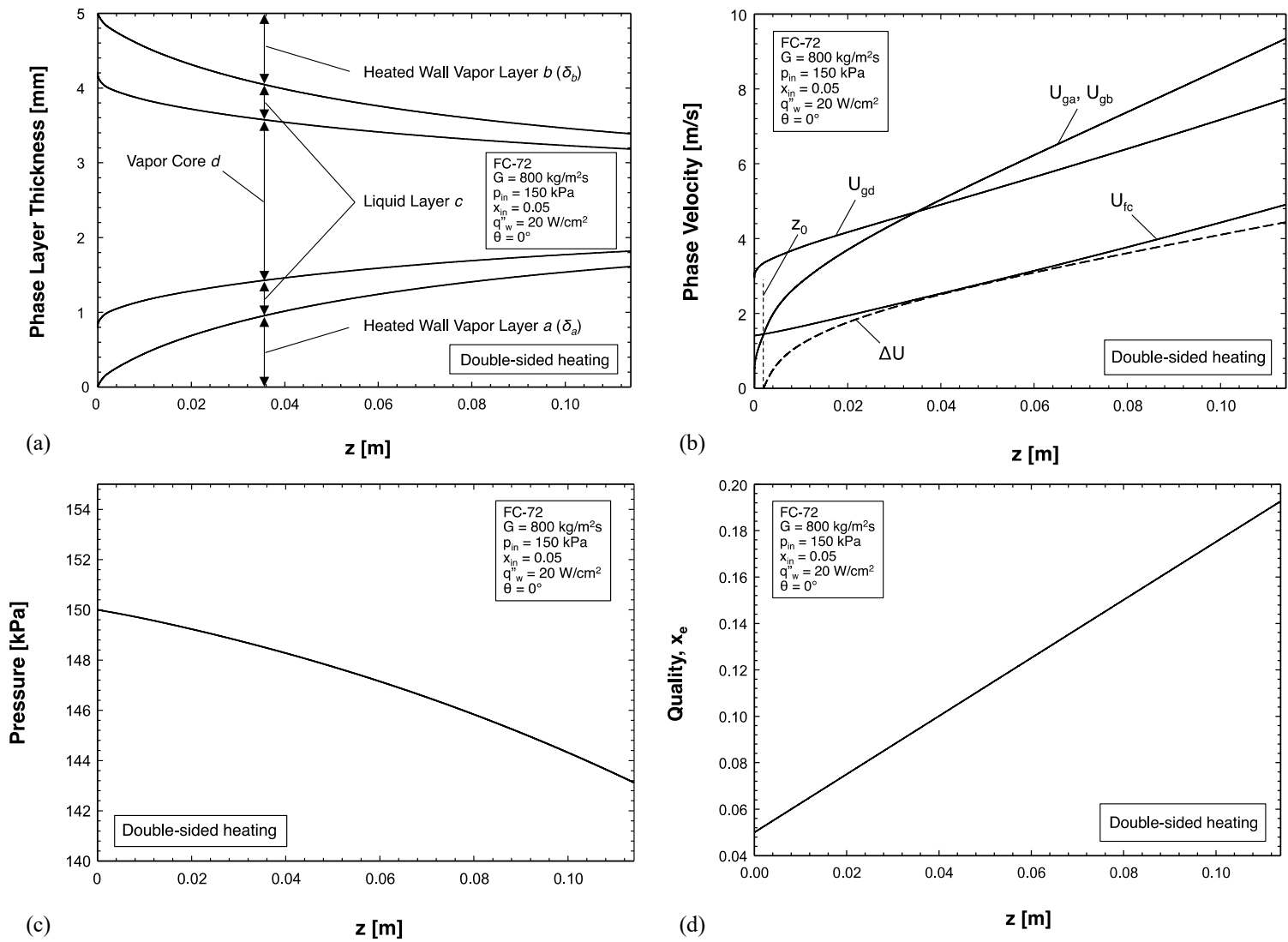
Fig. 6.2: Separated flow model predictions of (a) phase layer thicknesses, (b) phase velocities, (c) pressure, and (d) quality.

increasing shear despite its mass flow rate being conserved. In the separated flow model, the liquid layer is continuous around the central vapor core, but is shown in Fig. 6.2(a) divided into two layers. Figure 6.2(b) shows the variations of velocities of the individual layers along with velocity difference between the newly generated vapor layers and the liquid layer. The vapor core is faster than the other layers at $z = 0$. However, the newly generated vapor layer, with velocities U_{ga} and U_{gb}, overtake the vapor core along the heated portion of the channel. The liquid layer is quickly overtaken by the two newly generated vapor layers a short distance from the leading edges of the heated walls; this trend is also reflected in the axial variation of velocity difference, ΔU, between the two vapor layers and the liquid layer. Figures 6.2(c) shows the expected monotonic decrease in pressure along the heated portion of the channel. Figure 6.2(d) shows thermodynamic equilibrium quality increasing axially with a constant slope because of the uniform heat supply to the two-phase mixture by the two heated walls.

6.2 Interfacial Lift-off Model

The Interfacial Lift-off Model originally proposed by Galloway and Mudawar [49,50] has been confirmed in studies spanning two decades and including CHF for short and long heated walls, flat and curved walls, horizontal, vertical, and inclined channels, and flow boiling in both Earth gravity and microgravity [49,50,53,54,56,77-83]. This model is also adopted here to predict the present CHF data.

This model is based on a detailed depiction of interfacial behavior just prior to CHF as well as the trigger event for CHF. As heat fluxes approaches CHF, a wavy vapor layer is postulated to form along the heated wall, which buffers most liquid from contacting the

wall except in wetting fronts corresponding to troughs in the vapor wavy layer. Sustained boiling in the wetting fronts provides the last opportunity for cooling of the wall. The trigger event for CHF is postulated to occur as follows. The liquid contact in the wave troughs – wetting fronts - is maintained by curvature of liquid streamlines inducing a net pressure force on liquid towards the wall. This pressure force is resisted by momentum of vapor emanating within the wetting fronts normal to the wall. CHF is therefore triggered when the last increment in wall heat flux intensifies vapor momentum to a level that just exceeds the pressure force. This causes the wave trough to lift from the wall, and the wetting front to be extinguished as a source of cooling for the wall. As a wetting front is extinguished, the heat supplied from the wall attempts to conduct heat away from this wetting front to neighboring wetting fronts. The neighboring wetting fronts now face even greater heat flux, rendering them more likely to be extinguished by lifting from the wall. Wetting fronts are therefore extinguished in succession in an unstable manner, causing the classical unsteady rise in wall temperature associated with CHF.

Flow boiling with saturated inlet conditions poses great difficulty capturing near-wall interfacial behavior by high speed video because a liquid film is formed along the channel's perimeter surrounding a central vapor core. However, the wavy vapor layer has been clearly captured in the near-wall region in the present flow visualization experiments. The main difference between the present flows with saturated inlet conditions versus subcooled inlet conditions is the existence of the vapor core for the former. The wavy vapor layer behavior for saturated inlet conditions is depicted for single-sided and double-sided heating in Figs. 6.3(a) and 6.3(b), respectively, and the interfacial lift-off condition in Fig. 6.3(c).
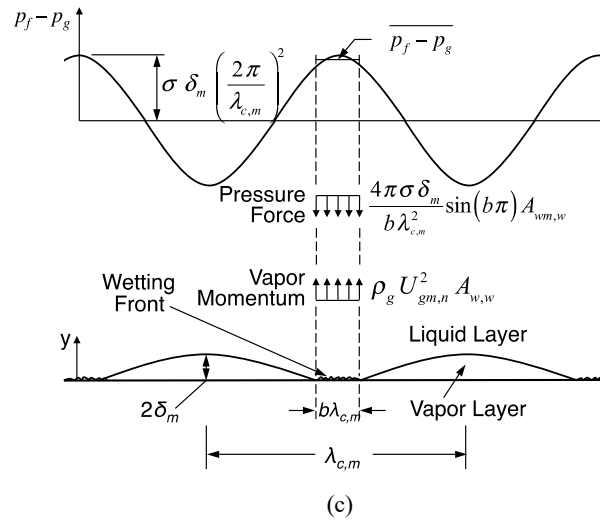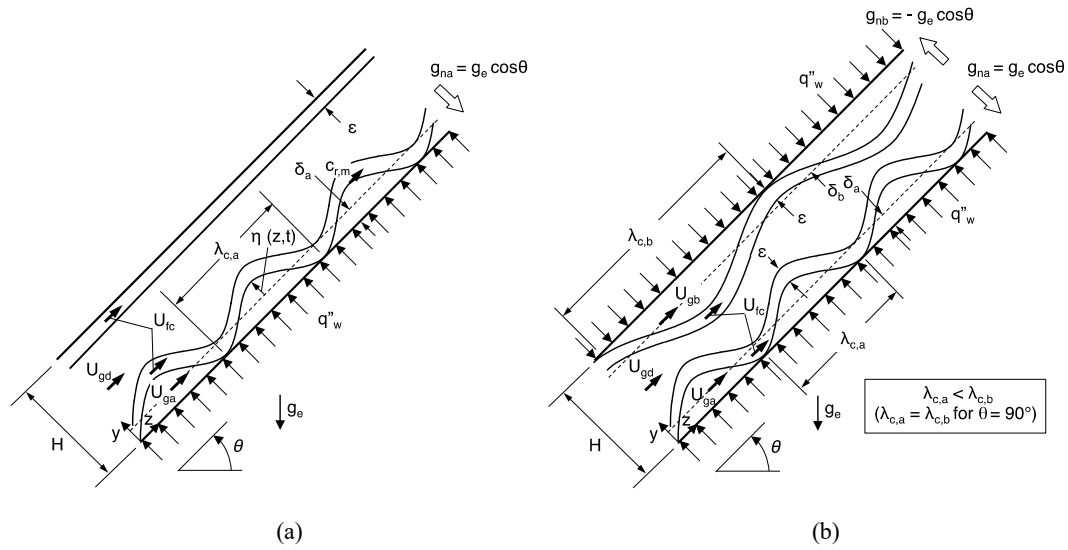
Fig. 6.3: Hydrodynamic instability of wavy vapor layers along heated walls for inclined channel just before CHF for (a) single-sided heating and (b) double-sided heating configurations. (c) Schematic representation of interfacial lift-off from heated wall in wetting front at CHF.

As with the original Interfacial Lift-off Model [49,50], the wavy interfacial behavior is described using classical instability theory [84,85]. A sinusoidal liquid-vapor interface is assumed between the liquid layer and wall vapor layer(s), resulting from velocity differences between the two layers, gravity component acting normal to the interface, and surface tension along the interface. The wavy interface is described by the perturbation function $\eta(z,t) = \eta_0 e^{i k_m (z - c_m t)}$, where η_0 is the wave amplitude, k_m the wave number, and c_m the wave speed. The wave speed is expressed $c_m = c_{r,m} + i\, c_{i,m}$, where $c_{r,m,}$ and $c_{i,m}$ are real and imaginary components, respectively. As shown in Fig. 6.3(a) and 6.3(b), the real component defines the actual propagation speed of the interface, while the imaginary component is associated with amplification or decay of the interfacial perturbation.

The interfacial instability model yields the following relation for the imaginary component,

$$c_{i,m} = \sqrt{\frac{\rho_f'' \rho_{gm}'' \left(U_{gm} - U_f\right)^2}{\left(\rho_f'' + \rho_{gm}''\right)^2} + \frac{\left(\rho_f - \rho_{gm}\right)}{\left(\rho_f'' + \rho_{gm}''\right)} \frac{g_{nm}}{k_m} - \frac{\sigma k_m}{\left(\rho_f'' + \rho_{gm}''\right)}} \,, \qquad (6.4)$$

where ρ_f'' and ρ_{gm}'' are modified density terms. The interface is deemed stable when $c_{i,m}$ < 0, implying the interfacial perturbation will decay with time, which would prevent the formation of wetting fronts. On the other hand, the interface is rendered unstable when $c_{i,m}$ > 0, meaning the perturbation would amplify, allowing wetting fronts to form along the wall. The onset of interfacial stability corresponding to $c_{i,m} = 0$ constitutes the minimum requirement for the perturbation to begin forming wetting fronts, and is therefore used in the Interfacial Lift-off Model to determine interfacial wavelength. Setting $c_{i,m}$ given by

Eq. (6.4) equal to zero yields the following relation for critical wave number, $k_{c,m}$, and critical wavelength, $\lambda_{c,m}$,

$$k_{c,m} = \frac{2\pi}{\lambda_{c,m}} = \frac{\rho_f'' \rho_{gm}'' \left(U_{gm} - U_f\right)^2}{2\sigma\left(\rho_f'' + \rho_{gm}''\right)} + \sqrt{\left[\frac{\rho_f'' \rho_{gm}'' \left(U_{gm} - U_f\right)^2}{2\sigma\left(\rho_f'' + \rho_{gm}''\right)}\right]^2 + \frac{\left(\rho_f - \rho_{gm}\right)g_{nm}}{\sigma}} \,, \quad (6.5)$$

where $\rho_f'' = \rho_f \coth\left(2\pi\varepsilon/\lambda_{c,m}\right)$ and $\rho_{gm}'' = \rho_g \coth\left(2\pi\delta_m/\lambda_{c,m}\right)$. For double-sided heating, however, critical wavelengths are different for the two opposite heated walls because of opposite directions of gravity components perpendicular to these walls. In Earth gravity, the gravity components normal to the upward-facing heated wall and downward-facing heated wall are expressed, respectively, as

$$g_{na} = g_e \cos\theta \qquad (6.6a)$$

and
$$g_{nb} = g_e \cos\left(\theta + \pi\right) = -g_e \cos\theta. \qquad (6.6b)$$

According to the Interfacial Lift-off Model, based on extensive evidence from flow visualization experiments, a continuous wetting front region of axial length z_m^* is formed along the leading edge of the heated wall, which is given by

$$z_m^* = z_{0,m} + \lambda_{c,m}\left(z_m^*\right), \qquad (6.7)$$

where z_0 is the distance from the leading edge to the axial location where heated wall vapor layer velocity just exceeds liquid layer velocity. Zhang *et al.* [53] statistically analyzed video segments captured just prior to CHF, and showed that waves generated at z_m^* have a tendency to preserve curvature as they propagate downstream. Therefore, in this study, the

curvatures of waves at CHF anywhere along the heated wall are assumed identical to that at z_m^*.

Illustrated in Fig. 6.3(c) is the trigger event for CHF according to the Interfacial Lift-off Model, where the normal momentum of vapor generated in the wetting front just exceeds the pressure force induced by streamline curvature that pushes the interface toward the heated wall. Zhang *et al.* [28] showed that the average pressure difference at the wetting front is given by

$$\overline{p_f - p_g} = \frac{4\pi\sigma\delta_m}{b\lambda_{c,m}^2}\sin(b\pi).$$

(6.8)

With the fluid entering the channel as a two-phase mixture, the heat flux, $q_{w,w}''$, required to convert saturated liquid to saturated vapor for incoming liquid in the wetting front can be expressed as

$$q_{wm,w}'' A_{wm,w} = \rho_g U_{gm,n} A_{wm,w}\left[h_{fg}\left(1 - x_{e,in}\right)\right],$$

(6.9)

where $A_{wm,w}$ is the wetting front's area and $U_{gm,n}$ the velocity of vapor normal to the heated wall. Equating the normal vapor momentum, $\rho_g U_{gm,n}^2$, to the average pressure difference acting on the interface in the wetting front, Eq. (6.8), and substituting into Eq. (6.9), yield the following relation for lift-off heat flux in the wetting front,

$$q_{wm,w}'' = \rho_g\left[h_{fg}\left(1 - x_{e,n}\right)\right]\sqrt{\frac{\overline{p_f - p_g}}{\rho_g}} = \rho_g\left[h_{fg}\left(1 - x_{e,n}\right)\right]\left[\frac{4\pi\sigma}{\rho_g}\frac{\sin(b\pi)}{b}\right]^{1/2}\frac{\delta_m^{1/2}}{\lambda_{c,m}}.$$

(6.10)

High speed video analysis of near-wall interfacial behavior by Sturgis and Mudawar [32,33] showed that the wetting front maintains an axial length as a fixed fraction $b = 0.20$ of the local wavelength. As liquid is converted to vapor only in the wetting fronts, CHF is calculated by multiplying the wetting front's lift-off heat flux by this fraction,

$$CHF_{pred,m} = b q''_{wm,w}. \tag{6.11}$$

Combining Eqs. (6.10) and (6.11) yields the following analytical expression for CHF,

$$CHF_{pred,m} = \rho_g \left[h_{fg} \left(1 - x_{e,in} \right) \right] \left[\frac{4\pi\sigma b \sin(b\pi)}{\rho_g} \right]^{1/2} \frac{\delta_m^{1/2}}{\lambda_{c,m}} \bigg|_{z^*}. \tag{6.12}$$

For double-sided heating, CHF is calculated for both upward-facing and downward facing walls separately. Then, CHF for a test case is chosen as the minimum of the two predicted CHF values,

$$CHF_{pred} = \min \left(CHF_{pred,a}, CHF_{pred,b} \right). \tag{6.13}$$

6.3 CHF Model Predictions

Before comparing CHF data to predictions of the Interfacial Lift-off Model, it is important to identify the range of operating conditions associated with formation of a wavy vapor layer. For subcooled inlet conditions, in Chapter 3 it was shown that CHF for an upward-facing heated wall yields interfacial behavior resembling that of pool boiling rather than exhibiting a wavy vapor layer for $G < 800$ kg/m^{2}s. They also observed a vapor layer with a stable interface for a downward-facing heated wall for $G < 800$ kg/m^{2}s. Additionally, the flow visualization results discussed earlier in the present study prove that the interfacial behavior for certain orientations is entirely gravity dominated for $G \leq 400$ kg/m^{2}s. Therefore, in the present study, only CHF data corresponding to $G \geq 800$ kg/m^{2}s are compared to predictions of the interfacial Lift-off Model.

Figures 6.4(a)-6.4(c) compare variations of CHF predictions and CHF data for single-sided heating with orientation for different mass velocities, and inlet qualities of $x_{e,in} = 0.0$
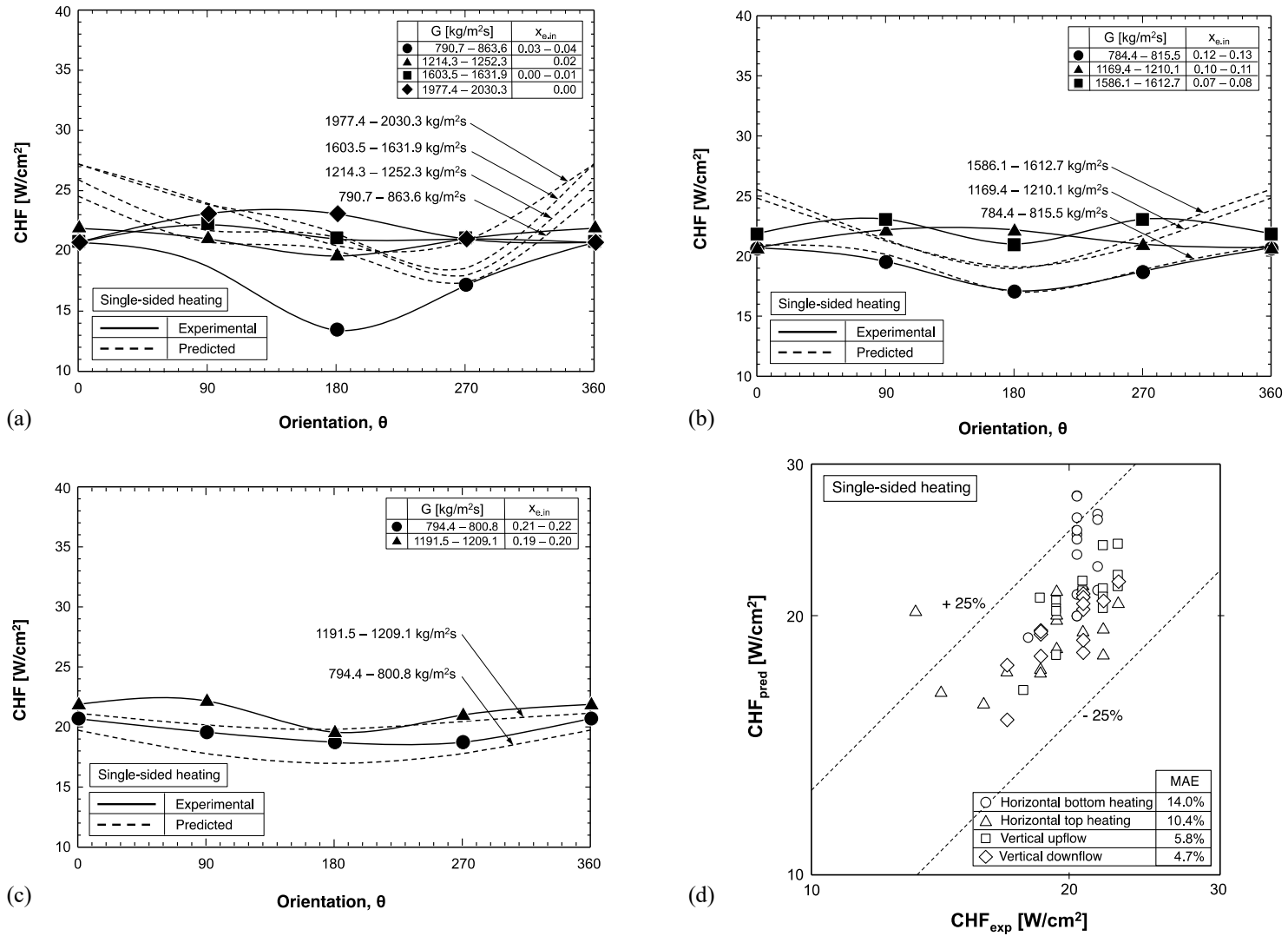
Fig. 6.4: Comparison of measured and predicted CHF with single-sided heating for (a) $x_{e,in}$ = 0.00-0.04, (b) $x_{e,in}$ = 0.07-0.13, and (c) $x_{e,in}$ = 0.19-0.22. (d) Predicted versus measured CHF for all test cases with single-sided heating.

– 0.04, 0.07 – 0.13, and 0.19 – 0.22, respectively. For G = 790.7 – 863.6 kg/m²s and $x_{e,in}$

= 0.03 – 0.04, Fig. 6.4(a) shows both predicted and measured CHF are highest for θ = 0°

and lowest for combinations of downflow and downward-facing heated wall orientations

(θ = 180° to θ = 270°). At higher mass velocities, the CHF data do not exhibit significant

variations with orientation, yet the model predictions still follow the trends for G = 790.7

– 863.6 kg/m²s. Highest discrepancy between predictions and experiments was observed

for lowest mass velocity G = 790.7 – 863.6 kg/m²s at θ = 180°. As stated earlier in this

section, only CHF data corresponding to $G \geq$ 800 kg/m²s are applicable to the interfacial

Lift-off Model. As we are in the transition mass velocity range with the lowest inlet quality,

the experimental observations are not able to be captured here. As inlet quality is increased,

Figs. 6.4(b) and 6.4(c), the model predictions improve in both magnitude and trend,

excepting the orientation θ = 0° in Fig. 6.4(b). Figure 6.4(d) compares the predictions of

the Interfacial Lift-off Model with CHF data for single-sided heating for $G \geq$ 800 kg/m²s.

The predictive accuracy of the model is assessed using mean absolute error (MEA), which

is defined as

$$MAE = \frac{1}{N}\sum \left| \frac{CHF_{pred} - CHF_{exp}}{CHF_{exp}} \right|. \tag{6.14}$$

Overall, vertical upflow (θ = 90°) and vertical downflow (θ = 270°) show the best

agreement, with MAEs of 5.8% and 4.7%, respectively, and horizontal upward-facing

heated wall (θ = 0°) and horizontal downward-facing heated wall (θ = 180°) showing

slightly higher MAEs of 14.0% and 10.4%, respectively.

Figures 6.5(a)-6.5(c) compare variations of CHF predictions and CHF data for double-sided heating with orientation for different mass velocities, and inlet qualities of $x_{e,in}$ = 0.00 – 0.04, 0.06 – 0.12, and 0.18 – 0.22, respectively. For the lowest $x_{e,in}$ range, Fig. 6.5(a) shows peak predicted CHF values for vertical upflow (θ = 90°), followed by vertical downflow (θ = 270°), and minimum values for horizontal flows (θ = 0° and 180°). While the model does capture the data trends in Fig. 6.5(a), it predicts a stronger orientation influence. However, the model shows better agreement with the data for the two higher quality ranges, Figs. 6.5(b) and 6.5(c). Figure 6.5(d) compares predictions of the Interfacial Lift-off Model with CHF data for double-sided heating for $G \geq 800$ kg/m²s. The model shows good overall predictions, with MAEs for horizontal flows (θ = 0° and 180°), vertical upflow (θ = 90°), and vertical downflow (θ = 270°) of 11.8%, 10.6% and 6.4%, respectively.

These results demonstrate that the combination of separated flow model and Interfacial Lift-off Model is as effective at predicting CHF for saturated inlet conditions as it is for subcooled inlet conditions in many prior studies [49,50,53,56,77-83]. In fact, the model shows better predictive accuracy for both single-sided and double-sided heating with higher inlet qualities than with lower qualities or subcooled inlet conditions.

6.4 Conclusions

This study explored flow boiling modelling of critical heat flux (CHF) of FC-72 along a rectangular channel with either one wall or two opposite walls heated for saturated inlet conditions. With an overall MAE $\leq$ 14%, this study shows that the combination of separated flow model and *Interfacial Lift-off Model* is very effective at predicting CHF for
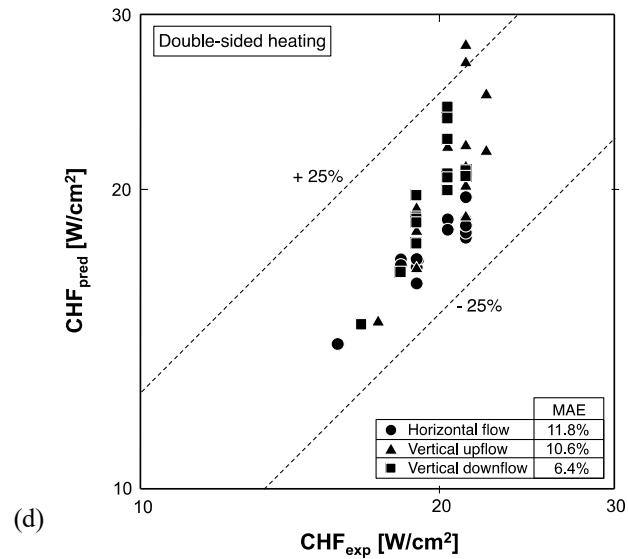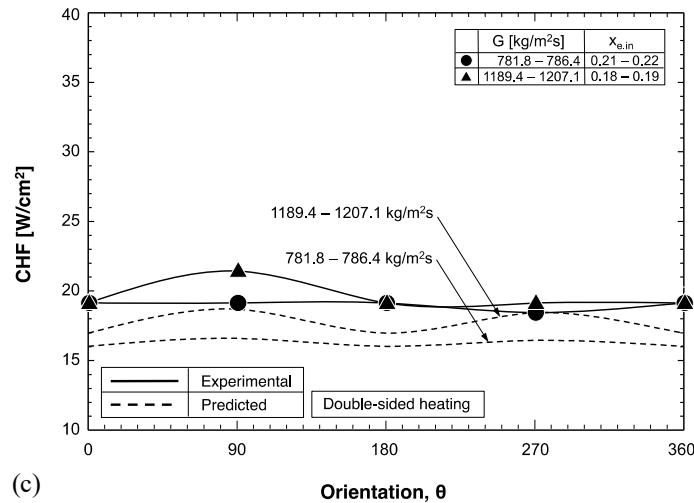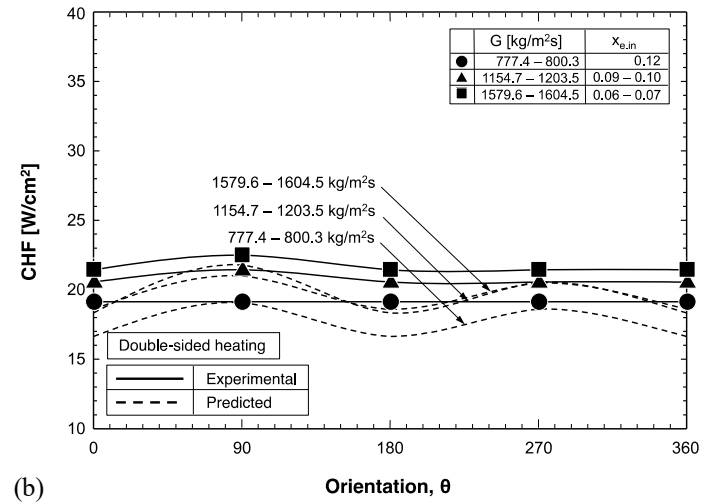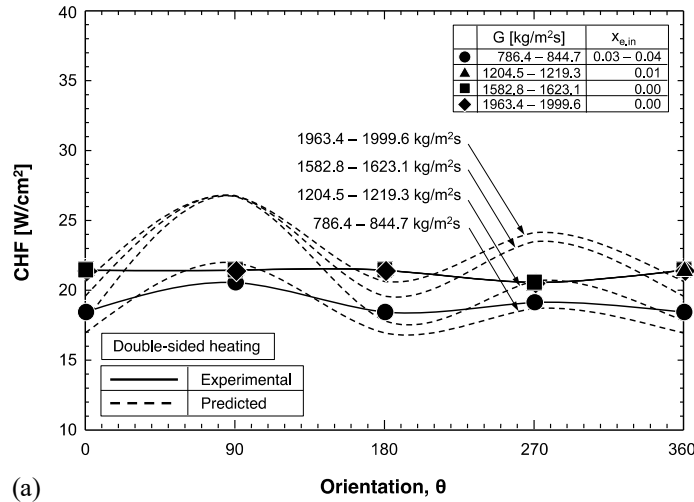
Fig. 6.5: Comparison of measured and predicted CHF with double-sided heating for (a) $x_{e,in}$ = 0.00-0.04, (b) $x_{e,in}$ = 0.06-0.12, and (c) $x_{e,in}$ = 0.18-0.22. (d) Predicted versus measured CHF for all test cases with double-sided heating.

saturated inlet conditions as it did for subcooled inlet conditions in prior studies. Increasing

inlet quality improves CHF predictions for both single-sided and double-sided heating.

CHAPTER 7. COMPUTATIONAL MODELING OF TURBUELNT EVAPORATING

FALLING FILMS

7.1 <u>Computational Methods</u>

7.1.1 <u>Computational Domain</u>

The data used to assess the accuracy of the computational model are obtained using the

Purdue University Boiling and Two-Phase Flow Laboratory (PU-BTPFL) falling film

facility depicted in Fig. 7.1(a). Fig. 7.1(b) shows a schematic diagram of the flow loop that

delivered deionized water at the desired flow rate, pressure and temperature to the test

chamber containing the falling-film test section. Figure 7.2(a) shows the construction of

the test chamber. Fig. 7.2(b) shows the provisions adopted to obtain accurate inner wall

temperature measurements. Detailed information about the experimental facility can be

found in the study by Shmerler and Mudawar [63]. Fig. 7.3 shows the domain used in the

computational model. Because of the symmetrical construction of the test section and

small ratio of film thickness to distance between the test section and test chamber walls,

the flow is assumed axisymmetric and two-dimensional. The computational domain

consists of the inlet reservoir, porous film distributor, and 1835-mm long annulus formed

between the outer wall of the 25.4-mm test section and Lexgard chamber. FLUENT

Analysis System in the Toolbox of ANSYS Workbench 12.1 [86] is used to compute the

(a)
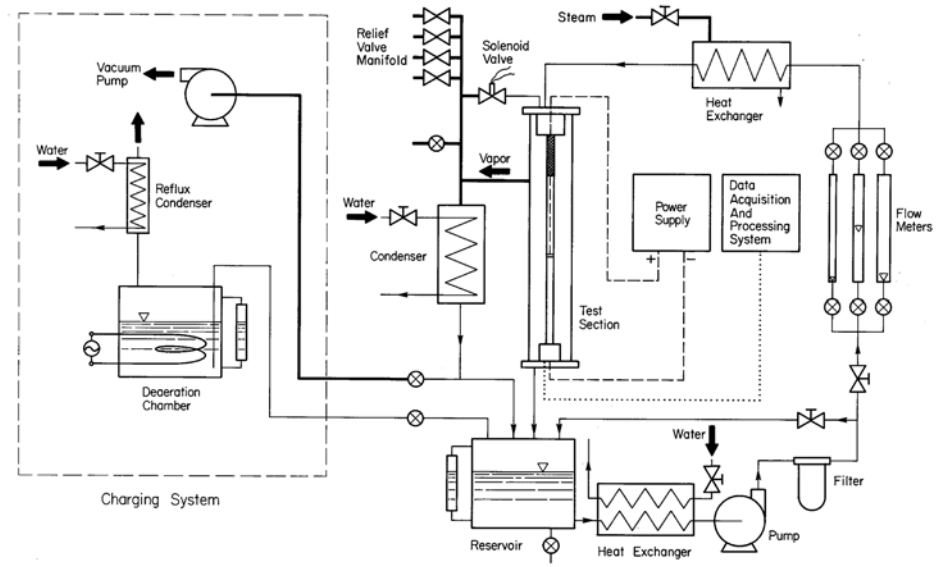
(b)

Fig. 7.1: (a) Photo of falling film facility. (b) Schematic diagram of flow loop.
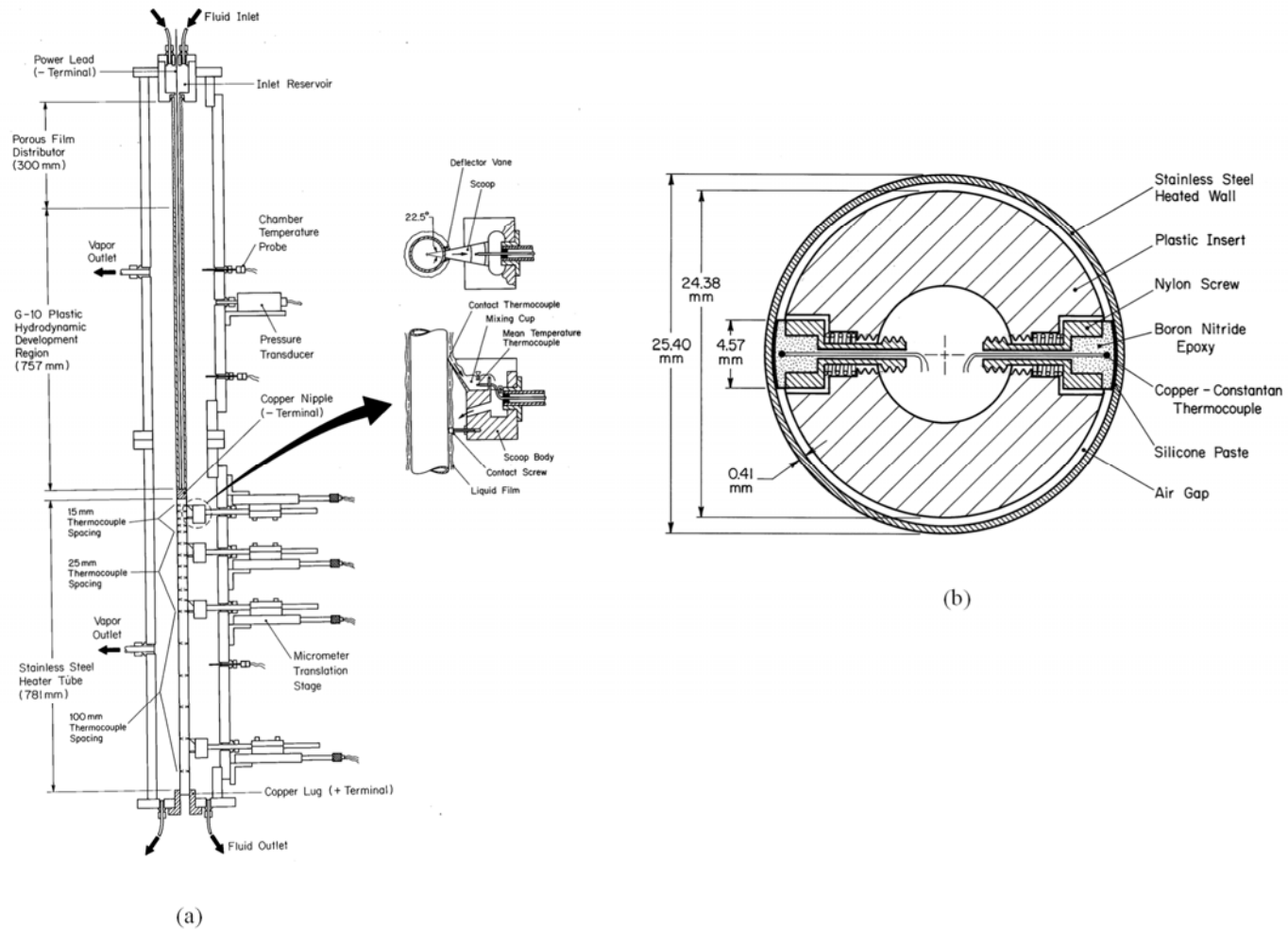
Fig. 7.2: (a) Cut-away view of test chamber. (b) Cross-sectional view of inner wall thermocouples.

Inlet

300
(Porous
Section)

6.1

12.7

28.6

757
(Adiabatic
Section)

r

x

781
(Heated
Section)

q''_w

All dimensions
in mm

Outlet
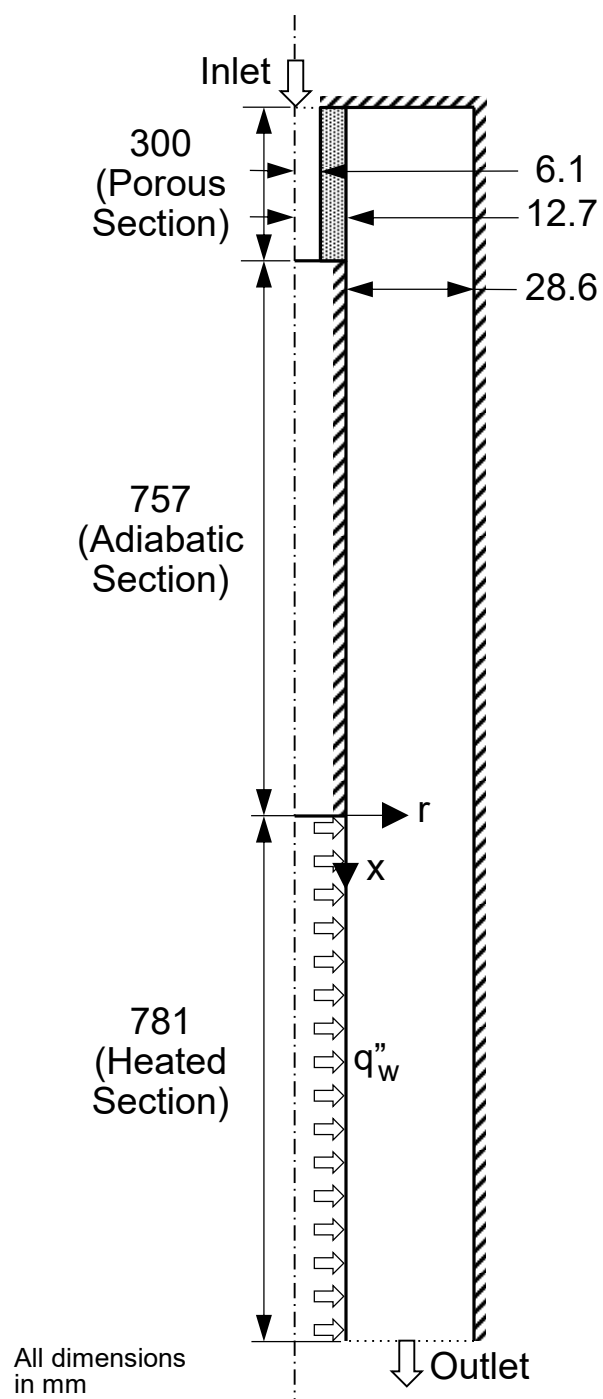
Fig. 7.3: Computational domain.

fluid flow and heat transfer parameters. The complete analysis is performed in the Project

Schematic of Workbench, including geometry creation, meshing, processing and post-

processing.

7.1.2 Governing Equations

The present model employs the standard two-equation $k-\omega$ turbulent model with shear

stress transport (SST) formulation as prescribed in the ANSYS Guide [86]. A key reason

for using the $k-\omega$ model is its ability to tackle turbulence dampening at the interface,

which is key to obtaining accurate temperature profiles adjacent to the interface, a feature

not available with other models, such as the popular $k-\varepsilon$ model. A turbulence dampening

factor of 10 is prescribed. Two-phase treatment follows the Volume of Fluid (VOF) model

[87], and solid–liquid interfaces are governed by continuities of both temperature and heat

flux. The VOF model in FLUENT is used to compute conservation equations for liquid

and vapor while also accounting for mass transfer between the two phases. The continuity

equations are expressed as [86]

liquid phase:
$$\frac{\partial}{\partial t}\left(\alpha_f \, \rho_f\right) + \nabla \cdot \left(\alpha_f \, \rho_f \, \vec{u}_f\right) = S_f \qquad (7.1a)$$

vapor phase:
$$\frac{\partial}{\partial t}\left(\alpha_g \, \rho_g\right) + \nabla \cdot \left(\alpha_g \, \rho_g \, \vec{u}_g\right) = S_g. \qquad (7.1b)$$

The momentum and energy equations, which are applied to the combined phases, are

expressed, respectively, as

momentum:
$$\frac{\partial}{\partial t}(\rho \vec{u}) + \nabla \cdot (\rho \vec{u} \vec{u}) = -\nabla p + \nabla \cdot \left[\mu\left(\nabla \vec{u} + \nabla \vec{u}^T\right)\right] + \rho \vec{g} + \vec{F} \qquad (7.2)$$

energy:
$$\frac{\partial}{\partial t}(\rho E) + \nabla \cdot \left(\vec{u}(\rho E + p)\right) = \nabla \cdot (k \nabla T) + Q \ . \qquad (7.3)$$

where E [J/kg] is the energy per unit mass, which is determined from

$$E = \frac{\alpha_f \rho_f E_f + \alpha_g \rho_g E_g}{\alpha_f \rho_f + \alpha_g \rho_g}, \tag{7.4}$$

where

$$\rho = \alpha_f \rho_f + \alpha_g \rho_g, \tag{7.5a}$$

$$\mu = \alpha_f \mu_f + \alpha_g \mu_g, \tag{7.5b}$$

and

$$k = \alpha_f k_f + \alpha_g k_g. \tag{7.5c}$$

In the present computations, mass transfer due to evaporation is accounted for by using the appropriate mass source terms, S_f and S_g, and the corresponding energy transfer term is accounted for as

$$Q = h_{fg} S_f. \tag{7.6}$$

7.1.3 Phase Change Model

The phase change model by Lee [73] commonly used with boiling and condensation situations attempts to maintain saturation conditions at the interface while allowing for mass and energy transfer in one of the phases. Physically, use of α_k multipliers in Eqs. (1.6a) and (1.6b) implies that mass transfer can occur only where phase k exists as long as the temperature condition is satisfied. Figure 7.4(a) shows the region where the source term is valid when using the Lee model for evaporation. Notice that phase change is allowed in the liquid phase and at the interface when $T > T_{sat}$. However, this is not physically what is expected in an evaporating falling film. By maintaining the wall heat flux at least 25% below the onset of boiling, phase change will take place at the film's interface but nowhere else within the liquid domain.

(a)

(b)
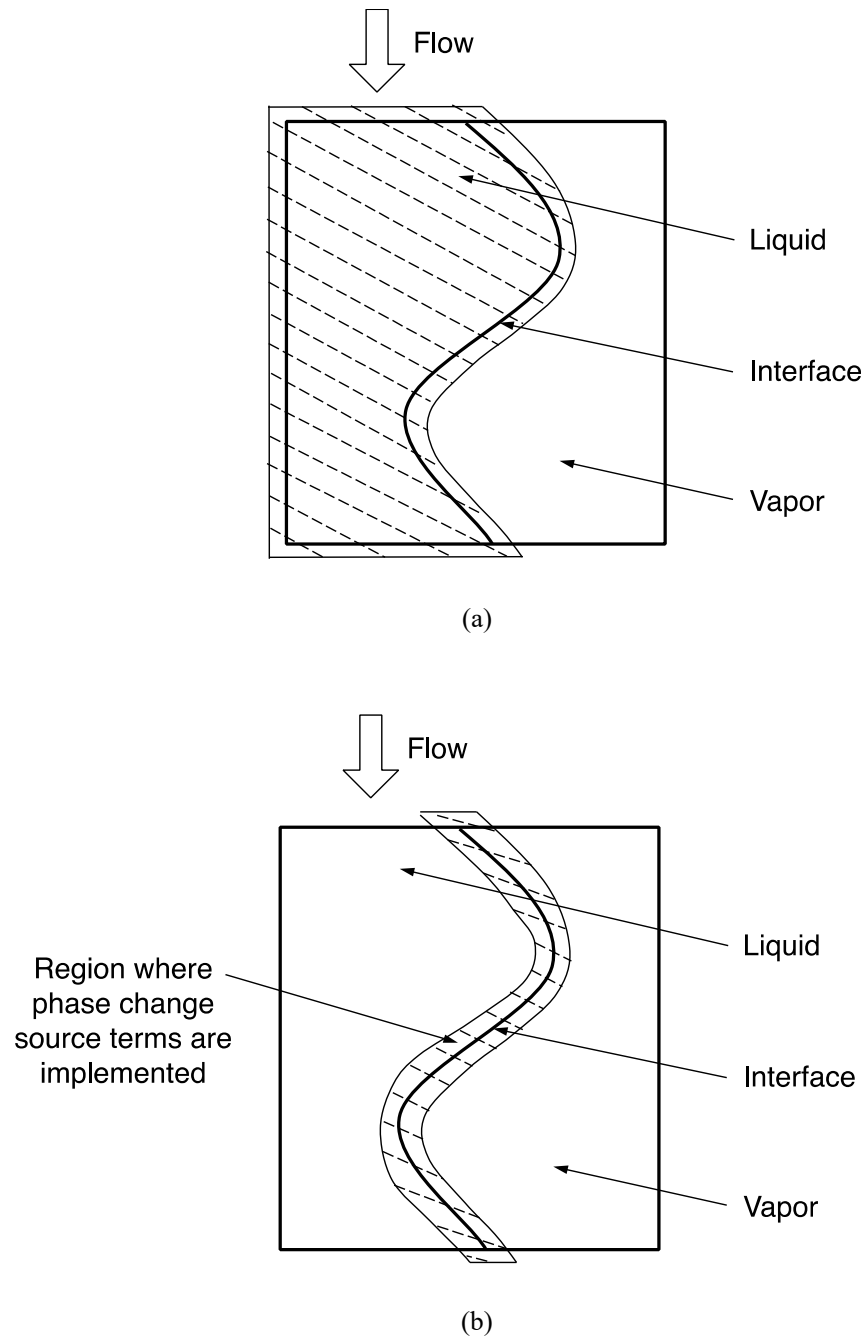
Fig. 7.4: Differences in enforcement of phase change source terms during evaporation using (a) Lee model [73], and (b) sharp interface and Tanasawa models [72].

Tanasawa model [72] (which is a simplified form of the Schrage [69] model) are better suited to the present situation because they allow mass transfer to occur only at the interface. Figures 7.4(b) shows where the source terms are valid when using the sharp interface model and Tanasawa model for evaporation. This domain is the result of the $\nabla \alpha_g$ multiplier yielding non-zero source terms in Eqs. (1.2) and (1.5) only at the interface. The sharp interface model converts any energy crossing the interface to phase change; this energy is not defined by the problem but realized in the solution. This solution can be different for different situations depending on how much energy crosses the interface versus being carried away by the liquid. What is being sought in the present evaporating film situation is the ability to predict and specify this energy so that T_{sat} is maintained at the interface. The sharp interface model can be utilized here if the temperatures of the interface and surrounding vapor are manually maintained at T_{sat}, or if energy transfer is confined to the interface with the vapor temperature maintained at T_{sat}. On the other hand, Tanasawa's model does not require placing any of these restrictions for the present situation, and is therefore the most convenient option, provided an appropriate value of γ is used. The Tanasawa's model is therefore adopted in all the present computations. Marek and Straub [71] determined the value of γ based on published data. They recommended $\gamma = 0.1 - 1$ for dynamically renewing water surfaces such as jets or moving films, and $\gamma < 0.1$ for stagnant surfaces. Hardt and Wondra [88] set $\gamma = 1$ for film boiling, and Magnini *et al.* [89] also set $\gamma = 1$ for laminar flow boiling based on a recommendation by Rose [90]. On the other hand, Kartuzova and Kassemi [91] used a relatively low value of $\gamma = 0.01$ in their simulation of ventless pressurization of a cryogenic storage tank.

It is observed that a low value of γ yields interfacial temperatures higher than T_{sat}. After testing different values of γ in the present study, it is determined that $\gamma = 0.1$ helps maintain interfacial temperature at T_{sat} with reasonable accurately. It is also worth noting that some of cases examined here are successfully modeled with γ values as high as 1, but these results are realized at the expense of reduced stability of the numerical solution. On the other hand, $\gamma < 0.1$ resulted in deviation of interfacial temperature from T_{sat} for several cases. Therefore, a constant value of $\gamma = 0.1$ is deemed most appropriate based on its ability to maintain interfacial temperature at $T_{sat} \pm 0.1°C$ for all test cases. Another reason for using this small value of γ is that it requires minimal energy to maintain T_{sat}. Using $\gamma = 0.1$, the mass flux obtained from Eq. (1.4) is used to calculate the mass source terms, S_g and S_f, according to Eq. (1.5), and the corresponding energy source term due to evaporation, Q [W/m^3], according to Eq. (7.6).

7.1.4 Grid Size

The grid system used in the present study consists of 1,397,474 nodes and 1,467,562 cells. Two finer grid systems, with 2,273,821 and 3,057,589 cells, were attempted and found to provide minimal influence on the computed results. The grid used is non-uniform, having greater density in the porous zone and near the wall and film interface, especially for the heated portion of the test section, in pursuit of superior accuracy in resolving key flow parameters. Turbulence is captured accurately near the wall by using a minimum of five cells within $y^+ < 5$.

7.2 Computational Results

7.2.1 Interfacial Waves

Interfacial waviness is an inherent feature of falling liquid films that influences mass, momentum and heat transfer characteristics. The waves can be assessed by examining both the temporal and spatial variations of the film thickness. The present computations are performed for film Reynolds numbers of Re = 4990 – 37,620 and Prandl numbers of $Pr_f =$ 1.75 – 5.42. Most cases are successfully modeled except those associated with low Re and low Pr_f numbers. At lower Pr_f numbers, it is found that it is very difficult to create the film for smaller Re cases. Hence, only 10 of the 13 cases tested yielded convergent solutions. Figure 7.5 shows instantaneous film profiles for three different Re values and $Pr_f = 5.42$. Notice that the average film thickness decreases with decreasing Re. The highest Re case also features a well-defined film substrate with the interface potentially masking high frequency perturbations. On the other hand, the lowest Re case shows more pronounced long waves with large fluctuations in substrate thickness. It should be noted that film formation at lower Re, especially for the lowest Pr_f of 1.75, is both more difficult to compute and prone to appreciable film breakup.

7.2.2 Heat Transfer Coefficient

The evaporation heat transfer coefficient is computed using local time averaged values of

$$h_E(x) = \frac{1}{\Delta t(x)} \int_0^{\Delta t(x)} h_E(x,t) \, dt. \qquad (7.7)$$
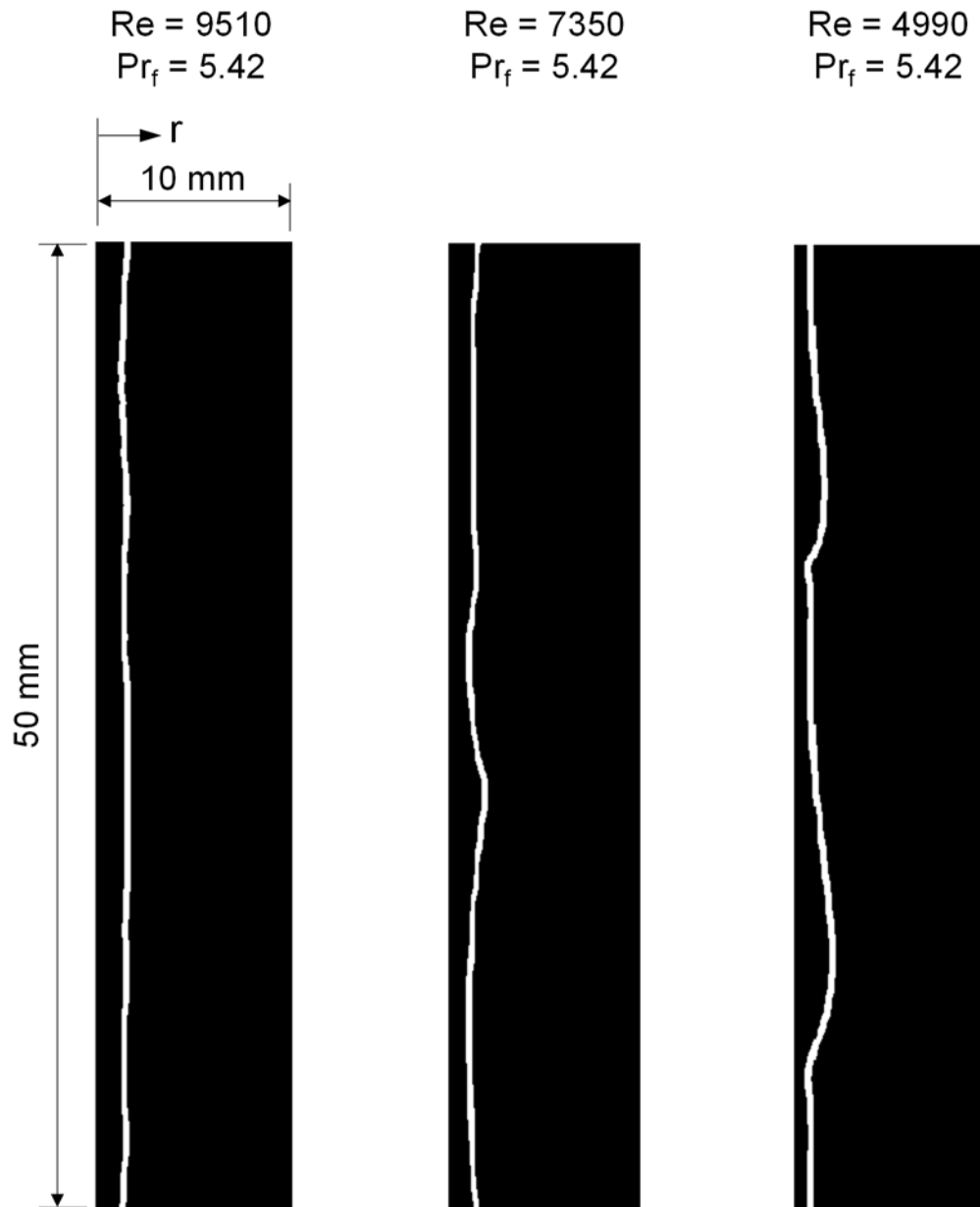
Fig. 7.5: Interfacial waves at axial distance centered 0.75 m from inlet of heated length for three Reynolds numbers and $Pr_f = 5.42$.

The period Δt is carefully chosen to include at least 30 periods of the dominant film profile. After a steady film is formed, it is observed that a 0.2-s period is sufficient to provide repeatable heat transfer values as explained in a recent study by Mascarenhas and Mudawar [92] involving turbulent falling films subjected to sensible heating.

Figures 7.6(a) – 7.6(d) show axial variations of the dimensionless evaporation heat transfer coefficient,

$$h_E^* = \frac{h_E \, v_f^{2/3}}{k_f \, g^{1/3}}, \tag{7.8}$$

along the heated length for different Reynolds numbers and $Pr_f = 1.72$, 3.07, 4.52 and 5.42, respectively. For each combination of Re and Pr_f, the plots show the experimental data, curve fit to the experimental data, and computed variations. For all cases, the data show a thermal development region persisting to over one half the heated length. Thermal development lengths are also evident in the computed variations, but they are prolonged for most cases compared to the data. Lack of a clearly defined downstream fully developed region is attributed to the inability of the phase change model to accurately account for interfacial energy transfer. Different values of γ in Eq. (1.4) provide different mass fluxes and therefore different energy transfer rates at the interface.

These results bring into question the choice of optimum value of γ as discussed earlier. A constant value of $\gamma = 0.1$ is used in the present study to achieve both numerical stability and uniformity in solution method. But using a constant value might be responsible, at least in part, for the prolonged thermal entrance lengths in the computed variations in Figs.
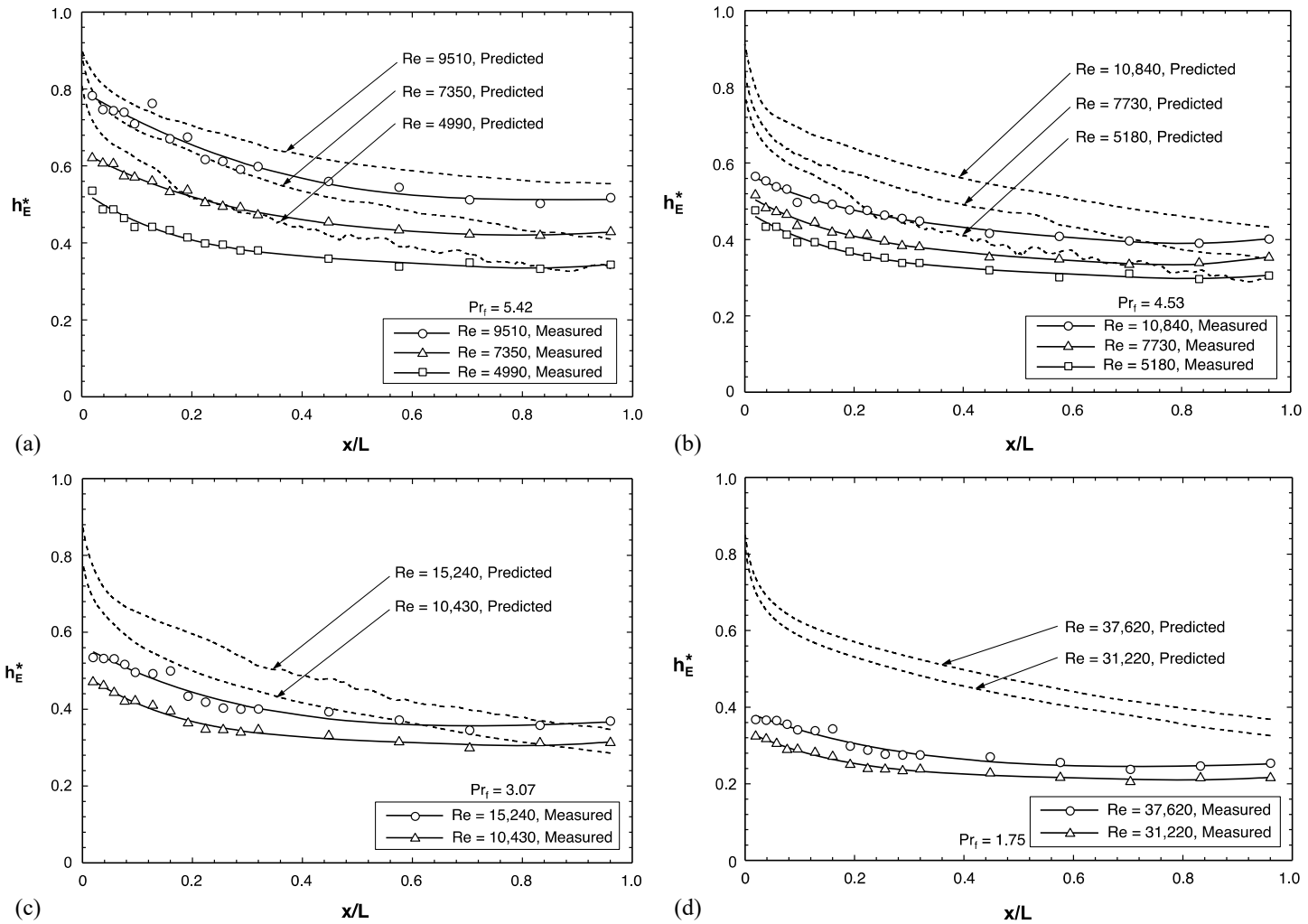
Fig. 7.6: Variations of measured and predicted dimensionless heat transfer coefficients along heated length of test section for different Reynolds numbers and (a) $Pr_f = 5.42$, (b) $Pr_f = 4.53$, (c) $Pr_f = 3.07$, and (d) $Pr_f = 1.75$.

7.6(a) – 7.6(d). Notice also that there is some departure between predicted and measured values in the upstream part of the thermal development region. The predicted values show a steeper drop near $x = 0$, compared to a milder drop for the experimental data. This difference might be related to the design of the test section, specifically at $x = 0$ and $x = L$, where the stainless steel tube is soldered to short copper cylinders that act as electrical terminals for the current supplied through the stainless steel wall. Axial heat conduction along the stainless steel wall towards the terminal blocks compromise the uniformity of wall heat flux at these locations and mask the sharp drop in wall temperature near $x = 0$. Overall, the computed results show reasonable agreement for the $Pr_f = 3.07$, 4.52 and 5.43 cases, but appreciable departure for the lowest $Pr = 1.72$ cases, where liquid viscosity is lowest.

The developing nature of the film makes it difficult to determine a universal correlation for the fully developed evaporation heat transfer coefficient. Shmerler and Mudawar [63] determined fully developed h_E^* by averaging values measured at $x/L = 0.576$, 0.704 and 0.832, outside the upstream thermal development region and the exit region. Using the same axial range of $x/L = 0.576$-0.832, the computed values are spatially averaged to yield the following dimensionless relation for "fully developed" evaporation heat transfer coefficient,

$$h_E^* = 0.00044 \, \text{Re}^{0.598} \text{Pr}_f^{0.975}, \tag{7.9}$$

as shown in Fig. 7.7(a), where all fluid properties are based on saturation conditions. Figure 7.7(b) shows this relation falling mostly between the correlations of Chun and Seban [62], and Shmerler and Mudawar [63].
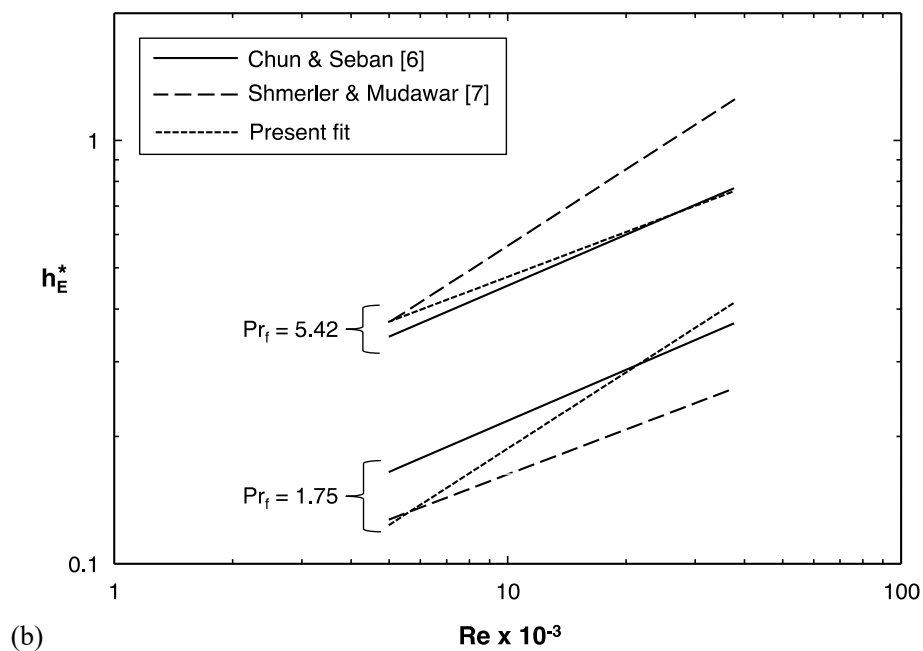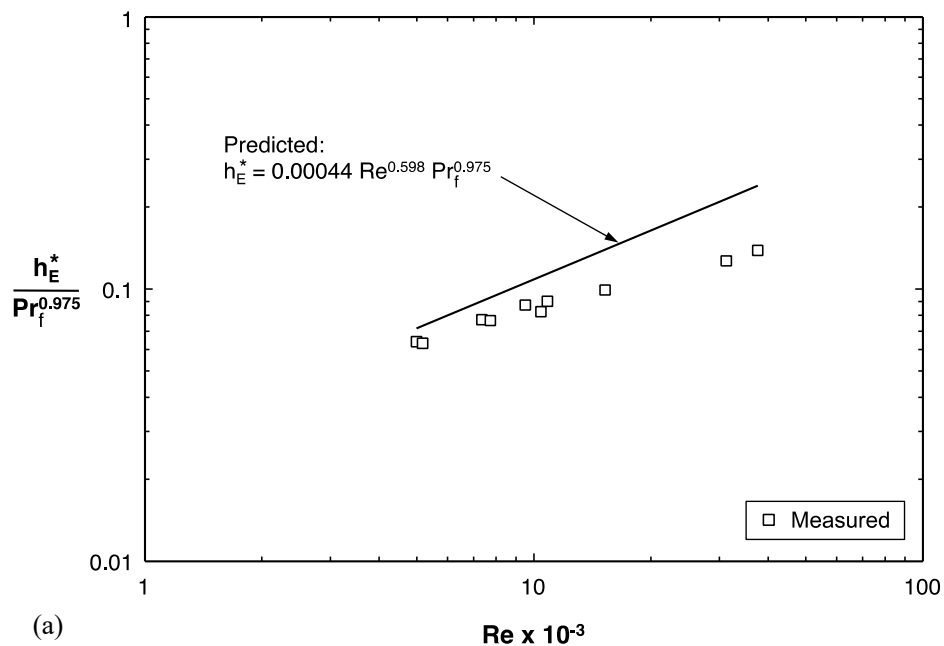
Fig. 7.7: (a) Comparison of measured and computed variations of dimensionless fully-developed evaporation heat transfer coefficient with Reynolds number for $Re = 4990$-$37,620$ and $Pr_f = 1.75$-5.42. (b) Comparison of computed variation of dimensionless fully-developed evaporation heat transfer coefficient with prior correlations for $Pr_f = 1.75$ and 5.42.

7.2.3 <u>Eddy Diffusivity and Velocity Profiles</u>

Analytical modeling of the film's fluid flow and heat transfer depends highly on the ability to accurately model turbulence structure across the film. Turbulence effects are reflected in the variation of eddy momentum diffusivity, ε_m, and eddy heat diffusivity, ε_h, across the film. For a turbulent falling film, the variations of shear stress and heat flux across the film are expressed as

$$\tau = \mu_f \left(1 + \frac{\varepsilon_m}{\nu_f} \right) \frac{\partial u}{\partial y} \tag{7.10}$$

and

$$q'' = -k_f \left(1 + \frac{\mathrm{Pr}_f}{\mathrm{Pr}_{f,T}} \frac{\varepsilon_m}{\nu_f} \right) \frac{\partial T}{\partial y}, \tag{7.11}$$

where $Pr_{f,T} = \dfrac{\varepsilon_m}{\varepsilon_h}$ is the turbulent Prandtl number.

Eddy diffusivity across a turbulent boundary layer is often modeled with the aid of a modified Van Driest formulation [93]. But eddy diffusivity profiles commonly utilized with internal or external flows single-phase flows [94,95] lack the ability to account for the dampening influence of surface tension on turbulence eddies near a liquid-vapor interface. Mills and Chung [96], Seban and Faghri [97], Hubbard *et al.* [98], and Mudawar and El-Masri [99] recommended different formulations to account for the dampening of eddy diffusivity near the interface. Mudawar and El-Masri developed a single continuous eddy diffusivity profile incorporating the Van Driest model near the wall, an experimental profile derived from open channel flow data for the bulk region of the film, and a dampening multiplier for interface region. The Mudawar and El-Masri profile is given by

$$\frac{\varepsilon_m}{\nu_f} = -\frac{1}{2} + \frac{1}{2}\sqrt{1 + 4K^2 \left(y^+\right)^2 \left(1 - \frac{y^+}{\delta_l^+}\right)^2 \left[1 - \exp\left\{-\frac{y^+}{A^+}\left(1 - \frac{y^+}{\delta_l^+}\right)^{1/2}\left(1 - \frac{0.865\ \mathrm{Re}_{crit}^{1/2}}{\delta_l^+}\right)\right\}\right]^2}, \quad (7.12)$$

where $K = 0.4$, $A^+ = 26$, and $\mathrm{Re}_{crit} = 97/Ka^{0.1}$ for sensible heating or $\mathrm{Re}_{crit} = 0.04/Ka^{0.37}$ for evaporative heating. They also recommended the following relation for turbulent Prandtl number,

$$\mathrm{Pr}_{f,T} = 0.66 + 1.4\exp\left(-15\frac{y^+}{\delta_l^+}\right). \quad (7.13)$$

Figure 7.8 compares the average eddy diffusivity profile across the film at an axial location of $x = 0.75$ m from the inlet of the heated length determined from the computational model with the Mudawar and El-Masri profile for three different cases. The average profile is obtained by averaging eddy diffusivity profiles for different subintervals within a period of a single dominant wave, as explained by Mascarenhas and Mudawar [92] for turbulent falling films subjected to sensible heating. Notice that, like the empirical profile, the computed eddy diffusivity is zero both at the wall and the film interface. There is also good overall agreement between the computed and empirical profiles in both shape and magnitude, evidenced by R-square fits of 0.96, 0.92 and 0.88 for $Re = 37,620$ and Pr_f = 1.75, $Re = 15,240$ and $Pr_f = 3.07$, and $Re = 9510$ and $Pr_f = 5.42$, respectively. These trends are also similar to those of the eddy diffusivity profiles computed by Mascarehnas and Mudawar for sensible heating.

Figure 7.9 shows x-velocity profiles across the film computed at $x = 0.75$ m for two cases: $Re = 37,620$ and $Pr_f = 1.75$, and $Re = 9510$ and $Pr_f = 5.42$. These velocity profiles
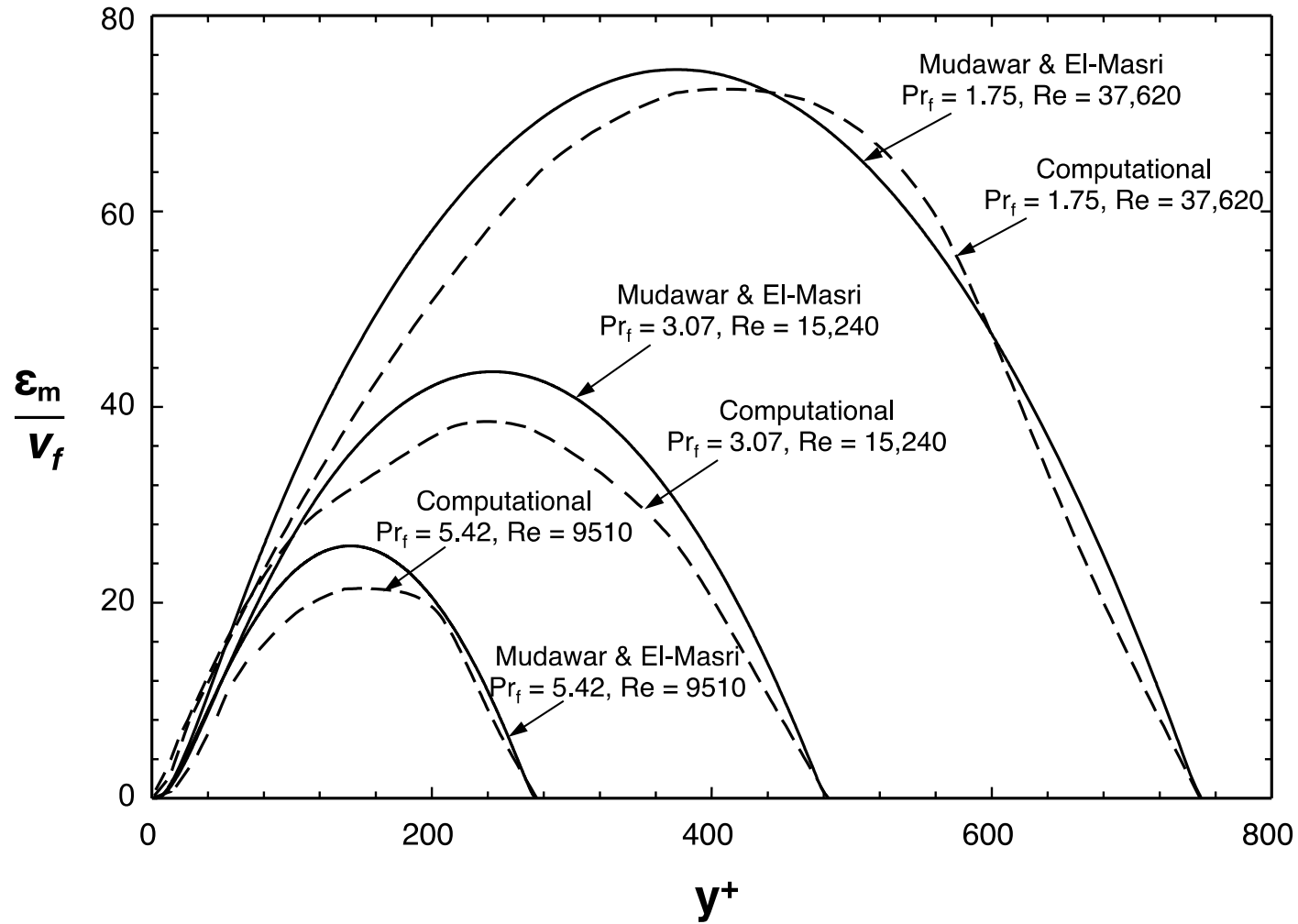
Fig. 7.8: Comparison of predicted eddy diffusivity profiles with Mudawar and El-Masri's [99] at axial distance 0.75 m from inlet of heated length for different Reynolds and Prandtl numbers.
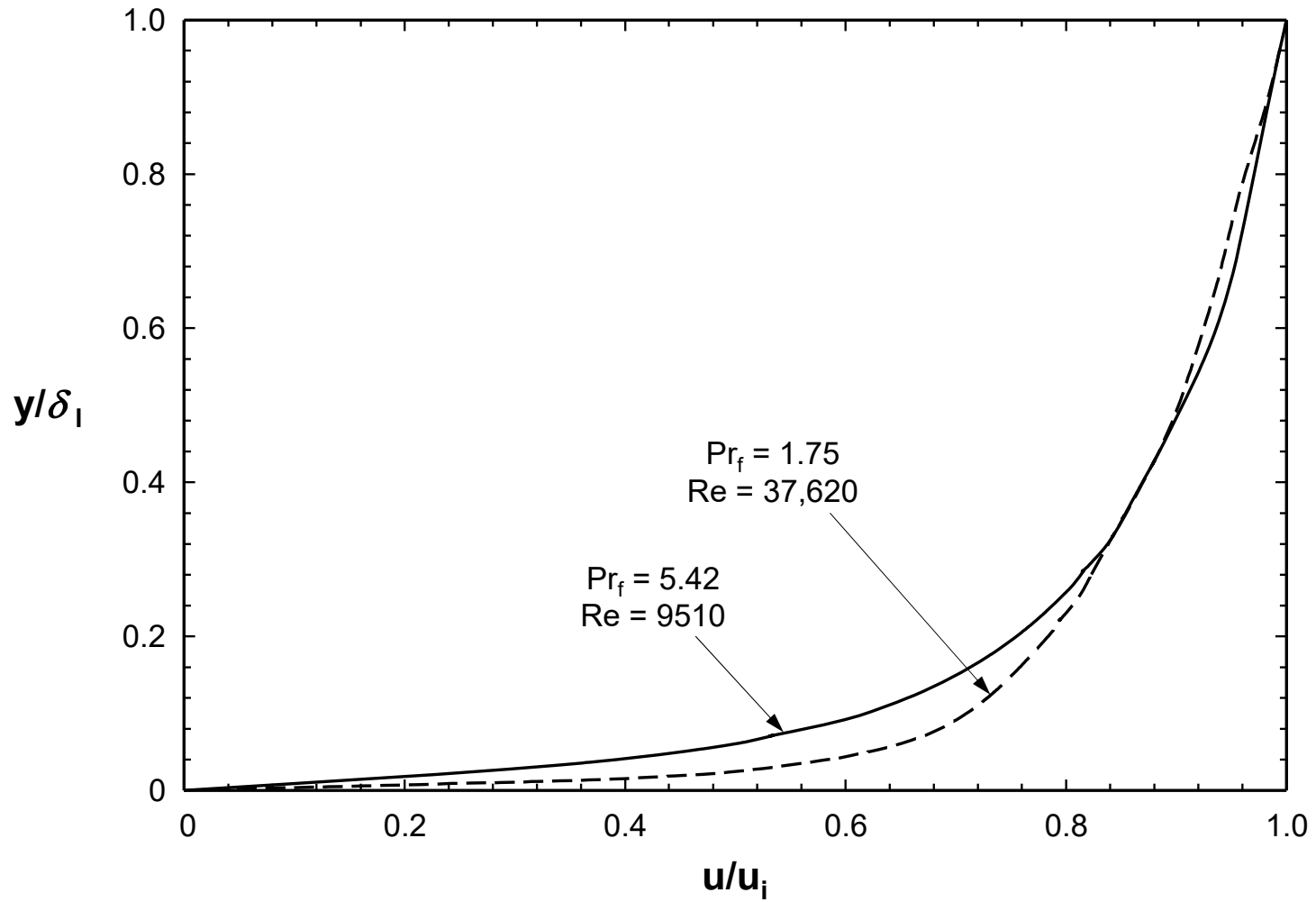
Fig. 7.9: Computed *x*-velocity profiles at axial distance 0.75 m from inlet to heated length for $Re = 9510$ and $Pr_f = 5.42$, and $Re = 37,620$ and $Pr_f = 1.75$.

are representative of turbulent boundary layer profiles with the higher velocity displaying steeper slope near the wall.

7.2.4 Temperature Profile

Eddy diffusivity and $Pr_{f,T}$ are also essential for analytical determination of temperature profile across the film. For a thermally fully developed film, the heat flux across the film is constant and equal to the wall heat flux, q''_w. Equation (7.11) shows that, at least for the fully developed region, temperature profile across the film acquires a large slope where $\dfrac{\varepsilon_m}{v_f}$ tends to zero, and a small slope where $\dfrac{\varepsilon_m}{v_f}$ tends to a maximum. This behavior is explained with the aid of Figs. 7.10(a) and 7.10(b). An eddy diffusivity profile is shown in Fig. 7.10(a) having zero values both at the wall and the interface, and a maximum somewhere in between, as depicted earlier in Fig. 7.8. Figure 7.10(b) shows the temperature profile acquires large slope both at the wall, where $T = T_w$, and the interface, where $T = T_{sat}$. The temperature profile displays an unusual temperature gradient at the interface, which is not commonly observed with turbulent thermal boundary layers for other flow situations.

Figs. 7.11(a) and (b) depict computed non-dimensional temperature profiles across the liquid film computed at four axial locations for $Re = 9510$ and $Pr_f = 5.42$, and $Re = 37,620$ and $Pr_f = 1.75$, respectively. The phase change model employed in this study is clearly capable of capturing the aforementioned temperature profile trends. Notice how the temperature profile features a sharp gradient near the interface, implying a finite heat flux is dissipated at the interface, and that the computed interface temperature is very close to
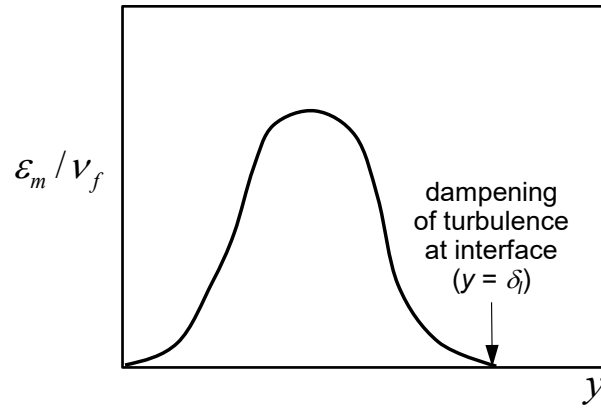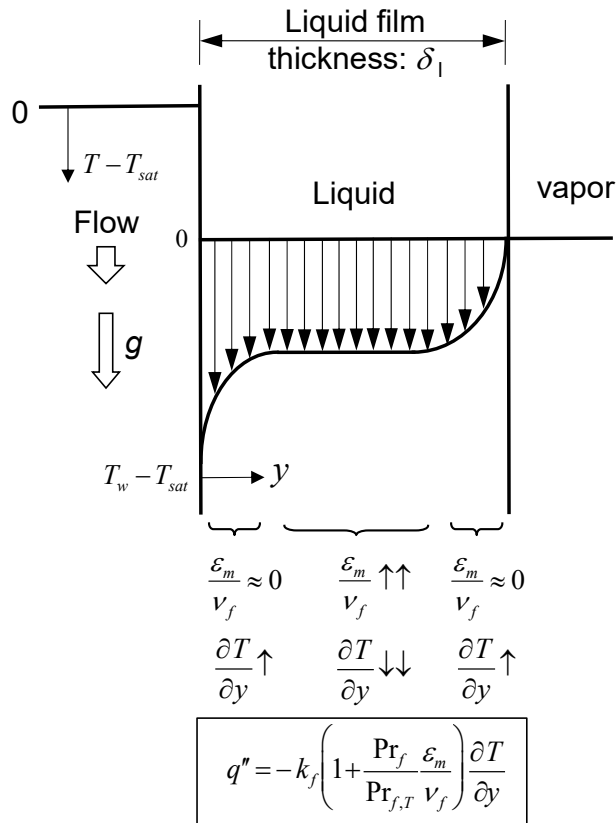
Fig. 7.10: Schematic representations of (a) eddy momentum diffusivity profile across the liquid film, and (b) influence of interfacial dampening of eddy momentum diffusivity on temperature profile.
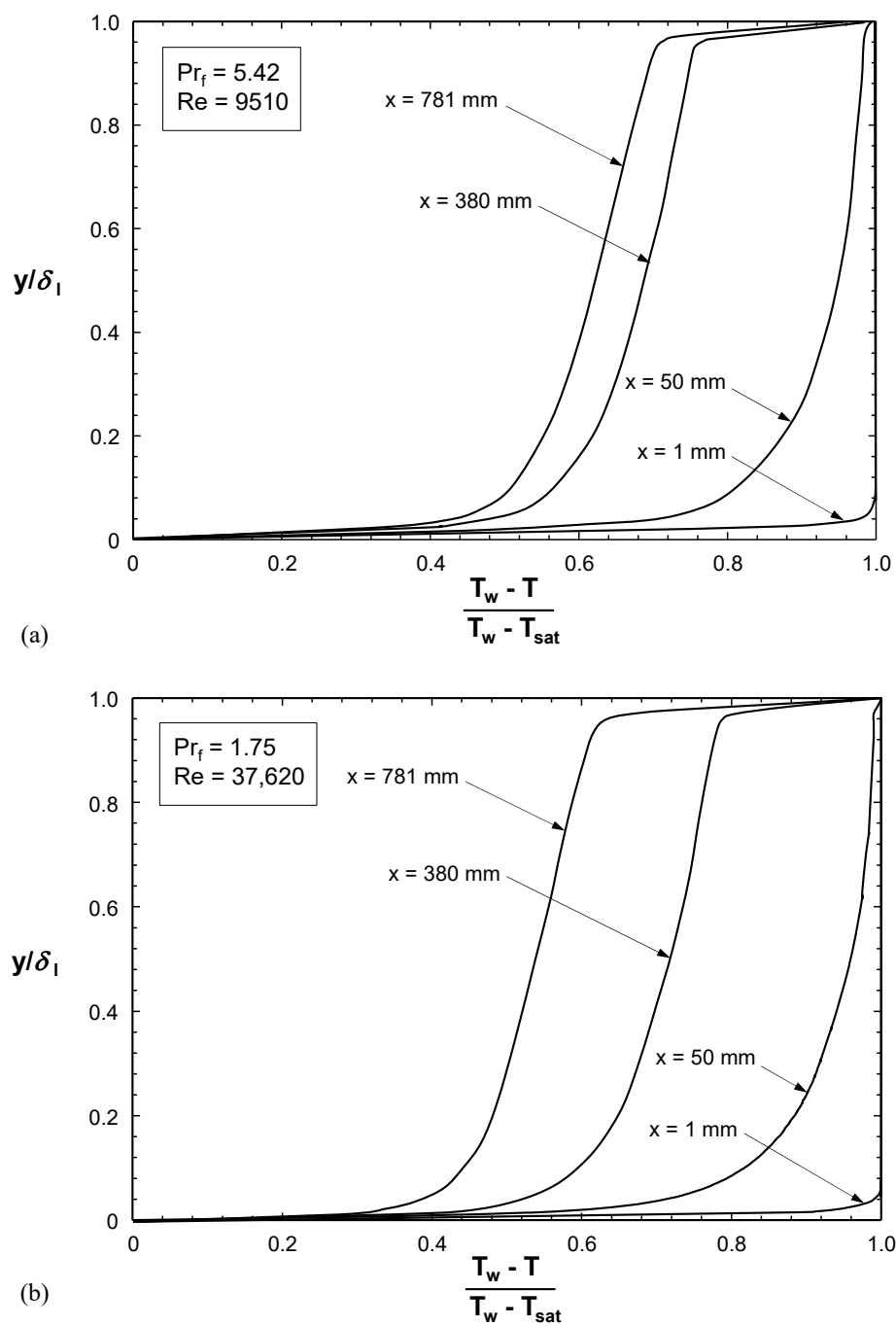
Fig. 7.11: Predicted development of temperature profiles along heated length for (a) $Re = 9510$ and $Pr_f = 5.42$, and (b) $Re = 37,620$ and $Pr_f = 1.75$.

T_{sat}. Additionally, the gradient near the interface is shown increasing axially, which suggests a larger fraction of the wall heat flux is being dissipated at the interface as the film flows downstream. These trends demonstrate that the phase change model adopted in this study is able to replicate the physical phenomena quite well. It is worth indicating that the same phase change model would have failed to capture the interfacial temperature gradient without the dampening of eddy diffusivity at the interface. On the other hand, the interfacial temperature gradient can be achieved without the complete dampening of eddy diffusivity at the interface if the heat flux at the interface is artificially increased. However, following the minimum energy principle, it is physically more realistic if the eddy diffusivity is a minimum.

Overall, these facts and temperature trends prove that the two-equation $k - \omega$ turbulent model, with shear stress transport (SST) formulation and a turbulence dampening factor of 10, is able to capture all the physical phenomena quite well, and therefore well suited for turbulent evaporating falling films.

The influence of interfacial dampening of eddy diffusivity is reflected in fundamental differences between sensible and evaporative heating of turbulent falling films. For sensible heating, the wall heat flux is absorbed by the film rather than dissipated at the interface. With a small heat flux at the interface, Eq. (7.11) indicated that the temperature profile will not acquire a steep gradient at the interface where $\dfrac{\varepsilon_m}{\nu_f}$ tends to zero. Figure 7.12 highlights the differences between temperature profiles for sensible and evaporative heating of turbulent falling films along the heated length. Sensible heating is shown yielding a steep gradient at the wall but not at the interface. Whereas, evaporative heating
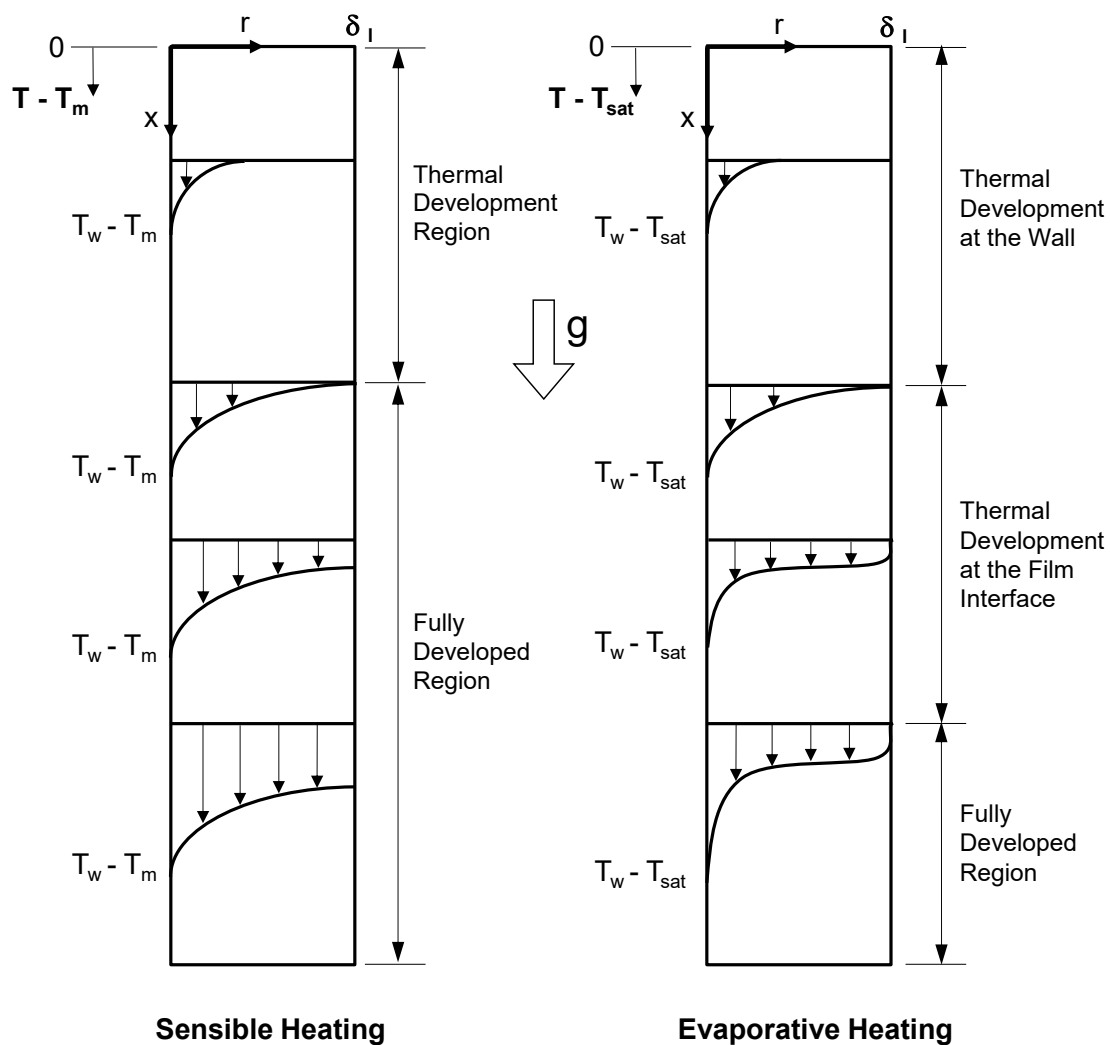
Fig. 7.12: Differences in thermal development between hydrodynamically fully developed falling films subjected to sensible heating and evaporative heating.

is shown yielding steep gradients both at the wall and the interface. Once the evaporating film becomes thermally fully developed, it is able to transfer all the wall energy across the film and to the interface without increasing the wall or film temperatures.

7.3 Conclusions

This section examined fluid flow and heat transfer characteristics of turbulent, free-falling liquid film subjected to evaporative heating. A computational model was developed for two-dimensional axisymmetric film flow on a vertical circular tube, with both the computational domain and operating conditions matching those of an experimental database for evaporating water films. Implemented in FLUENT, the model incorporates a phase change model suggested by Tanasawa [72], and is used to predict variations of the evaporative heat transfer coefficient along the heated length, as well as profiles of eddy diffusivity, flow velocity, and temperature across the film. Key findings from the study are as follows.

(1) Energy transfer at the film's interface is captured successfully with the aid of the Tanasawa phase change model. An accommodation coefficient of $\gamma = 0.1$ is successful at maintaining the film interface at saturation temperature for all the cases tested.

(2) The model predicts variations of the heat transfer coefficient along the heated length similar to those measured experimentally, but with a broader thermal development region.

(3) Predicted heat transfer coefficients for a broad range of Reynolds numbers and Prandtl numbers between 3.07 and 5.43 fall between predictions of two prior experimental correlations.

(4) The model predicts eddy diffusivity is fully dampened at the film interface. The predicted eddy diffusivity profile resembles the empirical profile recommended by Mudawar and El-Masri [99] for falling films in both trend and magnitude. The predicted velocity profiles follow expected trends.

(5) The temperature profile across the liquid film features a steep gradient near the film interface, which is attributed to the dampening of turbulence coupled with energy loss at the film interface.

(6) The two-equation $k-\omega$ turbulent model, with shear stress transport (SST) formulation and a turbulence dampening factor of 10 in FLUENT successfully capture the physics of falling films subjected to evaporative heating.

(7) This work points to the need for more sophisticated and miniaturized diagnostic tools to measure liquid film thickness, liquid velocity, liquid temperature and turbulence to refine phase change models and further assess the accuracy of computational techniques for study of phase change processes.

CHAPTER 8. COMPUTATIONAL INVESTIGATION OF VERTICAL UPFLOW CONDENSATION

8.1 Experimental Methods

The data used to assess the accuracy of the computational model are obtained using the PU-BTPFL flow condensation facility depicted in Fig. 8.1(a). Figure 8.2(b) provides a schematic of the flow loop that is used to supply FC-72 vapor to the condensation module. The system consists of three flow loops, a primary FC-72 condensation loop and two water cooling loops. Heat is extracted from the FC-72 first via the condensation module utilizing the first water loop, and again via a separate condenser utilizing the second water loop. Two separate FC-72 condensation modules are used, both utilizing tube-in-tube construction, and within which the FC-72 vapor is condensed by rejecting heat to water that is supplied in counterflow.

Illustrated schematically in Fig. 8.2(a), the first condensation module is used for heat transfer measurements. Superheated FC-72 vapor is supplied through the inner 304 stainless steel tube metallic tube and is cooled by water supplied in counterflow through the outer annulus. The inner tube has an 11.89-mm i.d. and wall thickness of 0.41 mm, while the outer tube, also made from 304 stainless steel, has a 22.48-mm i.d. This module features a condensation length of 1,259.8 mm. The small wall thickness of the inner tube, coupled with the relatively low thermal conductivity of stainless steel, is intended to

(a)

(b)
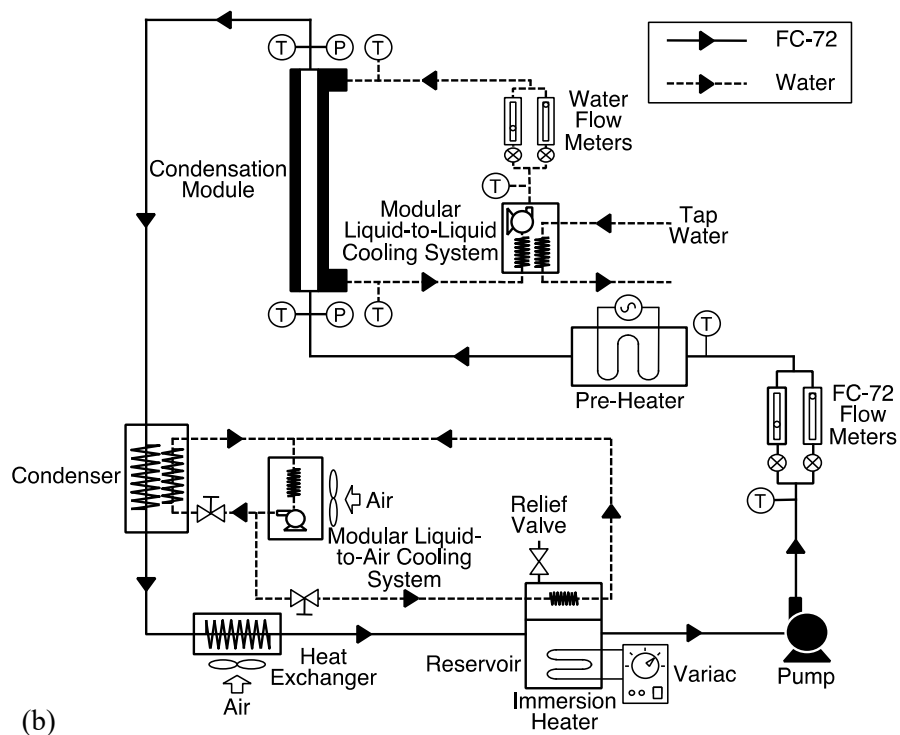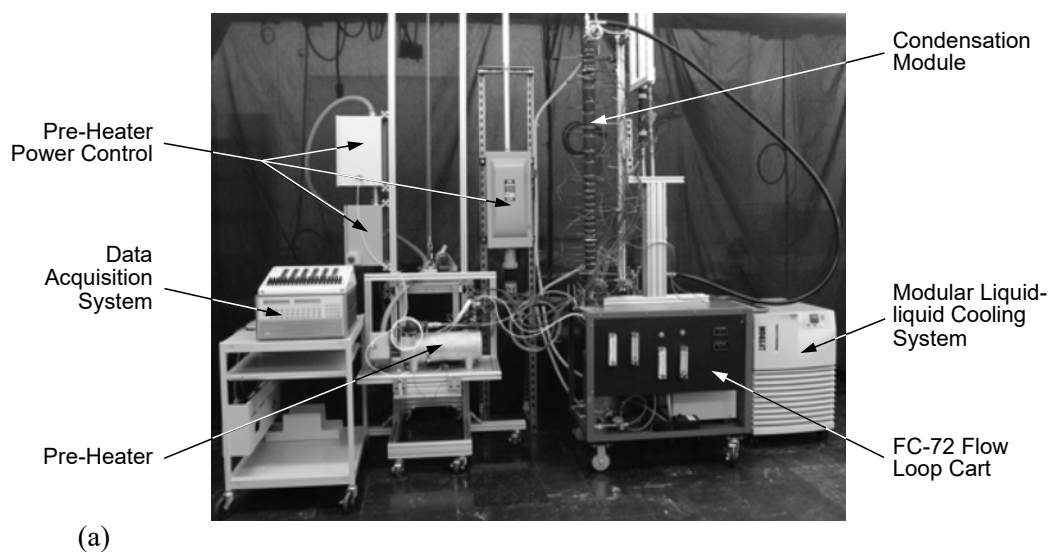
Fig. 8.1: (a) Photo of condensation facility. (b) Schematic of flow loop.
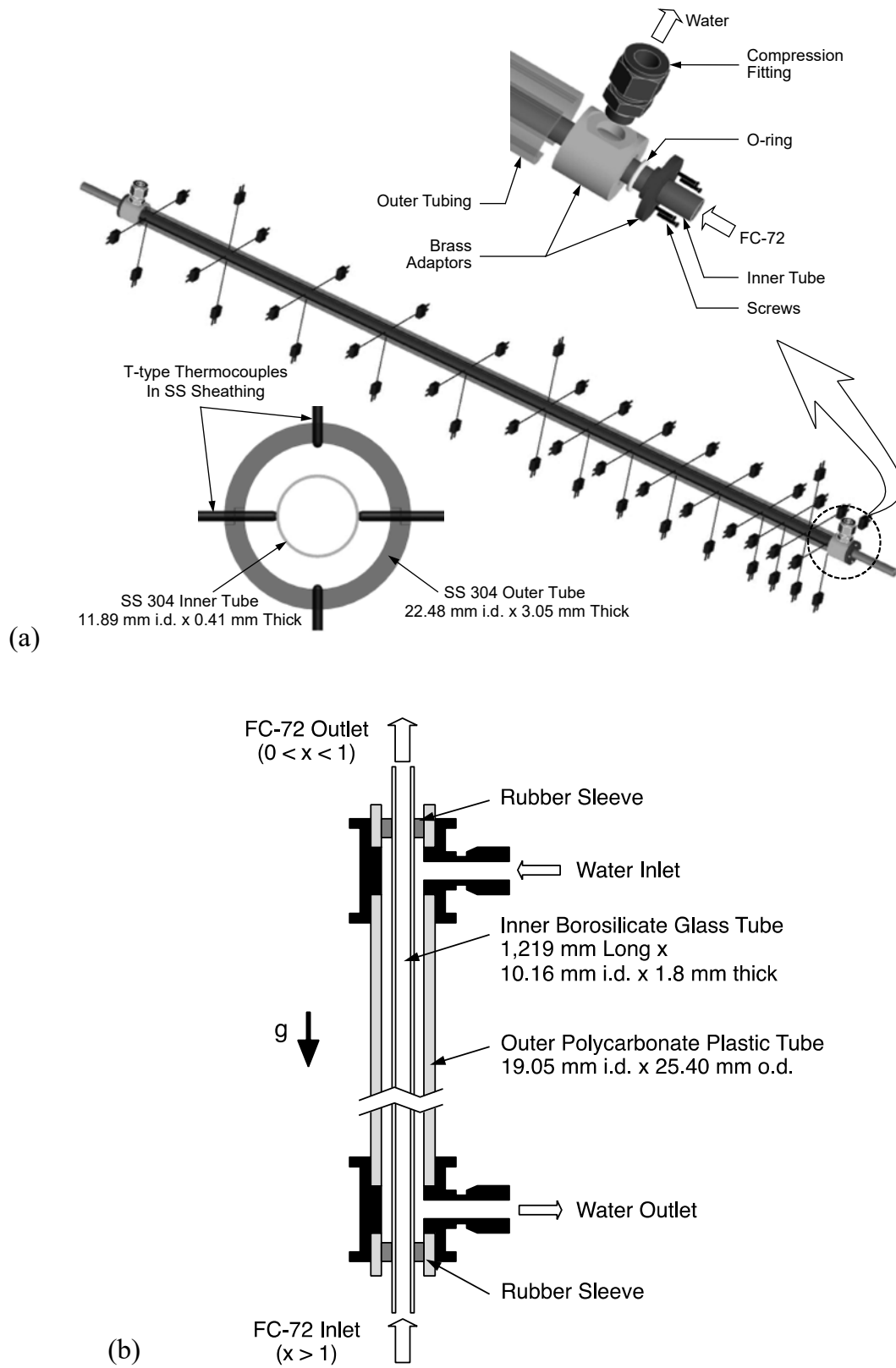
Fig. 8.2: (a) Condensation module for heat transfer measurements. (b) Condensation module for flow visualization.

minimize axial conduction along the condensation length. Two sets of diametrically opposite type-T thermocouples are attached to the outer surface of the inner tube at 14 axial locations to measure the outer wall temperature. The water temperature is also measured at the same 14 different axial locations. FC-72 pressure is measured at the inlet and outlet of the condensation length. The operating conditions for the condensation module used for heat transfer measurements are provided in Table 8.1. These are the same conditions used in the computational model.

Shown in Fig. 8.2(b), the flow visualization module also features a tube-in-tube construction, with the FC-72 flowing through the inner tube and water through the outer annulus. The inner borosilicate glass tube has a 10.16-mm i.d. and a wall thickness of 1.8 mm. The outer polycarbonate (Lexan) plastic tube has an inner diameter of 19.05 mm. This module features a condensation length of 1,219.0 mm. The inlets and outlets for the FC-72 and water are fitted with Type-T thermocouples and pressure transducers. Flow visualization is achieved with the aid of a high-speed Photron Fastcam Ultima APX video camera system.

8.2 Computational Methods

Governing equation used in this section for flow condensation are the same as that used for evaporating falling films. For complete formulation please refer to section 7.1.2.

8.2.1 Computational Domain and Mesh Size Independence

Figures 8.3(a) and 8.3(b) show the geometry adopted in modeling upflow annular condensation, and computational domain, respectively. Figure 8.3(b) also shows the

Table 8.1: Operating conditions for the test cases from the experimental study also used in the computational simulation.

Test case	G [kg/m^{2}s]	p_{in} [kPa]	T_{in} [K]	$x_{e,in}$	G_w [kg/m^{2}s]	$T_{w,in}$ [°C]	$T_{w,out}$ [°C]	$q''_{wall,avg}$ [W/cm^2]
1	58.4	104.5	345.3	1.15	55.5	293.1	303.6	-2.15
2	116.7	108.0	347.7	1.16	92.5	294.4	303.4	-3.10
3	194.3	114.2	342.2	1.09	154.2	295.1	302.1	-3.85
4	271.5	124.6	345.0	1.09	215.8	295.1	301.6	-5.23
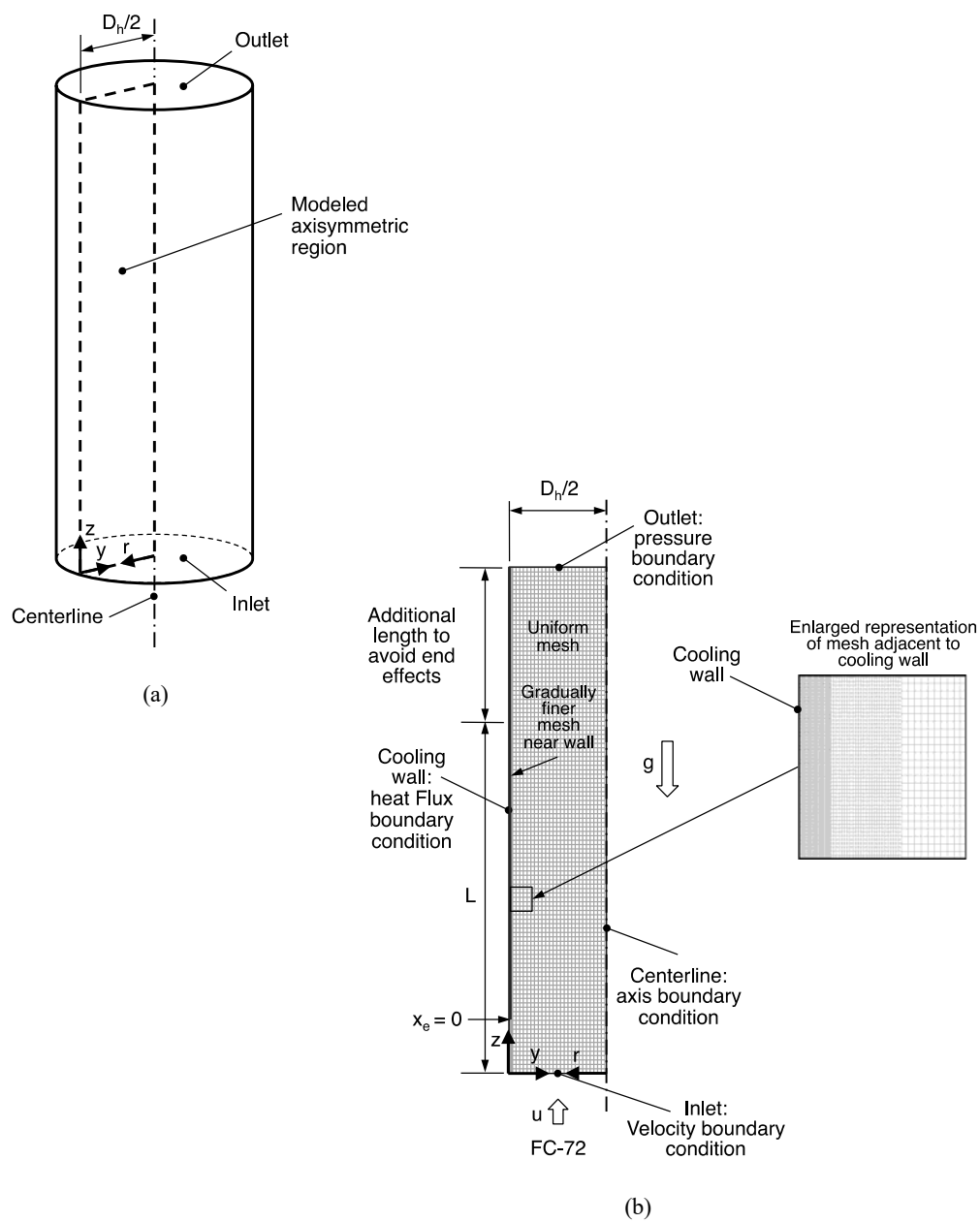
Fig. 8.3: (a) Cylindrical domain for the computational model. (b) 2-D axisymmetric domain modeled in the present study.

boundary conditions used in the computational model. The flow is assumed axisymmetric and two-dimensional. The width of the domain is half the hydraulic diameter, $D_h/2 = 5.945$ mm, and the computational condensation length used is $L = 0.8$ m; this length is shorter than the actual length of the experimental test section as thermocouple measurements were only available up to $L = 0.8$ m. The actual length of the domain is set longer to avoid any end effects at the outlet. The mesh used has quadrilateral shape with uniform grid size in most of the domain, but with gradual refinement in a region adjacent to the condensing wall to accurately capture the formation of the liquid film and local turbulence as depicted in Fig. 8.3(b).

Figure 8.4(a) shows computed values of the heat transfer coefficient spatially averaged over the region 0.2 m $< z <$ 0.8 m for test case 4 in Table 8.1 corresponding to $G = 271.5$ kg/m^{2}s, the highest mass velocity tested. The region $z <$ 0.2 m is intentionally excluded from the averaging due to relatively poor prediction in the two-phase developing region by FLUENT as discussed later. Figure 8.4(a) shows asymptotic values of the average heat transfer coefficient are realized for mesh sizes below about 10 μm. In the present study, a minimum size of $\Delta c = 2$ μm is used near the wall, which resulted in a minimum of five cells near the wall within $y^+ <$ 5. For the same case of $G = 271.5$ kg/m^{2}s, Fig. 8.4(b) shows the variation of wall y^+ (*i.e., y^+* corresponding the first cell nearest to the wall) along the condensing length. The values shown are representative of wall y^+ values used to achieve convergence for all the operating conditions given in Table 8.1.
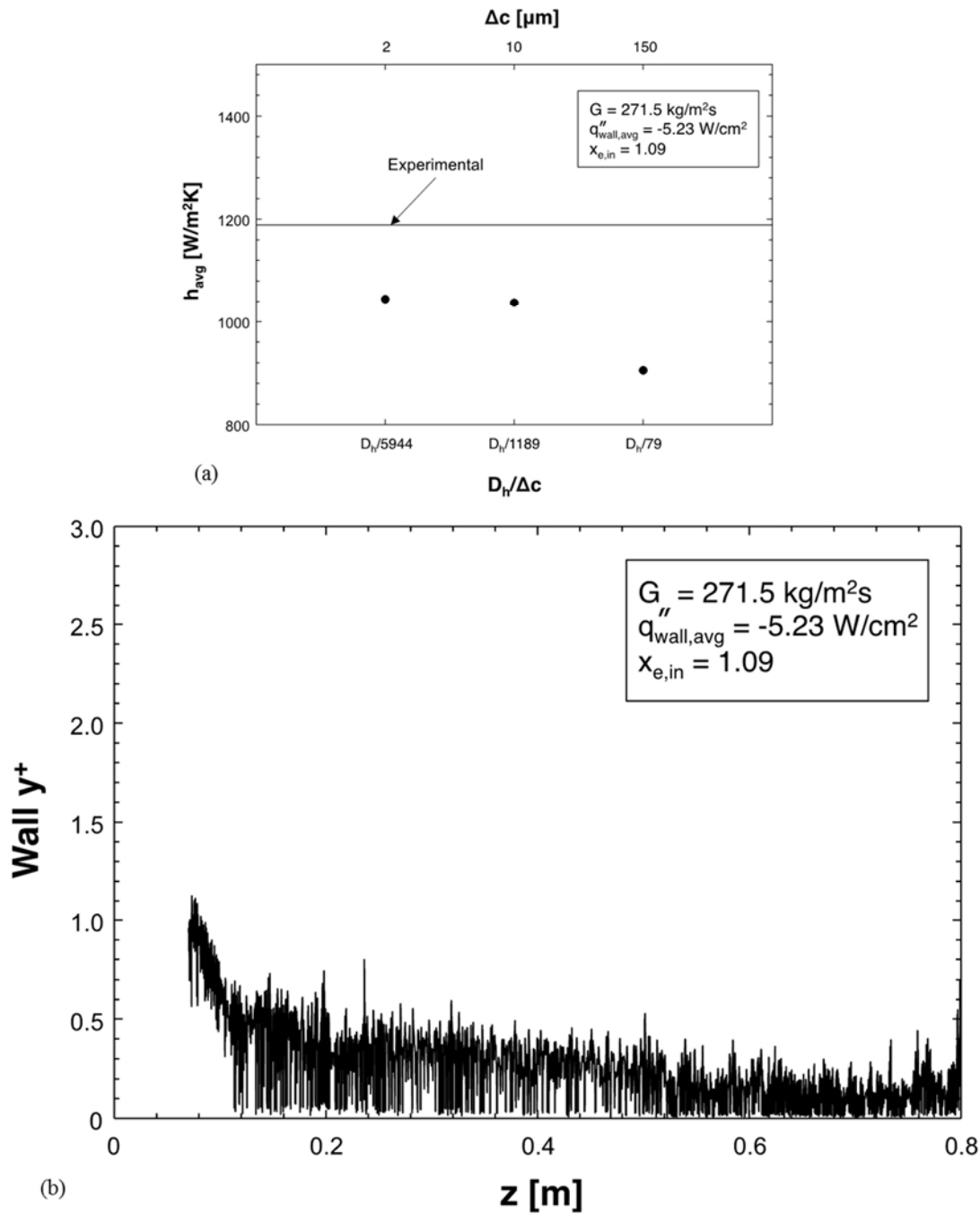
Fig. 8.4: (a) Analysis of grid independence based on spatially averaged condensation heat transfer coefficient. (b) Variation of wall y^+ along condensation length for test case 4 in Table 8.1.

8.2.2 Initialization and Boundary Conditions

In both the experiments and computational model, FC-72 enters the circular channel as pure vapor superheated $9 - 16°C$, and inlet velocity is determined as $u = G/\rho_g$ based on inlet conditions provided in Table 8.1. Turbulence intensity, I, is estimated using the following formula derived from an empirical correlation for pipe flows [86]

$$I = \frac{u'}{\bar{u}} = 0.16\left(\text{Re}_{D_h}\right)^{-1/8}. \tag{8.1}$$

The wall heat flux profile is provided as boundary condition at the wall using user defined functions (UDFs) in FLUENT. The wall heat flux is determined from the local differential sensible heat rise of the cooling water between consecutive waterside thermocouples,

$$q''_{wall} = \frac{\dot{m}_w c_{pw,f}\left(T_{i+1} - T_i\right)}{\pi D_h}. \tag{8.2}$$

Figures 8.5(a) and 8.5(b) show, respectively, axial variations of the experimentally determined wall heat flux, and both water and wall temperatures for the four FC-72 mass velocities given in Table 8.1. Surface conditions consisting of roughness height, roughness constant and contact angle were set to default values of 0 m, 0.5 and 90°, respectively; a sensitivity study showed these parameters have minimal influence on computed values of the condensation heat transfer coefficient.

As indicated in a recent study by Lee *et al.* [100], it is very difficult to initiate a continuous liquid film in the upstream developing region of the flow channel. Following their computational technique, a very thin liquid film of thickness δ_i is initially applied from z_0 (where $x_e = 1$) along the entire condensation length to expedite convergence time.
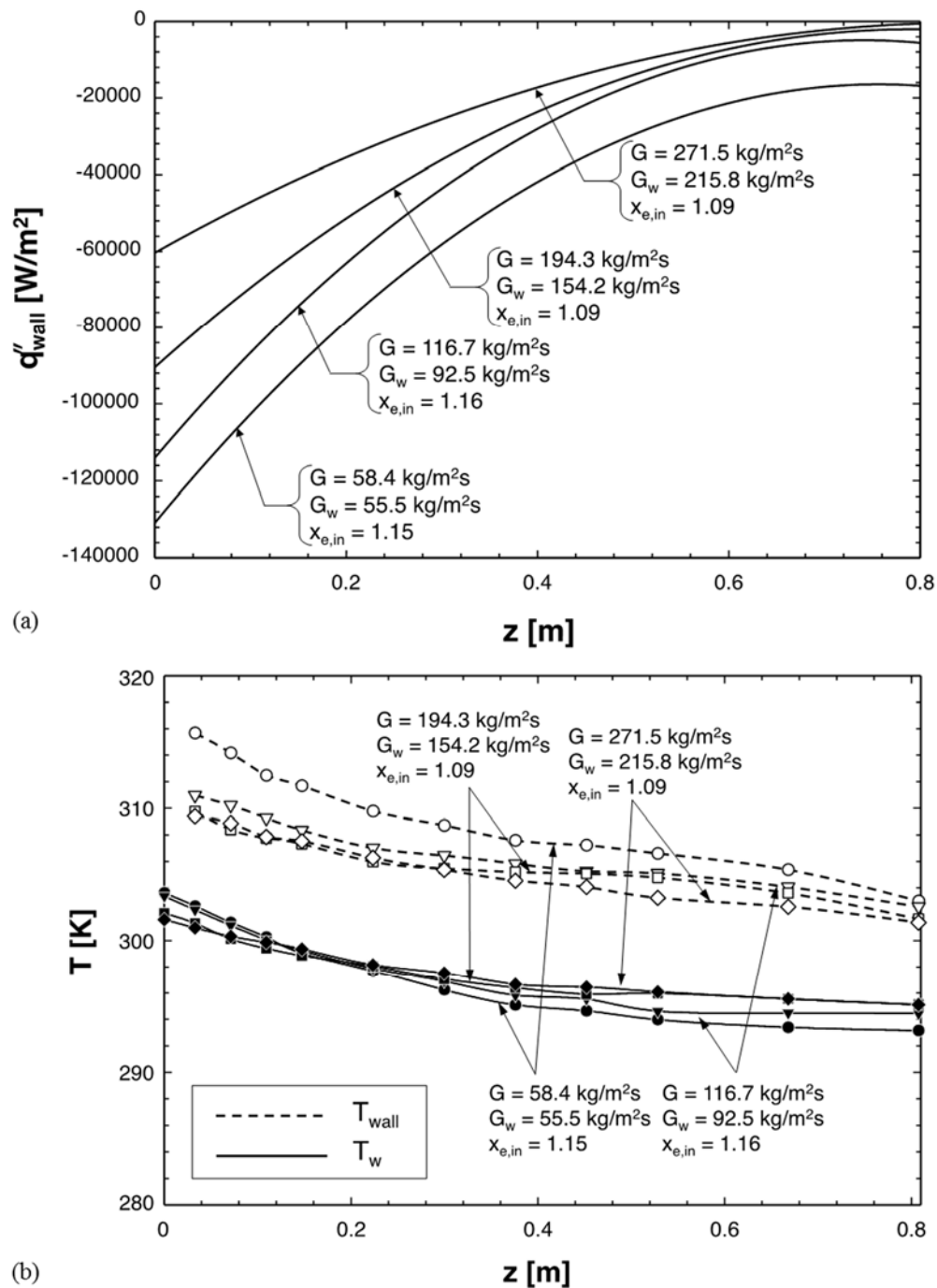
Fig. 8.5: Experimentally determined axial variations of (a) wall heat flux and (b) water temperature and outer wall temperature for four test conditions.

Applying this initial thickness to the entire condensation length is crucial for vertical upflow since the combination of a highly turbulent vapor core and gravity opposite to the flow direction would shear the film faster than with vertical downflow. Additionally, phase change models are incapable of predicting the location where liquid film is initiated. To overcome this difficulty, as suggested by Lee *et al.*, an average liquid film thickness is obtained from an annular flow model [101] for the developing length between $z = z_0$ and $z = 0.05$ m to determine δ_i. The location z_0 corresponding to $x_e = 1$ for each of the four test cases is determined from the simple energy balance

$$x_e = 1 + \frac{c_{p,g}\left(T_g - T_{sat}\right)}{h_{fg}}.$$

(8.3)

The calculated initial liquid film thicknesses are in the range of $\delta_i = 35 - 60$ μm, which are less than 0.6% of the channel diameter. The computed convergent thickness is observed to be significantly greater than the initial thickness estimated from upstream conditions.

8.3 Computational Results

8.3.1 Interfacial Behavior

Interfacial waviness, liquid entrainment and liquid deposition are inherent features of annular flow condensation. Figure 8.6(a) shows predicted interfacial behavior for $G = 271.5$ kg/m²s and a segment of the channel centered at $z = 590$ mm; individual images in the sequence are $\Delta t = 0.0004$ s apart. The predictions show complicated interfacial behavior in the liquid film along the wall. Waves in the film's interface generate small liquid masses that are first entrained into the vapor core and then deposited back upon the
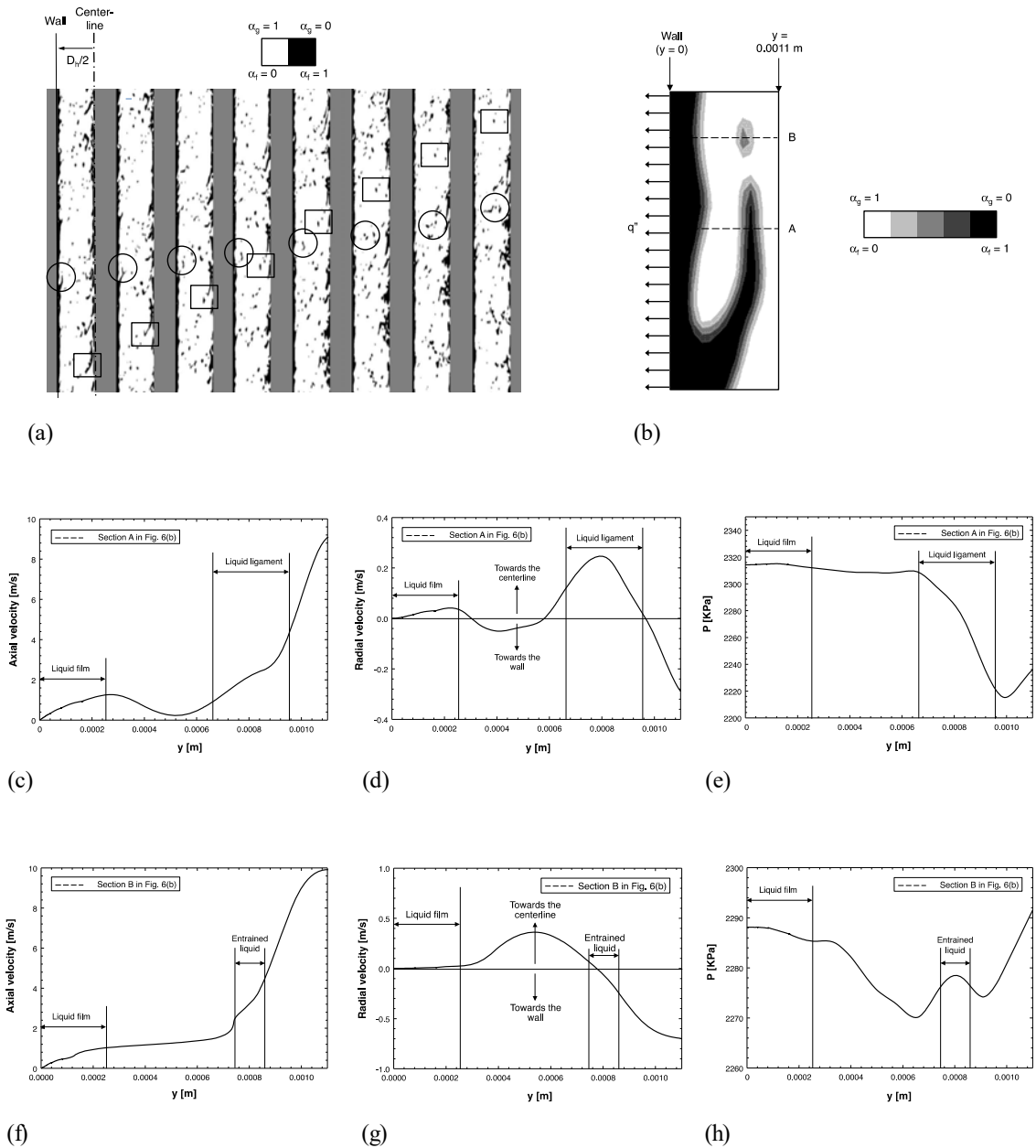
Fig. 8.6: (a) Computed sequential images of climbing film in outlet region centered at z = 590 mm for G = 271.5 kg/m^{2}s and G_w = 215.8 kg/m^{2}s; individual images in the sequence are separated by 0.0004 s. (b) Enlarged view of features in the circular area of the fist image in Fig. 8.6(a). (c) Variation of axial velocity across section A in Fig. 8.6(b). (d) Variation of radial velocity across section A. (e) Variation of pressure across section A. (f) Variation of axial velocity across section B in Fig. 8.6(b). (g) Variation of radial velocity across section B. (h) Variation of pressure across section B.

liquid film. Other interfacial features include liquid ligaments from the liquid film that are elongated, creating a necking region, before snapping and being pushed away from the wall. These latter features appear to possess sufficient radial momentum to be pushed towards the centerline rather than be re-deposited upon the wall liquid film. These features are captured in the circular areas in Fig. 8.6(a), where an elongated liquid protrusion is captured with an adjoining small liquid mass upstream. The small liquid mass is shown being quickly re-deposited upon the wall liquid film, while the liquid ligament jets forward and away from the wall, creating a necking region, before being pinched away and projected towards the centerline. The axisymmetric domain produces vapor radial motion towards the centerline, causing liquid to accumulate around the centerline rather than be dispersed uniformly in the vapor core. The rectangular areas in Fig. 8.6(a) show liquid breaking away from the centerline region and being projected towards the wall. Overall, the present computations show both the wall and centerline are primary locations for liquid accumulation. Previous studies on turbulent two-phase flow with entrained bubbles have shown a tendency of the bubbles to move away from the wall because of decreased effectiveness of bubble-induced skin friction drag reduction (BDR) [102]. In another study [103], numerical simulations of liquid droplets in turbulent vapor flow have shown a tendency of droplet migration away from the wall.

The near wall interfacial features discussed in the previous section are explained quantitatively using Fig. 8.6(b), which depicts an enlargement of features captured in the circular area within the first image in Fig. 8.6(a). Figures 8.6(c), 8.6(d) and 8.6(e) show local variations of axial velocity, radial velocity and pressure, respectively, across section A in Fig. 8.6(b), which includes the wall liquid film and extended liquid ligament. The

axial velocity profile in Fig. 8.6(c) shows the liquid ligament lying in the relatively high velocity region of the turbulent vapor core. Figure 8.6(d) shows the radial velocity of the liquid ligament is positive, indicating a tendency for the ligament to be projected towards the centerline. Figure 8.6(e) shows pressure decreases across the liquid ligament, which is further evidence of the ligament tending to move away from the wall.

Figures 8.6(f), 8.6(g) and 8.6(h) show the local variations of axial velocity, radial velocity and pressure, respectively, across section B in Fig. 8.6(b), which includes the wall liquid film and small entrained liquid mass. The axial velocity profile in Fig. 8.6(f) shows this mass lying in the relatively high velocity region of the turbulent vapor core, similar to the ligament in section A. Figure 8.6(g) shows the radial velocity of the liquid mass is close to zero but mostly negative, which implies a tendency to be deposited back upon the wall liquid film. Figure 8.6(h) shows a local rise in pressure across the liquid mass within a region of mostly increasing pressure away from the wall, another indication of a tendency of this liquid to de deposited upon the wall liquid film.

Figures 8.7(a) show sequential images of FC-72 condensing along the inner wall of the glass tube of the flow visualization test module, centered at $z = 190$ mm, for $G = 53.3$ kg/m^{2}s. Figure 8.7(b) shows computed images at the same location for $G = 58.4$ kg/m^{2}s, test case 1 in Table 8.1, obtained from the heat transfer measurements test module. As discussed by Park *et al.* [67], this condition is representative of the onset of *flooding* according to the Wallis relation [104]. The interface in the flow visualization sequence shows the liquid film exhibiting a combination of small ripples and large waves, with liquid
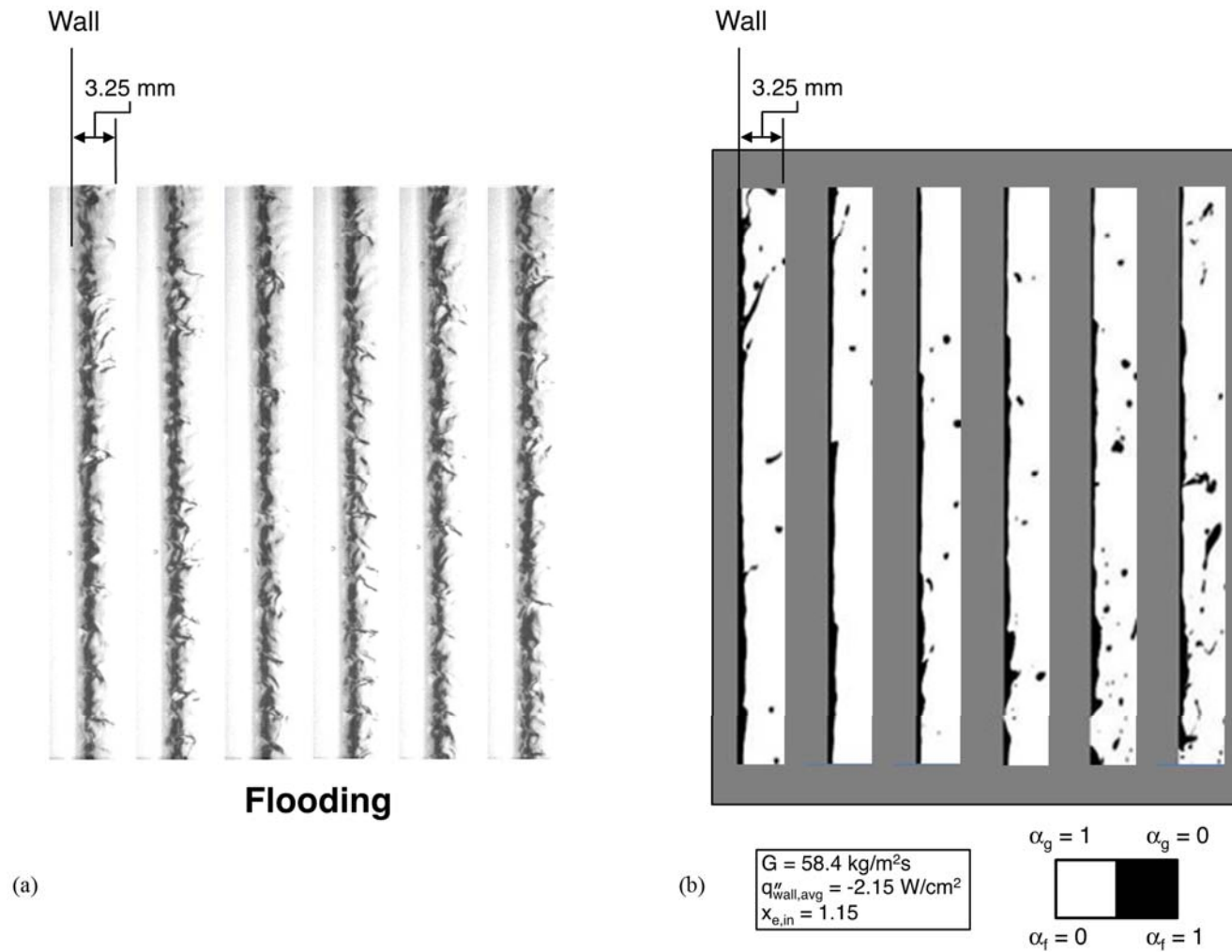
Fig. 8.7: (a) Experimentally obtained sequential images of liquid film in inlet region (centered at z = 190 mm) of flow visualization module with G = 53.3 kg/m^{2}s and G_w = 73.4 kg/m^{2}s corresponding to flooding conditions. (b) Computed sequential images of film at same axial location with G = 58.4 kg/m^{2}s and G_w = 55.5 kg/m^{2}s. Individual images in both sequences are separated by 0.0125 s.

ligaments emanating towards the centerline. The computational images show large waves with liquid ligaments, with smaller ripples superimposed on the large waves.

Figure 8.8(a) shows sequential images of FC-72 condensing along the inner wall of the glass tube of the flow visualization test module, centered at z = 987 mm, for G = 106.5 kg/m²s, which correspond to *climbing film* conditions, as indicated by Park *et al.* [67]. Because heat flux data from the heat transfer measurements module that are used as boundary condition for the computations are only available up to the last thermocouple location at z = 0.80 m, it is impossible to directly compare computed versus flow visualization results for z = 987 mm. However, conditions upstream of z = 0.80 m are also associated with climbing film conditions [67]. Figures 8.8(b) and 8.8(c) show computed images for G = 116.7 and 271.5 kg/m²s, respectively, centered at z = 590 mm. Both experimental results, Fig. 8.8(a), and computed results, Figs. 8.8(b) and 8.8(c), show shear driven flow with the liquid film flowing firmly upwards, with both interfacial ripples and small liquid masses entrained in the vapor core.

8.3.2 Heat Transfer Results

Figure 8.9(a) shows the computed instantaneous variation of the heat transfer coefficient along the flow direction for G = 194.3 kg/m²s. Notice the large local fluctuations, given the complex interfacial behavior of the thin annular film. These fluctuations are extremely difficult to capture experimentally because of wall temperature dampening provided by the thermal mass of the stainless steel tube. In recent computational studies involving sensible heating [92] and evaporative heating of turbulent free-falling films in Chapter 7, heat transfer plots were comparatively smoother. While free
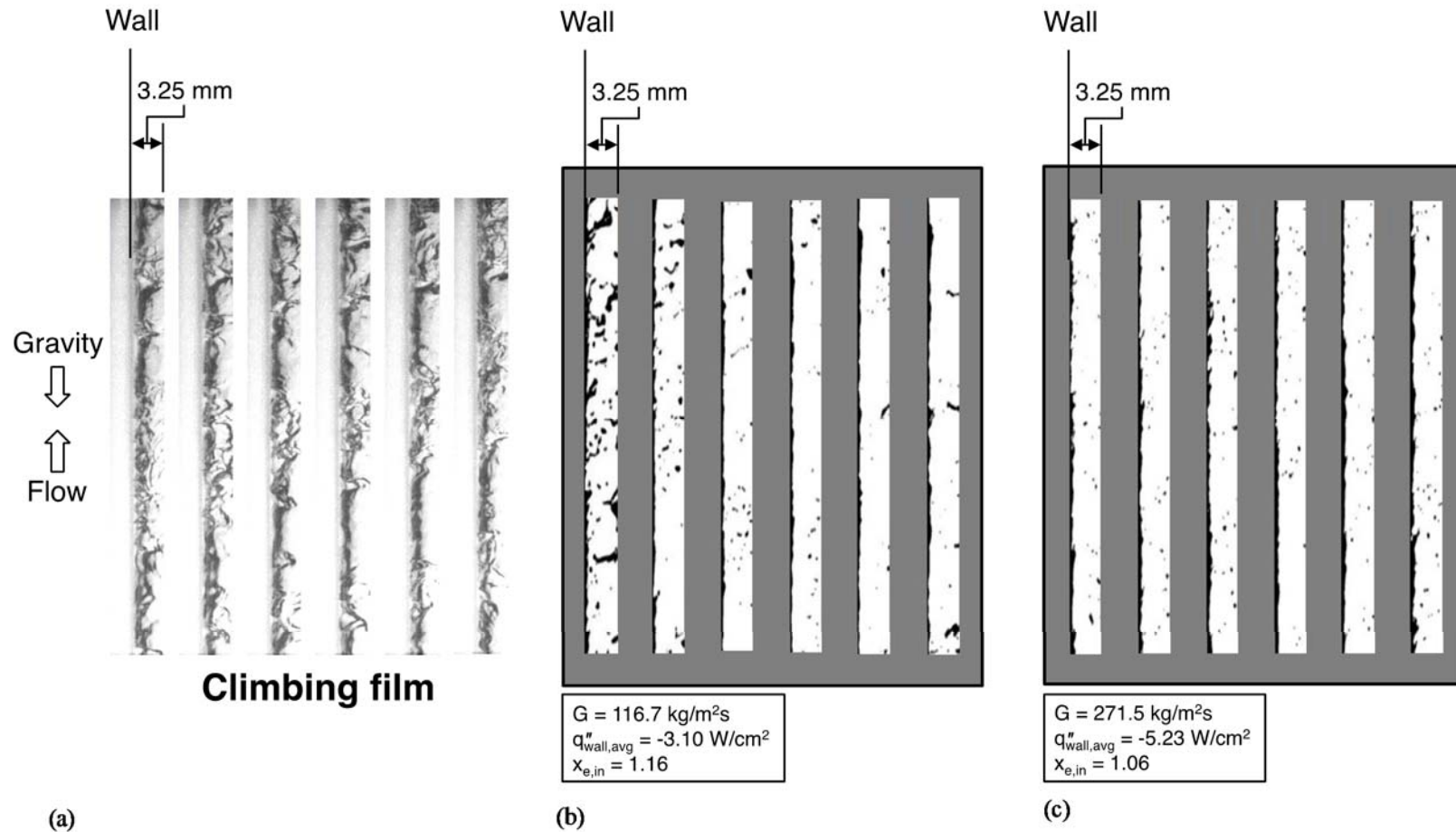
Fig. 8.8: (a) Experimentally obtained sequential images of of liquid film in outlet region (centered at $z = 952$ mm) of flow visualization module with $G = 106.5$ kg/m^{2}s and $G_w = 97.8$ kg/m^{2}s corresponding to climbing film flow. (b) Computed sequential images of film in outlet region (centered at $z = 590$ mm) with $G = 116.7$ kg/m^{2}s and $G_w = 92.5$ kg/m^{2}s. (c) Computed sequential images of film in outlet region (centered at $z = 590$ mm) with $G = 271.5$ kg/m^{2}s and $G_w = 215.8$ kg/m^{2}s. Individual images in all three sequences are separated by 0.0125 s.
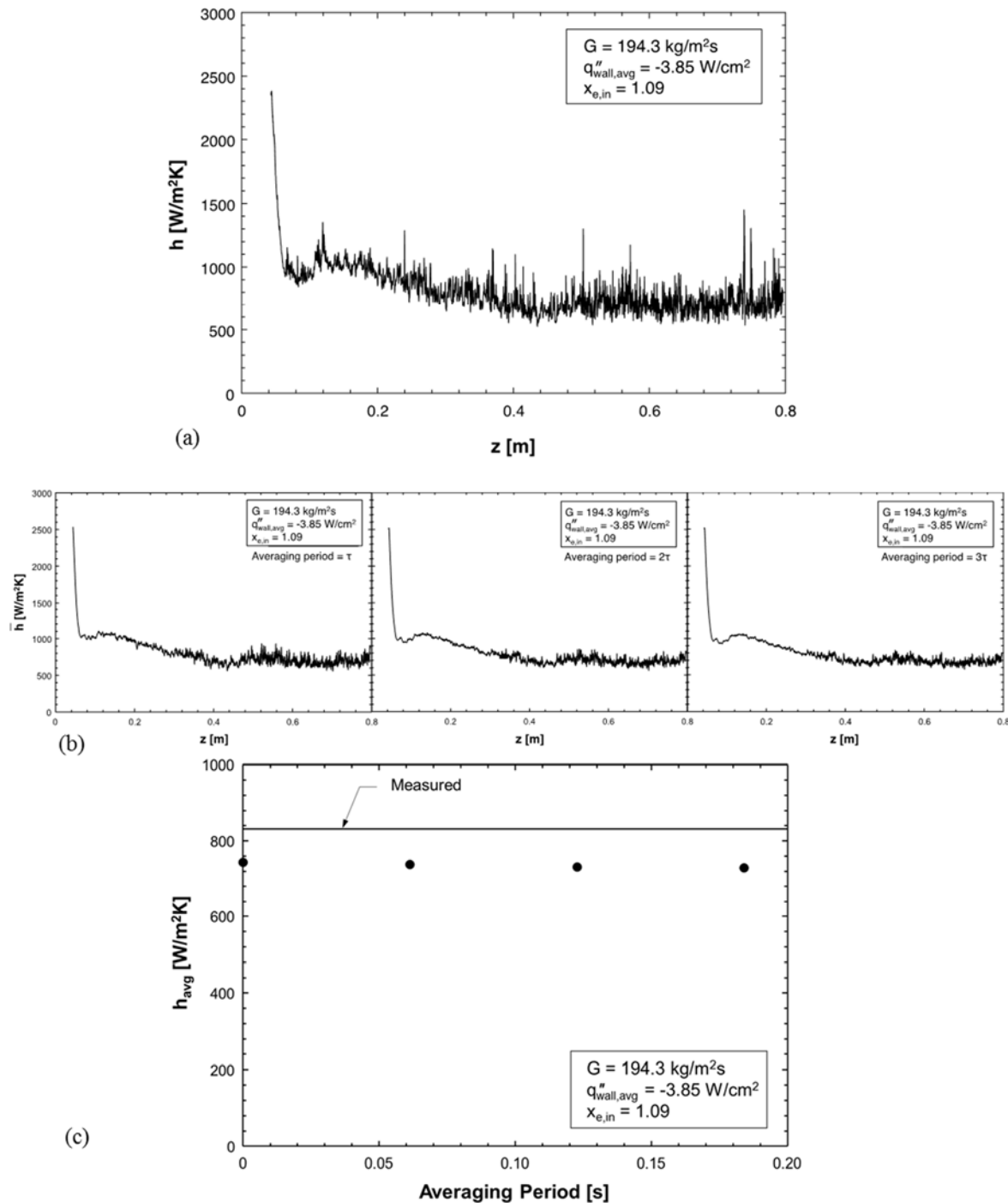
Fig. 8.9: (a) Axial variations of instantaneous computed local condensation heat transfer coefficients. (b) Axial variations of computed local condensation heat transfer coefficients averaged over different time periods. (c) Variation of average local heat transfer coefficients with averaging time period.

-falling films also exhibit complex interfacial waviness, any wall temperature fluctuations resulting from these waves are greatly reduced by the relatively large thickness of a free-falling film compared to the much smaller thickness of a shear-driven film in annular condensing flows. Interfacial waves in the latter are felt immediately at the wall, while waves in falling films are more remote from the wall.

Hence, it is important to assess the significance of the relatively large fluctuations in Fig. 8.9(a) by time-averaging the computed heat transfer coefficient results. An averaging time period is defined as

$$\tau = \frac{L}{U_{g,in}},\tag{8.4}$$

where L = 0.8 m is the modeled condensation length and $U_{g,in}$ the inlet vapor velocity of the superheated FC-72. The local condensation heat transfer coefficient is averaged over period τ according to relation

$$\overline{h}(z) = \frac{1}{\tau}\int_0^\tau h(z,t)\,dt.\tag{8.5}$$

Figure 8.9(b) shows heat transfer coefficient plots averaged over periods τ, 2τ and 3τ. Notice the gradual decline in fluctuations that result from increasing the averaging period. Figure 8.9(c) shows the spatial average of the heat transfer coefficient over the region 0.2 m $< z <$ 0.8 m is fairly insensitive to averaging period. This proves that the spatial average of the heat transfer coefficient is captured quite consistently, even on an instantaneous basis. This is especially important given the large computational time required to compute an average over a very long period.

Figures 8.10(a), 8.10(b), 8.10(c) and 8.10(d) compare axial variations of the computed local condensation heat transfer coefficient, time-averaged over period τ, to experimentally
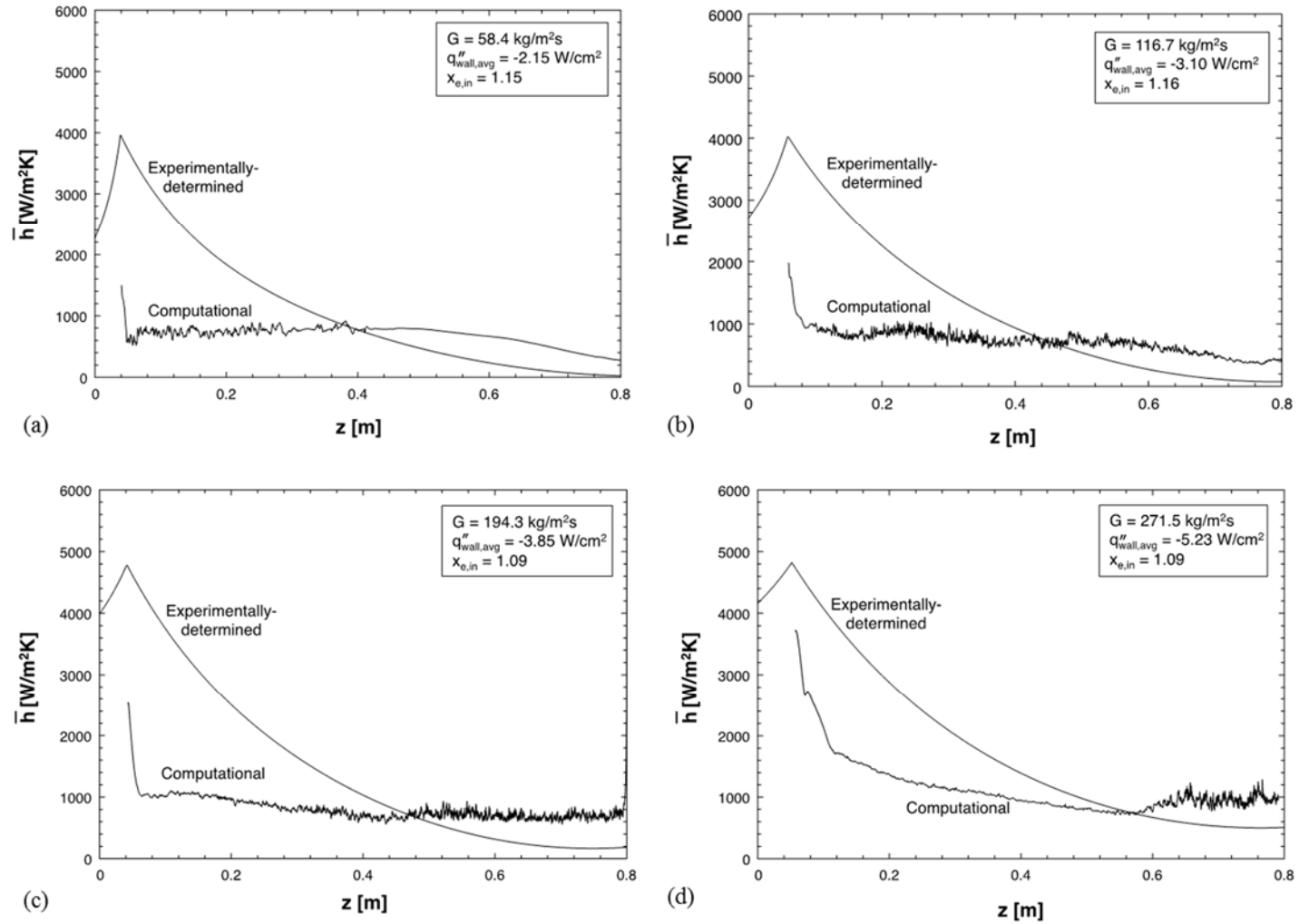
Fig. 8.10: Comparison of experimental and computed local condensation heat transfer coefficients for (a) $G = 58.4$ kg/m^{2}s, (b) $G = 116.7$ kg/m^{2}s, (c) $G = 194.3$ kg/m^{2}s, and (d) $G = 271.5$ kg/m^{2}s.

-determined variations for four FC-72 mass velocities of G = 58.4, 116.7, 194.3, and 271.5 kg/m^{2}s, respectively. As indicated earlier, the computations are initiated where x_e = 0 rather than the superheated inlet. Overall, there is fair agreement in the downstream region but not the inlet region. Additionally, predictions in the downstream region appear to improve with increasing mass velocity, with G = 271.5 kg/m^{2}s showing the best downstream agreement. Overall, local values are under-predicted upstream and over-predicted downstream for all mass velocities. The deviation between the experimental and computational results can be attributed to the inability of the computational model to accurately capture film thickness and turbulence in the inlet region, while doing a better job as the film gets thicker. In the inlet region, as discussed earlier, the phase change model is not able to initiate the liquid film, leading the authors to use an initial film thickness, δ_i, which affects the accuracy in this region. Nonetheless, the computational model is able to capture the spatially averaged measured values over the region 0.2 m $<$ z $<$ 0.8 m quite well as shown in Fig. 8.11.

8.3.3 Wall and Film Temperature Results

Figures 8.12(a), 8.12(b), 8.12(c) and 8.12(d) compare axial variations of computed local time-averaged wall temperature with experimental data for G = 58.4, 116.7, 194.3, and 271.5 kg/m^{2}s, respectively. The time-averaging period is the same as that used for the heat transfer plots in Figs. 8.10(a) to 8.10(d). For all four cases, the experimental wall temperatures exhibit an almost linear decline with z, while the computational result feature more significant variations, which under-predict the data upstream and over-predict downstream. When compared to the experimental data, predicted wall temperatures are
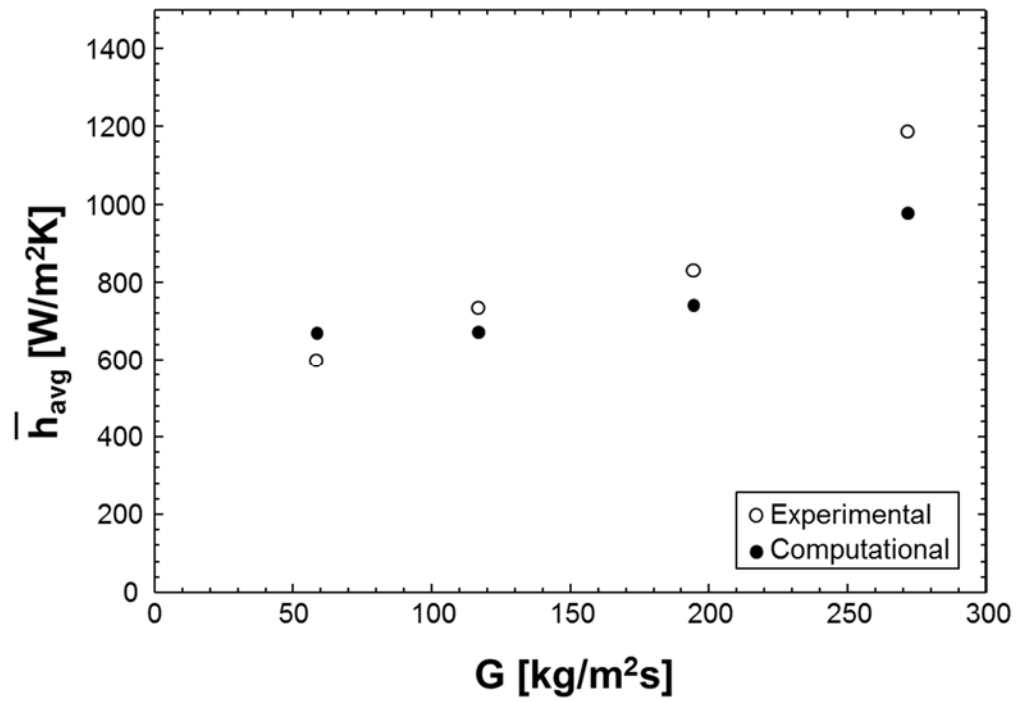
Fig. 8.11: Comparison of experimental and computed spatially averaged condensation heat transfer coefficient versus mass velocity.
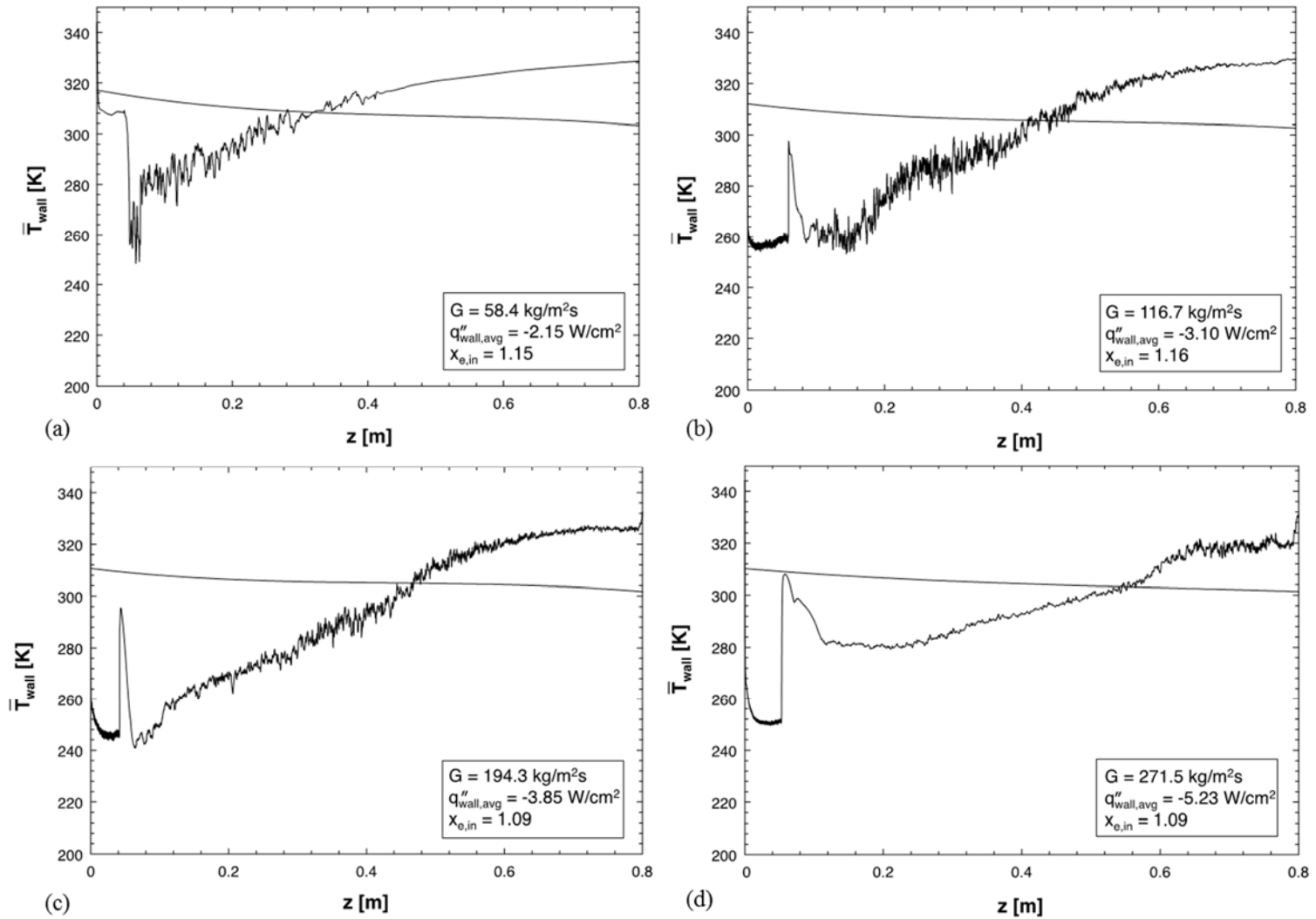
Fig. 8.12: Comparison of experimental and computed local wall temperature for (a) $G = 58.4$ kg/m^{2}s, (b) $G = 116.7$ kg/m^{2}s, (c) $G = 194.3$ kg/m^{2}s, and (d) $G = 271.5$ kg/m^{2}s.

seen to increase along the channel. The under prediction of heat transfer data in the inlet region and improvement in the downstream region, as discussed earlier, cause a similar trend in the predicted wall temperatures. However, as shown in Fig. 8.13, the computational model shows good accuracy in capturing the spatially averaged measured wall temperatures over the region 0.2 m $< z <$ 0.8 m.

Figures 8.14(a), 8.14(b), 8.14(c), and 8.14(d) show, for $G = 58.4$, 116.7, 194.3, and 271.5 kg/m^{2}s, respectively, temperature variations across the liquid and vapor phases at two axial locations of $z = 390$ and 590 mm. For the lowest flow rate of $G = 58.4$ kg/m^{2}s, Fig. 8.14(a), almost the entire cross-section is covered with liquid at both axial locations. Once the flow has changed phase completely to liquid, no more mass transfer can occur as heat is being extracted from the FC-72, which is why the saturation temperature is not achieved across the channel for this lowest mass velocity. Predicting complete phase change to liquid can also be in part a result of the mass intensity factor of $r_i = 10,000$ being too high for this low mass velocity. In both axial locations of $z = 390$ and 590 mm, the interfacial temperature for all three higher mass velocities of $G = 116.7$, 194.3 and 271.5 kg/m^{2}s is maintained within only $\pm$ 3°C of saturation temperature. Also for the same three mass velocities, there is an appreciable temperature drop across the liquid-vapor interface. Predicting a temperature across the vapor core close to saturation and capturing a temperature drop at the interface are both crucial to validating the phase change model. These same interfacial temperature trends were captured in Chapter 7 and also in the study by Lee *et al.* [100] to validate phase change models for falling film evaporation and downflow condensation, respectively. In Chapter 7, I reasoned that the large temperature drop across the liquid film interface is caused by interfacial dampening of eddy diffusivity
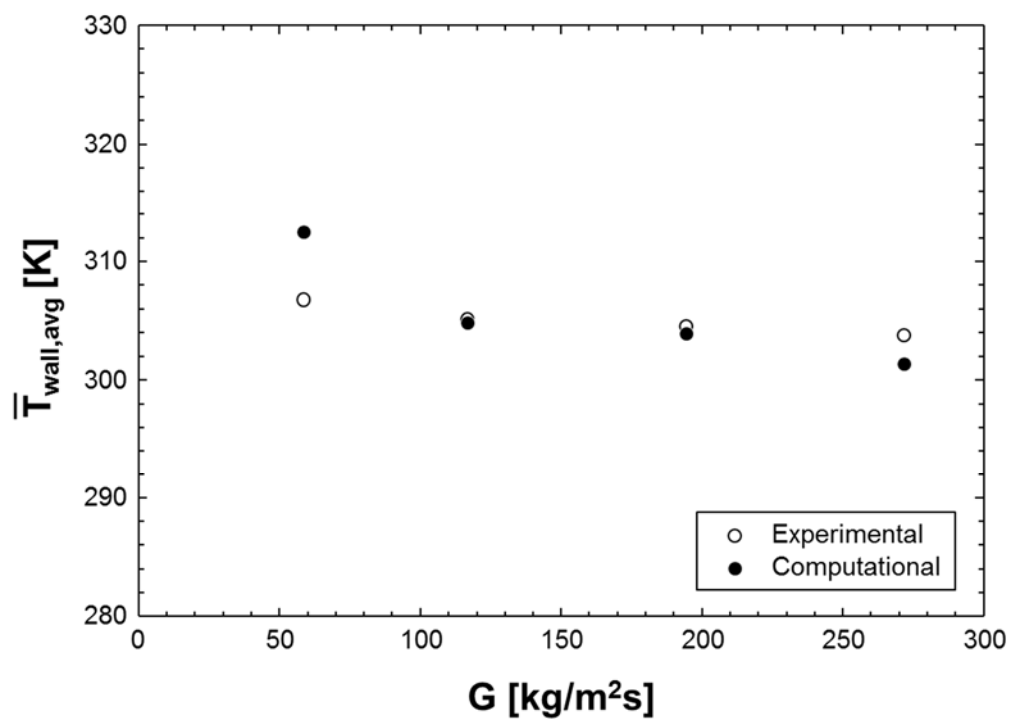
Fig. 8.13: Comparison of experimental and computed spatially averaged wall
temperature versus mass velocity.
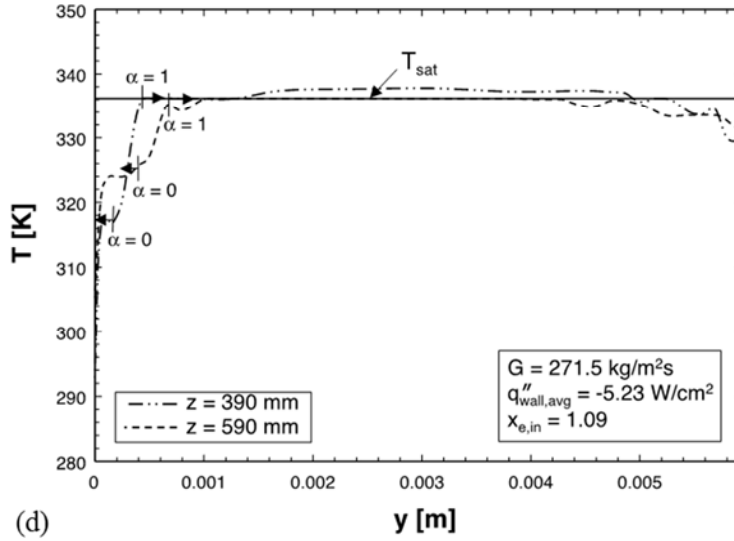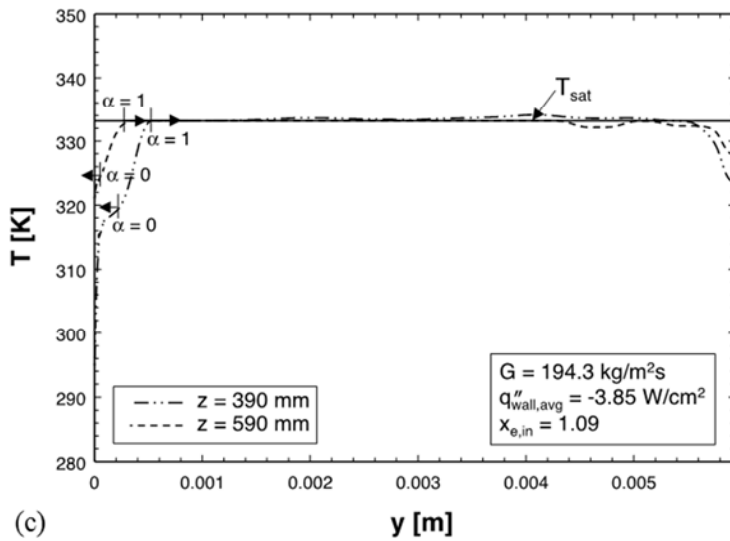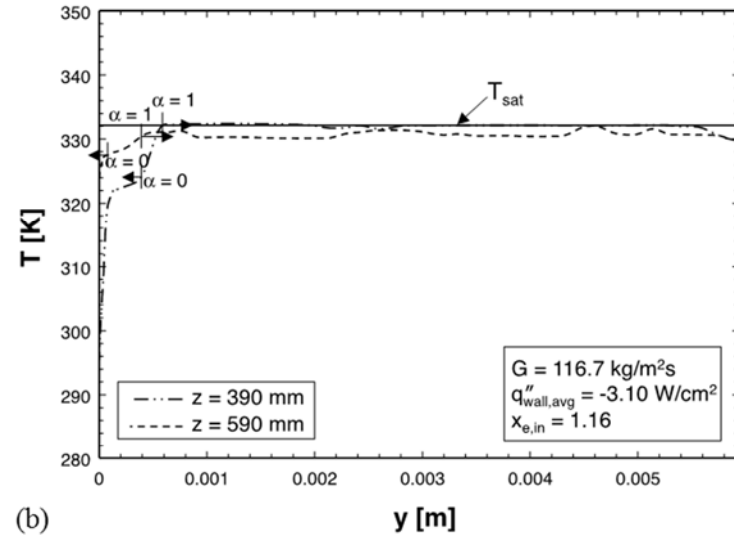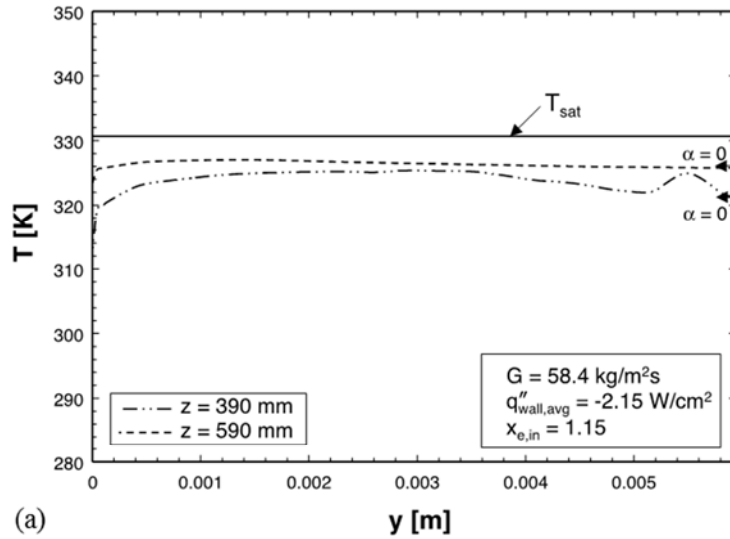
Fig. 8.14: Variation of computed fluid temperature with radial distance from the wall at two axial locations for (a) $G = 58.4$ kg/m^{2}s, (b) $G = 116.7$ kg/m^{2}s, (c) $G = 194.3$ kg/m^{2}s, and (d) $G = 271.5$ kg/m^{2}s.

due to surface tension. The temperature is seen to drop near the center of the channel and is lower than saturation temperature. As discussed in \relation to Fig. 8.6, this is caused by entrained liquid from the wall, where the temperature is lower than saturation, tending towards the center of the channel.

8.4 <u>Conclusions</u>

This study explored condensation of FC-72 in vertical upflow both experimentally and computationally. The computational model incorporates Lee's phase change model [73] in FLUENT and is used to predict variations of void fraction, condensation heat transfer coefficient, wall temperature and temperature profile across the liquid film. The key findings from the study are as follows.

(1) The computational model is capable of capturing the observed complex flow behavior across the condensing tube, including interfacial waviness, liquid entrainment in the vapor core and liquid deposition upon the film corresponding to flooding and climbing film conditions.

(2) The model under-predicts the local measured condensation heat transfer coefficient in the upstream region of the condensation tube and over-predicts downstream. However, the measured spatially averaged condensation heat transfer coefficient is captured with good accuracy.

(3) The model also under-predicts the local measured wall temperature in the upstream region of the condensation tube and over-predicts downstream. Nonetheless, the measured spatially averaged wall temperature is predicted quite accurately.

(4) Predicted film temperature profiles show an appreciable temperature gradient at the liquid-vapor interface while also maintaining saturation temperature in the vapor core, which help validate the effectiveness of Lee's phase change model [73] in capturing interfacial mass transfer.

(5) Further enhancement of predictive accuracy will acquire switching from 2-D to 3-D modeling. Equally important is the need for more sophisticated diagnostic tools to measure velocity field and temperature within the wall liquid film, as well as map the interfacial waviness of the film.

CHAPTER 9. FUTURE WORK

Researchers at the Purdue University Boiling and Two-Phase Flow Laboratory (PU-BTPFL) have been working in collaboration with the NASA Glenn Research Center to study the influence of gravity on both flow boiling and condensation. The present study investigated different phase change methods experimentally, theoretically and computationally, that are associated with this collaborative effort. Future studies are expected to accomplish the following tasks.

(1)   Assist collaborators from the NASA Glenn Research Center in conducting future parabolic flight experiments for flow condensation and flow boiling, as well as preparations for experiments onboard the International Space Station.

(2)   Investigate transient flow and thermal loop behavior to understand various flow instabilities observed in a two-phase flow loop.

(3)   Extend the computational models for evaporating falling films and flow condensation to study flow boiling, and investigate interfacial behavior and temperature profiles and compare predictions to experimental data. Use the extensive review in Appendix A to choose computational schemes that best meet the specific application requirement. An ultimate objective is working toward a possibility of being able to predict all complicated two-phase phenomena.

(4)	Develop new computational strategies in multiphase flows and phase change for flow boiling, flow condensation, evaporating falling films and film boiling.

LIST OF REFERENCES

LIST OF REFERENCES

[1]   I. Mudawar, Two-phase micro-channel heat sinks: theory, applications and limitations, J. Electronic Packaging - Trans. ASME 133 (2011) 041002.

[2]   P.J. Marto, V.J. Lepere, Pool boiling heat transfer from enhanced surfaces to dielectric fluids, J. Heat Transfer – Trans. ASME 104 (1982) 292-299.

[3]   I. Mudawar, T.M. Anderson, Optimization of extended surfaces for high flux chip cooling by pool boiling, J. Electronic Packaging- Trans. ASME 115 (1993) 89-100.

[4]   H.J. Lee, S.Y. Lee, Heat transfer correlation for boiling flows in small rectangular horizontal channels with low aspect ratios, Int. J. Multiphase Flow 27 (2001) 2043-2062.

[5]   S. Mukherjee, I. Mudawar, Smart pumpless loop for micro-channel electronic cooling using flat and enhanced surfaces, IEEE Transactions-CPMT: Components and Packaging Technologies 26 (2003) 99-109.

[6]   J. Lee, I. Mudawar, Low-temperature two-phase micro-channel cooling for high-heat-flux thermal management of defense electronics, IEEE Transactions-CPMT: Components and Packaging Technologies 32 (2009) 453-465.

[7]   M. Monde, T. Inoue, Critical heat flux in saturated forced convective boiling on a heated disk with multiple impinging jets, J. Heat Transfer – Trans. ASME 113 (1991) 722-727.

[8]   D.C. Wadsworth, I. Mudawar, Enhancement of single-phase heat transfer and critical heat flux from an ultra-high-flux-source to a rectangular impinging jet of dielectric liquid, J. Heat Transfer – Trans. ASME 114 (1992) 764-768.

[9]   D.D. Hall, I. Mudawar, Experimental and numerical study of quenching complex-shaped metallic alloys with multiple, overlapping sprays, Int. J. Heat Mass Transfer 38 (1995) 1201-1216.

[10]   L. Lin, R. Ponnappan, Heat transfer characteristics of spray cooling in a closed loop, Int. J. Heat Mass Transfer 46 (2003) 3737-3746.

[11]   M. Visaria, I. Mudawar, Theoretical and experimental study of the effects of spray orientation on two-phase spray cooling and critical heat flux, Int. J. Heat Mass Transfer 51 (2008) 2398-2410.

[12]   M.K. Sung, I. Mudawar, Experimental and numerical investigation of single-phase heat transfer using a hybrid jet-impingement/micro-channel cooling scheme, Int. J. Heat Mass Transfer 49 (2006) 682-694.

[13]   D.D. Hall, I. Mudawar, Ultra-high critical heat flux (CHF) for subcooled water flow boiling - II. High-CHF database and design parameters, Int. J. Heat Mass Transfer 42 (1999) 1429-1456.

[14]   F.P. Chiaramonte, J.A. Joshi, Workshop on critical issues in microgravity fluids, transport, and reaction processes in advanced human support technology - final report, NASA TM-2004-212940, 2004.

[15]   The National Academies, Recapturing a future for space exploration: life and physical sciences research for a new era, National Academies Press, Washington, DC, 2011.

[16]   A.E. Dukler, J.A. Fabre, J.B. McQuillen, R. Vernon, Gas-liquid flow at microgravity conditions: flow patterns and their transitions, Int. J. Multiphase Flow 14 (1988) 389-400.

[17] C. Colin, A. Kamp, J. Fabre, Influence of gravity on void distribution in two-phase gas-liquid flow in pipe, Advances Space Research 13 (1993) 141-145.

[18]   T.R. Reinarts, Adiabatic two phase flow regime data and modeling for zero and reduced (horizontal flow) acceleration fields, Ph.D. thesis, Texas A&M University, TX, 1993.

[19]   W.S. Bousman, Studies of two-phase gas-liquid flow in microgravity, Ph.D. thesis, University of Houston, TX, 1994.

[20]   W.S. Bousman, J.B. McQuillen, L.C. Witte, Gas-liquid flow patterns in microgravity: Effects of tube diameter, liquid viscosity and surface tension, Int. J. Multiphase Flow 22 (1996), 1035-1053.

[21]   B. Choi, T. Fujii, H. Asano, K. Sugimoto, A study of gas-liquid two-phase flow in a horizontal tube under microgravity, Annals N.Y. Acad. Sci. 974 (2002) 316-327.

[22]   M. Misawa, An experimental and analytical investigation of flow boiling heat transfer under microgravity conditions, Ph.D. thesis, University of Florida, 1993.

[23]   M. Saito, N. Yamaoka, K. Miyazaki, M. Kinoshita, Y. Abe, Boiling two-phase flow under microgravity, Nuclear Engng Design 146 (1994) 451-461.

[24]   H. Ohta, Experiments on microgravity boiling heat transfer by using transparent heaters, Nuclear Engng Design 175 (1997) 167-180.

[25]   D. Brutin, V.S. Ajaev, L. Tadrist, Pressure drop and void fraction during flow boiling in rectangular minichannels in weightlessness, Appl. Thermal Engng 51 (2013) 1317-1327.

[26]   Y. Ma, J.N. Chung, An experimental study of critical heat flux (CHF) in microgravity forced-convection boiling, Int. J. Multiphase Flow 27 (2001) 1753-1767.

[27]   A.H. Howard, I. Mudawar, Orientation effects on pool boiling CHF and modeling of CHF for near-vertical surfaces, Int. J. Heat Mass Transfer 42 (1999) 1665-1688.

[28]   H. Zhang, I. Mudawar, M.M. Hasan, CHF model for subcooled flow boiling in Earth gravity and microgravity, Int. J. Heat Mass Transfer 50 (2007) 4039-4051.

[29]   H. Zhang, I. Mudawar, M.M. Hasan, 2007, Assessment of dimensionless CHF correlations for subcooled flow boiling in microgravity and reduced gravity, Int. J. Heat Mass Transfer 50 (2007) 4568-4580.

[30]   C. Konishi, H. Lee, I. Mudawar, M.M. Hasan, H.K. Nahra, N.R. Hall, J.D. Wagner, R.L. May, J.R. Mackey, Flow boiling in microgravity: part 1 – Interfacial behavior and experimental heat transfer results, Int. J. Heat Mass Transfer 81 (2015) 705-720.

[31]   C. Konishi, H. Lee, I. Mudawar, M.M. Hasan, H.K. Nahra, N.R. Hall, J. D. Wagner, and R. L. May, J. R. Mackey, Flow boiling in microgravity: part 2 – Critical heat flux interfacial behavior, experimental data, and model, Int. J. Heat Mass Transfer 81 (2015) 721-736.

[32] J.C. Sturgis, I. Mudawar, Critical heat flux in a long, rectangular channel subjected to one-sided heating - I. Flow visualization, Int. J. Heat Mass Transfer 42 (1999) 1835-1847.

[33] J.C. Sturgis, I. Mudawar, Critical heat flux in a long, rectangular channel subjected to one-sided heating - II. Analysis of CHF data, Int. J. Heat Mass Transfer 42 (1999) 1849-1862.

[34] C.R. Kharangate, I. Mudawar, M.M. Hasan, Photographic study and modeling of critical heat flux in horizontal flow boiling with inlet vapor void, Int. J. Heat Mass Transfer 55 (2012) 4154-4168.

[35] C.R. Kharangate, I. Mudawar, M.M. Hasan, Experimental and theoretical study of critical heat flux in vertical upflow with inlet vapor void, Int. J. Heat Mass Transfer 55 (2012) 360-374.

[36] W.M. Rohsenow, A method of correlating heat transfer data for surface boiling liquids, Trans. ASME 74 (1952) 969–978.

[37] S. Levy, Prediction of the critical heat flux in forced convection flow, GEAP-3961, General Electric Co., San Jose, CA, 1962.

[38] W.R. Gambill, Generalized prediction of burnout heat flux for flowing, subcooled, wetting liquids, Chem. Eng. Prog. Symp. Ser. 59 (1963) 71–87.

[39] B.P. Avksentyuk, Critical feat fluxes with forced flow of subcooled and saturated liquids, Therm. Eng. 35 (1988) 694–697.

[40] M. Siman-Tov, W.R. Gambill, W.R. Nelson, A.E. Ruggles, G.L.Yoder, Thermal-hydraulic correlations for the advanced neutron source reactor fuel element design and analysis, in: Y.A. Hassan, L.E. Hochreiter (Eds.), Nuclear reactor thermal-hydraulics, ASME HTD, Vol. 190, 1991, pp. 63–78.

[41] Y. Katto, H. Ohno, An improved version of the generalized correlation of critical heat flux for the forced convective boiling in uniformly heated vertical tubes, Int. J. Heat Mass Transfer 27 (1984) 1641-1648.

[42] D.C. Groeneveld, L.K.H. Leung, P.L. Kirillov, V.P. Bobkov, I.P. Smogalev, V.N. Vinogradov, X.C. Huang, E. Royer, The 1995 look-up table for critical heat flux in tubes, Nuclear Engineering Design 163 (1996) 1-23.

[43]   D.D. Hall, I. Mudawar, Critical heat flux (CHF) for water flow in tubes - I. Compilation and assessment of world CHF data, Int. J. Heat Mass Transfer 43 (2000) 2573-2604.

[44]   D.D. Hall, I. Mudawar, Critical heat flux (CHF) for water flow in tubes - II. Subcooled CHF correlations, Int. J. Heat Mass Transfer 43 (2000) 2605-2640.

[45]   C. Konishi, I. Mudawar, Review of flow boiling and critical heat flux in microgravity, Int. J. Heat Mass Transfer 80 (2015) 469-493.

[46]   S.S. Kutateladze, A.I. Leont'ev, Some applications of the asymptotic theory of the turbulent boundary layer, Proc. 3rd Int. Heat Transfer Conf., Vol. 3, Chicago, Illinois, 1966, pp. 1–6.

[47]   J. Weisman, B.S. Pei, Prediction of critical heat flux in flow boiling at low qualities, Int. J. Heat Mass Transfer 26 (1983) 1463–1477.

[48]   C.H. Lee, I. Mudawar, A mechanistic critical heat flux model for subcooled flow boiling based on local bulk flow conditions, Int. J. Multiphase Flow 14 (1988) 711–728.

[49]   J.E. Galloway, I. Mudawar, CHF mechanism in flow boiling from a short heated wall-part 1. Examination of near-wall conditions with the aid of photomicrography and high-speed video imaging, Int. J. Heat Mass Transfer 36 (1993) 2511–2526.

[50]   J.E. Galloway, I. Mudawar, CHF mechanism in flow boiling from a short heated wall-part 2. Theoretical CHF model, Int. J. Heat Mass Transfer 36 (1993) 2527–2540.

[51]   D.E. Maddox, I. Mudawar, Single- and two-phase convective heat transfer from smooth and enhanced microelectronic heat sources in a rectangular channel, J. Heat Transfer-Trans. ASME 111 (1989) 1045-1052.

[52]   T.C. Willingham, I. Mudawar, Forced-convection boiling and critical heat flux from a linear array of discrete heat sources, Int. J. Heat Mass Transfer 35 (1992) 2879-2890.

[53]   H. Zhang, I. Mudawar, M.M. Hasan, Experimental and theoretical study of orientation on flow boiling CHF, Int. J. Heat Mass Transfer 45 (2002) 4463-4477.

[54] C. Konishi, I. Mudawar, M.M. Hasan, Investigation of the influence of orientation on critical heat flux for flow boiling with two-phase inlet, Int. J. Heat Mass Transfer 61 (2013) 176-190.

[55] H. Zhang, I. Mudawar, M.M. Hasan, Investigation of interfacial behavior during the flow boiling CHF transient, Int. J. Heat Mass Transfer 47 (2004) 1275-1288.

[56] H. Zhang, I. Mudawar, M.M. Hasan, Flow boiling CHF in microgravity, Int. J. Heat Mass Transfer 48 (2005) 3107-3188.

[57] W. Wilke, Wärmeübergang an rieselfilme, VDI Forschungsheft 490 (1962) 1-36.

[58] G.J. Gimbutis, A.J. Drobacivius, S.S. Sinkunas, Heat transfer of a turbulent water film at different initial flow conditions and high temperature gradients, Proc. 6th Int. Heat Transfer Conf., Vol. 1, Toronto, Canada, pp. 321-326, 1978.

[59] J.A. Shmerler, I. Mudawar, Local heat transfer coefficient in wavy free-falling turbulent liquid films undergoing uniform sensible heating, Int. J. Heat Mass Transfer 31 (1988) 67-77.

[60] N.M. Al-Najem, K.Y. Ezuddin, M.A. Darwish, Heat transfer analysis of preheated turbulent falling films in vertical tube evaporators, Desalination 115 (1998) 43-55.

[61] X. Ye, W. Yan, Z. Jiang, C. Li, Hydrodynamics of free-falling turbulent wavy films and implications for enhanced heat transfer, Heat Transfer Engng 23 (2002) 48-60.

[62] K.R. Chun, R.A. Seban, Heat transfer to evaporating liquid films, J. Heat Transfer – Trans. ASME 93 (1971) 391-396.

[63] J.A. Shmerler, I. Mudawar, Local evaporative heat transfer coefficient in turbulent free-falling liquid films, Int. J. Heat Mass Transfer 31 (1988) 731-742.

[64] H. Struve, Der wärmeübergang an einen verdampfenden rieselfilm, VDI Forschungsheft Hft, 1969.

[65] T. Fujita, T. Ueda, Heat transfer to falling films and film breakdown-II, Int. J. Heat Mass Transfer 21 (1978) 109-118.

[66] I. Park, S. Kim, I. Mudawar, Experimental measurement and modeling of downflow condensation in a circular tube, Int. J. Heat Mass Transfer 57 (2013) 567–581.

[67] I. Park, I. Mudawar, Climbing film, flooding and falling film behavior in upflow condensation in tubes, Int. J. Heat Mass Transfer 65 (2013) 44-61.

[68] F. Gibou, L. Chen, D. Nguyen, S. Banerjee, A level set based sharp interface method for the multiphase incompressible Navier–Stokes equations with phase change, J. Computational Physics 222 (2007) 536–555.

[69] R.W. Schrage, A theoretical study of interphase mass transfer, Columbia University Press, New York, 1953.

[70] M. Knudsen, The kinetic theory of gases. Some modern aspects, Methuen's Monographs on Physical Subjects, London, UK, 1934.

[71] R. Marek, J. Straub, Analysis of the evaporation coefficient and the condensation coefficient of water, Int. J. Heat Mass Transfer 44 (2001) 39–53.

[72] I. Tanasawa, Advances in condensation heat transfer, in Advances in heat transfer, J.P. Hartnett, T.F. Irvine, eds., Academic Press, San Diego, CA, 1991.

[73] W.H. Lee, A pressure iteration scheme for two-phase flow modeling, in Multiphase transport fundamentals, reactor safety, applications, T.N. Veziroglu, ed., Vol. 1, Hemisphere Publishing, Washington, DC, 1980.

[74] W. Qu, I. Mudawar, S.-Y. Lee, S.T. Wereley, Experimental and computational investigation of flow development and pressure drop in a rectangular micro-channel, J. Electronic Packaging – Trans. ASME 128 (2006) 1-9.

[75] T.H. Lyu, I. Mudawar, I., Statistical investigation of the relationship between interfacial waviness and sensible heat transfer to a falling liquid film, Int. J. Heat Mass Transfer 34 (1991) 1451-1464.

[76] M.S. Bhatti, R.K. Shah, Turbulent and transitional convective heat transfer in ducts, in Handbook of single-phase convective heat transfer, S. Kakac, R.K. Shah, W. Aung, eds., John Wiley and Sons, NY, 1987.

[77] J.E. Galloway, I. Mudawar, Critical heat flux enhancement by means of liquid subcooling and centrifugal force induced by flow curvature, Int. J. Heat Mass Transfer 35 (1992) 1247-1260.

[78]   J.E. Galloway, I. Mudawar, A theoretical model for flow boiling CHF from concave heaters, J. Heat Transfer – Trans. ASME 117 (1995) 698-707.

[79]   C.O. Gersey, I. Mudawar, Effects of heater length and orientation on the trigger mechanism for near-saturated flow boiling CHF - I. Photographic and statistical characterization of the near-wall interfacial features, Int. J. Heat Mass Transfer 38 (1995) 629-642.

[80]   C.O. Gersey, I. Mudawar, Effects of heater length and orientation on the trigger mechanism for near-saturated flow boiling CHF - II. CHF model, Int. J. Heat Mass Transfer 38 (1995) 643-654.

[81]   J.C. Sturgis, I. Mudawar, Critical heat flux in a long, curved channel subjected to concave heating, Int. J. Heat Mass Transfer 42 (1999) 3831-3848.

[82]   J.C. Sturgis, I. Mudawar, Assessment of CHF enhancement mechanisms in a curved, rectangular channel subjected to concave heating, J. Heat Transfer – Trans. ASME 121 (1999) 394-404.

[83]   H. Zhang, I. Mudawar, M.M. Hasan, Experimental assessment of the effects of body force, surface tension force, and inertia on flow boiling CHF, Int. J. Heat Mass Transfer 45 (2002) 4079-4095.

[84]   H. Lamb, Hydrodynamics, 6th ed., Dover Publications, NY, 1945.

[85]   L. M. Milne-Thompson, Theoretical hydrodynamics, 4th ed., Macmillan, NY, 1960.

[86]   ANSYS FLUENT 12.1 in Workbench User's Guide. ANSYS Inc., Canonsburg, PA, 2009.

[87]   C.W. Hirt, B.D. Nichols, Volume of fluid (VOF) method for the dynamics of free boundary, J. Computational Physics 39 (1981) 201–225.

[88]   S. Hardt, F. Wondra, Evaporation model for interfacial flows based on a continuum-field representation of the source terms, J. Computational Physics 227 (2008) 5871–5895.

[89]   M. Magnini, B. Pulvirenti, J.R. Thome, Numerical investigation of hydrodynamics and heat transfer of elongated bubbles during flow boiling in a microchannel, Int. J. Heat Mass Transfer 59 (2013) 451–471.

[90] J.W. Rose, On interphase matter transfer, the condensation coefficient and dropwise condensation, Proc. Royal Society of London A 411 (1987) 305–311.

[91] O. Kartuzova, M. Kassemi, Modeling interfacial turbulent heat transfer during ventless pressurization of a large scale cryogenic storage tank in microgravity, 47th AIAA/ASME/SAE/ASEE Joint Propulsion Conf. & Exhibit, San Diego, CA, 2011.

[92] N. Mascharehnas, I. Mudawar, Investigation of eddy diffusivity and heat transfer coefficient for free-falling turbulent liquid films subjected to sensible heating, Int. J. Heat Mass Transfer 64 (2013) 647–660.

[93] E.R. Van Driest, On turbulent flow near a wall, J. Aeronautical Sciences 23 (1956) 1007-1011.

[94] W.M. Kays, Heat transfer to the transpired turbulent boundary layer, Int. J. Heat Mass Transfer 15 (1972) 1023-1044.

[95] W.M. Kays, M.E. Crawford, Convective heat and mass transfer, 2nd ed., McGraw-Hill, New York, 1980.

[96] A.F. Mills, D.K. Chung, Heat transfer across turbulent falling films, Int. J. Heat Mass Transfer 16 (1973) 694-696.

[97] R.A. Seban, A. Faghri, Evaporation and heating with turbulent falling liquid films, J. Heat Transfer - ASME Trans. 98 (1976) 315-318.

[98] G.L. Hubbard, A.F. Mills, D.K. Chung, Heat transfer across a turbulent falling film with concurrent vapour flow, J. Heat Transfer – ASME Trans. 98 (1976) 319-320.

[99] I. Mudawar, M.A. El-Masri, Momentum and heat transfer across freely-falling turbulent liquid films, Int. J. Multiphase Flow 12 (1986) 771-790.

[100] H. Lee, C.R. Kharangate, N. Mascharehnas, I. Park, I. Mudawar, Experimental and computational investigation of vertical downflow condensation, Int. J. Heat Mass Transfer 85 (2015) 865–879.

[101] H. Lee, I. Mudawar, M.M. Hasan, Experimental and theoretical investigation of annular flow condensation in microgravity, Int. J. Heat Mass Transfer 61 (2013) 293-309.

[102] M. Mattson, K. Mahesh, Simulation of bubble migration in a turbulent boundary layer, Physics of Fluids, 23 (2011) 045107.

[103] S. Mortazavi, G. Tryggvason, A numerical study of motion of drops in Poiseuille flow. Part 1. Lateral migration of one drop, J. Fluid Mech. 411 (2000) 325-350.

[104] G.B. Wallis, Flooding velocities for air and water in vertical tubes, No. AEEW-R-123, United Kingdom Atomic Energy Authority, Reactor Group, Atomic Energy Establishment, Winfrith, Dorset, England, 1961.

[105] I. Mudawar, Assessment of high-heat-flux thermal management schemes, IEEE Trans.-CPMT: Components Packaging Technologies 24 (2001) 122–141.

[106] I. Mudawar, Recent advances in high-flux, two-phase thermal management, J. Thermal Science Engng Applications – Trans. ASME 5 (2013) 021012.

[107] I. Mudawar, T.M. Anderson, Optimization of extended surfaces for high flux chip cooling by pool boiling, J. Electronic Packaging - Trans. ASME 115 (1993) 89-100.

[108] S. Mukherjee, I. Mudawar, Pumpless loop for narrow channel and micro-channel boiling from vertical surfaces, J. Electronic Packaging – Trans. ASME 125 (2003) 431-441.

[109] J. Lee, I. Mudawar, Critical heat flux for subcooled flow boiling in micro-channel heat sinks, Int. J. Heat Mass Transfer 52 (2009) 3341-3352.

[110] M.E. Johns, I. Mudawar, An ultra-high power two-phase jet-impingement avionic clamshell module, J. Electronic Packaging – Trans. ASME 118 (1996) 264-270.

[111] J.W. Rose, Dropwise condensation theory and experiment: a review, J. Power Energy 216 (2002) 115-128.

[112] K.A. Swensen, Further studies in filmwise condensation of steam on horizontal finned tubes, Masters Thesis, Naval Postgraduate School, Monterey, CA, 1992.

[113] J.R. Thome, Condensation in plain horizontal tubes: recent advances in modelling of heat transfer to pure fluids and mixtures, J. Brazilian Society Mech. Sciences Engng 27 (2005) 23-30.

[114] M.M. Shah, An improved and extended general correlation for heat transfer during condensation in plain tubes, HVAC&R Research 15 (2009) 889-913.

[115] S.M. Kim, I. Mudawar, Universal approach to predicting two-phase frictional pressure drop for adiabatic and condensing mini/micro-channel flows, Int. J. Heat Mass Transfer 55 (2012) 3246–3261.

[116] S.M. Kim, I. Mudawar, Universal approach to predicting heat transfer coefficient for condensing mini/micro-channel flows, Int. J. Heat Mass Transfer 56 (2013) 238–250.

[117] S.M. Kim, I. Mudawar, Theoretical model for annular flow condensation in rectangular micro-channels, Int. J. Heat Mass Transfer 55 (2012) 958-970.

[118] S.M. Kim, I. Mudawar, Theoretical model for local heat transfer coefficient for annular flow boiling in circular mini/micro-channels, Int. J. Heat Mass Transfer 73 (2014) 731-742.

[119] G. Ryskin, L.G. Leal, Numerical solution of free-boundary problems in fluid mechanics. Part 2. Buoyancy-driven motion of a gas bubble through a quiescent liquid, J. Fluid Mechanics 148 (1984) 19-35.

[120] S. Takagi, Y. Matsumoto, Three-dimensional deformation of a rising Bubble, Proc. German-Japanese Symp. on Multi-Phase Flow, Karlsruhe, Germany, pp. 499-511, 1994.

[121] P.J. Shopov, P.D. Minev, I.B. Bazhekov, Z.D. Zapryanov, Interaction of a deformable bubble with a rigid wall at moderate Reynolds numbers, J. Fluid Mechanics 219 (1990) 241-271.

[122] J. Fukai, Y. Shiiba, T. Yamamoto, O. Miyatake, D. Poulikakos, C.M. Megaridis, Z. Zhao, Wetting effects on the spreading of a liquid droplet colliding with a flat surface: experiment and modeling, Physics Fluids 7 (1995) 236-247.

[123] M. Sussman, P. Smereka, S. Osher, A level set approach for computing solutions to incompressible two-phase flows, J. Computational Physics 114 (1994) 146-159.

[124] M. Rudman, Volume-tracking methods for interfacial flow calculations, Int. J. Numerical Methods Fluids 24 (1997) 671-691.

[125] O. Ubbink, R.I. Issa, A method for capturing sharp fluid interfaces on arbitrary meshes, J. Computational Physics 153 (1999) 26-50.

[126] W.F. Noh, P. Woodward, SLIC (simple line interface calculation), in Proc. Fifth Int. Conf. Numerical Methods in Fluid Dynamics, Twente University, Enschede, pp. 330-340, 1976.

[127] D.L. Youngs, Time-dependent multi-material flow with large fluid distortion, in Numerical methods for fluid dynamics, K.W. Morton and M.J. Baines (Eds.), Academic Press, New York pp. 273-285, 1982.

[128] W.J. Rider, D.B. Kothe, Reconstructing volume tracking, J. Computational Physics 141 (1998) 112-152.

[129] D.J. Benson, Volume of fluid interface reconstruction methods for multi-material problems, Applied Mechanics Reviews 55 (2002) 151–165.

[130] G.R. Price, G.T. Reader, R.D. Rowe, J.D. Bugg, A piecewise parabolic interface calculation for volume tracking, Proc. Sixth Annual Conf. of CFD Society of Canada, University of Victoria, Victoria, British Columbia, Vol. 11, pp. 9-14, 1998.

[131] I. Ginzburg, G. Wittum, Two-phase flows on interface refined grids modeled with VOF, staggered finite volumes, and spline interpolants, J. Computational Physics 166 (2001) 302–335.

[132] G. Russo, P. Smereka, A remark on computing distance functions, J. Computational Physics 163 (2000) 51-67.

[133] Y.C. Chang, T.Y. Hou, B. Merriman, S. Osher, A level set formulation of Eulerian interface capturing methods for incompressible fluid flows, J. Computational Physics 124 (1996) 449-464.

[134] Y. Zhang, Q. Zou, D. Greaves, Numerical simulation of free-surface flow using the level-set method with global mass correction, Int. J. Numerical Methods Fluids 63 (2010) 651-680.

[135] G. Son, V.K. Dhir, Numerical simulation of film boiling near critical pressures with a level-set method, J. Heat Transfer – Trans. ASME 120 (1998) 183–192.

[136] R.P. Fedkiw, T. Aslam, B. Merriman, S. Osher, A non-oscillatory Eulerian approach to interfaces in multimaterial flows (the ghost fluid method), J. Computational Physics 152 (1999) 457–492.

[137] M. Kang, R.P. Fedkiw, X.-D. Liu, A Boundary condition capturing method for multiphase incompressible flow, J. Scientific Computing 15 (2000) 323–360.

[138] M. Sussman, E.G. Puckett, A coupled level set and volume-of-fluid method for computing 3D and axisymmetric incompressible two-phase flows, J. Computational Physics 162 (2000) 301–337.

[139] D. Enright, R. Fedkiw, J. Ferziger, I. Mitchell, A hybrid particle level set method for improved interface capturing, J. Computational Physics 183 (2002) 83–116.

[140] D.L. Sun, W.Q. Tao, A coupled volume-of-fluid and level set (VOSET) method for computing incompressible two-phase flows, Int. J. Heat and Mass Transfer 53 (2010) 645–655.

[141] J. Glimm, J.W. Grove, X.L. Li, W. Oh, D.H. Sharp, A critical analysis of Rayleigh–Taylor growth rates, J. Computational Physics 169 (2001) 652-677.

[142] S.O. Unverdi, G. Tryggvason, A front-tracking method for viscous, incompressible, multi-fluid flows, J. Computational Physics 100 (1992) 25–37.

[143] G. Tryggvason, B. Bunner, A. Esmaeeli, D. Juric, N. Al-Rawahi, W. Tauber, J. Han, S. Nas, Y.-J. Jan, A front-tracking method for the computations of multiphase flow, J. Computational Physics 169 (2001) 708–759.

[144] M.R.H. Nobari, G. Tryggvason, Numerical simulations of three-dimensional drop collisions, AIAA J. 34 (1996) 750-755.

[145] T. Yabe, F. Xiao, T. Utsumi, The constrained interpolation profile (CIP) method for multiphase analysis, Computational Physics 169 (2001) 556-593.

[146] D. Jacqmin, Calculation of two-phase Navier–Stokes flows using phase-field modeling, J. Computational Physics 155 (1999) 96-127.

[147] Y.Y. Yan, Y.Q. Zu, A lattice Boltzmann method for incompressible two-phase flows on partial wetting surface with large density ratio, J. Computational Physics 227 (2007) 763-775.

[148] Y.Y. Yan, Y.Q. Zu, Numerical modelling based on lattice Boltzmann method of the behaviour of bubbles flow and coalescence in microchannels, Proc. 6th Int. Conf. on Nanochannels, Microchannels, and Minichannels, Darmstadt, Germany, pp. 313-319, 2008.

[149] J.U. Brackbill, D.B. Kothe, C. Zemach, A continuum method for modeling surface tension, J. Computational Physics 100 (1992) 335–354.

[150] C.S. Peskin, Numerical analysis of blood flow in the heart, J. Computational Physics 25 (1977) 220-252.

[151] B. Lafaurie, C. Nardone, R. Scardovelli, S. Zaleski, G. Zanetti, Modelling merging and fragmentation in multiphase flows with SURFER, J. Computational Physics 113 (1994) 134–147.

[152] Y. Renardy, M. Renardy, PROST: A parabolic reconstruction of surface tension for the volume-of-fluid method, J. Computational Physics 183 (2002) 400-421.

[153] E. Aulisa, S. Manservisi, R. Scardovelli, A novel representation of the surface tension force for two-phase flow with reduced spurious currents, Computational Methods Applied Mechanical Engng 195 (2006) 6239-6257.

[154] S. Shin and D. Juric, Modeling three-dimensional multiphase flow using a level contour reconstruction method for front tracking without connectivity, J. Computational Physics 180 (2002) 427-470.

[155] B.A. Nichita, J.R. Thome, A level set method and a heat transfer model implemented into FLUENT for modeling of microscale two phase flows, AVT-178 Specialists' Meeting on System Level Thermal Management for Enhanced Platform Efficiency, Bucharest, Romania, 2010.

[156] H. Ganapathy, A. Shooshtari, K. Choo, S. Dessiatoun, M. Alshehhi, M. Ohadi, Volume of fluid-based numerical modeling of condensation heat transfer and fluid flow characteristics in microchannels, Int. J. Heat Mass Transfer 65 (2013) 62–72.

[157] D. Sun, J. Xu, and L. Wang, Development of a vapor–liquid phase change model for volume-of-fluid method in FLUENT, Int. Communications Heat Mass Transfer 39 (2012) 1101–1106.

[158] B. Paul, Complication of evaporation coefficient, American Rocket Soc. J. 32 (1962) 1321-1328.

[159] H. Wang, S.V. Garimella, J.Y. Murthy, Characteristics of evaporating thin film in a microchannel, Int. J. Heat Mass Transfer 50 (2007) 3933–3942.

[160] E.O. Doro, Computational modeling of falling liquid film free surface evaporation, Doctoral dissertation, Georgia Institute of Technology, Atlanta, GA, 2012.

[161] M. Huang, Z. Yang, Y. Duan, D. Lee, Bubble growth for boiling bubbly flow for R141b in serpentine tube, J. Taiwan Inst. Chemical Engineers 42 (2011) 727–734.

[162] P.C. Wayner Jr., Intermolecular forces in phase-change heat transfer: 1998 Kern award review, AIChE J. 45 (1999) 2055–2068.

[163] S. Chen, Z. Yang, Y. Duan, Y. Chen, and D. Wu, Simulation of condensation flow in a rectangular microchannel, Chemical Engng Processing: Process Intensification 76 (2014) 60–69.

[164] M. Bahreini, A. Ramiar, A.A. Ranjbar, Numerical simulation of bubble behavior in subcooled flow boiling under velocity and temperature gradient, Nuclear Engng Design 293 (2015) 238-248.

[165] S.C.K. De Schepper, G.J. Heynderichx, G.B. Marin, Modeling the evaporation of a hydrocarbon feedstock in the convection section of a steam cracker, Computers Chemical Engng 33 (2009) 122–132.

[166] Z. Liu, B. Sundén, J. Yuan, VOF modeling and analysis of filmwise condensation between vertical parallel plates, Heat Transfer Research 43 (2012) 47–68.

[167] R. Zhuan and W. Wang, Simulation on nucleate boiling in micro-channel, Int. J. Heat Mass Transfer 53 (2010) 502–512.

[168] S. Petrovic, T. Robinson, R.L. Judd, Marangoni heat transfer in subcooled nucleate pool boiling, Int. J. Heat Mass Transfer 47 (2004) 5115–5128.

[169] P. Arlabosse, L. Tadrist, H. Tadrist, J. Pantaloni, Experimental analysis of the heat transfer induced by thermocapillary convection around a bubble, J. Heat Transfer – Trans. ASME 122 (2000) 66–73.

[170] J.R. Thome, V. Dupont, A.M. Jacobi, Heat transfer model for evaporation in microchannels. Part I: presentation of the model, Int. J. Heat Mass Transfer 47 (2004) 3375–3385.

[171] N. Zhang, D.F. Chat, Models for enhanced boiling heat transfer by unusual Marangoni effects under microgravity conditions, Int. Communications Heat Mass Transfer 26 (1999) 1081–1090.

[172] S. Jeon, S. Kim and G. Park, Numerical study of condensing bubble in subcooled boiling flow using volume of fluid model, Chemical Engng Science 66 (2011) 5899–5909.

[173] S. Kim and G. Park, Interfacial heat transfer of condensing bubble in subcooled boiling flow at low pressure, Int. J. Heat Mass Transfer 54 (2011) 2962–2974.

[174] E. Krepper, B. Koncar, Y. Egorov, CFD modelling of subcooled boiling - concept, validation and application to fuel assembly design, Nuclear Engng Design 237 (2007) 716–731.

[175] W.E. Ranz, W.R. Marshall, Evaporation from drops - Part I, Chemical Engng Progress 48 (1952) 141–146.

[176] Y.Q. Zu, Y.Y. Yan, S. Gedupudi, T.G. Karayiannis and D.B.R. Kenning, Confined bubble growth during flow boiling in a mini-/micro-channel of rectangular cross-section part II: approximate 3-D numerical simulation, Int. J. Thermal Sciences 50 (2011) 267–273.

[177] S. Gedupudi, Y.Q. Zu, T.G. Karayiannis, D.B.R. Kenning, Y.Y. Yan, Confined bubble growth during flow boiling in a mini/micro-channel of rectangular cross-section part I: experiments and 1-D modelling, Int. J. Thermal Sciences 50 (2011) 250–266.

[178] Y. Zhang, A. Faghri, M.B. Shafii, Capillary blocking in forced convection condensation in horizontal miniature channels, J. Heat Transfer – Trans. ASME 123 (2001) 501–511.

[179] S.W.J. Welch, J. Wilson, A volume of fluid based method for fluid flows with phase change, J. Computational Physics 160 (2000) 662-682.

[180] C. Kunkelmann, Numerical modeling and investigation of boiling phenomena, PhD thesis, Technische Universität Darmstadt, Germany, 2011.

[181] D. Juric, G. Tryggvason, Computations of boiling flows, Int. J. Multiphase Flow 24 (1998) 387-410.

[182] Y. Sato, B. Niceno, A sharp-interface phase change model for a mass conservative interface tracking method, J. Computational Physics 249 (2013) 127–161.

[183] C. Kunkelmann, P. Stephan, CFD simulation of boiling flows using the volume-of-fluid method within OPENFOAM, Numerical Heat Transfer Part A 56 (2009) 631–646.

[184] G. Son, V.K. Dhir, N. Ramanujapu, Dynamics and heat transfer associated with a single bubble during nucleate boiling on a horizontal surface, J. Heat Transfer – Trans. ASME 121 (1999) 623–632.

[185] D.Q. Nguyen, R.P. Fedkiw, M. Kang, A boundary condition capturing method for incompressible flame discontinuities, J. Computational Physics 172 (2001) 71-98.

[186] S.W.J. Welch, Local simulation of two-phase flows including interface tracking with mass transfer, J. Computational Physics 121 (1995) 42–54.

[187] G. Son, V.K. Dhir, Numerical simulation of saturated film boiling on a horizontal surface, J. Heat Transfer – Trans. ASME 119 (1997) 25-54.

[188] G. Tomar, G. Biswas, A. Sharma, A. Agrawal, Numerical simulation of bubble growth in film boiling using a coupled level-set and volume-of-fluid method, Physics Fluids 17 (2005) 112103.

[189] D. Jamet, O. Lebaigue, N. Coutris, J. Delhaye, The second gradient method for the direct numerical simulation of liquid–vapor flows with phase change, J. Computational Physics 169 (2001) 624-651.

[190] Z. Dong, W. Li, Y. Song, A numerical investigation of bubble growth on and departure from a superheated wall by lattice Boltzmann method, Int. J. Heat Mass Transfer 53 (2010) 4908–4916.

[191] T. Inamuro, M. Yoshino, H. Inoue, R. Mizuno, F. Ogino, A lattice Boltzmann method for a binary miscible fluid mixture and its application to a heat-transfer problem, J. Computational Physics 179 (2002) 201–215.

[192] H.W. Zheng, C. Shu, Y.T. Chew, A lattice Boltzmann model for multiphase flows with large density ratio, J. Computational Physics 218 (2006) 353–371.

[193] R. Zhang, H. Chen, Lattice Boltzmann method for simulations of liquid-vapor thermal flows, Physical Review E 67 (2003) 066711.

[194] P.C. Wayner Jr., Evaporation and stress in the contact line region, Proc. Engng Foundation Conf. on Pool and External Flow Boiling, Santa Barbara, CA, pp. 251–256, 1992.

[195] J.H. Lay, V.K. Dhir, Shape of a vapor stem during nucleate boiling of saturated liquids, J. Heat Transfer – Trans. ASME 117(1995) 394–401.

[196] S. Singh, V.K. Dhir, Effect of gravity, wall superheat and liquid subcooling on bubble dynamics during nucleate boiling, in Microgravity fluid physics and heat transfer, V.K. Dhir (Ed.), Begell House, New York, pp. 106–113, 2000.

[197] H.S. Abarajith, V.K. Dhir, Effect of contact angle on the dynamics of a single bubble during pool boiling using numerical simulations, Proc. ASME Int. Mechanical Engineering Congress & Exposition, New Orleans, LA, 2002

[198] W. Fritz, Maximum volume of vapor bubbles, Phys. Z. 36 (1935) 379-384.

[199] G. Son, N. Ramanujapu, V.K. Dhir, Numerical simulation of bubble merger process on a single nucleation site during pool nucleate boiling, J. Heat Transfer – Trans. ASME 124 (2002) 51–62.

[200] A. Mukherjee, V.K. Dhir, Study of lateral merger of vapor bubbles during nucleate pool boiling, J. Heat Transfer - Trans. ASME 126 (2004) 1023–1039.

[201] H.S. Aparajith, V.K. Dhir, G. Son, Numerical simulation of the dynamics of multiple bubble merger during pool boiling under reduced gravity, Multiphase Science Technology 18 (2006) 277-304.

[202] D. Li, V.K. Dhir, Numerical study of single bubble dynamics during flow boiling, J. Heat Transfer – Trans. ASME 129 (2007) 864–876.

[203] G. Son, V.K. Dhir, Numerical simulation of nucleate boiling on a horizontal surface at high heat fluxes, Int. J. Heat Mass Transfer 51 (2008) 2566- 2582.

[204] W. Lee, G. Son, J.J. Jeong, Numerical analysis of bubble growth and departure from a microcavity, Numerical Heat Transfer B 58 (2010) 323–342.

[205] W. Lee, G. Son, Numerical simulation of boiling enhancement on a microstructured surface, Int. Communications Heat Mass Transfer 38 (2011) 168-173.

[206] Y. Nam, E. Aktinol, V.K. Dhir, Y.S. Ju, Single bubble dynamics on a superhydrophilic surface with artificial sites, Int. J. Heat Mass Transfer 54 (2011) 1572–1577.

[207] J. Wu, V.K. Dhir, Numerical simulation of dynamics and heat transfer associated with a single bubble in subcooled boiling and in the presence of noncondesables, J. Heat Transfer – Trans. ASME 133 (2011) 041502.

[208] J. Wu, V.K. Dhir, J. Qian, Numerical simulation of subcooled nucleate boiling by coupling level set method with moving mesh method, Numerical Heat Transfer B 51 (2007) 535–563.

[209] W. Lee, G. Son, H.Y. Yoon, Numerical study of bubble growth and boiling heat transfer on a microfinned surface, Int. Communications Heat Mass Transfer 39 (2012) 52-57.

[210] V.K. Dhir, G. R. Warrier, E. Aktinol, D. Chao, J. Eggers, W. Sheredy, W. Booth, Nucleate pool boiling experiments (NPBX) on the International Space Station," Microgravity Science Technology 24 (2011) 307–325.

[211] J.F. Zhao, Z.D. Li, L. Zhang, Numerical simulation of single bubble pool boiling in different gravity conditions, American Institute of Physics (AIP) Conf. Proc. 1376 (2011) 565–568.

[212] E. Aktinol, V.K. Dhir, Numerical simulation of nucleate boiling phenomenon coupled with thermal response of the solid, Microgravity Science Technology 24 (2012) 255–265.

[213] P.C. Stephan, C.A. Busse, Analysis of the heat transfer coefficient of grooved heat pipe evaporator walls, Int. J. Heat Mass Transfer 35 (1992) 383–391.

[214] C. Kunkelmann, P. Stephan, Numerical simulation of the transient heat transfer during nucleate boiling of refrigerant HFE-7100, Int. J. Refrigeration 33 (2010) 1221-1228.

[215] C. Kunkelmann, P. Stephan, Modification and extension of a standard volume-of-fluid solver for simulating boiling heat transfer, in: Proc. 5th European Conf. on Computational Fluid Dynamics ECCOMAS CFD2010, Lisbon, Portugal, 2010.

[216] C. Kunkelmann, K. Ibrahem, N. Schweizer, S. Herbert, P. Stephan, T. Gambaryan-Roisman, The effect of three-phase contact line speed on local evaporative heat transfer: Experimental and numerical investigations, Int. J. Heat Mass Transfer 55 (2012) 1896-1904.

[217] A. Sielaff, J. Dietl, S. Herbert, P. Stephan, The influence of system pressure on bubble coalescence in nucleate boiling, Heat Transfer Engng 35 (2014) 420– 429.

[218] Z.H. Chen, Y. Utaka, On heat transfer and evaporation characteristics in the growth process of a bubble with microlayer structure during nucleate boiling, Int. J. Heat Mass Transfer 81 (2015) 750–759.

[219] H.W. Jia, P. Zhang, X. Fu, S.C. Jiang, A numerical investigation of nucleate boiling at a constant surface temperature, Applied Thermal Engng 88 (2015) 248–257.

[220] H.Y. Yoon, S. Koshizuka, Y. Oka, Direct calculation of bubble growth, departure, and rise in nucleate pool boiling, Int. J. Multiphase Flow 27 (2001) 277-298.

[221] S. Shin, S.I. Abdel-Khalik, D. Juric, Direct three-dimensional numerical simulation of nucleate boiling using the level contour reconstruction method, Int. J. Multiphase Flow 31 (2005) 1231-1242.

[222] Y. Sato, S. Lal, B. Niceno, Computational fluid dynamics simulation of single bubble dynamics in convective boiling flows, Multiphase Science Technology 25 (2013) 287–309.

[223] K. Ling, Z.Y. Li, W.Q. Tao, A direct numerical simulation for nucleate boiling by the VOSET method, Numerical Heat Transfer A 65 (2014) 949-971.

[224] H.B. Ma, P. Cheng, B. Borgmeyer, Y.X. Wang, Fluid flow and heat transfer in the evaporating thin film region, Microfluid Nanofluid 4 (2008) 237–243.

[225] G. Tryggvason, J.C. Lu, Direct numerical simulations of flows with phase change, Procedia IUTAM 15 (2015) 2-13.

[226] S. Lal, Y. Sato, B. Niceno, Direct numerical simulation of bubble dynamics in subcooled and near-saturated convective nucleate boiling, Int. J. Heat Fluid Flow 51 (2015) 16-28.

[227] R.C. Lee, J.E. Nydahl, Numerical calculation of bubble growth in nucleate boiling from inception to departure, J. Heat Transfer – Trans. ASME 111 (1989) 474–479.

[228] M.G. Cooper, A.J.P. Lloyd, The microlayer in nucleate boiling, Int. J. Heat Mass Transfer 12 (1969) 895–913.

[229] S.W.J. Welch, Direct simulation of vapor bubble growth, Int. J. Heat Mass Transfer 41 (1998) 1655–1666.

[230] S. aus der Wiesche, Bubble growth and departure during nucleate boiling: the occurrence of heat flux reversal, Proc. 4th Int. Conf. Computational Heat and Mass Transfer, Paris, France, vol. 2, Paper ICCHMT2005-107, 2005.

[231] T. Kunugi, N. Saito, Y. Fujita, A. Serizawa, Direct numerical simulations of pool and forced convection flow boiling phenomena, Proc. 12th Int. Heat Transfer Conf., Grenoble, France, vol. 3. pp. 497–502, 2002.

[232] T. Kunugi, MARS for multiphase calculation, Computational Fluid Dynamics J. 9 (2001) 563-561.

[233] S. Koshizuka, Y. Oka, Moving-particle semi-implicit method for fragmentation of incompressible fluid, Nuclear Science Engng 123 (1996) 421-434.

[234] S. Ryu, S. Ko, Direct numerical simulation of nucleate pool boiling using a two-dimensional lattice Boltzmann method, Nuclear Engng Design 248 (2012) 248-262.

[235] S. Gong, P. Cheng, A lattice Boltzmann method for simulation of liquid–vapor phase-change heat transfer, Int. J. Heat Mass Transfer 55 (2012) 4923-4927.

[236] T. Sun , W. Li , S. Yang, Numerical simulation of bubble growth and departure during flow boiling period by lattice Boltzmann method, Int. J. Heat Fluid Flow 44 (2013) 120–129.

[237] A. Esmaeeli and G. Tryggvason, Computations of film boiling. Part I: numerical method, Int. J. Heat Mass Transfer 47 (2004) 5451-5461.

[238] A. Esmaeeli and G. Tryggvason, Computations of film boiling. Part II: multi-mode film boiling, Int. J. Heat Mass Transfer 47 (2004) 5463-5476.

[239] A. Esmaeeli and G. Tryggvason, A front tracking method for computations of boiling in complex geometries, Int. J. Multiphase Flow 30 (2004) 1037-1050.

[240] F. Bazdidi-Tehrani, S. Zaman, Two-phase heat transfer on an isothermal vertical surface: a numerical simulation, Int. J. Heat Fluid Flow 23 (2002) 308–316.

[241] G. Son, V. K. Dhir, A level set method for analysis of film boiling on an immersed solid surface, Numerical Heat Transfer B 52 (2007) 153-177.

[242] G. Son, V.K. Dhir, Three-dimensional simulation of saturated film boiling on a horizontal cylinder, Int. J. Heat Mass Transfer 51 (2008) 1156–1167.

[243] K. Kim, G. Son, Numerical analysis of film boiling in liquid jet impingement, Numerical Heat Transfer A 64 (2013) 695-709.

[244] S.W.J. Welch, T. Rachidi, Numerical computation of film boiling including conjugate heat transfer, Numerical Heat Transfer B 42 (2002) 35–53.

[245] D.K. Agarwal, S.W.J. Welch, G. Biswas, F. Durst, Planar simulation of bubble growth in film boiling in near-critical water using a variant of the VOF method, J. Heat Transfer – Trans. ASME 126 (2004) 329–338.

[246] M.H. Yuan, Y.H. Yang, T.S. Li, Z.H. Hu, Numerical simulation of film boiling on a sphere with a volume of fluid interface method, Int. J. Heat Mass Transfer 51 (2008) 1646-1657.

[247] R. Arevalo, D. Antunez, L. Rebollo, A. Abanades, Estimation of radiation coupling factors in film boiling around spheres by mean of Computational Fluid Dynamics (CFD) tools, Int. J. Heat Mass Transfer 78 (2014) 84-89.

[248] D. Banerjee, V.K. Dhir, Study of subcooled film boiling on a horizontal disc: Part I—Analysis, J. Heat Transfer – Trans. ASME 123 (2001) 271–284.

[249] D. Banerjee, V.K. Dhir, Study of subcooled film boiling on a horizontal disc: Part 2—Experiments," J. Heat Transfer – Trans. ASME 123 (2001) 285–293.

[250] S.W. Welch, G. Biswas, Direct simulation of film boiling including electrohydrodynamic forces, Physics of Fluids 19 (2007) 012106.

[251] G. Tomar, G. Bisawas, A. Sharma, S.W.J. Welch, Influence of electric field on saturated film boiling, Physics of Fluids 21 (2009) 032107.

[252] D.Z. Guo, D.L. Sun, Z.Y. Li, W.Q. Tao, Phase change heat transfer simulation for boiling bubbles arising from a vapor film by the VOSET method, Numerical Heat Transfer A 59 (2011) 857–881.

[253] Y.-Y. Tsui, S.-W. Lin, Y.-N. Lai, F.-C. Wu, Phase change calculations for film boiling flows, Int. J. Heat Mass Transfer 70 (2014) 745–757.

[254] N. Al-Rawahi, G. Tryggvason, Numerical simulation of dendritic solidification with convection: two–dimensional geometry, J. Computational Physics 180 (2002) 471–496.

[255] M. Reimann, U. Grigull, Wärmeubergang bei freier konvektion und filmsieden im kritischen gebiet von wasser und kohlendioxid, Warme- und Stoffübertragung 8 (1975) 229–239.

[256] P.J. Berenson, Film-boiling heat transfer from a horizontal surface, J. Heat Transfer – Trans ASME 83 (1961) 351–356.

[257] V.V. Klimenko, Film boiling on a horizontal plate—new correlation, Int. J. Heat Mass Transfer 24 (1981) 69–79.

[258] Q. Li, Q.J. Kang, M.M. Francois, Y.L. He, K.H. Luo, Lattice Boltzmann modeling of boiling heat transfer: The boiling curve and the effects of wettability, Int. J. Heat Mass Transfer 85 (2015) 787–796.

[259] A. Mukherjee, S.G. Kandlikar, Numerical simulation of growth of a vapor bubble during flow boiling of water in a microchannel, J. Microfluidics Nanofluidics 1 (2005) 137–145.

[260] W. Lee, G. Son, Bubble dynamics and heat transfer during nucleate boiling in a microchannel, Numerical Heat Transfer A 53 (2008) 1074–1090.

[261] Y. Suh, W. Lee, G. Son, Bubble dynamics, flow, and heat transfer during flow boiling in parallel microchannels, Numerical Heat Transfer A 54 (2008) 390–405.

[262] A. Mukherjee, Contribution of thin-film evaporation during flow boiling inside microchannels, Int. J. Thermal Sciences 48 (2009) 2025–2035.

[263] A. Mukherjee, S.G. Kandlikar, The effect of inlet constriction on bubble growth during flow boiling in microchannels, Int. J. Heat Mass Transfer 52 (2009) 5204–5212.

[264] A. Mukherjee, S.G. Kandlikar, Z.J. Edel, Numerical study of bubble growth and wall heat transfer during flow boiling in a microchannel, Int. J. Heat Mass Transfer 54 (2011) 3702-3718.

[265] S. Zhou, X. Xu, B.G. Sammakia, Modeling of boiling flow in microchannels for nucleation characteristics and performance optimization, Int. J. Heat Mass Transfer 64 (2013) 706–718.

[266] Z. Yang, X.F. Peng, P. Ye, Numerical and experimental investigation of two phase flow during boiling in a coiled tube, Int. J. Heat Mass Transfer 51 (2008) 1003–1016.

[267] C. Fang, M. David, A. Rogacs, K. Goodson, Volume of fluid simulation of boiling two-phase flow in a vapor venting microchannel, Frontiers Heat Mass Transfer 1 (2010) 013002.

[268] J. Wei, L. Pan, D. Chen, H. Zhang, J. Xu and Y. Huang, Numerical simulation of bubble behaviors in subcooled flow boiling under swing motion, Nuclear Engng Design 241 (2011) 2898-2908.

[269] R. Zhuan and W. Wang, Simulation of subcooled flow boiling in a micro-channel, Int. J. Refrigeration 34 (2011) 781 -795.

[270] G.R. Warrier, N. Basu, V.K. Dhir, Interfacial heat transfer during subcooled flow boiling, Int. J. Heat Mass Transfer 45 (2002) 3947-3959.

[271] S.J. Kim, G.C. Park, Development of an orthogonal double-image processing algorithm to measure bubble volume in a two-phase flow, Nuclear Engng Technology 39 (2007) 313–326.

[272] R. Zhuan and W. Wang, Flow pattern of boiling in microchannel by numerical simulation, Int. J. Heat Mass Transfer 55 (2012) 1741-1753.

[273] L. Pan, Z Tan, D. Chen, L. Xue, Numerical investigation of vapor bubble condensation characteristics of subcooled flow boiling in vertical rectangular channel, Nuclear Engng Design 248 (2012) 126-136.

[274] M. Magnini, B. Pulvirenti, J.R. Thome, Numerical investigation of the influence of leading and sequential bubbles on slug flow boiling within a microchannel, Int. J. Thermal Sciences 71 (2013) 36–52.

[275] D. Lorenzini, Y.K. Joshi, CFD analysis of flow boiling in a silicon microchannel with non-uniform heat flux. Proc. ASME 2015 13th Int. Conf. on Nanochannels, Microchannels, and Minichannels, San Francisco, California, USA, 2015.

[276] H. Lee, D.D. Agonafer, Y. Won, F. Houshmand, C. Gorle, M. Asheghi, K.E. Goodson, Thermal modeling of extreme heat flux microchannel coolers for GaN-on-SiC semiconductor devices, J. Electronic Packaging – Trans. ASME 138 (2016) 010907.

[277] Z. Pan, J.A. Weibel, S.V. Garimella, A saturated-interface-volume phase change model for simulating flow boiling, Int. J. Heat Mass Transfer 93 (2016) 945–956.

[278] M. Magnini, J.R. Thome, Computational study of saturated flow boiling within a microchannel in the slug flow regime, J. Heat Transfer – Trans. ASME 138 (2016) 021502.

[279] H.L. Wu, X.F. Peng, P. Ye, Y. Gong, Simulation of refrigerant flow boiling in serpentine tubes, Int. J. Heat Mass Transfer 50 (2007) 1186–1195.

[280] N. Kurul, M.Z. Podowski, Multidimensional effects in forced convection subcooled boiling, Proc. 9th Int. Heat Transfer Conf., Jerusalem, Israel, vol. 2, pp. 21-26, 1990.

[281] G.G. Bartolomej, V.M. Chanturiya, Experimental study of true void fraction when boiling subcooled water in vertical tubes, Thermal Engineering 14 (1967) 123–128.

[282] G.G. Bartolomej, V.G. Brantov, Y.S. Molochnikov, An experimental investigation of true volumetric vapour content with subcooled boiling in tubes, Thermal Engineering 29 (1982) 132–135.

[283] E. Krepper, R. Rzehak, CFD for subcooled flow boiling: simulation of DEBORA experiments, Nuclear Engng Design 241 (2011) 3851–3866.

[284] E. Krepper, R. Rzehak, C. Lifante, T. Frank, CFD for subcooled flow boiling: coupling wall boiling and population balance models, Nuclear Engng Design 255 (2013) 330–346.

[285] S.M. Kim, J. Kim, I. Mudawar, Flow condensation in parallel micro-channels – Part 1: Experimental results and assessment of pressure drop correlations, Int. J. Heat Mass Transfer 55 (2012) 971–983.

[286] J. Yuan, C. Wilhelmsson, B. Sunden, Analysis of water condensation and two-phase flow in a channel relevant for plate heat exchangers, in Advanced computational methods in heat transfer IX, B. Sunden and C. Brebbia (Eds.), WIT Press, pp. 351–360, 2006.

[287] E. Da Riva, D. Del Col, Effect of gravity during condensation of R134a in a circular minichannel, Microgravity Science Technology 23 (2011) 87–97.

[288] A. Alizadehdakhel, M. Rahimi, A.A. Alsairafi, CFD modeling of flow and heat transfer in a thermosyphon, Int. Communications Heat Mass Transfer 37 (2010) 312–318.

[289] Z. Yin, Y. Guo, B. Sunden, Q. Wang, M. Zeng, Numerical simulation of laminar film condensation in a horizontal minitube with and without non-condensable gas by the VOF method, Numerical Heat Transfer A 68 (2015) 958–977.

[290] G.-D. Qiu, W.-H. Cai, S.-L. Li, Z.-Y. Wu, Y.-Q. Jiang, Y. Yao, Numerical simulation on forced convective condensation of steam upward flow in a vertical pipe, Advances Mechanical Engng 2014 (2014) 589250.

[291] G.D. Qiu, W.H. Cai, Z.Y. Wu, Y. Yao, Y.Q. Jiang, Numerical simulation of forced convective condensation of propane in a spiral tube, J. Heat Transfer – Trans. ASME 137 (2015) 041502.

[292] J. Zhang, W. Li, W.J. Minkowycz, Numerical simulation of condensation for R410A at varying saturation temperatures in mini/micro tubes, Numerical Heat Transfer A 69 (2015) 464–478.

[293] X.L. Liu, P. Cheng, Lattice Boltzmann simulation of steady laminar film condensation on a vertical hydrophilic subcooled flat plate, Int. J. Heat Mass Transfer 62 (2013) 507–514.

[294] X.L. Liu, P. Cheng, Lattice Boltzmann simulation for dropwise condensation of vapor along vertical hydrophobic flat plates, Int. J. Heat Mass Transfer 64 (2013) 1041–1052.

[295] H.J. Chung, H.C. No, Simultaneous visualization of dry spots and bubbles for pool boiling of R-113 on a horizontal heater, Int. J. Heat Mass Transfer 46 (2003) 2239–2251.

[296] I.-C. Chu, H.C. No, C.-H. Song, Observation of high heat flux boiling structures in a horizontal pool by a total refection technique, 14th Int. Topical Meeting on Nuclear Reactor Thermal Hydraulics (NURETH-14), Toronto, Canada, Paper 401, 2011.

[297] Y. Heng, A. Mhamdi, S. Gross, A. Reusken, M. Buchholz, H. Auracher, W. Marquardt, Reconstruction of local heat fluxes in pool boiling experiments along the entire boiling curve from high resolution transient temperature measurements, Int. J. Heat Mass Transfer 51 (2008) 5072–5087.

[298] S. Moghaddam, K. Kiger, Physical mechanisms of heat transfer during single bubble nucleate boiling of FC-72 under saturation conditions—I. experimental investigation, Int. J. Heat Mass Transfer 52 (2009) 1284–1294.

[299] E. Barrau, N. Rivière, Ch. Poupot, A. Cartellier, Single and double optical probes in air-water two-phase flows: real time signal processing and sensor performance, Int. J. Multiphase Flow 25 (1999) 229–256.

[300] S. Kim, X. Y. Fu, X. Wang, M. Ishii, Development of the miniaturized four-sensor conductivity probe and the signal processing scheme, Int. J. Heat Mass Transfer 43 (2000) 4101–4118.

[301] H.M. Prasser, A. Bottger, J. Zschau, A new electrode-mesh tomography for gas–liquid flows, Flow Measurement Instrumentation 9 (1998) 111–119.

[302] T.H. Lyu, I. Mudawar, Determination of wave-induced fluctuations of wall temperature and convective heat transfer coefficient in the heating of a turbulent falling liquid film, Int. J. Heat Mass Transfer 34 (1991) 2521-2534.

[303] T.H. Lyu, I. Mudawar, Simultaneous measurements of thickness and temperature profile in a wavy liquid film falling freely on a heating wall, Experimental Heat Transfer 4 (1991) 217-233.

[304] I. Mudawar, R.A. Houpt, Mass and momentum transport in smooth falling liquid films laminarized at relatively high Reynolds numbers, Int. J. Heat Mass Transfer 36 (1993) 3437-3448.

[305] I. Mudawar, R.A. Houpt, Measurement of mass and momentum transport in wavy-laminar falling liquid films, Int. J. Heat Mass Transfer 36 (1993) 4151-4162.

[306] T.G. Theofanous, J.P. Tu, A.T. Dinh, T.N. Dinh, The boiling crisis phenomenon: Part I: Nucleation and nucleate boiling phenomenon, Exp. Thermal Fluid Science 26 (2002) 775–792.

[307] T.G. Theofanous, J.P. Tu, A.T. Dinh, T.N. Dinh, The boiling crisis phenomenon: Part II: dryout dynamics and burnout, Exp. Thermal Fluid Science 26 (2002) 793–810.

[308] S. Khodaparast, N. Borhani, G. Tagliabue, J. Thome, A micro particle shadow velocimetry (μPSV) technique to measure flows in microchannels, Experiments Fluids 54 (2013) 1474.

[309] M. Abe, E. Longmire, K. Hishida, M. Maeda, A comparison of 2D and 3D PIV measurements in an oblique jet, J. Visualization 3 (2000) 165-173.

[310] M.P. Arroyo, K. Hinsch, Recent developments of PIV towards 3D measurements, in Partcle image velocimetry: new developments and recent applications, A. Schroeder, C.E. Willert (eds.), Topics in Applied Physics, Vol. 112, Springer, Berlin, Germany, pp. 127-154, 2008.

[311] C. Gerardi, J. Buongiorno, L.W. Hu, T. McKrell, Study of bubble growth in water pool boiling through synchronized, infrared thermometry and high-speed video, Int. J. Heat Mass Transfer 53 (2010) 4185–4192.

[312] X. Duan, B. Phillips, T. McKrell, J. Buongiorno, Synchronized high-speed video, infrared thermometry, and particle image velocimetry data for validation of interface-tracking simulations of nucleate boiling phenomena, Experimental Heat Transfer 26 (2013) 169–197.

[313] S. Thomas, A. Esmaeeli, G. Tryggvason, Multiscale computations of thin films in multiphase flows, Int. J. Multiphase Flow 36 (2010) 71–77.

[314] R. Ranjan, J.Y. Murthy, S.V. Garimella, A microscale model for thin-film evaporation in capillary wick structures, Int. J. Heat Mass Transfer 54 (2011) 169–179.

[315] S. Narumanchi, A. Troshko, D. Bharathan, V. Hassani, Numerical simulations of nucleate boiling in impinging jets: applications in power electronic cooling, Int. J. Heat Mass Transfer 51 (2008) 1–12.

[316] Y. Liu, T. Olewski, L.N. Véchot, Modeling of a cryogenic liquid pool boiling by CFD simulation, J. Loss Prevention Process Industries 35 (2015) 125-134.

[317] S.M. Kim, I. Mudawar, Universal approach to predicting saturated flow boiling heat transfer in mini/micro-channels - Part I. Dryout incipience quality, Int. J. Heat Mass Transfer 64 (2013) 1226-1238.

[318] S.M. Kim, I. Mudawar, Universal approach to predicting saturated flow boiling heat transfer in mini/micro-channels - Part II. Two-phase heat transfer coefficient, Int. J. Heat Mass Transfer 64 (2013) 1239-1256.

[319] Y. Katto and M. Kunihiro, Study of the mechanism of burn-out in boiling system of high burn-out heat flux, Bulletin JSME 16 (1973) 1357-1366.

[320] A. Lefebvre, Atomization and sprays, Hemisphere Publishing, New York, 1988.

[321] J.D. Bernardin, I. Mudawar, A cavity activation and bubble growth model of the Leidenfrost point, J. Heat Transfer - Trans. ASME 124 (2002) 864-874.

APPENDIX

APPENDIX A. REVIEW OF COMPUTATIONAL STUDIES ON BOILING AND

CONDENSATION

A.1 <u>Introduction</u>

A.1.1 <u>Addressing the Myriad of Important Boiling and Condensation Configurations</u>

For many decades, thermal management systems in many applications have employed single-phase methods to meet specific cooling requirements. These systems include both natural convection and forced convection configurations. However, the recent rapid rise in rate of heat dissipation in many applications, coupled with the need to decrease the size of cooling hardware, has rendered single-phase systems incapable of meeting cooling requirements. This trend includes applications such as computer electronics and data centers, medical x-ray equipment, hybrid vehicle power electronics and heat exchangers for hydrogen storage in automobiles, fusion reactor blankets, particle accelerator targets, magnetohydrodynamic generator electrode walls, defense radars, rocket engine nozzles, and both laser and microwave directed-energy weapons [1,105,106]. Lack of effectiveness of single-phase methods has spurred a transition to two-phase systems to capitalize upon the high heat transfer coefficients associated with both boiling and condensation. The cooling advantages of two-phase systems are derived from their reliance on both sensible and latent heat of the working fluid compared to sensible heat alone for single-phase systems.

Early implementation of phase change cooling was focused on passive heat pipes that rely on capillary forces in a wicking structure to circulate coolant between evaporating (heat acquisition) and condensing (heat rejection) terminals of a closed tubular structure. But several fundamental limitations of heat pipes, especially small coolant flow rate, place stringent upper performance limits that fall short of cooling requirements in many emerging technologies [105]. This shortcoming shifted interest to other passive, unwicked cooling schemes, especially pool-boiling thermosyphons, which rely on buoyancy to circulate coolant between a lower boiling (heat acquisition) and upper condensing (heat rejection) sections of a closed vessel [2,3,107]. Here too, limited cooling performance spurred new innovations in passive cooling, such as the use of a pumpless loop consisting of two vertical tubes connected atop to a liquid reservoir fitted with a condenser [5,108]. In this system, the boiler is connected to one of the vertical tubes, and large vapor void reduces fluid density in the boiler tube compared to the other liquid tube, causing static pressure imbalance and triggering fluid circulation within the loop. The added benefits of coolant motion in the pumpless loop are also realized in semi-passive falling film cooling systems [59,63], where liquid from a small reservoir falls by gravity as a thin film along the heat dissipating surface, and vapor is lifted by buoyancy to the upper condensation section; the liquid is recollected in the reservoir passively by vapor condensation, assisted by a small pump to maintain constant liquid level in the reservoir. Further improvements in cooling performance involve the use of mechanically driven pumped loops to enhance cooling performance by increasing coolant velocity along the boiling surface. The simplest pumped loop configuration relies on flow boiling along a flow channel [52]. This configuration evolved in recent years to loops utilizing mini- or micro-channels, which

offer the advantages of increased heat transfer coefficient, compact and lightweight cooling hardware, and small coolant inventory [4,6,109]. Two pumped-loop competitors to mini/micro-channel cooling are jet-impingement cooling [7,8,110] and spray cooling [9,10]. The main difference between the two is that coolant in jet impingement is supplied to the heat-dissipating surface in liquid form, but broken into small liquid droplets prior to impact in spray cooling. Yet, additional enhancement in cooling performance of pumped loops is achieved with "hybrid" cooling configurations that combine the merits of micro-channel and jet-impingement cooling [12].

In a closed system, enhanced boiling performance often requires commensurate improvements in heat rejection by condensation using a variety of configurations, such as drop-wise condensation [111], falling film condensation on tubes [112] and vertical surfaces [99], and flow condensation in tubes [113]. Often cited as complicating factors in modeling film condensation, both external and internal, are interfacial waves and suppression of turbulence along the liquid-vapor interface [99].

One important conclusion that can be drawn from trends in the development of thermal management systems is the myriad of possible boiling and condensation configurations, which greatly complicate efforts to develop universal predictive tools for system design and optimization.

A.1.2 <u>Predictive Methods for Two-Phase Flow and Heat Transfer</u>

Undoubtedly, the most popular approach to predicting boiling and condensing flows is the use of empirical or semi-empirical correlations. A key drawback to this approach is most correlations are limited to one or a few fluids, and to narrow ranges of geometrical

and flow parameters. Most thermal management system designers are compelled to extrapolate predictions to other fluids or conditions beyond the validity range of a given correlation, which often leads to highly erroneous design decisions. A more effective tool is the use of "universal correlations" that are derived from large databases encompassing many coolants and very broad ranges of both geometrical and flow parameters [114-116].

Another approach to predicting two-phase behavior is the use of theoretical models. Unfortunately, only a few such models are available, which are limited to very basic flow configurations such as falling films [99], annular flow condensation [117], and annular flow boiling [118].

Because of limitations of both empirical correlations and theoretical models, there is now a great deal of interest in the use of computational fluid dynamics (CFD) simulations to predict phase-change processes. The main advantages of this technique are the ability to predict transient fluid flow and heat transfer behavior, and provide detailed spatial and temporal distributions of phase velocities and temperatures, and void fraction. However, while CFD simulations have shown great success and versatility in predicting single-phase flows, their effectiveness for two-phase flows has not been fully realized. Presently, despite some recent promising results, two-phase simulations are quite expensive, very time consuming, and limited to only simple flow configurations.

A.1.3 <u>Review Objectives</u>

The main goal of this paper is to review the large pool of articles addressing CFD simulations of boiling and condensation. This includes (1) popular two-phase computational schemes and key differences between schemes, (2) surface tension

modeling in conjunction with different schemes, (3) different approaches to predicting interfacial mass, momentum and energy transfer, and (4) boiling and condensation articles involving comparison of predictions of CFD schemes with experiments and correlations. This review will be concluded with key recommendations for improving predictive capabilities of computational schemes.

A.2 Two-Phase Computational Schemes

A.2.1 Solution of Continuum Two-Phase Conservation Equations

Modeling two-phase flow and heat transfer requires accurate prediction of the behavior of each phase and interactions along the interface between phases. Several numerical methods are available for this purpose. Most popular CFD methods involve solving conservation equations using macroscopic depiction of the fluids, where fluid matter is described as consisting of a sufficiently large number of molecules that continuum hypothesis for fluid properties is valid. The mass, momentum and energy equations are expressed, respectively, as

$$\frac{\partial}{\partial t}(\rho) + \nabla \cdot (\rho \vec{u}) = 0, \tag{A.1}$$

$$\frac{\partial}{\partial t}(\rho \vec{u}) + \nabla \cdot (\rho \vec{u} \vec{u}) = -\nabla p + \nabla \cdot \left[\mu \left(\nabla \vec{u} + \nabla \vec{u}^T \right) \right] + \rho \vec{g} + \vec{F}_s, \tag{A.2}$$

and
$$\frac{\partial}{\partial t}(\rho E) + \nabla \cdot \left[\vec{u} (\rho E + p) \right] = \nabla \cdot (k \nabla T) + Q. \tag{A.3}$$

While most popular methods are based on this macroscopic depiction, there is now increasing interest in computational methods at the mesoscale, where fluid matter is considered a collection of atoms, which is much smaller than macroscale but larger than

single atom ("atomistic" scale). This section will discuss the different methods used in two-phase simulations with focus on those employing conservations equations at the macroscale.

A.2.2 <u>Moving Mesh and Lagrangian Methods</u>

Early approaches to simulating two-phase flows included use of separate, boundary-fitted grids for each phase. Using this *Lagrangian* scheme, Ryskin and Leal [119] simulated the rise of a buoyancy-driven deformable bubble in quiescent liquid. Governing equations were solved separately for each phase and boundary conditions along the interface matched iteratively. While Ryskin and Leal employed a 2-D axisymmetric domain, Takagi and Matsumoto [120] simulated unsteady bubble rise in 3-D domain. Methods using boundary-fitted grids provide the highest accuracy in predictive capability among the different computational methods.

An alternative *moving-mesh Lagrangian* method allows the grid to follow boundaries of phases during interface deformation as illustrated in Fig. A.1(a). Studies using this method include deformation of a buoyant bubble by Shopov *et al.* [121], and droplet impacting a solid wall by Fukai *et al*. [122]. Overall, Lagrangian and moving-mesh methods involve very complex formulations and hence have only been applied to very simple two-phase flow configurations.
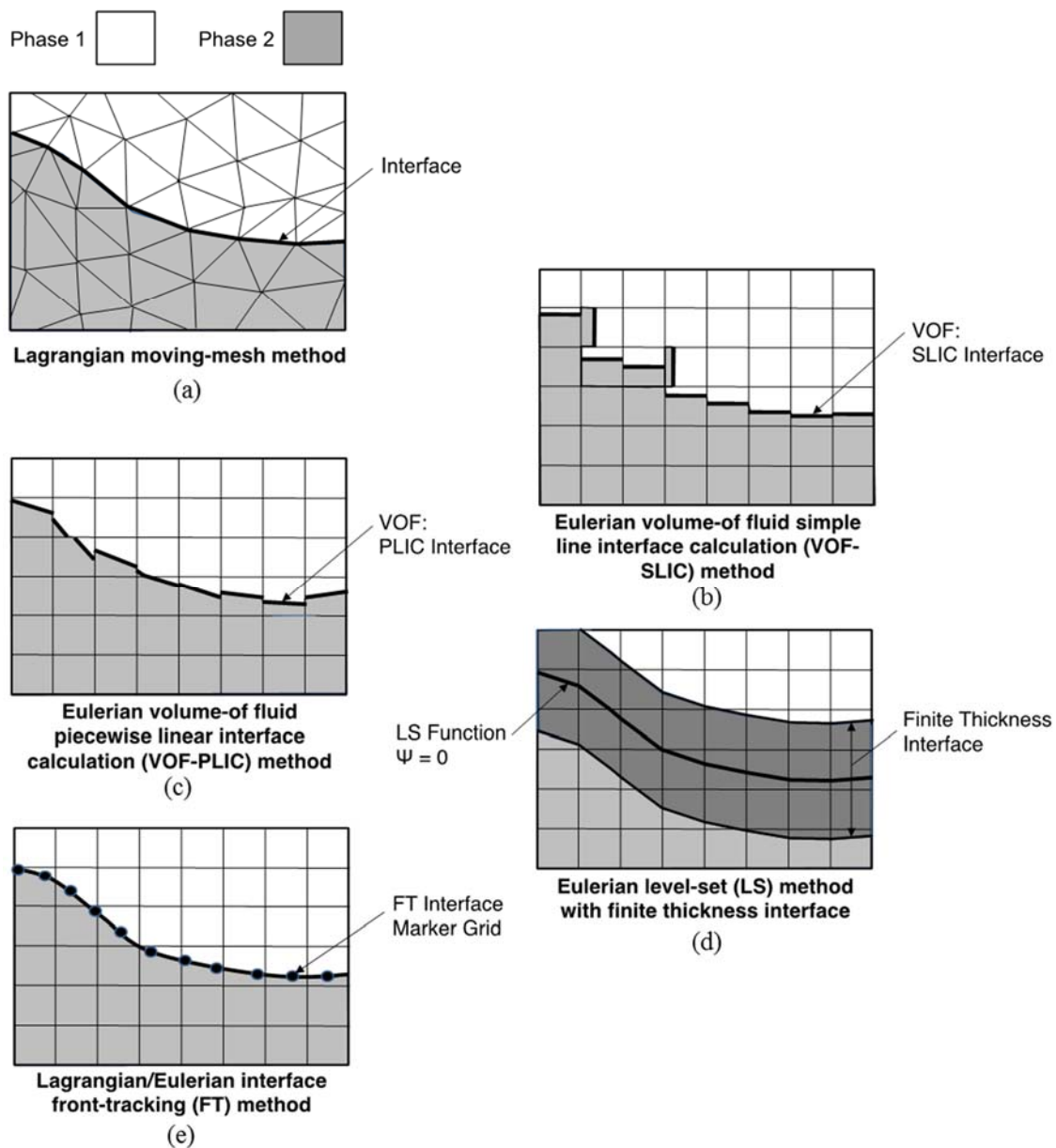
Fig. A.1: Interfacial computational grids for (a) Lagrangian moving-mesh method, (b) Eulerian volume-of-fluid simple line interface calculation (VOF-SLIC) method, (c) Eulerian volume-of-fluid piecewise linear interface calculation (VOF-PLIC) method, (d) Eulerian level-set (LS) method with finite thickness interface, and (e) Lagrangian/Eulerian interface front-tracking (FT) method.

A.2.3 <u>Interface-Capturing Methods</u>

Common Eulerian schemes used to simulate two-phase flows are termed interface-capturing methods. Most popular among these are the *volume of fluid* (VOF) method [87] and the *level-set* (LS) method [123].

A.2.3.1 <u>Volume of Fluid (VOF) Method</u>

The VOF method captures the interface using a color function C representing volume fraction with a value between 0 and 1, where 0 implies the cell is completely occupied by one phase, and 1 by the other, and the interface is identified by cells having values between 0 and 1. For flows without phase change, the color function is advected by velocity field according to the equation

$$\frac{\partial}{\partial t}\left(C\right)+\vec{u}\cdot\nabla\left(C\right)=0. \tag{A.4}$$

The velocity field is obtained by solving the momentum (Navier-Stokes) equation. Because the interface is tracked by 0 to 1 color value, VOF methods are inherently conservative, which is a major advantage when solving conservation equations. However, they suffer inability to capture the interface accurately.

VOF methods can be divided into two categories: those that do not use interface reconstruction and others that do. Methods not requiring interface reconstruction include donor-acceptor scheme by Hirt and Nicholas [87], *flux corrected transport* (FCT) scheme by Rudman [124], and *compressive interface capturing scheme for arbitrary meshes* (CICSAM) by Ubbink and Issa [125]. These schemes use a color value of 0 to indicate one phase and 1 the other phase, with the interface identified by a value of 0.5. The

transition from 0 to 1 occurs across a finite thickness interface encompassing multiple cells. In these schemes, Eq. (A.4) is modified for incompressible fluids as

$$\frac{\partial}{\partial t}(C) + \nabla \cdot (\vec{u}\, C) = 0, \tag{A.5}$$

which can be solved by different combinations of upwind and/or downwind schemes. After solving Eq. (A.5), the interface appears smeared across multiple cells and set to a finite thickness.

The second and more popular category of VOF methods involves interface reconstruction, where interface shape is solved using *piecewise constant* or *piecewise linear* schemes. Unlike the first category of VOF methods, these schemes capture the interface with zero thickness. They include *simple line interface calculation* (SLIC) [126], which is a piecewise constant scheme, and *piecewise linear interface calculation* (PLIC) [127], a piecewise linear scheme. As shown in Fig. A.1(b), the interface in SLIC is orientated with x- or y-axis of domain (sidewalls of rectangular mesh cell). On the other hand, as shown in Fig. A.1(c), the interface in PLIC is set by a straight line/plane whose direction is dictated by vector normal to the interface. Orientation of the normal vector for a specific cell containing the interface is obtained by interrogating volume fractions of all neighboring cells. Once the direction of the interface is computed, this vector is oriented in such a manner that the volume fraction of the cell is maintained. Although the original PLIC scheme by Youngs [127] is still widely used, alternative PLIC schemes have also been recommended [128,129]. A key concern with PLIC schemes is interface discontinuity (jump) between cells as depicted in Fig. A.1(c). Some improvements to the PLIC scheme have been proposed that depart from piecewise linear formulation [130,131].

In all interface reconstruction schemes, once interface reconstruction is completed, the advection step given by Eq. (A.4) is performed to proceed with the numerical solution.

In VOF methods, the density, viscosity and thermal conductivity of the fluid are determined, respectively, as

$$\rho = \alpha_g \rho_g + \left(1 - \alpha_g\right)\rho_f, \tag{A.6a}$$

$$\mu = \alpha_g \mu_g + \left(1 - \alpha_g\right)\mu_f, \tag{A.6b}$$

and
$$k = \alpha_g k_g + \left(1 - \alpha_g\right)k_f, \tag{A.6c}$$

where α_g is the volume fraction, which is related to the color function, C, by the relation

and
$$\alpha = \frac{1}{V} \iiint_V C \, dV. \tag{A.7}$$

A.2.3.2 Level-Set (LS) Method

The second type of interface-capturing methods is the Level-set (LS) method. This method uses a function, ψ, to define distance from the interface as shown in Fig. A.1(d). This function has a value of $\psi = 0$ at the interface (called zero level set), and is positive in one phase and negative in the other. In the absence of phase change, this function is advected by velocity field according to the equation

$$\frac{\partial}{\partial t}\left(\psi\right) + \vec{u} \cdot \nabla\left(\psi\right) = 0. \tag{A.8}$$

With the LS method, interface location is known only implicitly by the given values of ψ, therefore its location is captured by interpolating ψ values on the grid. This method is

able to capture complicated interface topologies quite well, but with time evolution, ψ cannot maintain the property of a signed distance function and therefore might not remain a smooth function. This leads to error in interface curvature calculations, as well as causes serious mass conservation errors. To correct this problem, ψ needs to be re-initialized every few time steps, and is transformed into a scalar field that satisfies the property of the signed function with the same zero level set. This is commonly achieved by a technique recommended by Sussman *et al.* [123] involving iterative solution of the following relations

$$\frac{\partial \psi}{\partial t} = \frac{\psi_0}{\sqrt{\psi_0^2 + h^2}} \left[1 - \left| \nabla \psi \right| \right]$$
(A.9)

and
$$\psi(x,0) = \psi_0,$$
(A.10)

where h is cell width, which is used to preclude zero denominator in Eq. (A.9). Russo and Smereka [132] showed the re-initialization step could cause errors in the solution, and suggested improvements to the method of Sussman *et al.* to correct the problem. Overall, the mass conservation errors are compounded for relatively long time durations. To correct this problem, investigators resort to employing explicit methods to force mass conservation [133,134].

Son and Dhir [135] used the following relations to determine fluid properties in their LS scheme:

$$\rho = \rho_g + (\rho_f - \rho_g) H,$$
(A.11a)

$$\mu^{-1} = \mu_g^{-1} + (\mu_f^{-1} - \mu_g^{-1}) H,$$
(A.11b)

and
$$k^{-1} = k_g^{-1} + (k_f^{-1} - k_g^{-1}) H,$$
(A.11c)

where k_g is assumed to be zero, and H is the smoothed *Heaviside function* proposed earlier by Sussman *et al.* Use of harmonic mean, Eqs. (A.11b) and (A.11c), instead of arithmetic mean, Eqs. (A.6a)-(A.6c), is not uncommon even for VOF methods. Smoothing of the Heaviside function in LS methods serves to remove numerical instabilities that arise from discontinuities in fluid properties, and is accomplished by using the following relations:

$$H = 1 \text{ for } \psi \geq 1.5\, h, \tag{A.12c}$$

$$H = 0 \text{ for } \psi \leq -1.5\, h, \tag{A.12b}$$

and

$$H = 0.5 + \frac{\psi}{3h} + \frac{1}{2\pi}\sin\left(2\pi\frac{\psi}{3h}\right) \text{ for } |\psi| \leq 1.5\, h. \tag{A.12c}$$

This technique sets interface thickness equal to $3h$, or three cell widths, as shown in Fig. A.1(d).

Notice that properties are smeared out across multiple cells when using the Heaviside function. A key concern with this smearing effect is that phase change occurs only at the interface. To help resolve this issue, Fedkiw *et al.* [136] introduced the *ghost fluid* (GF) method, which involves including an additional artificial fluid cell implicitly representing the Rankine-Hugoniot jump condition at the interface. Kang *et al.* [137] used this GF method in conjunction with the LS scheme to study incompressible multiphase flows.

To tackle both mass conservation errors of the LS method and inaccurate interface capture of the VOF method, an improved *Coupled Level-set/Volume of Fluid* (CLSVOF) method [138,139] has been proposed. This method combines the merits of both earlier methods, while minimizing their errors. With the CLSVOF method, the distance function advection equation is solved first, followed by interface reconstruction using the LS method, which corrects the inaccuracies in interface capture of the VOF method. The VOF

method is used to re-initialize ψ, thus tackling the mass conservation issues of the LS method. Another similar yet simpler approach is the *Coupled Volume of Fluid and Level-set* (VOSET) method [140]. This method only solves for C advection, Eq. (A.4), in the VOF method, but calculates LS function ψ using a simple iterative geometric operation, which is then used to calculate only geometric parameters and fluid properties at the interface.

A.2.4 <u>Interface Front-Tracking Methods</u>

Interface *front-tracking* (FT) methods combine the advantages of both the Lagrangian and Eulerian perspectives by using fixed and moving grids. Using the FT scheme, Grimm *et al.* [141] treated both phases separately, but Unverdi and Tryggvason [142] and Tryggvason *et al.* [143] used one set of equations for both phases. Unverdi and Tryggvason's FT method, which is illustrated in Fig. A.1(e), employs a regular structured grid to track the flow in both phases, and a finer marker cell grid to track the interface. Location of the finer grid is advected by velocity field according to the following equation:

$$\frac{d}{dt}\left(\vec{x}_{front}\right) = \vec{u}_{front},$$ (A.13)

where $\vec{x}_{front}$ is the position of the front, and $\vec{u}_{front}$ the velocity of the front at that position, interpolated from the fixed grid. While FT methods do a good job calculating interface curvatures and handling multiple interfaces, they require explicit treatment for interface breakup and coalescence [144]. Property variations in Unverdi and Tryggvason's FT method are given by

$$\rho = \rho_g + \left(\rho_f - \rho_f\right)I \qquad\qquad\text{(A.14a)}$$

and
$$\mu = \mu_g + \left(\mu_f - \mu_g\right)I, \qquad\qquad\text{(A.14b)}$$

where I is the *indicator function*, which, like the Heaviside function discussed earlier, is used to smooth properties across the interface.

A.2.5 Other Methods

Other methods that have been developed for fixed grids include the *constrained interpolation profile* (CIP) method [145] and *phase-field* (PF) method [146]. Yabe *et al.* [145] developed the CIP method for multiphase flows to tackle loss of information inside the computational grid resulting from the discretization process, and conserves mass accurately at the interface. This method transforms the color function into a smooth function by using a Lagrangian invariant solution scheme for advection. While most finite interface thickness schemes discussed earlier employ mathematical functions to smooth fluid properties across multiple cells, the PF method is based on the concept of diffuse interface with finite thickness [146]. The phases are defined by a phase-field parameter, C_{PF}, which, in contrast with the color function, C, is a physical parameter, and is constant within each phase and varies across the interface. Interface tracking is achieved by solving the following advection-diffusion equation:

$$\frac{\partial}{\partial t}\left(C_{PF}\right) + \left(\vec{u}\cdot\nabla\right)C_{PF} = \nabla.\left(\kappa_m\nabla\varphi\right), \qquad\qquad\text{(A.15)}$$

where κ_m is the diffusion parameter and φ the chemical potential defining the rate of change of free energy.

Yet another vastly different solution method, which is based on mesoscale formulation, is the Lattice-Boltzmann (LB) method [147,148]. Instead of solving the Navier–Stokes equation, the LB method involves solving discrete Boltzmann equation. To recover macroscopic fluid motion, the mesoscale physics is reduced to simplified microscopic models or mesoscopic kinetic equations. In contrast with methods requiring solution of the non-linear Navier–Stokes equation, the LB method solves semi-linear equations; it also does not require explicit tracking of the interface. This method is beyond the scope of the present study, and therefore excluded from further review.

A.3 <u>Surface Tension Modeling</u>

Accurate capture of the interface requires a method for modeling surface tension force effects. The most popular method to addressing these effects is the *Continuum Surface Force* (CSF) model proposed by Brackbill *et al.* [149]. When solving the momentum equation

$$\frac{\partial}{\partial t}\left(\rho \vec{u}\right)+\nabla\cdot\left(\rho\,\vec{u}.\vec{u}\right)=-\nabla p+\nabla\cdot\left[\mu\left(\nabla\vec{u}+\nabla\vec{u}^{T}\right)\right]+\rho\,\vec{g}+\vec{F}_{s} \qquad (A.16)$$

with fixed grid methods, the surface tension force, $\vec{F}_{s}$, according to the CSF model for constant surface tension is defined as

$$\vec{F}_{s}=\sigma\,\kappa\,\delta_{s}\,\vec{n}, \qquad (A.17)$$

where δ_{s} is the Dirac delta function, which has finite value at the interface and zero values everywhere else away from the interface,

$$\vec{n}=\frac{\nabla c}{\left|\nabla c\right|}, \qquad\qquad (A.18a)$$

$$\kappa = \nabla \cdot \vec{n} \, , \qquad\qquad\qquad \text{(A.18b)}$$

and c is a parameter defined based on the method used. With the LS method, c is replaced by distance function, ψ. Because ψ is a continuous function, the interface normal vector according to Eq. (A.18a) can be calculated quite accurately. With the VOF method, on the other hand, c is replaced by volume fraction α. Because of surface discontinuities, this model precludes accurate determination of the normal vector. With the FT method, Eq. (A.17) uses interfacial curvature along the finer grid to calculate surface tension force. The force is then distributed over the fixed grid using Peskin's *immersed boundary method* [150] to conserve force when moving across grids.

Another promising method to calculating surface tension force effects is the *Continuum Surface Stress* (CSS) model by Lafaurie *et al*. [151], which has certain advantages compared to the CFS model. The CSS model features conservative formatting, and does not require explicit calculation of curvature, rendering it especially useful for sharp corners.

Even though surface tension models have been successfully used in numerical schemes, they are known to artificially induce *spurious currents* when capturing the interface. These are non-physical vortex currents induced close to the interface, resulting in unrealistic deformations and therefore compromising interface curvature calculations. These currents are caused mostly by inability to balance pressure gradient with surface tension force. Recently, investigators have recommended methods to suppress these spurious currents [152,153]

While finite thickness schemes are solved using surface tension force, the PF method uses fluid free energy. An example of this approach is a study by Jacqmin *et al*. [146],

where surface tension force is calculated according to

$$\vec{F}_s = -C_{PF}\nabla\varphi,$$ (A.19)

φ being the chemical potential defining the rate of change of free energy.

A.4 <u>Implementing Mass Transfer in Two-Phase Schemes</u>

A.4.1 <u>Different approaches to Solving Conservation Equations and accounting for Interfacial Mass, Momentum and Energy Transfer</u>

Phase change methods add multiple complications to two-phase schemes developed to track or capture the interface. In the presence of interfacial mass transfer, interface topology tends to be less stable, and numerical schemes must be able to tackle this issue. Phase change methods also require accurate estimation and implementation of mass, momentum, and heat transfer across the interface. With phase change, mass transfer rate, $\dot{m}$, normal to the interface, which is positive for evaporation and negative for condensation, is given by

$$\dot{m} = \rho_g\left(\vec{u}_g - \vec{u}_i\right).\vec{n} = \rho_f\left(\vec{u}_f - \vec{u}_i\right).\vec{n}.$$ (A.20)

The jump conditions for velocity, momentum transfer rate, and energy transfer rate across the interface are given, respectively, by

$$\left(\vec{u}_g - \vec{u}_f\right).\vec{n} = \dot{m}\left(\frac{1}{\rho_g} - \frac{1}{\rho_f}\right),$$ (A.21)

$$\dot{m}\left(\vec{u}_g - \vec{u}_f\right) = \left(\tau_g - \tau_f\right).\vec{n} - \left(p_g - p_f\right)\mathbf{I}.\vec{n} + \sigma\kappa\vec{n},$$ (A.22)

and
$$q_i'' = \dot{m}\,h_{fg},$$ (A.23)

where I is an Idemfactor, and the energy jump relation accounts only for latent heat transfer transfer.

In a two-phase scheme with phase change, the above jump conditions are usually used at the interface, while the mass, momentum and energy conservation equations given by Eqs. (A.1), (A.2) and (A.3), respectively, are solved for the interior of each phase. The VOF method employs separate conservation equations for liquid and vapor that account for mass transfer between phases using mass source and mass sink terms. The continuity equations in the VOF method are expressed as

$$\frac{\partial}{\partial t}\left(\alpha_k \rho_k\right) + \nabla \cdot \left(\alpha_k \rho_k \vec{u}_k\right) = S_k , \qquad (A.24)$$

where subscript k refers to either liquid, f, or vapor, g, and S_k [kg/m^{3}s] is the mass source term for phase k associated with the phase change.

As will become evident from the large pool of studies to be reviewed below, there is no universal approach to formulating a numerical solution to a two-phase flow problem involving phase change. When working with a fixed grid and using separate continuity equations for the two phases, phase change is accounted for using mass source and mass sink terms, or mass jump conditions are applied to the two phases separately. If the momentum equations are solved in combined form for both phases, as given by Eq. (A.2), then only surface tension forces need to be included in the governing equation, and the other terms in Eq. (A.22) need not be used. This is because pressure, shear stress and momentum flux due to mass transfer are already accounted for. Like the continuity equation, when the energy equation is solved in combined form, energy transfer due to phase change can be accounted for with either source terms or jump conditions along the

interface. Son and Dhir [135] adopted a yet different approach is which mass source was used in the continuity equation, but not the energy equation. They solved the energy equation by setting the temperature of the saturated phase equal to saturation temperature to ensure that energy transfer at the interface due to phase change is correctly account for.

Therefore, it is important to identify differences between solution procedures adopted by different researchers and appreciate the physical basis behind these procedures.

A.4.2 Mass Transfer Models

A.4.2.1 Energy Jump Condition

One of the most popular tools to account for interfacial phase change is the Rankine-Hugoniot jump condition [68]. Here, mass transfer rate is based on net energy transfer across the interface, including heat transfer due to conduction in the two phases to or from the interface.

$$q_i'' = \vec{n} \cdot \left(k_f \nabla T_f - k_g \nabla T_g \right) = \dot{m} \, h_{fg}, \qquad (A.25)$$

where $\dot{m}$ [kg/m^{2}s] is the mass flux due to phase change at the interface. Eq. (A.25) neglects the small kinetic energy contributions affecting micro-scale mass transfer. A substitute version for Eq. (A.25) is [154]

$$q_i'' = \left(k_f \left. \frac{\partial T}{\partial \vec{n}} \right|_f - k_g \left. \frac{\partial T}{\partial \vec{n}} \right|_g \right) = \dot{m} \, h_{fg}. \qquad (A.26)$$

The volumetric mass source term, S [kg/m^{3}s], is determined according to the relation

$$S_g = -S_f = \dot{m} \left| \nabla \alpha_g \right|, \qquad (A.27)$$

where $\left|\nabla\alpha_g\right|$ for a particular cell of the computational domain is obtained from

$$\left|\nabla\alpha_g\right| = \frac{1}{V}\int\left|\nabla\alpha_g\right|dV = \frac{A_{int}}{V},$$ (A.28)

where A_i is the interfacial area in the cell and V the cell volume.

In simplified form, Nichita and Thome [155] determined the volumetric mass source term from gradients of temperature and void fraction of liquid in the interfacial cell,

$$S_g = -S_f = \frac{k\left(\nabla T.\nabla\alpha_f\right)}{h_{fg}},$$ (A.29)

where k is the effective thermal conductivity given by Eq. (A.6c). Ganapathy *et al*. [156] used a similar formulation for the source term. Eq. (A.29) is less accurate than Eqs. (A.25) and (A.26) because of the simplifying assumptions used. For example, use of effective thermal conductivity is not physical for calculating phase change at the interface since mass transfer should not depend on conductivity of the saturated phase. During boiling, the liquid phase is saturated and vapor phase unsaturated, as it can be superheated. During condensation, the vapor phase is saturated and liquid phase unsaturated, as it can be subcooled. To correct this error for both condensation and boiling situations, where saturated and unsaturated phases are present, Sun *et al*. [157] recommended an alternative simplified form based on the assumptions of negligible heat conduction in the saturated vapor ($k_{sat} = 0$) due to constant vapor temperature, and linear temperature variation in the subcooled liquid near the interface,

$$S_{sat} = -S_{unsat} = \frac{2k_{unsat}\left(\nabla T.\nabla\alpha_{unsat}\right)}{h_{fg}}.$$ (A.30)

Use of simplified source term models is quite common because they simplify source term calculation and implementation in commercial software packages, since they rely only on volume fraction and temperature gradient information within the current cell. Because these models are based on specific assumptions, they should only be used after confirming the suitability of these assumptions to the specific phase change problem being addressed.

While the phase change model based on the Rankine-Hugoniot jump condition is physically based and therefore free from empiricism, it does not account for kinetic energy contributions. Also, notice that $\left| \nabla \alpha_g \right|$ in Eq. (A.27) is non-zero only at the interface, which limits mass transfer at the interface. This condition cannot tackle subcooled inlet boiling and superheated inlet condensation situations with no preexisting interfaces. Use of this model has been seen in situations involving nucleate pool boiling, film boiling, flow boiling, and flow condensation.

A.4.2.2 Schrage Model

Schrage [69] used kinetic theory of gases to propose a mass transfer model in the 1950s based on the Hertz-Knudsen equation [70]. He assumed vapor and liquid are in saturation states, but allowed for jump in temperature and pressure across the interface, i.e., $T_{sat}(p_f)$ $= T_{f,sat} \neq T_{sat}(p_g) = T_{g,sat}$. Kinetic theory of gases was used to relate the flux of molecules crossing the interface during phase change to the temperature and pressure of the phases. A fraction γ is used to define the number of molecules changing phase and transferring across the interface, and $1 - \gamma$ the fraction reflected. Relations for γ_c and γ_e, corresponding to situations involving condensation and evaporation, where defined, respectively, as

$$\gamma_c = \frac{number\ of\ molecules\ absorbed\ by\ liquid\ phase}{number\ of\ molecules\ impinging\ on\ liquid\ phase} \qquad \text{(A.31a)}$$

and $$\gamma_e = \frac{number\ of\ molecules\ transferred\ to\ vapor\ phase}{number\ of\ molecules\ emitted\ from\ liquid\ phase}. \qquad \text{(A.31b)}$$

According to the above definitions, $\gamma_c = 1$ corresponds to perfect condensation, where all impinging molecules are absorbed by the liquid phase. Conversely, $\gamma_e = 1$ represents perfect evaporation, where all emitted molecules are transferred to the vapor phase. The net mass flux across the interface, $\dot{m}$ [kg/m²s], is determined from the difference between liquid-to-vapor and vapor-to-liquid mass fluxes,

$$\dot{m} = \frac{2}{2-\gamma_c}\sqrt{\frac{M}{2\pi R}}\left[\gamma_c \frac{p_g}{\sqrt{T_{g,sat}}} - \gamma_e \frac{p_f}{\sqrt{T_{f,sat}}}\right], \qquad \text{(A.32)}$$

where R is the universal gas constant (8.314 J/mol.K), M the molecular weight, p_g and $T_{g,sat}$ are the vapor's pressure and saturation temperature at the interface, and p_f and $T_{f,sat}$ the liquid's pressure and saturation temperature, also at the interface. Generally, the evaporation and condensation fractions are considered equal and represented by a single *accommodation coefficient γ*. This simplifies Eq. (A.32) to the following form:

$$\dot{m} = \frac{2\gamma}{2-\gamma}\sqrt{\frac{M}{2\pi R}}\left[\frac{p_g}{\sqrt{T_{g,sat}}} - \frac{p_f}{\sqrt{T_{f,sat}}}\right]. \qquad \text{(A.33)}$$

A major difficulty in using the above relation is that γ is an unknown quantity, and a few investigators have attempted to determine its value by comparing model predictions to experimental data. For example, using published data, Marek and Straub [71] concluded that γ is between 0.1 to 1 for jets and moving films, and below 0.1 for stagnant liquid surfaces. Also using information from published literature, Paul [158] recommended a

value between 0.02 and 0.04 for water during evaporation. Rose [90] recommended a value close to unity for dropwise condensation based on a review of available experimental data. Wang *et al*. [159] suggested an experimentally determined value of $\gamma = 1$ for non-polar liquids. Hardt and Wondra [88] and Magnini *et al*. [89] also used $\gamma = 1$ for film boiling. For evaporating falling films, as discussed in Chapter 7, I recommend a value of $\gamma = 0.1$, but indicate that higher values in the range of $\gamma = 0.1 - 1$ do not compromise the model's predictive accuracy, but do influence numerical stability. Doro [160] used $\gamma = 0.5$ for evaporating falling films. Kartuzova and Kassemi [91] recommended a low value of $\gamma = 0.01$ for turbulent phase change in a cryogenic storage tank in microgravity. Huang *et al*. [161] used a value of $\gamma = 0.03$ for bubbly flow of R141b in a serpentine tube.

Tanasawa [72] further simplified the Schrage model by suggesting that, for small interfacial temperature jump, mass flux is linearly dependent on temperature jump between the interface and vapor phase. This simplifies the model to the form

$$\dot{m} = \frac{2\gamma}{2-\gamma}\sqrt{\frac{M}{2\pi R}}\left[\frac{\rho_g h_{fg}\left(T - T_{sat}\right)}{T_{sat}^{3/2}}\right],\tag{A.34}$$

where T_{sat} is determined at local pressure. The volumetric mass source term for both the Schrage model, Eq. (A.32), and Tanasava model, Eq. (A.34), is given by

$$S_g = -S_f = \dot{m}\left|\nabla\alpha_g\right|.$$

Tansawa's model is a good approximation of the original Schrage formulation for most phase change phenomena other than at micro and nano scales, where interfacial temperature jump cannot always be neglected. At those scales, interfacial curvature can cause appreciable Laplace pressure, and Vander Walls forces on solid-liquid interfaces can become sufficiently significant to cause non-equilibrium between the phases [162]. In their

investigation of evaporation across a liquid-vapor interface, Hardt and Wondra [88]

provided a simple method to assess deviation of interfacial temperature from T_{sat}. As

shown in Fig. A.2, they plotted the deviation of dimensionless interfacial temperature

versus the dimensionless parameter $x = \eta_e d / k_f$, where η_e is the evaporation heat transfer

coefficient given by

$$\eta_e = \frac{2\gamma}{2-\gamma} \frac{h_{fg}^2}{\sqrt{2\pi R_{gas}}} \frac{\rho_g}{T_{sat}^{3/2}},$$
(A.35)

and d the distance of the liquid-vapor interface from the wall. Using the example of water

evaporation at atmospheric conditions with an accommodation coefficient of $\gamma = 0.1$, they

showed deviation of interfacial temperature increases with decreasing d. The

dimensionless deviation is close to 0.01 at $d \approx 81$ μm, and increases to 0.1 at $d \approx 7$ μm. It

is therefore important to assess such deviations in interfacial temperature before opting to

use Tanasawa's simplified formulation to model micro- and nano-scale phenomena.

Overall, the Schrage model is both physically based and accounts for kinetic energy

effects. As indicated earlier, a key challenge in using this model is deciding which value

to use for the accommodation coefficient in the range of $0 < \gamma \leq 1$. The optimum value for

this coefficient is obtained from experimental data. In chapter 7, I recommended another

procedure to setting the value of γ based on deviation of interfacial temperature from T_{sat}.

This procedure is initiated by setting $\gamma = 0$, then gradually increasing γ until the deviation

between interface temperature and T_{sat} is minimized to an acceptable level. Another

challenge in using the Schrage model is the dependence of volumetric mass source term on

$|\nabla\alpha_g|$, which has non-zero value only at the interface, allowing phase change to occur
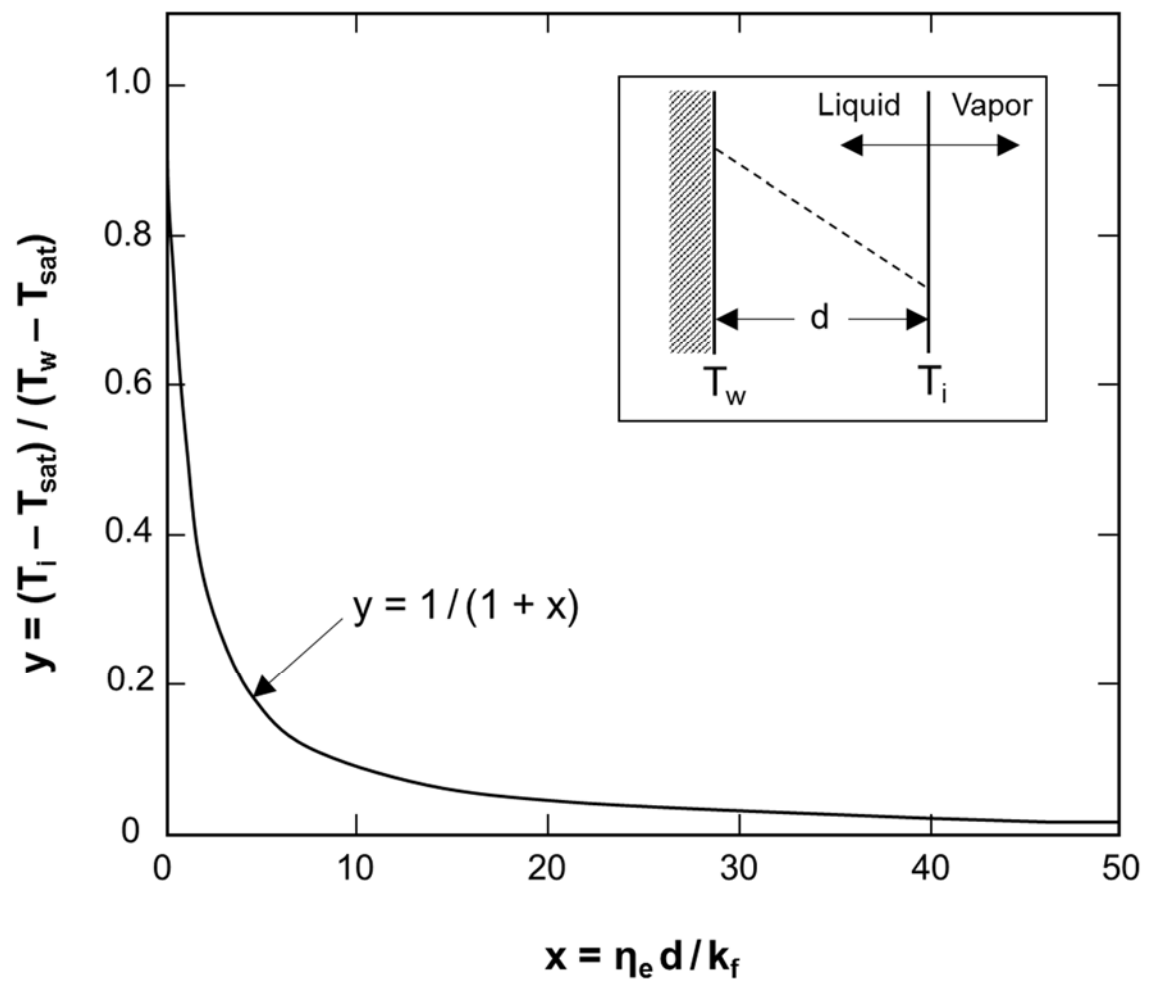
Fig. A.2: Variation of deviation of dimensionless interface temperature with dimensionless distance from the wall to the interface. Adapted from Hardt and Wondra [88].

only along the two-phase interface. This model tends to maintain T_{sat} because deviation of interfacial temperature from T_{sat} increases the rate of mass transfer along the interface, which in turn reduces the temperature deviation. The Schrage model has been used to investigate nucleate pool boiling, flow boiling, film boiling, and evaporating falling films.

A.4.2.3 Lee Model

Lee [73] developed a simplified saturation model for evaporation and condensation processes. The key premise of this model is that phase change is driven primarily by deviation of interfacial temperature from T_{sat}, and phase change rate is proportional to this deviation. Therefore, phase change occurs while maintaining temperatures of the saturated phase and interface equal to T_{sat}. The model assumes mass is transferred at constant pressure and quasi-thermo-equilibrium state according to the following relations:

$$S_g = -S_f = r_i\, \alpha_g \rho_g \frac{\left(T - T_{sat}\right)}{T_{sat}} \text{ for condensation } (T < T_{sat}) \qquad \text{(A.36a)}$$

and
$$S_g = -S_f = r_i\, \alpha_f \rho_f \frac{\left(T - T_{sat}\right)}{T_{sat}} \text{ for evaporation } (T > T_{sat}), \qquad \text{(A.36b)}$$

where r_i is an empirical coefficient called *mass transfer intensity factor* and has the units of s^{-1}. While the Lee model consistently aims to decrease the deviation from T_{sat}, there is great variability in the choice of r_i value. Researchers have used a very wide range of values, ranging from 0.1 to 1×10^7 s^{-1}, in attempts to achieve least deviation. Overall, optimum value of r_i depends on many factors, including, but not limited to, specific phase-change phenomenon, flow rate, mesh size, and computational time step. A key challenge in using the Lee model is that different r_i values have been recommended by different

researchers for similar experimental configurations, depending on specific setup of numerical model used.

Chen *et al*. [163] suggested a substitute version to the Lee model, given by

$$S_g = -S_f = r_{i,m} \alpha_g \rho_g \left(T - T_{sat}\right) \text{ for condensation } (T < T_{sat}), \qquad \text{(A.37a)}$$

and

$$S_g = -S_f = r_{i,m} \alpha_f \rho_f \left(T - T_{sat}\right) \text{ for evaporation } (T > T_{sat}), \qquad \text{(A.37b)}$$

eliminating T_{sat} from numerators of the source terms, and employing a modified mass transfer intensity factor, $r_{i,m}$.

While many researchers have used the Lee model in simulations, some [164-166] have shown that this model is essentially a derivative of the Schrage model. Overall, the Lee model is a simplified saturation model that does not set limits on the value of mass transfer intensity factor r_i. While this lack of specificity is advantageous in that it allows investigators to assign their own optimum value, it also points to a lack of strong physical basis for the model. The model's tendency to maintain saturation temperature in both the saturated phase and along the interface serves as a good starting point to investigating rather complicated phase change phenomena without delving into the complex physics of the configuration in question. Unlike the Schrage model, which allows phase change only along the interface, the Lee model allows for phase change both along the interface and within the saturated phase. This is evidenced by the use of void fraction multipliers in the source terms, rendering the Lee model capable of accommodating phase change both within the vapor phase and along the interface for condensation, Eq. (A.36a), and within the liquid phase and along the interface for evaporation, Eq. (A.36b). This feature allows

the model to simulate full scale flow boiling and flow condensation processes with relative ease, albeit with rather reduced accuracy.

A summary of the three mass transfer models discussed in sections A.4.2.1-A.4.2.3, along with their important assumptions and applications, is provided in Table A.1.

A.4.2.4 <u>Other Techniques for Simulating Mass Transfer</u>

Other methods have also been used to simulate phase change, which rely on experimental data or heat transfer correlations. Zhuan and Wang [167] used a Marangoni heat flux correlation [168,169] to calculate mass transfer rate during the initial phase of nucleate boiling, and a bubble growth rate correlation [170,171] to estimate mass transfer during the subsequent phase. Jeon *et al*. [172] used an experimental heat transfer correlation developed by Kim and Park [173] for condensation to estimate source terms in their investigation of subcooled boiling. Krepper *et al*. [174] used the following simple relations for mass transfer flux to model subcooled flow boiling:

$$\dot{m}_f = \max\left\{\frac{h_i\left(T_{sat}-T\right)}{h_{fg}}, 0\right\} \text{ for subcooled liquid at the interface } (T < T_{sat}), \quad \text{(A.38a)}$$

and
$$\dot{m}_g = \max\left\{\frac{h_i\left(T-T_{sat}\right)}{h_{fg}}, 0\right\} \text{ for superheated liquid at the interface } (T > T_{sat}), \text{(A.38b)}$$

where h_i is the heat transfer coefficient given by Ranz and Marshall [175]. Because these methods are correlation based, they should only be applied to the range of, and with fluids for which these correlations were developed. Zu *et al*. [176] adopted a different empirical

Table A.1: Popular mass transfer models used in phase change simulations.

Mass Transfer Model	Energy jump condition [68]	Schrage model [69]	Lee model [73]
General form	$$\dot{m}_g = -\dot{m}_f = \frac{\vec{n}.\left(k_f \nabla T_f - k_g \nabla T_g\right)}{h_{fg}}$$	$$\dot{m}_g = -\dot{m}_f = \frac{2}{2-\gamma_c}\sqrt{\frac{M}{2\pi R}}\left[\gamma_c \frac{p_g}{\sqrt{T_{g,sat}}} - \gamma_e \frac{p_f}{\sqrt{T_{f,sat}}}\right]$$	$$S_g = -S_f = r_i \alpha_g \rho_g \frac{\left(T - T_{sat}\right)}{T_{sat}}$$ for condensation ($T < T_{sat}$) $$S_g = -S_f = r_i \alpha_f \rho_f \frac{\left(T - T_{sat}\right)}{T_{sat}}$$ for evaporation ($T > T_{sat}$).
Simplified form	$$S_g = -S_f = \frac{k\left(\nabla T \cdot \nabla \alpha_f\right)}{h_{fg}} \quad [155]$$	$$\dot{m}_g = -\dot{m}_f = \frac{2\gamma}{1-\gamma}\sqrt{\frac{M}{2\pi R}}\left[\frac{\rho_g h_{fg}\left(T - T_{sat}\right)}{T_{sat}^{3/2}}\right] \quad [72]$$	
Basis	- Physics-based model relying on energy jump across vapor-liquid interface	- Physics-based model based on kinetic theory of gases	- Simplified model with phase change defined such that saturating conditions at the interface can be achieved
Kinetic energy contribution	- Does not account for kinetic energy contribution	- Accounts for kinetic energy contribution	- Does not account for kinetic energy contribution
Interfacial temperature	- Different methods/assumptions in numerical scheme used to maintain interfacial temperature at T_{sat}	- Aims to maintain interfacial temperature at T_{sat} with the aid of empirical coefficient γ	- Aims to maintain interfacial temperature at T_{sat} with the aid of empirical coefficient r_i
Source term implementation	- Implemented at vapor-liquid interface - Requires identifiable interface-for model to predict phase change	- Implemented at vapor-liquid interface - Requires identifiable interface-for model to predict phase change	- Implemented at vapor-liquid interface and in saturated phase - Can perform bulk phase change calculations - Does not require preexisting interface

Mass Transfer Model	**Energy jump condition** [68]	**Schrage model** [69]	**Lee model** [73]
Empirical coefficients		- Empirical coefficient γ needs to be assigned - Value of γ is usually based on experimental data	- Empirical coefficient r_i needs to be assigned - Value of r_i is based on minimizing deviation of interface temperature from T_{sat}
Phase change configurations addressed in literature	- Nucleate pool boiling - Film boiling - Flow boiling - Condensation	- Nucleate pool boiling - Film boiling - Flow boiling - Evaporating falling films	- Flow boiling - Condensation

approach to model "pseudo-nucleate boiling," where vapor was artificially injected through an inlet located on the heated wall to simulate a nucleation site, followed by vapor generation at the bubble and superheated wall contact area based on experimental observations [177]. Using the VOF model to capture the interface during flow condensation, Zhang *et al.* [178] incorporated a large artificial source term to force interface temperature to T_{sat}, then calculated energy and mass source terms using the updated temperature field.

Overall, while empirical models do simplify numerical solutions, they are often derived for specific fluids and valid over specific ranges of flow parameters. They are also based on specific assumptions that may not be valid for phase change configurations different from the ones they are based upon.

A.4.3 <u>Incorporating Source Terms at Two-Phase Interface</u>

There are multiple ways in which source terms are incorporated in the computational grid. A common method is to include them in cells crossing the interface. This method was used in conjunction with the VOF scheme by Welch and Wilson [179], who calculated the mass source term by combining interfacial relations for heat transfer and continuity across the interface.

$$\left(\vec{u}_g - \vec{u}_i\right).\vec{n} - \left(\vec{u}_f - \vec{u}_i\right).\vec{n} = \left(\frac{1}{\rho_g} - \frac{1}{\rho_f}\right)\frac{q_i^{''}}{h_{fg}}, \tag{A.39}$$

where the mass flux source term is given by $q_i^{''}/h_{fg}$.

Another common method is to smear the source term across a finite thickness of the interface. This is the method that was adopted by Son and Dhir [135] in their LS scheme. The mass flux source term, $\dot{m}$, appears in the following continuity equation:

$$\nabla . \vec{u} = \left(\frac{1}{\rho_g} - \frac{1}{\rho_f} \right) \dot{m} . \nabla H , \qquad (A.40)$$

where H is the Heaviside function described earlier. Because H in their study varies across three cells, the mass term is smeared across the same three cells. Another approach to smearing the source term was recently recommended by Hardt and Wondra [88]. They first mathematically smeared source and sink terms across multiple cells on the grid around the interface. They then artificially shifted the source and sink terms towards the individual phases. Figure A.3(a) shows how Kunkelmann [180] smeared the source and sink terms using the Hardt and Wondra technique. The smearing process is initiated with a sharp interface, with the source and sink terms concentrated at the interface. After the smearing process is completed, the source (positive) terms and sink (negative) terms are shifted away from the interface. Figure A.3(b) provides a 1-D depiction of cells around the interface, with source and sink terms after the smearing. Figures A.3(c) and A.3(d) show volume fraction and corresponding mass source and sink terms across multiple cells, respectively. During evaporation, for example, the generated mass of vapor is concentrated on the vapor side of the grid, and the lost mass of liquid on the liquid side. While this method correctly conserves mass, it is not physically correct, since it artificially shifts the mass generation or loss that occur at the interface towards the respective phases. Nonetheless, this method does appear to improve stability of numerical schemes. This method can also be applied to
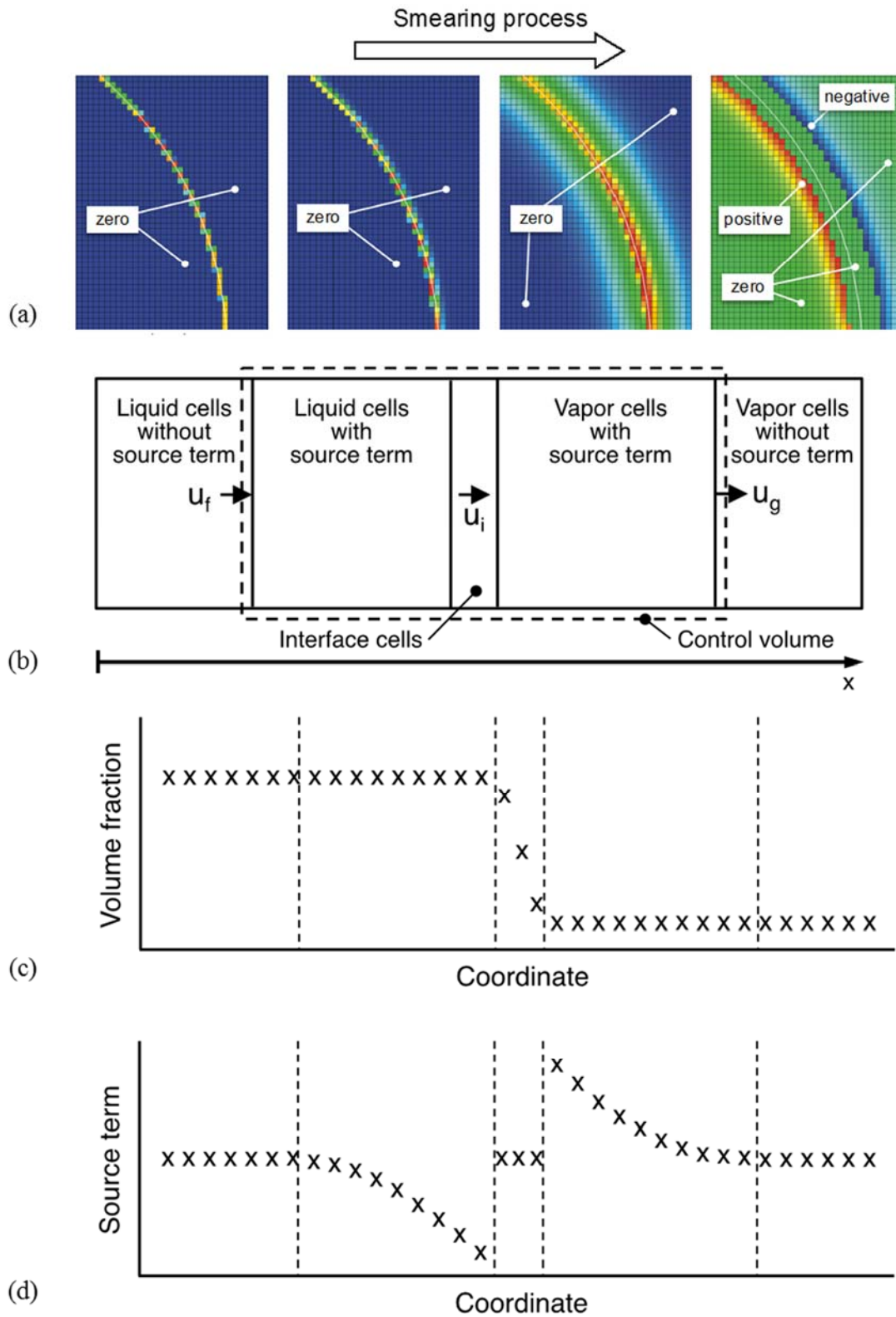
Fig. A.3: (a) Illustration of smearing process around two-phase interface. (b) 1-D control volume of smeared interface. (c) Variation of volume fraction in control volume depicted in part (b). (d) Source term distribution in control volume depicted in part (b). Adapted from Kunkelmann [180].

condensation configurations by shifting the generated mass of liquid to liquid side, and lost mass of vapor to vapor side.

A third approach to implementing mass transfer was adopted by Juric and Tryggvason [181], who solved iteratively for velocity of the interface markers. This method can accurately capture interfacial topologies in simple two-phase situations, but less so in complicated scenarios like flow boiling.

A.4.4 <u>Early Implementation of Phase Change across Numerical Schemes</u>

The past few decades have witnessed widespread implementation of phase change models into a variety of computational schemes. A variety of test cases have been investigated to assess the validity of the phase change models used. They include 1-D Stephan problem [68,88,135,179,182], 1-D sucking interface problem [179,182,183] 2-D horizontal film boiling [135,179,181], 2-D and/or 3-D growth of spherical vapor bubble in superheated liquid [182,183], 2-D and/or 3-D bubble growth due to gravity [182], and 2-D and/or 3-D bubble growth and departure from heated wall [182-184].

Welch and Wilson [179] used the VOF method with Youngs' enhancement [127] for interface advection and phase change based on energy jump condition to solve the 1-D Stephan problem, 1-D sucking interface problem, and 2-D film boiling problem. Son and Dhir [135] used the LS method developed by Sussman *et al*. [123] and phase change based on energy jump condition to investigate interface evolution during film boiling. While use of Continuum Surface Force (CSF) model in the VOF and LS methods works well in flows without phase change, it is less accurate with phase change. To solve problems with CSF, Nguyen *et al*. [185] and Gibou *et al*. [68] used the ghost-fluid (GF) model in conjunction

with the LS scheme and phase change based on energy jump condition. As indicated earlier, the GF model involves implicit representation of the Rankine-Hugoniot jump condition at the interface by adding an artificial fluid cell. For Lagrangian schemes, Welch [186] and Son and Dhir [187] implemented phase change using triangular grid and moving coordinate scheme, respectively. Welch used a phase change model based on energy jump condition. Tomar *et al*. [188] implemented phase change in the CLSVOF scheme to investigate film boiling and bubble formation. Juric and Tryggvason [181] extended the FT scheme to film boiling with phase change based on Tanasawa's model. Shin and Juric [154] used the FT scheme with level contour reconstruction in 3-D domain with phase change based on energy jump condition to investigate film boiling. Sato and Niceno [182] implemented phase change using the mass-conservative CIP method to simulate bubble growth and nucleate boiling with phase change based on energy jump condition. Jamet *et al*. [189] constructed a phase-field model for liquid-vapor flows with phase change. Dong *et al*. [190] implemented phase change in the phase-field LB method by calculating heat and mass transfer using the thermal LB method by Inamuro *et al*. [191] combined with a multiphase model by Zheng *et al*. [192]. Zhang and Chen [193] implemented phase change in a pseudopotential LB approach to model nucleate boiling.

A.5 Applications in Boiling and Condensation

A.5.1 Boiling

A.5.1.1 Bubble Nucleation, Growth and Departure

The nucleate boiling process is characterized by liquid-to-vapor phase change from nucleation sites on a heated wall. A finite degree of wall superheat is necessary for

nucleation to commence at the onset of nucleate boiling (ONB). Nucleate boiling at low heat fluxes is characterized by discrete bubbles growing and departing from the nucleation sites. High heat fluxes increase active nucleation site density, with bubbles showing tendency to merge laterally. Important considerations necessary to simulate these flows include nucleation site density and heated wall thermal response, in addition of course to bubble dynamics and heat and mass transfer. Table A.2 summarizes published studies concerning simulation of bubble nucleation, growth, and departure during boiling.

In their numerical study of bubble growth, Lee and Nydahl [227] used simplified depiction where the bubble was assumed to acquire hemispherical shape, trapping a wedge-shaped liquid micro-layer at the wall, whose thickness was based on a model by Cooper and Lloyd [228]. Welch [229] used a finite-volume method and a moving unstructured mesh in conjunction with an interface tracking scheme to predict bubble growth, but did not simulate micro-layer formation. In most studies, the thin liquid micro-layer is considered a region of extremely high heat transfer coefficient [195].

Dhir and co-workers published a series of very successful simulations of bubble growth and departure in pool boiling, including the first complete simulation of saturated nucleate pool boiling by Son *et al*. [184]. They used the LS scheme and implemented phase change based on energy jump condition in 2-D axisymmetric domain that was subdivided into micro and macro regions as shown in Fig. A.4(a). This is a form of multiscale modeling, where a separate model is used to solve the high-resolution portion of the domain, avoiding the need for finer mesh in this region. Lubrication theory [194,195] was used to model radial variation of the micro-layer thickness. Conservation of mass, momentum and energy

Table A.2: Summary of computational studies related to bubble nucleation, growth and departure in boiling processes.

Author(s)	Boiling Configuration	Test Fluid	Multiphase Scheme	Mesh[a]	Mass Source Terms[b]	Remarks
				Level-Set (LS) Method		
Son *et al.* (1999) [184]	Single bubble, nucleate pool boiling	Water	LS in 2-D axisymmetric domain	$R/l_o \times H/l_o$: 1×3 where l_o is characteristic length defined as $$l_0 = \sqrt{\frac{\sigma}{g(\rho_f - \rho_g)}}$$ Mesh: 96×288	$$\dot{m}_g = \frac{k \cdot \nabla T}{h_{fg}}$$ where $k^{-1} = k_f^{-1} H$ and H is Heaviside function from Sussman *et al.* [123]	– First paper involving complete numerical simulation of bubble growth, including micro-layer effects – Uses lubrication theory [194,195] to simulate micro-layer evaporation – Predicts cyclical variations in wall heat flux – Bubble growth pattern compares well with experimental observations – Shows bubble growth rate increases with wall superheat
Singh and Dhir (2000) [196]	Single bubble, subcooled nucleate pool boiling	Water	LS in 2-D axisymmetric domain	$R/l_o \times H/l_o$: 1×3 Mesh: 96×288	$$\dot{m}_g = \frac{k \cdot \nabla T}{h_{fg}}$$ where $k^{-1} = k_f^{-1} H$	– Bubble growth investigated by modifying earlier model [184] to account for subcooling effects – Predicts higher subcooling decreases bubble growth rate and departure diameter, and increases bubble growth period
Abarajith and Dhir (2002) [197]	Single bubble, nucleate pool boiling with varying contact angle	Water, PF 5060	LS in 2-D axisymmetric domain	$R/l_o \times H/l_o$: 1×4 Mesh: 98×298	$$\dot{m}_g = \frac{k \cdot \nabla T}{h_{fg}}$$ where $k^{-1} = k_f^{-1} H$	– Bubble growth investigated by modifying earlier model [184] to account for contact angle (1-90°) effects – Predicts increasing contact angle increases bubble departure diameter – Good agreement achieved with Fritz correlation [198] – Because of small contact angle of PF 5060, smaller departure diameter predicted for PF 5060 compared to water

Son *et al.* (2002) [199]	Multiple bubble vertical merging, nucleate pool boiling	Water	LS in 2-D axisymmetric domain	Domain: 2.5 mm × 10 mm Mesh cell width: 26 μm	$\dot{m}_g = \dfrac{k \cdot \nabla T}{h_{fg}}$ where $k^{-1} = k_f^{-1} H$	– Studied bubble growth and merger from same nucleation site using model similar to [184] – Bubble vertical merger lead to premature bubble departure of lower bubble – Bubble merger process compares well experimental observations – Increasing wall superheat increases vapor removal rate
Mukherjee and Dhir (2004) [200]	Multiple bubble lateral merging, nucleate pool boiling	Water	LS in 3-D domain	$L/l_o × W/l_o × H/l_o$: 1 × 1 × 2 Mesh: 72 × 72 × 144	$\dot{m}_g = \dfrac{k_f \cdot \nabla T}{h_{fg}}$ uses $k^{-1} = k_f^{-1} H$ in energy equation	– Studied bubble growth and merger laterally across multiple nucleation sites using model similar to [184] – Different lateral bubble orientations investigated – Bubble merger predicted to increase heat transfer rate – Good agreement in bubble shape and growth rate with experimental observations
Aparajith *et al.* (2006) [201]	Single bubble and multiple bubbles, nucleate pool boiling in reduced gravity	Water, PF 5060	LS in 3-D domain	For 1×10⁻⁵g_e: Domain: 114 mm × 114 mm × 229 mm Mesh: 96 × 96 × 192 For 1×10⁻²g_e: Domain: 7.34 mm × 7.34 mm × 14.68 mm Mesh: 192 × 192 × 384	$\dot{m}_g = \dfrac{k \cdot \nabla T}{h_{fg}}$ where $k^{-1} = k_f^{-1} H$	– Studied bubble growth rate and merger in reduced gravity using model similar to [184] – Numerical results show, for water, departure diameter $D_d \approx g^{-0.5}$ and growth time, $t_d \approx g^{-0.93}$, and, for PF 5060, $D_d \approx g^{-0.42}$ and $t_d \approx g^{-0.82}$ – Bubble departure diameter and time period reduced with reduced cavity spacing, with minimum around 0.25 D_d (departure diameter for single bubble) – Similar Nusselt numbers achieved for two gravity cases

Li and Dhir (2007) [202]	Single bubble, nucleate flow boiling	Water	LS in 3-D domain	Mesh: 144 × 96 × 48	$\dot{m}_g = \dfrac{k \cdot \nabla T}{h_{fg}}$ where $k^{-1} = k_f^{-1} H$	– Studied bubble growth in slow flow boiling using model similar to [184] – Velocity of liquid varied from 0.076 – 0.23 m/s, orientations from horizontal to vertical upflow, gravity from $0.0001g_e$ to $1g_e$ – Upstream and downstream contact angles provided as input to model – Bubble motion captured well by model – Showed bubble diameter decreases with increasing flow velocity, but increases when gravity component perpendicular to flow direction is decreased – Showed high flow velocity negates effect of gravity on bubble liftoff diameter and growth period
Son and Dhir (2008) [203]	Nucleate pool boiling at high heat fluxes	Water	LS with ghost fluid (GF) method in 2-D and 3-D domains	Non-uniform grid away from wall For 2-D domain: $L/l_o \times H/l_o$: 2 × 50 Mesh: 192 × 4800 For 3-D domain: $L/l_o \times W/l_o \times H/l_o$: 2 × 2 × 20 Mesh: 64 × 64 × 640	$\dot{m}_g = \dfrac{k_f \cdot \nabla T_f}{h_{fg}}$ uses $k^{-1} = k_f^{-1} F_\psi$ in energy equation, where F_ψ is fractional function [203]	– Studied nucleate boiling using model similar to [184] in fine 2-D and coarse 3-D domains – Showed high wall superheat of 25°C causes multiple bubble mergers, leading to formation of large vapor columns – Heat flux predictions in 2-D domain within ±25% of correlation
Lee et al. (2010) [204]	Nucleate pool boiling from microcavity	Water	LS with ghost fluid (GF) method in 2-D axisymmetric domain	Non-uniform grid away from wall Domain: 5 mm × 14.2 mm Mesh cell spacing: 0.01 mm	$\dot{m}_g = \dfrac{k_f \cdot \nabla T_f}{h_{fg}}$ uses $k^{-1} = k_f^{-1} F$ in energy equation	– Studied nucleate boiling on microcavity including simplified micro-layer model [183] and effects of solid wall – Different cavity shapes compared, and truncated conical cavity found more effective for nucleation than cylindrical and conical cavities

Lee and Son (2011) [205]	Nucleate pool boiling on microstructured surface	Water	LS with ghost fluid (GF) method in 2-D axisymmetric domain	Domain: 1.92 mm × 5.76 mm Mesh cell spacing: 0.01 mm	$\dot{m}_g = \dfrac{k \cdot \nabla T_f}{h_{fg}}$ where $k^{-1} = k_f^{-1} F_\psi$ and F_ψ is fractional function	– Studied nucleate boiling on microstructured surface using model similar to [204] – Varying cavity diameter between 0.1 to 0.6 mm showed little influence on boiling heat transfer – Multistep cavity showed best performance, and microstructured cavities provided 43-81% enhancement in boiling heat transfer
Nam *et al.* (2011) [206]	Single bubble, nucleate pool boiling on superhydrophilic surface ($\varphi = 10°$)	Water	LS in 2-D axisymmetric domain	$R/l_o \times H/l_o$: 1 × 3 Mesh: 96 × 288	$\dot{m}_g = \dfrac{k \cdot \nabla T}{h_{fg}}$ where $k^{-1} = k_f^{-1} H$	– Bubble growth investigated by modifying earlier model [184] to account for effects of superhydrophilic surface ($\varphi = 10°$) – Experiments showed bubble departure diameter is ~2.5 times smaller, and growth period ~4 time shorter on superhydrophilic surface compared to oxidized hydrophilic Si surface – Predictions of bubble shape and growth history agree well with experimental results
Wu and Dhir (2011) [207]	Single bubble, subcooled nucleate pool boiling with non-condensables	Water	LS in 2-D axisymmetric domain, and moving mesh method [208]	$R/l_o \times H/l_o$: 1 × 2 Mesh: 128 × 256	$\dot{m}_g = \dfrac{k \cdot \nabla T}{h_{fg}}$ where $k^{-1} = k_f^{-1} H$	– Bubble growth investigated to account for effects of micro-layer and non-condensables in 5°C subcooled liquid – Predicts increasing non-condensables increases bubble equivalent-diameter at any time during bubble growth – Non-condensables found to have minor effect on Nusselt number – Predicts reduced gravity causes upward flow of liquid at top of bubble

Table A.2: Continued

Lee *et al.* (2012) [209]	Nucleate pool boiling on microfinned surface	Water	LS with ghost fluid (GF) method in 2-D axisymmetric domain	Non-uniform grid away from wall Domain: 1.28 mm × 5.12 mm Mesh cell spacing: 0.01 mm	$\dot{m}_g = \dfrac{k_e \cdot \nabla T_f}{h_{fg}}$ uses $k_e^{-1} = k_f^{-1} F_\psi F_\omega + k_s^{-1}(1 - F_\omega)$ in energy equation, where F_ψ is fractional function and F_ω additional LS fractional function between liquid and solid	– Studied nucleate boiling on microcavity between microfins using model similar to [204] – Microfinned surface increased boiling heat transfer by 40-60% compared to plain surface – Bubble enhancement pronounced when bubble fin contact occurs, which increases liquid micro-layer area
Dhir *et al.* (2012) [210]	Single bubble, nucleate pool boiling in micro-gravity	Perfluoro-n-hexane	LS in 2-D axisymmetric domain	$R/l_o \times H/l_o$: 1 × 3 Mesh: 96 × 288	$\dot{m}_g = \dfrac{k \cdot \nabla T}{h_{fg}}$ where $k^{-1} = k_f^{-1} H$	– Studied bubble growth in microgravity using model similar to [184] and effect of dissolved gas [207] – Bubble shown to grow with no tendency to depart, similar to experimental observations – At high superheat, multiple bubble mergers observed, consistent with experiments
Zhao *et al.* (2012) [211]	Single bubble, nucleate pool boiling in micro-gravity	Water	LS in 2-D axisymmetric domain	$R/l_o \times H/l_o$: 1 × 3 Mesh: 100 × 300	$\dot{m}_g = \dfrac{k \cdot \nabla T}{h_{fg}}$ where $k^{-1} = k_f^{-1} H$	– Studied bubble growth in varying gravity including effect of micro-layer – Departure diameter decreases and growth period increases with decreasing wall superheat – Growth period and departure diameter decrease with decreasing contact angle and increase with decreasing gravity – Area averaged heat flux proportional to 1.5[th] power of wall superheat for different gravities

Aktinol and Dhir (2012) [212]	Single bubble, nucleate pool boiling, solid wall included in simulations	Water	LS in 2-D axisymmetric domain	Domain: 2.5 mm × 10 mm $R/l_o \times H/l_o$: 1 × 4	$$\dot{m}_g = \frac{k \cdot \nabla T}{h_{fg}}$$ where $k^{-1} = k_f^{-1} H$	– Studied bubble growth by including effects of solid wall, using model similar to [184] – Iterative procedure used to match temperature and heat flux at solid wall – Time dependent heat flux distribution varied by four orders of magnitude, with peak near triple point where micro-layer evaporation occurs – Waiting time decreases with increasing superheat; wall thickness has significant impact on waiting time
Kunkelmann and Stephan (2009) [183]	Single bubble, nucleate pool boiling	HFE-7100	VOF in fine 2-D axisymmetric domain (using OpenFOAM)	Domain: 2 mm × 4 mm	$$\eta_e = \frac{2\gamma}{2-\gamma} \frac{h_{fg}^2}{\sqrt{2\pi R_{gas}}} \frac{\rho_g}{T_{sat}^{3/2}}$$ where $\gamma = 1$ $$\dot{m}_g = \frac{\eta_e \left(T - T_{sat}\right)}{h_{fg}}$$ Procedure to smear mass source term is similar to that by Hardt and Wondra [88]	– Simulated nucleate boiling for single bubble including simplified model for micro-layer from [213] – Bubble growth and departure predictions provided – No comparisons made with experiments
Kunkelmann and Stephan (2010) [214]	Single bubble, nucleate pool boiling	HFE-7100	VOF with LS for interface reconstruction in a 2-D axisymmetric domain (using OpenFOAM)	Non-uniform grid Finest mesh cell size: 4 μm	$$S_g = \frac{k_f \cdot \nabla T \cdot \vec{A}_{int}}{h_{fg} V}$$ Procedure to smear mass source term is similar to that by Hardt and Wondra [88]	– Simulated nucleate boiling, including micro-layer model and transient conduction in solid wall – Using LS method helped resolve issues with VOF at three-phase contact line, and also reduced mesh reqd. – Bubble growth rate and departure diameter agree with experiments

Kunkelmann and Stephan (2010) [215]	Single bubble and multiple bubbles, nucleate pool boiling	HFE-7100	VOF with LS in 3-D domain (using OpenFOAM)	Non-uniform grid Finest mesh cell size: 4 µm	$S_g = \dfrac{k_f \cdot \nabla T \cdot \vec{A}_{\text{int}}}{h_{fg} V}$ Procedure to smear mass source term is similar to that by Hardt and Wondra [88]	− Investigated nucleate boiling of single bubble and multiple bubbles using formulation similar to [214] − Predictions for single bubble growth and departure show reasonable agreement with experimental data − Lateral bubble merger shown to form droplets inside merged bubble as observed in experiments
Kunkelmann and Stephan (2012) [216]	Single bubble, nucleate pool boiling in reduced gravity, microlayer evaporation	FC-72	VOF with LS in 2-D domain (using OpenFOAM)	Non-uniform grid Finest mesh cell size: 4 µm	$S_g = \dfrac{k_f \cdot \nabla T \cdot \vec{A}_{\text{int}}}{h_{fg} V}$ Procedure to smear mass source term is similar to that by Hardt and Wondra [88]	− Investigated nucleate boiling of single bubble at 0.2 g_e, using three-phase contact line formulation from [214] − Predictions for advancing and receding contact lines agree well with experimental observations − Predictions reveal heat transfer at three-phase contact line governed by micro-layer evaporation and transient conduction
Sielaff *et al.* (2015) [217]	Multiple bubbles, nucleate pool boiling, bubble coalescence	FC-72	VOF in 3-D domain (using OpenFOAM)	Domain: 2 mm × 2 mm× 2 mm Mesh cell size at interface: 5 µm	$S_g = \dfrac{k_f \cdot \nabla T \cdot \vec{A}_{\text{int}}}{h_{fg} V}$ Procedure to smear mass source term is similar to that by Hardt and Wondra [88]	− Investigated nucleate boiling during coalescence of two bubbles at different pressures, with micro-layer effects accounted for using simplified formulation similar to [183] − Predicted residual droplet formation in merged bubble for certain pressures − Heat transfer predictions compare well with experiments

Chen and Utaka (2015) [218]	Single bubble, nucleate pool boiling	Water	VOF in 2-D axisymmetric domain (using Fluent)	Domain: 6 mm radius, 10 mm fluid, 2 mm solid height Minimum mesh cell size: 2.5 μm	$\eta_e = \dfrac{2\gamma}{2-\gamma}\dfrac{h_{fg}^2}{\sqrt{2\pi R_{gas}}}\dfrac{\rho_g}{T_{sat}^{3/2}}$ where $\gamma = 1$ $q_i'' = \dfrac{T_f - T_{sat}}{\dfrac{\Delta l}{k_f} + \dfrac{1}{\eta_e}}$ where Δl is normal distance between superheated liquid cell and interface $\dot{m}_g = \dfrac{q_i''}{h_{fg}}$	− Investigated nucleate bubble growth, with micro-layer evaporation accounted for as source term − Simulated bubble growth to detachment − Predictions of maximum micro-layer radius agree with experiments − Predicts micro-layer becomes thinner during bubble growth, followed by dryout commencing at center of micro-layer and growing outwards
Jia *et al.* (2015) [219]	Single bubble, nucleate pool boiling	R113	VOF in 2-D domain	Domain: 2.5 mm × 4 mm Mesh cell size: 50 μm	$\eta_e = \dfrac{2\gamma}{2-\gamma}\dfrac{h_{fg}^2}{\sqrt{2\pi R_{gas}}}\dfrac{\rho_g}{T_{sat}^{3/2}}$ where $\gamma = 1$ $\dot{m}_g = \dfrac{\eta_e\left(T - T_{sat}\right)}{h_{fg}}$ $q_i'' = \dot{m}_g h_{fg}$ Procedure to smear mass source term is similar to that by Hardt and Wondra [88]	− Investigated nucleate bubble growth, including micro-layer evaporation as in [213] − Bubble shape predictions agree well with experiment, but departure time is over-predicted
Other Methods						
Yoon *et al.* (2001) [220]	Single bubble, subcooled nucleate pool boiling	Water	Mesh free (MPS-MAFL) method in 2-D domain	Domain: 10 mm × 15 mm Number of initial computing points: 4393	Evaporation and condensation rates calculated based on interface heat flux	− Used mesh free method to simulate bubble growth and departure, without accounting for micro-layer effects − Bubble growth rate compares well with prior experiments; bubble dynamics follow Fritz correlation [198]

Shin *et al.* (2005) [221]	Single bubble, nucleate pool boiling	Water	Level contour reconstruction method (LCRM) in 3-D domain	$L/l_o \times W/l_o \times H/l_o$: 6.44 × 6.44 × 5.6 Mesh: 46 × 46 × 40 $L/l_o \times W/l_o \times H/l_o$: 4.2 × 4.2 × 5.6 Mesh: 30 × 30 × 40 $L/l_o \times W/l_o \times H/l_o$: 3.08 × 3.08 × 5.6 Mesh: 22 × 22 × 40	$q_i'' = \left(k_f \left. \dfrac{\partial T}{\partial \vec{n}} \right|_f - k_g \left. \dfrac{\partial T}{\partial \vec{n}} \right|_g \right)$ $\dot{m}_g = \dfrac{q_i''}{h_{fg}}$	− Used LCRM method to simulate bubble nucleation, without accounting for micro-layer effects − Effects of nucleation site density incorporated in model − Good agreement with Nusselt number correlations achieved
Sato and Niceno (2013) [182]	Nucleate pool boiling, bubble growth and departure from single cavity	Water	Mass conservative constrained interpolation profile (CIP) method in 3-D domain	Domain: 8 mm × 8 mm × 16 mm Minimum mesh cell size (for three separate grids): 0.125 mm, 0.083, 0.063 mm	$q_i'' = \vec{n} \cdot \left(k_f \nabla T_f - k_g \nabla T_g \right)$ $\dot{m}_g = \dfrac{q_i''}{h_{fg}}$ $S_g = \dot{m}_g |\nabla \alpha_g| = \dot{m}_g \dfrac{A_{int}}{V}$	− Investigated nucleate boiling using mass conservative method, including micro-layer effects [213] − Predicted bubble shapes and bubble departure rates compare well with experimental data − Mass conservation strictly followed
Sato *et al.* (2013) [222]	Single bubble, horizontal and vertical nucleate flow boiling, bubble growth and departure	Water	Mass conservative constrained interpolation profile (CIP) method in 3-D domain	Horizontal Flow: Domain: 12 mm × 8 mm × 10 mm Vertical Flow: Domain: 32 mm × 8 mm × 10 mm Minimum mesh cell size: 62.5 μm	$q_i'' = \vec{n} \cdot \left\{ \left(k_f + k_T \right) \nabla T_f - \left(k_g + k_T \right) \nabla T_g \right\}$ where k_T is turbulent thermal conductivity $\dot{m}_g = \dfrac{q_i''}{h_{fg}}$ $S_g = \dot{m}_g |\nabla \alpha_g| = \dot{m}_g \dfrac{A_{int}}{V}$	− Investigated nucleate flow boiling in horizontal and vertical orientations, incorporating turbulence effects in earlier model [182] − Bubble shape, lift-off time, and lift-off diameter investigated − Predictions show good agreement with prior experiments and simulations by Li and Dhir [202]

Ling *et al.* (2014) [223]	Single bubble and two bubbles, nucleate pool boiling, bubble merger	Water	Coupled volume-of-fluid and level set (VOSET) method in 2-D domain	Domain: 10 mm × 10 mm Minimum mesh cell size: 1/8 mm	$q_i'' = \left(k_f \left.\dfrac{\partial T}{\partial \vec{n}}\right\|_f - k_g \left.\dfrac{\partial T}{\partial \vec{n}}\right\|_g \right)$ $\dot{m}_g = \dfrac{q_i''}{h_{fg}}$	– Investigated nucleate bubble growth and departure for single bubble and multiple bubbles, including micro-layer effects according to model by Ma *et al.* [224] – Employed temperature interpolation method at interface instead of constant vapor temperature assumption made in many studies – Heat flux predictions agree well prior with correlation
Tryggvason and Lu (2014) [225]	Nucleate pool and flow boiling, bubble growth and departure from single cavity	Water	Front-tracking (FT) method in 3-D domain	Domain: 7.5 mm × 7.5 mm × 7.5 mm Mesh: 64 × 64 × 64	$q_i'' = \left(k_f \left.\dfrac{\partial T}{\partial \vec{n}}\right\|_f - k_g \left.\dfrac{\partial T}{\partial \vec{n}}\right\|_g \right)$ $\dot{m}_g = \dfrac{q_i''}{h_{fg}}$	– Used FT method to simulate bubble nucleation from single nucleation site, without accounting for micro-layer effects – Preliminary results obtained for vertical orientation with and without flow
Lal *et al.* (2015) [226]	Horizontal subcooled flow boiling, bubble growth and departure from single cavity	Water	Mass conservative constrained interpolation profile (CIP) method in 3-D domain	Domain: 12 mm × 8 mm × 10 mm Number of mesh cells: 1,244,160	$q_i'' = \vec{n}.\left(k_f \nabla T_f - k_g \nabla T_g \right)$ $\dot{m}_g = \dfrac{q_i''}{h_{fg}}$ $S_g = \dot{m}_g \left	\nabla \alpha_g\right	= \dot{m}_g \dfrac{A_{\text{int}}}{V}$	– Investigated nucleate bubble growth and departure for subcooled flow boiling – Simulations capture bubble elongation and enhanced cooling due to bubble motion – Bubble equivalent diameter and bubble base diameter overpredicted – Simulations compare well with experimental observations of bubble growth

a   Indicated mesh sizes are optimum sizes chosen by original authors in simulations

b   (1) Positive and negative signs of mass source term may differ from those used by original authors due to differences in definition used. (2) Some variations in mass source terms are expected due to scalar versus vector definitions. (3) Only source term formulations are described in this table; exact usage in continuity equations should be obtained from original sources. (4) Micro-layer formulation is not included in description of source term in this table.
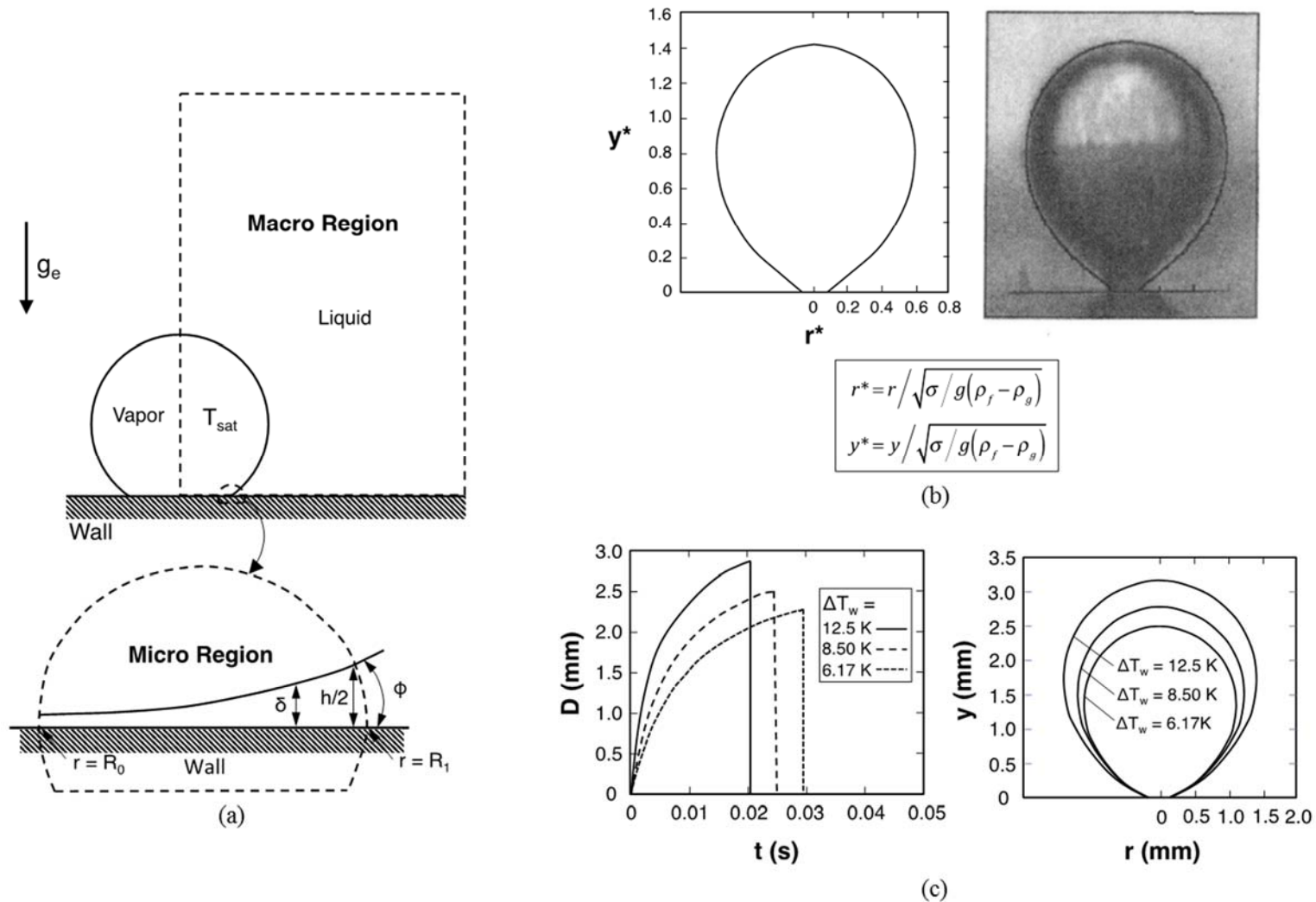
Fig. A.4: (a) Computational domain used for simulation of bubble nucleation in pool boiling with micro and macro regions. (b) Bubble shape predictions using 2-D axisymmetric model with LS scheme and energy jump condition, compared to captured image for water with $\Delta T_w = 8.5°C$ and $\varphi = 50°$. (c) Effects of wall superheat on bubble growth, and bubble shape at departure for water with $\varphi = 38°$. Adapted from Son *et al.* [184].

in the micro-layer were presented, respectively, as

$$\frac{\partial \delta}{\partial t} = \vec{v}_f - \frac{q''}{\rho_f h_{fg}},$$

(A.41)

$$\frac{\partial p_f}{\partial r} = \mu_f \frac{\partial^2 \bar{u}_f}{\partial y^2},$$

(A.42)

and

$$q'' = k_f \frac{(T_w - T_i)}{\delta}.$$

(A.43)

In the macro region, they used the LS scheme for interface tracking. The vapor temperature was set equal to T_{sat}, and effective conductivity was dependent on conductivity of liquid alone and given by

$$k^{-1} = k_f^{-1} H.$$

(A.44)

Son *et al.* used this approach to investigate bubble shape during growth and departure from a single nucleation site. For a wall superheat of 8.5°C, simulation results of bubble growth compare well with experimental data, as shown in Fig. A.4(b), though slight differences are evident in the neck region. They were also successful in predicting the effects of superheat on bubble growth rate and departure diameter as shown in Fig. A.4(c). Singh and Dhir [196] extended the model to subcooled nucleate pool boiling and showed that increased subcooling decreases bubble growth rate and departure diameter and increases growth period. Abarajith and Dhir [197] extended this model to investigate the influence of fluid properties, surface wettability, and contact angle. They showed that dielectric fluid PF-5060, whose surface tension is much smaller than that for water, produces smaller growth rate and smaller departure diameter than water. Nam *et al.* [206] studied bubble dynamics of water on a superhydrophilic surface and, once again, showed good agreement with experiments. By adding the species conservation equation to earlier

formulations, Wu and Dhir [207] investigated the effects of noncondensables on subcooled pool boiling using the coupled level set and moving mesh method developed by Wu *et al.* [208]. They found that noncondensables have minimal influence on heat transfer. Aparajith *et al.* [201] extended the 2-D model of Son *et al.* [184] to 3-D, and numerically simulated bubble growth for water and PF-5060 in reduced gravity, concluding that departure diameter and bubble growth time vary with gravity according to $D_d \sim g^{-0.5}$ and $t_d \sim g^{-0.9}$, respectively. Dhir *et al.* [210] then studied bubble growth of perfluoro-n-hexane for $g/g_e = 1 \times 10^{-7}$ and showed excellent agreement with experimental data. Studies by a different group showed that decreasing gravity increases growth time and departure diameter [211]. Son *et al.* [199] and Mukherjee and Dhir [200] simulated vertical bubble merger from a single nucleation site in 2-D domain, and lateral bubble merger from separate nucleation sites in 3-D domain, respectively, and, in both cases, achieved good agreement with experimental data. All earlier studies by Dhir and co-workers employed constant wall temperature, thereby neglecting thermal response of the wall. Aktinol and Dhir [212] incorporated wall response in their simulations and concluded that wall heat flux varies by up to four orders of magnitude during bubble growth. They also found that wall thickness and material have a significant impact on waiting time between successive nucleations.

More recently, Dhir and co-workers also addressed the influence of slow fluid motion on bubble growth and departure. Li and Dhir [202] simulated single bubble nucleation in horizontal flow and vertical upflow for liquid flow velocities from 0.076 to 0.23 m/s in 3-D domain, using experimental contact angle data as input to the model. Fig. A.5(a) and A.5(b) compare experimental results and numerical predictions of volume fraction for a
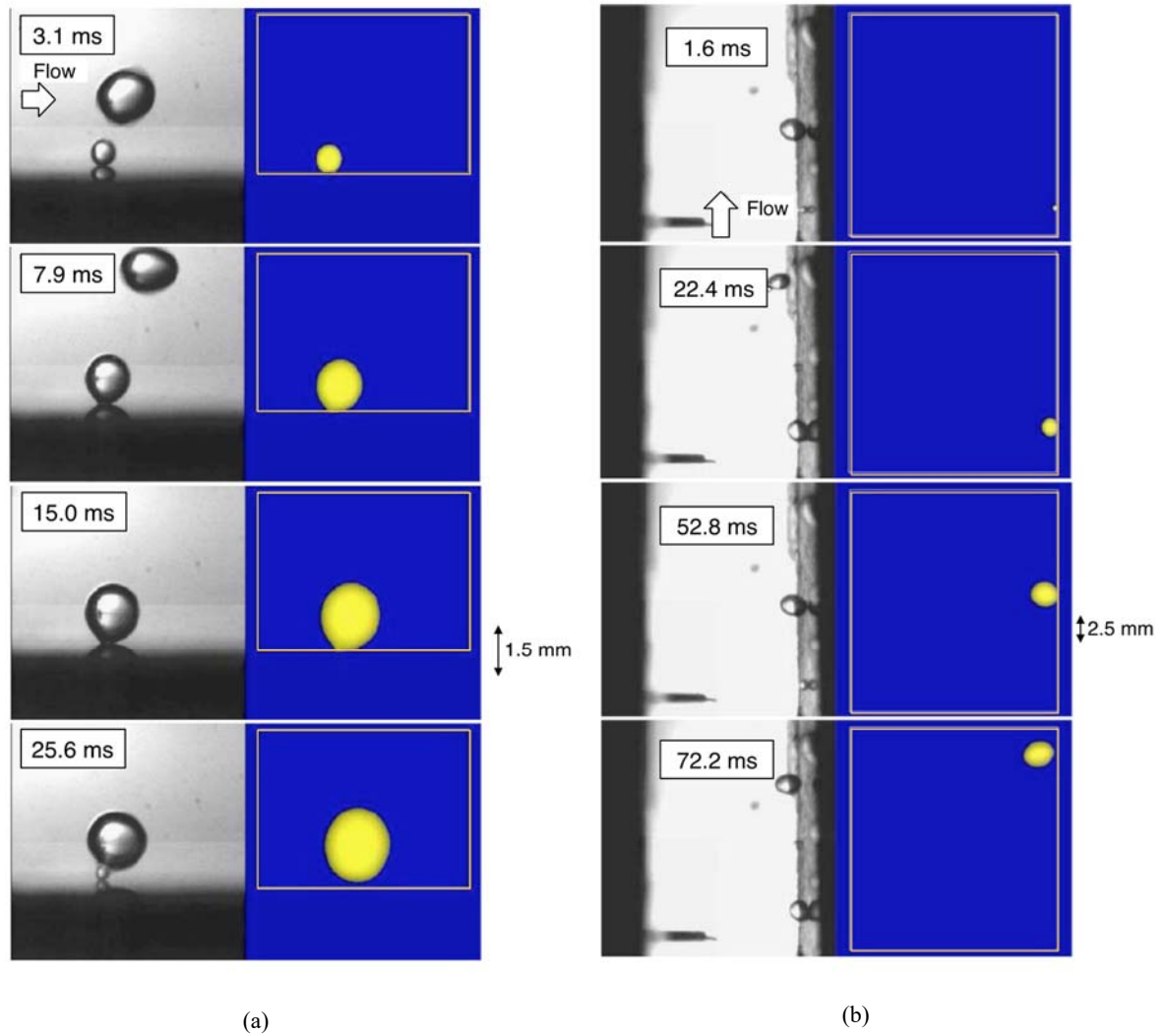
Fig. A.5: Predictions of bubble shape for single bubble during flow boiling of water at 0.076 m/s and $\Delta T_w = 5.3°C$ using LS scheme in 3-D domain and energy jump condition, and corresponding experimental images for (a) horizontal orientation, and (b) vertical upflow orientation. Adapted from Li and Dhir [202].

liquid velocity of 0.076 m/s and 5.3°C wall superheat for horizontal flow and vertical upflow, respectively. They achieved good agreement for horizontal flow, with the bubble initially assuming spherical shape and then getting tilted in the flow direction and growing asymmetrically. For vertical upflow, reasonable agreement was achieved in terms of bubble location and shape, sliding motion, and eventual lift-off from the wall. More recently, Son and Dhir [203] revisited the problem of nucleate pool boiling, by addressing high wall heat fluxes. By implementing the GF method and LS scheme, they used 2-D and 3-D simulations to demonstrate a significant increase in bubble merger in both vertical and lateral directions at high heat fluxes.

Using a simulation approach similar to that of Dhir and co-workers but with a simplified micro-layer model from [183], Lee *et al*. [204] investigated bubble growth on a microcavity. Lee and Son [205] and Lee *et al*. [209] continued pursuing this approach to study boiling heat transfer enhancement on microstructured and microfined surfaces, respectively.

Kunkelmann and Stephan [183] simulated bubble growth using the VOF scheme in the CFD software OpenFOAM in 2-D axisymmetric domain, with phase change based on Tanasawa's model. Unlike the approach used by Dhir and co-workers, Kunkelmann and Stephan used a micro-layer model developed by Stephan and Busse [213] to study bubble growth and departure on a heated wall. They complemented this study with simulations of nucleate boiling of HFE-7100 using a coupled VOF and LS model in OpenFOAM, but with phase change based on energy jump condition [214,215]. This approach greatly reduced mesh refinement requirements at the interface. They examined single bubble growth and departure, and lateral bubble merger, while also including micro-layer effects

at the three-phase contact line. In a separate study, Kunkelmann *et al*. [216] investigated both experimentally and numerically the effects of three-phase contact line on evaporative heat transfer. Sielaff *et al*. [217] used a VOF scheme similar to [183], with phase change based on energy jump condition, to study lateral bubble coalescence; their simulations were able to capture residual droplets in merged bubbles. Chen and Utaka [218] solved micro-layer evaporation separately using experimentally measured micro-layer thickness, and implemented computed mass, momentum and energy source terms in the VOF scheme. Jia *et al*. [219] used the micro-layer formulation by Stephan and Busse [213] in their VOF scheme.

Sato and Niceno [182] studied nucleate boiling using the mass conservative constrained interpolation profile (CIP) scheme in 3-D domain, including a micro-layer treatment similar to that of Kunkelmann and Stephan [183], with phase change based on energy jump condition. Figure A.6(a) shows a sample of Sato and Niceno's bubble growth sequence during nucleate boiling in water, along with the temperature and velocity fields. Bubbles are depicted growing and departing, followed by emergence of a new bubble at the nucleation site. Figure A.6(b) shows corresponding temporal variations of integrated wall heat flux and bubble radius, which also shows minimum heat flux coinciding with bubble departure from the wall. Figure A.6(c) shows predictions agree quite well with experimental results in terms of bubble shape and bubble departure period. Sato *et al*. [222] later extended the model to vertical and horizontal flow boiling by incorporating in the phase change model turbulent thermal conductivity according to

$$q_i^{"} = \vec{n} \cdot \left\{ \left(k_f + k_T \right) \nabla T_f - \left(k_g + k_T \right) \nabla T_g \right\}, \tag{A.45}$$

(a)

(b)

(c)
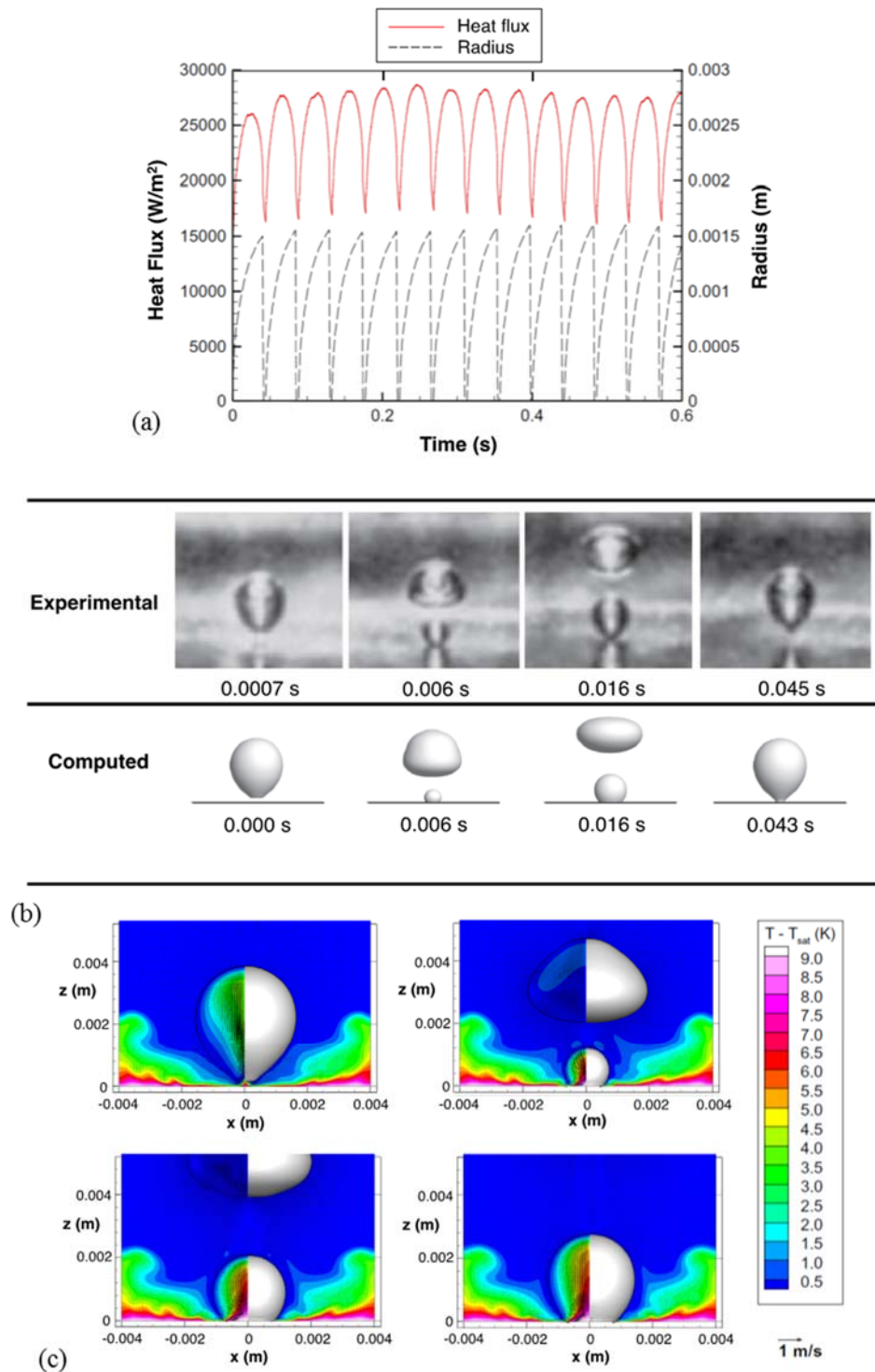
Fig. A.6: Predictions of bubble growth in saturated nucleate pool boiling of water computed using mass conservative CIP scheme in 3-D domain and energy jump condition. (a) Temporal variations of area averaged wall heat flux and bubble radius. (b) Comparison of computed and experimental bubble shape. (c) Bubble growth predictions, with right half of bubble showing bubble shape and left half temperature field; total duration of sequence is approximately 0.027 s. Adapted from Sato and Niceno [182].

and demonstrated reasonable agreement with experiments. Lal *et al*. [226] investigated near-saturated flow boiling using Sato and Niceno's [182] model, but used a very fine grid, and were therefore able to account for turbulence without using Eq. (A.45). They achieved good overall agreement of bubble shape and diameters with experimental data. It should be mentioned that this CIP method conserves mass, while the FT and LS methods do not.

In another study, Ling *et al*. [223] studied nucleate boiling of a single bubble, two-bubbles, and bubble mergers using the VOSET scheme in 2-D domain with the micro-layer model of Ma *et al*. [224]. There have also been a number of studies of bubble nucleation, growth and departure that do not account for micro-layer evaporation effects. Among those, Aus der Wiesche [230] simulated nucleate pool boiling with the VOF scheme. Kunugi *et al*. [231] used a different method for interface reconstruction called *Multi-Interface Advection and Reconstruction Solver* (MARS) developed in [232] in the VOF scheme to study bubble nucleation in pool boiling and flow boiling. Tryggvason and Lu [225] used the FT scheme to simulate nucleate boiling in 3-D domain. Shin *et al*. [221] extended the LCRM method also to simulate nucleate boiling in 3-D domain. Yoon *et al*. [220] used the mesh free technique (MPS-MAFL) developed by Koshizuka *et al*. [233] to simulate bubble growth, departure and rise in nucleate pool boiling. Some bubble nucleation simulations have also been performed using LB methods [234-236].

A.5.1.2 Film Boiling

Film boiling involves formation of a continuous vapor film on the heated wall, blocking any wetting of the wall by liquid. Therefore, the wall heat transfer coefficient is considerably poorer than in nucleate boiling. Here, vapor bubbles are released with rather

uniform frequency from the wavy liquid-vapor interface, rather than from the wall, which is why film boiling is easier to model than nucleate boiling. This relative simplicity has spurred a large number of studies aiming to simulate film boiling as a precursor to future, more complex phase change phenomena. Table A.3 provides a summary of prior studies involving simulations of film boiling.

Early film boiling simulations were performed by Son and Dhir's [187], who adopted a moving body-fitted coordinate system. They used 2-D axisymmetric domain and modeled surface tension using the continuum surface force (CSF) model by Brackbill *et al*. [149]. Son and Dhir's model showed good predictions of bubble size and breakoff diameter, while Nusselt number predictions were lower than experimental data. However, this model is applicable only as long as a single interface is present. Therefore, once the bubble detaches, and multiple interfaces are formed, the computation is brought to an end. Also using a moving body-fitted coordinate system, Banerjee and Dhir [248,249] investigated subcooled film boiling on a horizontal disc in 2-D axisymmetric domain. They achieved good agreement with experiments in terms of interface shape, temporal position of interface, interface growth rate, and wall heat flux.

Juric and Tryggvason [181] simulated film boiling using the FT scheme in 2-D domain, with phase change based on Tanasawa's model [72], but did not encounter the disjointed interface problem. By inputting wall heat flux as boundary condition instead of wall temperature (as was used in many other studies), they studied growth of initial instability of the film along with bubble departure. Figure A.7(a) shows predictions for a Morton

Table A.3. Summary of numerical studies on film boiling.

Author(s)	Two-phase system	Test Fluid	Multiphase Scheme	Mesh[a]	Mass Source terms[b]	Remarks
				FT Method		
Juric and Tryggvason (1998) [181]	Film boiling on a horizontal surface	Hydrogen (Morton number defined separately)	FT in 2-D domain	For Morton number $Mo =1e$-3: $L/l_s \times H/l_s$: 57.4×180 where l_s is length scale defined as $l_s = \left(\dfrac{\mu_f^2}{g_e\rho_f^2}\right)^{1/3}$ Mesh: 150×300 For Morton number $Mo =1e$-6: $L/l_s \times H/l_s$: 121×363	$\varphi_e = \dfrac{2\gamma}{2-\gamma}\dfrac{h_{fg}}{\sqrt{2\pi R_{gas}}}\dfrac{1}{(v_g - v_g)T_{sat}^{3/2}}$ where $\gamma = 1$ $\dot{m}_g = \varphi_e f$ Where f is a function of different parameters including the interface temperature and saturation temperature. The complete form for $\dot{m}_g$ can be found in [181]	– Studied film boiling by providing a wall heat flux boundary condition – Used an iterative procedure to calculate the interface velocity and interface temperatures – Simulations predicted bubble growth and departure pattern which did not exactly match experimental observations – Overall predicted heat transfer rates and wall temperatures showed good agreement with experiments
Shin and Juric (2002) [154]	Film boiling on a horizontal surface	unknown fluid	FT with level contour reconstruction method in 3-D domain	Domain 1: 0.08 m $\times 0.08$ m $\times 0.16$ m Mesh: $30 \times 30 \times 60$ Domain 2: 0.16 m $\times 0.16$ m $\times 0.32$ m Mesh: $60 \times 60 \times 120$	$q_i'' = \left(k_f\left.\dfrac{\partial T}{\partial \vec{n}}\right|_f - k_g\left.\dfrac{\partial T}{\partial \vec{n}}\right|_g\right)$ $\dot{m}_g = \dfrac{q_i''}{h_{fg}}$	– Studied film boiling on horizontal a horizontal surface to understand single bubble and multiple bubble interactions by removing the iterative procedure by [181] – Results showed method is able to capture interface merging and breakup during film boiling
Esmaeeli and Tryggvason (2004) [237]	Film boiling on a horizontal surface	Water	FT in 3-D domain	Domain: $\lambda_{d3} \times \lambda_{d3} \times 2\lambda_{d3}$, where λ_{d3} is 3-D most dangerous wavelength defined as $\lambda_{d3} = \sqrt{2}\lambda_{d2}$, where λ_{d2} is 2-D most dangerous wavelength defined as $\lambda_{d2} = 2\pi\sqrt{\dfrac{3\sigma}{g\left(\rho_f - \rho_g\right)}}$ Mesh: $96 \times 96 \times 192$	$q_i'' = \left(k_f\left.\dfrac{\partial T}{\partial \vec{n}}\right|_f - k_g\left.\dfrac{\partial T}{\partial \vec{n}}\right|_g\right)$ $\dot{m}_g = \dfrac{q_i''}{h_{fg}}$	– Studied film boiling on a horizontal plate by removing the iterative procedure by [181] – Predictions obtained for bubble growth – For high superheats, as the bubble grows, mushroom shaped behavior was observed

Esmaeeli and Tryggvason (2004) [238]	Multimode film boiling across a horizontal surface	Water	FT in 2-D and 3-D domain	For 2-D domain: $10\lambda_{d2} \times 2\lambda_{d2}$ Mesh: 1280 × 256 For 3-D domain 1: $\lambda_{d3} \times \lambda_{d3} \times 2\lambda_{d3}$ Mesh: 96 × 96× 192 For 3-D domain 2: $1.4\lambda_{d3} \times 1.4\lambda_{d3} \times 1.4\lambda_{d3}$ Mesh: 128 × 128× 128	$q_i'' = \left(k_f \left.\frac{\partial T}{\partial \vec{n}}\right	_f - k_g \left.\frac{\partial T}{\partial \vec{n}}\right	_g \right)$ $\dot{m}_g = \frac{q_i''}{h_{fg}}$	− Studied film boiling on a horizontal plate using the method by [237] and simulated multimode film boiling − Predicted bubble distribution behavior for bubbles generated at multiple nodes in the domain − High superheats showed interaction between vapor jets generated at different nodes − Nusselt number predictions agreed well with correlation
Esmaeeli and Tryggvason (2004) [239]	Film boiling on a single horizontal cylinder and multiple cylinders	Water and unknown fluid[c]	FT in 3-D domain	Domain: 0.06 m × 0.06 m × 0.15 m Mesh: 64 × 64× 160	$q_i'' = \left(k_f \left.\frac{\partial T}{\partial \vec{n}}\right	_f - k_g \left.\frac{\partial T}{\partial \vec{n}}\right	_g \right)$ $\dot{m}_g = \frac{q_i''}{h_{fg}}$	− Studied film boiling on horizontal cylinder/s using the method by [237] and included effect of immersed solid − Results qualitatively matched expected film boiling behavior
LS Method						
Son and Dhir (1998) [135]	Film boiling on a horizontal surface	Water	LS in 2-D axisymmetric domain	Domain: Width is $2\lambda_{d2}/\sqrt{2\pi}$ with node center and antinode center being the endpoints. Mesh: 128 × 256	$\dot{m}_g = -\frac{k \cdot \nabla T}{h_{fg}}$ where $k^{-1} = k_g^{-1}(1-H)$ and H is Heaviside function from Sussman *et al.* [123]	− Studied film boiling near critical pressures for varying wall superheats − For low superheats, interface rises, bubbles break off, and the interface drops down alternatively at the nodes and the antinodes − At high superheats, stable vapor jets are formed at the both nodes and antinodes, and bubbles are released at the top of vapor columns − Interface behavior was in good agreement with experimental observations − Nusselt number predictions agreed well with correlations
Bazdidi-Tehrani and Zaman (2002) [240]	Film boiling on a vertical surface	Water	LS in 2-D axisymmetric domain	Domain: $\lambda_{d,KH} \times \lambda_{d,KH}/2$ where λ_{dKH} is the most dangerous Kelvin–Helmholtz instability wavelength. Mesh: 256 × 128	$\dot{m}_g = -\frac{k \cdot \nabla T}{h_{fg}}$ where $k^{-1} = k_g^{-1}(1-H)$	− Studied film boiling in vertical orientation − Predicted heat transfer coefficients show reasonable agreement with analytical model and experimental data

Table A.3: Continued

Son and Dhir (2007) [241]	Film boiling on a horizontal cylinder	Water	LS with ghost fluid method in 2-D axisymmetric domain and 3-D domain	Non-uniform grid away from cylinder For 2-D domain: $\lvert L/l_o\rvert \leq 3.3$ and $-3.6 \leq H/l_o \leq 11.5$ where l_o is the characteristic length defined as $$l_0 = \sqrt{\frac{\sigma}{g\left(\rho_f - \rho_g\right)}}.$$ Minimum mesh cell size: $0.005 l_o$ For 3-D domain: $\lvert L/l_o\rvert \leq 3.3$, $-3.6 \leq H/l_o \leq 11.5$ and $\lvert W/l_o\rvert \leq \sqrt{3}\pi$ Minimum mesh cell size: $0.085 l_o$	$q_i'' = \vec{n}\,.\left(k_f \nabla T_f - k_g \nabla T_g\right)$ $\dot{m}_g = \dfrac{q_i''}{h_{fg}}$	− Studied film boiling on a horizontal cylinder and included effect of immersed solid − Nusselt number predictions compared well with correlations available in literature
Son and Dhir (2008) [242]	Film boiling on a horizontal cylinder	Water	LS with ghost fluid method in 3-D domain	Non-uniform grid away from cylinder Domain: $\lvert L/l_o\rvert \leq 3.3$, $-3.6 \leq H/l_o \leq 11.5$ and $\lvert W/l_o\rvert \leq 0.5 c\lambda_{dF}$ where λ_{dF} is the most dangerous wavelength for a flat plate and c was varied from 0 to 1. Minimum mesh size in x and y direction: $0.01 l_o$. Minimum mesh size in z direction: $0.057 l_o$	$q_i'' = \vec{n}\,.\left(k_f \nabla T_f - k_g \nabla T_g\right)$ $\dot{m}_g = \dfrac{q_i''}{h_{fg}}$	− Studied film boiling simulation on a horizontal cylinder − For large diameters, bubbles were released at different circumferential locations of the cylinder. For small diameters, discrete bubbles are observed being released on the top of the cylinders. For even smaller diameters, bubble mergers were observed − Nusselt number predictions compared well with correlation
Gibou et al. (2007) [68]	Film boiling on a horizontal surface	unknown fluid[c]	LS with ghost fluid method in 2-D domain	Domain: $\lambda_{d2} \times 3\lambda_{d2}$ Mesh: 140×420	$q_i'' = \vec{n}\,.\left(k_f \nabla T_f - k_g \nabla T_g\right)$ $\dot{m}_g = \dfrac{q_i''}{h_{fg}}$	− Studied film boiling on a horizontal surface − Results showed correct qualitative behavior expected in film boiling − Long vapor jets with vapor bubbles at its top are observed which matches with prior studies like [179]

Kim and Son (2013) [243]	Film boiling during circular jet impingement on a horizontal surface	Water	LS in 2-D axisymmetric domain with a thin film model close to the wall	Domain: 6.4 mm × 15 mm Minimum mesh cell sizes (for three separate grids): 0.01 mm, 0.005 mm, 0.001 mm	$q_i'' = (1-\alpha_a)\vec{n}.\left(k_f \nabla T_f - k_g \nabla T_g\right)$ where α_a is void fraction of surrounding air. $\dot{m}_g = \dfrac{q_i''}{h_{fg}}$	– Studied film boiling during jet impingement on a flat surface – Coarser meshes were used along with a thin film model, and results were compared well to finer meshes where the thin film model was not required – Obtained good agreement between both approaches
				VOF Method		
Welch and Wilson (2000) [179]	Film boiling on a horizontal surface	unknown fluid[c]	VOF in 2-D domain	For wall superheat of 5 K and 10 K: Domain 1: $\lambda_{d2}/2 \times 3\lambda_{d2}/2$ Mesh: 64 × 192 Domain 2: $\lambda_{d2}/2 \times 3\lambda_{d2}$ Mesh: 64× 384 For high heat flux case: Domain: Test case by Juric and Tryggvason [181] was studied. Mesh: 64 × 320	$q_i'' = \left(k_f \left.\dfrac{\partial T}{\partial \vec{n}}\right|_f - k_g \left.\dfrac{\partial T}{\partial \vec{n}}\right|_g\right)$ $\dot{m}_g = \dfrac{q_i''}{h_{fg}}$	– Studied saturated film boiling on a horizontal surface – Results showed correct qualitative behavior expected in film boiling – Nusselt number predictions compared well with correlation – For high heat flux test case, results of bubble shape, velocity field and temperature field are similar to those obtained by [181]
Welch and Rachidi (2002) [244]	Film boiling on a horizontal surface including effect of the solid wall	Water	VOF in 2-D domain	Fluid domain: $\lambda_{d2}/2 \times \lambda_{d2}$, Solid domain: $\lambda_{d2}/2 \times \lambda_{d2}/2$ Mesh for fluid domain: 180× 360	$q_i'' = \left(k_f \left.\dfrac{\partial T}{\partial \vec{n}}\right|_f - k_g \left.\dfrac{\partial T}{\partial \vec{n}}\right|_g\right)$ $\dot{m}_g = \dfrac{q_i''}{h_{fg}}$	– Studied film boiling simulation on a horizontal surface including conjugate heat transfer near critical pressures – Results showed solid increasing the temperature fluctuations at the solid boundary – Predicted quasi-steady periodic Nusselt numbers agreed reasonably with correlations
Agarwal *et al.* (2004) [245]	Film boiling on a horizontal surface	Water	VOF in 2-D domain	Domain: $\lambda_{d2}/2 \times \lambda_{d2}$ Mesh: 180× 360	$q_i'' = \left(k_f \left.\dfrac{\partial T}{\partial \vec{n}}\right|_f - k_g \left.\dfrac{\partial T}{\partial \vec{n}}\right|_g\right)$ $\dot{m}_g = \dfrac{q_i''}{h_{fg}}$	– Studied film boiling on a horizontal surface – Captured typical behavior of bubble growth and departure with its periodic nature was – Maximum heat transfer was directly related to minimum film thickness – Nusselt numbers were slightly under-predicted when compared to correlations

Hardt and Wondra (2008) [88]	Film boiling on a horizontal surface	unknown fluid[c]	VOF in 2-D domain	Domain: $\lambda_{d2}/2 \times 3\lambda_{d2}$ Mesh 1: 64 × 192 Mesh 2: 100 × 300	$\eta_e = \dfrac{2\gamma}{2-\gamma} \dfrac{h_{fg}^2}{\sqrt{2\pi R_{gas}}} \dfrac{\rho_g}{T_{sat}^{3/2}}$ where $\gamma = 1$ $\dot{m}_g = \dfrac{\eta_e (T - T_{sat})}{h_{fg}}$ Mass source term was smeared across the interface using a new scheme	− Studied film boiling on a horizontal surface − Mushroom shaped bubbles connected to vapor jets were identified − Behavior matched what was observed by [68]
Yuan et al. (2008) [246]	Natural and forced convection film boiling around a sphere	Water	VOF in 2-D domain with body fitted coordinates	Domain: 0.1 m × 0.2 m Mesh: 120 × 120	$q_i'' = \left(\left(k_f \left.\dfrac{\partial T}{\partial \bar{n}}\right|_f - k_g \left.\dfrac{\partial T}{\partial \bar{n}}\right|_g \right) + \Psi \right)$ Where Ψ is radiation heat transfer participating in phase change $\dot{m}_g = \dfrac{q_i''}{h_{fg}}$	− Studied natural convection and forced convection film boiling around a sphere − Energy term included the effect of radiation heat transfer − Interface movement agreed well with experimental observations − Heat transfer coefficients were consistent with experimental data and correlations
Sun et al. (2012) [157]	Film boiling on a horizontal surface	unknown fluid[c]	VOF in 2-D domain (using Fluent)	Domain: $\lambda_{d2}/2 \times \lambda_{d2}$ Mesh: 64 × 128	$S_{sat} = -S_{unsat} = \dfrac{2k_{unsat} (\nabla T \cdot \nabla \alpha_{unsat})}{h_{fg}}$ $Q_i = -S_{sat} h_{fg}$	− Studied film boiling to check validity of new proposed mass and energy source terms − Nusselt number predictions agreed well with correlation in literature
Arevalo et al. (2014) [247]	Film boiling on a spherical surface	Water	VOF in 2-D domain (using Fluent)	Domain: 0.05 mm × 0.1 mm Sphere diameter = 0.0127 m Mesh no. of cells: 24,000	$S_g = -S_f = \dfrac{k (\nabla T \cdot \nabla \alpha_f)}{h_{fg}}$ where $k = \alpha_g k_g + (1 - \alpha_g) k_f$ $Q_i = S_f h_{fg}$	− Studied film boiling around a sphere − Predictions showed wavy vapor behavior of the interface and generation and detachment of vapor slugs − Predicted heat flux data was consistent with experimental data and correlations

<p style="text-align:center">Table A.3: Continued</p>

				Other Methods		
Son and Dhir (1997) [187]	Film boiling on a horizontal surface	Water, benzene and R113	Moving coordinate system method in 2-D axisymmetric domain	Width of domain is $2\lambda_{d2}/\sqrt{2\pi}$ where λ_{d2} is the 2-D most dangerous wavelength with node center and antinode center being the endpoints. Mesh size: 81 × 84	$\bar{m}_g = \dfrac{c_{p,g}\Delta T}{h_{fg}\,\text{Pr}_g\,\text{Re}_g}\dfrac{\sqrt{x_\varepsilon^2 + y_\varepsilon^2}}{J}\theta_\eta$ where J is Jacobian, ε and η are transformed coordinates	− First study on saturated film boiling with two bubble system, one at node and another at antinode − Results captured spatial and temporal variations of the interface − Simulation could not handle multiple interfaces and hence ended when bubble broke off − Heat transfer was under predicted when compared to prior correlation
Banerjee and Dhir (2000) [248,249]	Subcooled film boiling on a horizontal surface	Water and PF 5060	Moving coordinate system method in 2-D axisymmetric domain	Width of domain is $\lambda_{d2}/\sqrt{2\pi}$. Mesh in vapor domain: 42 × 22. For saturated case: Mesh in liquid domain: 42 × 42 For subcooled case: Mesh in liquid domain: 42 × 72	Modified version of non-dimensionless mass source used by [187] to include effect of subcooling.	− Studied subcooled film boiling using model similar to [187] − Condensation was observed on the top portion of the interface while evaporation in the thin film region close to the wall − Numerical simulations did a good job in predicting different parameters related to bubble growth and wall heat flux for PF 5060
Tomar *et al.* (2005) [188]	Film boiling on a horizontal surface	Water and R134a	CLSVOF in 2-D domain	Domain: $\lambda_{d2}/2 \times \lambda_{d2}$ Mesh: 180 × 360	$q_i'' = \left(k_f \left.\dfrac{\partial T}{\partial \vec{n}}\right|_f - k_g \left.\dfrac{\partial T}{\partial \vec{n}}\right|_g\right)$ $\dot{m}_g = \dfrac{q_i''}{h_{fg}}$	− Studied film boiling on a flat surface − Bubbles were formed alternatively at the nodes and antinodes − Above certain superheats, long vapor columns with bubbles on top were observed like that obtained in other studies − Near critical pressures, frequency of bubble detachment is higher for R134a in comparison to water − Space averaged Nusselt number is highest at the point of bubble detachment

Table A.3: Continued

Welch and Biswas (2007) [250]	Film boiling on a horizontal surface including effect of electric field	Water	CLSVOF in 2-D domain	Domain: $\lambda_{d2}/2 \times \lambda_{d2}/2$ Mesh: 200 × 200	$q_i'' = \left(k_f \left. \dfrac{\partial T}{\partial \vec{n}} \right\|_f - k_g \left. \dfrac{\partial T}{\partial \vec{n}} \right\|_g \right)$ $\dot{m}_g = \dfrac{q_i''}{h_{fg}}$	− Studied film boiling including effects of electrohydrodynamics. − Results showed correct qualitative behavior − Alternate bubble generations at node and antinode were captured
Tomar *et al.* (2009) [251]	Multimode film boiling on a horizontal surface including effect of electric field	Water and R123a	CLSVOF in 2-D domain	Domain 1: $3\lambda_{d2} \times \lambda_{d2}$ Mesh cell size: $\lambda_{d2}/214$ Domain 2: $5\lambda_{d2} \times \lambda_{d2}$ Mesh cell size: $\lambda_{d2}/248$	$q_i'' = \left(k_f \left. \dfrac{\partial T}{\partial \vec{n}} \right\|_f - k_g \left. \dfrac{\partial T}{\partial \vec{n}} \right\|_g \right)$ $\dot{m}_g = \dfrac{q_i''}{h_{fg}}$	− Studied multimode film boiling including effects of electrohydrodynamics. − Wavelength of instability was a function of electric field − Low gravity was tested and it effected density of bubble formation sites − Bubbles shapes were effected by strong electric fields − Numerical results showed electric field increasing Nusselt numbers and bubble release frequency
Guo *et al.* (2011) [252]	Film boiling on a horizontal surface	Water and unknown fluid[c]	VOSET in 2-D domain	Domain 1: $\lambda_{d2} \times \lambda_{d2}$ Mesh cell size: 64 × 64 Domain 2: $\lambda_{d2} \times 3\lambda_{d2}$ Mesh cell size: 64 × 192	$q_i'' = \left(k_f \left. \dfrac{\partial T}{\partial \vec{n}} \right\|_f - k_g \left. \dfrac{\partial T}{\partial \vec{n}} \right\|_g \right)$ $\dot{m}_g = \dfrac{q_i''}{h_{fg}}$	− Studied film boiling on a horizontal surface − Predicted Nusselt numbers agreed with correlations − Film boiling of water near critical pressures agreed qualitatively with experimental observations
Tsui *et al.* (2014) [253]	Film boiling on a horizontal surface and a cylindrical surface	Water	Modified VOF in 2-D domain	For horizontal surface: Domain $\lambda_{d2} \times \lambda_{d2}/2$ Mesh: 180 × 360 For cylindrical surface: Domain: $7D \times 15D$, $D =$ 0.213 mm Mesh no. of cells in half domain: 48800	$q_i'' = \left(k_f \left. \dfrac{\partial T}{\partial \vec{n}} \right\|_f - k_g \left. \dfrac{\partial T}{\partial \vec{n}} \right\|_g \right)$ $\dot{m}_g = \dfrac{q_i''}{h_{fg}}$	− Studied film boiling on flat and circular surfaces − For flat surface film boiling was captured well and Nusselt numbers compared well with semi-empirical correlation − For cylindrical surface, qualitative boiling behavior was captured well, but not the Nusselt numbers

a   Indicated mesh sizes are optimum sizes chosen by original authors in simulations

b   (1) Positive and negative signs of mass source term may differ from those used by original authors due to differences in definition used. (2) Some variations in mass source terms are expected due to scalar versus vector definitions. (3) Only source term formulations are described in this table; exact usage in continuity equations should be obtained from original sources.

c   Please refer to original article for fluid properties used

$$Mo = \mu_f^4 \, g \big/ \left(\rho_f \sigma^3 \right)$$

$$q''* = \frac{\bar{q}_w''}{\rho_g k_f h_{fg} \Big/ \left[\rho_f c_{p,f} \left\{ \mu_f^2 \big/ \left(g \rho_f^2 \right) \right\}^{1/3} \right]}$$

$$t* = t \Big/ \left[\left\{ \mu_f^2 \big/ \left(g \rho_f^2 \right) \right\}^{1/3} \Big/ g \right]^{1/2}$$

$$T* = \frac{T}{\left(\rho_g h_{fg} \right) \big/ \left(\rho_f c_{p,f} \right)}$$

$Mo = 1 \times 10^{-3}$, $q''* = 10$

$t* = 2$ $t* = 14$

$t* = 30$ $t* = 40$

$Mo = 1 \times 10^{-6}$, $q''* = 20$

$t* = 2$ $t* = 14$

$t* = 30$ $t* = 40$

(a)   (b)
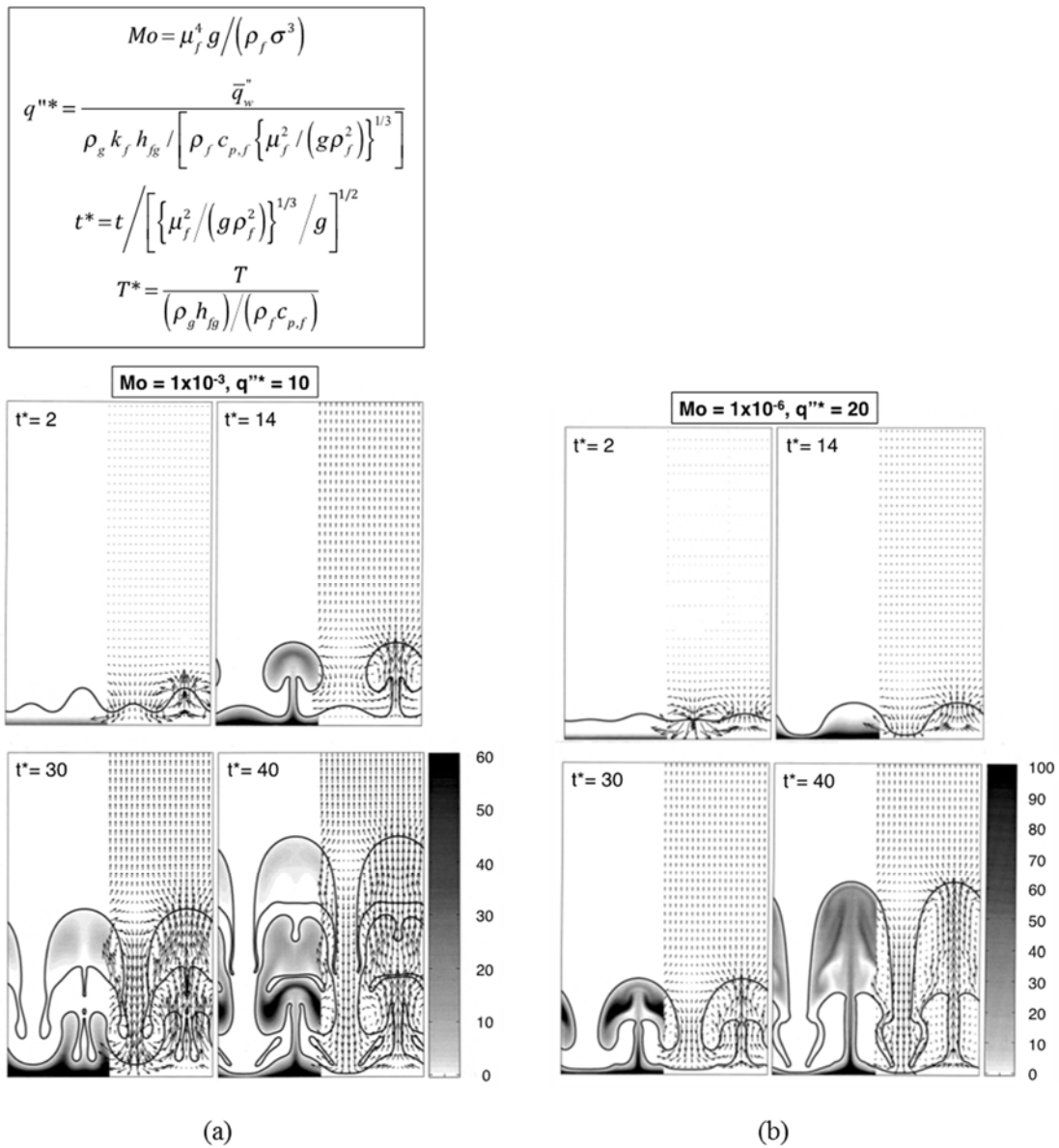
Fig. A.7: Simulations of hydrogen film boiling using FT scheme in 2-D domain with Tanasawa phase change model for different times: (a) $Mo = 1 \times 10^{-3}$ and $q''* = 10$. (b) $Mo = 1 \times 10^{-6}$ and $q''* = 20$. The vapor-liquid interface is shown as solid black line, with temperature field plotted to the left and velocity vectors to the right of domain. Adapted from Juric and Tryggvason [181].

number of $Mo = 1\text{x}10^{-3}$ with a relatively low value of dimensionless heat flux of $q''* =$ 10 at different dimensionless times $t*$. Shown is the liquid-vapor interface undergoing a Rayleigh-Taylor instability, and the vapor bubble subsequently pinching-off and rising. For a lower $Mo = 1\text{x}10^{-6}$ and higher $q''* = 20$, Fig. A.7(b) shows the vapor being converted into a mushroom shaped bubble, preventing pinch-off of its stem. While the predicted bubble shape did not exactly match experiments, both heat transfer rate and wall temperature showed good agreement with correlations. Shin and Juric [154] simulated film boiling on a horizontal surface in 3-D domain using the level contour reconstruction method assuming interface is maintained at T_{sat}, with phase change based on energy jump condition. Their approach eliminated the iterative procedure used by Juric and Tryggvason to match interface velocity. Esmaeeli and Tryggvason [237,238] also eliminated the iterative procedure in simulations of film boiling on a horizontal surface using 3-D domain, with phase change based on energy jump condition. Later, they used the same scheme to investigate film boiling on a single horizontal cylinder and multiple cylinders [239], by incorporating an immersed boundary method [254] to tackle uneven surfaces. Figure A.8 shows their predictions for a bubble pinching off from the cylinder in 3-D domain. Notice how, as vapor is generated and bubble grows, the upper half portion becomes tighter and lower half thinner. Eventually, the bubble is pinched off and surface tension pulls the interface back, re-initiating the process is a repeatable manner.

Son and Dhir [135] investigated film boiling using the LS method in 2-D axisymmetric domain with phase change based on energy jump condition, but unlike their earlier work [187], the newer model was capable of tackling multiple interfaces. They assumed constant
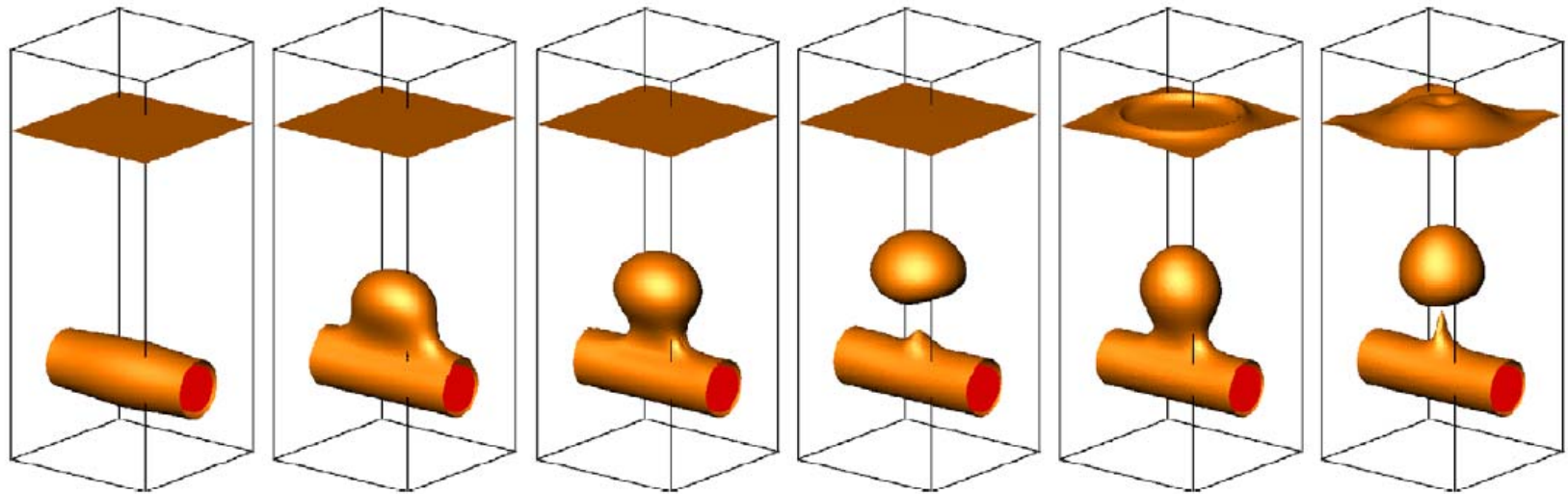
Fig. A.8: Simulations of film boiling on a horizontal cylinder using the FT method in 3-D domain with energy jump condition. Domain size is 0.06 m × 0.06 m × 0.15 m, and simulation parameters are $\Delta T_w = 10°C$, $\rho_f / \rho_g = 40$, $\mu_f / \mu_g = 10$, $k_f / k_g = 40$, $c_{p,f} / c_{p,g} = 10$, $h_{fg} = 10$ kJ/kg. Adapted from Esmaeeli and Tryggvason [239].

liquid temperature equal to T_{sat}, and an effective conductivity dependent on conductivity of vapor alone,

$$k^{-1} = k_g^{-1}(1 - H)\cdot \tag{A.46}$$

Figure A.9(a) shows evolution of the interface in water for three wall superheats of ΔT_w = 10, 22, and 30°C. Notice, for all superheats, how discrete bubbles are released at interfacial nodes and antinodes. At the higher superheat, long vapor jets form simultaneously below the bubbles at the nodes and antinodes. The numerical simulations predict average wall heat flux values of $\overline{q}_w^{''}$ = 9.28, 21.60 and 29.90 W/cm² for ΔT_w = 10, 22, and 30°C, respectively. The computed modes bear reasonable similarity with experimental results by Reimann and Grigull [255] corresponding to $\overline{q}_w^{''}$ = 16.21, 21.49, and 27.10 W/cm², as shown in Fig. A.9(b). In addition, Nusselt number predictions are within those based on the Berenson [256] and Klimenko [257] correlations. Bazdidi-Tehrani and Zaman [240] extended the LS method to saturated film boiling on a vertical wall. Son and Dhir [241] used the ghost fluid (GF) method in conjunction with their LS scheme to investigate film boiling on a horizontal cylinder in 2-D and 3-D domains, also accounting for the cylinder wall. Son and Dhir [242] the explored the effects of decreasing cylinder diameter on film boiling in 3-D domain, and the simulated trends were consistent with prior experimental data. Gibou *et al.* [68] also implemented the GF method in conjunction with the LS scheme to study film boiling in 2-D domain and obtained good qualitative results. Kim and Son [243] investigated film boiling in a simple jet impingement configuration.
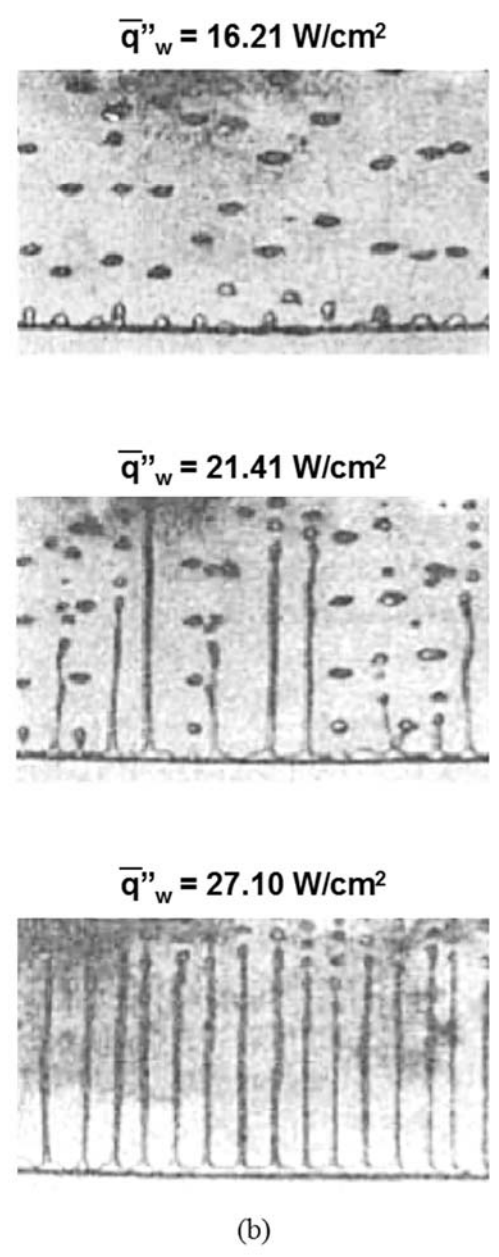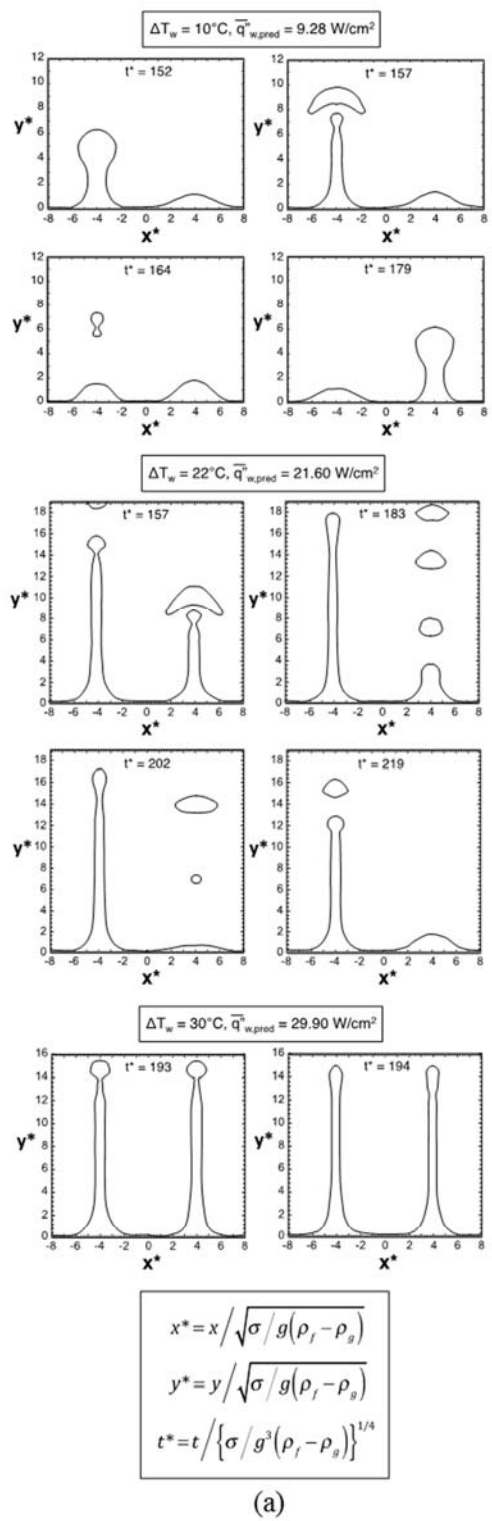
Fig. A.9: (a) Simulation results for film boiling of water using LS scheme in 2-D domain with energy jump condition for ΔT_w = 10, 22, and 30°C. (b) Experimental results for film boiling of water for different heat fluxes. Adapted from Son and Dhir [135].

Welch and Wilson [179] were the first to implement the VOF method in boiling situations, with phase change based on energy jump condition, and tested their approach with film boiling in 2-D domain. Their simulation results compare well with those of Son and Dhir [135] and Juric and Tryggvason [181], who used different numerical schemes. Figures A.10(a) and A.10(b) show simulation results for bubbles pinching off the vapor-liquid interface, and corresponding temporal variations of Nusselt number, respectively. Figure A.10(b) shows the time-averaged Nusselt number agrees with predictions based on the Berenson correlation [256]. Simulations at higher heat flux predicted mushroom shaped behavior similar to that from [181]. Welch and Rachidi [244] extended the Welch and Wilson model by incorporating the solid wall in the computational domain, therefore incorporating all three phases: liquid, vapor, and solid. Agarwal *et al*. [245] also used the VOF scheme to investigate bubble growth and heat transfer in film boiling in 2-D domain, but Nusselt number was under-predicted compared to predictions based on the Berenson [256] and Klimenko's [257] correlations. Hardt and Wondra [88] used the VOF scheme with Tanasawa's phase change model to study film boiling in 2-D domain. They developed a different mass source term smearing scheme at the interface to decrease numerical instabilities as discussed earlier. Their simulations produced mushroom shaped bubbles with long jets connecting the bubbles to the vapor film at the wall. Yuan *et al*. [246] used the VOF scheme to investigate both natural convection and forced convection film boiling on a sphere in non-orthogonal body-fitted coordinates. Sun *et al*. [157] studied 2-D film boiling using the VOF scheme along with their simplified conductivity formulation.
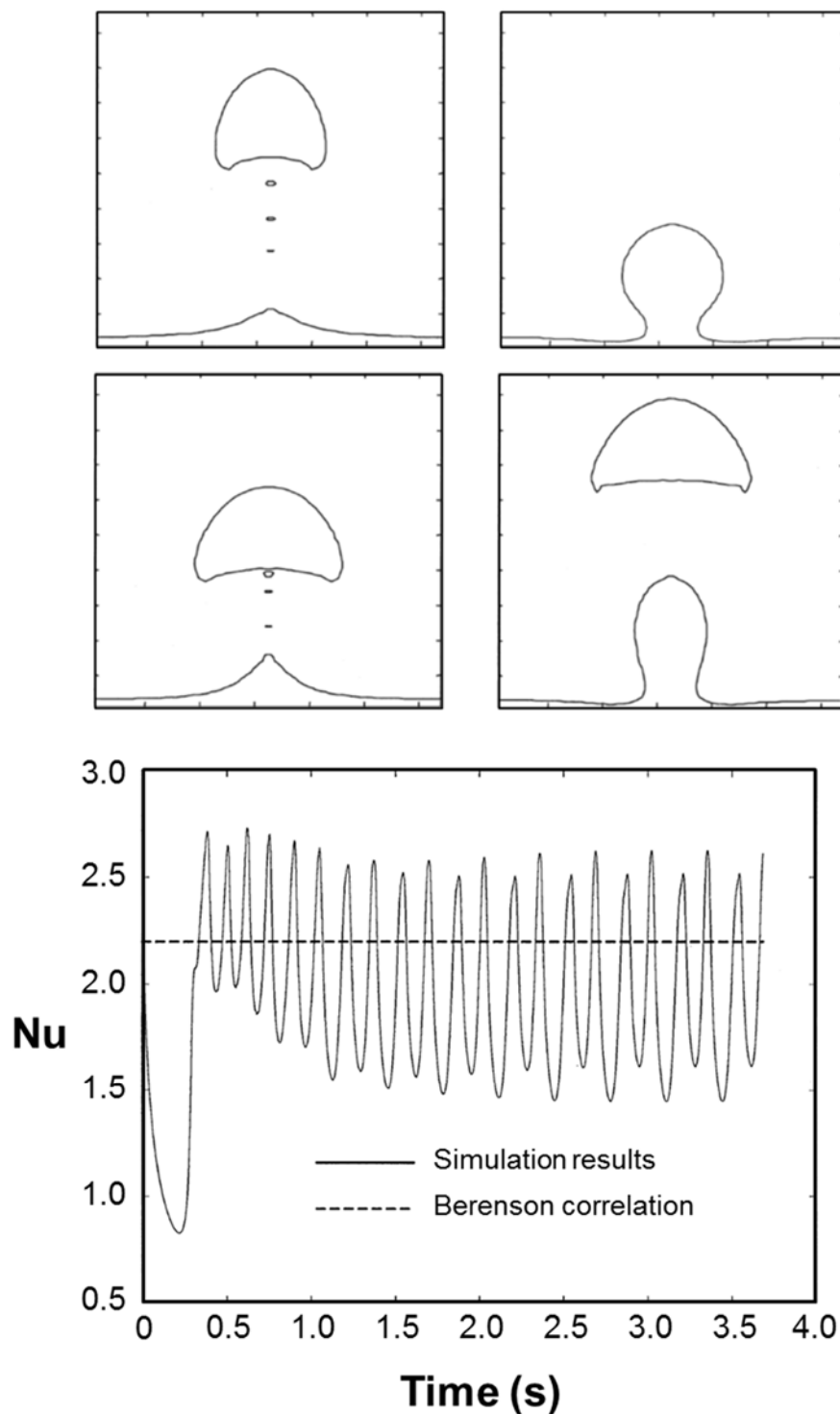
Fig. A.10: (a) Simulation results of film boiling using VOF scheme in 2-D domain with energy jump condition. (b) Comparison of simulation results of Nusselt number and prediction of prior correlation. Operating conditions for simulations are: T_{sat} = 500 K, p_{sat} = 1.013x10^5 Pa, σ = 0.1 N/m, h_{fg} = 10 kJ/kg, ΔT_w = 10°C, ρ_f = 200 kg/m^3, ρ_g = 5 kg/m^3, $c_{p,f}$ = 400 J/kg.K, $c_{p,g}$ = 200 J/kg.K, k_f = 40 W/m.K, k_g = 1 W/m.K, μ_f = 0.1 Pa.s, and μ_g = 0.005 Pa.s. Adapted from Welch and Wilson [179].

Another example of VOF-based simulation is an investigation of film boiling on a spherical surface by Arevalo *et al*. [247].

Several other methods have also been used to simulate film boiling. Using the CLSVOF scheme, Tomar *et al*. [188] showed bubbles generating alternatively at nodes and anti-nodes and, above certain superheat values, captured long vapor jets below the bubbles, similar to simulation results of Son and Dhir [135]. They studied film boiling of both R134a and water, and found that bubble frequency is higher for R134a. Welch and Biswas [250] and Tomar *et al*. [251] explored the effects of applying an electric field on film boiling by coupling electrohydrodynamics with the CLSVOF method. Guo *et al*. [252] simulated film boiling on a horizontal wall using the VOSET method. Tsui *et al*. [253] used a modified VOF method to simulate horizontal film boiling. Li *et al*. [258] used a hybrid LB scheme, where the LB method was used to simulate fluid flow, but the energy equation was solved using a traditional finite difference scheme. They were able to simulate, not only film boiling, but the entire boiling curve, including nucleate, transition, and film boiling, and demonstrated quantitative agreement with experimental results.

A.5.1.3 Flow Boiling

In the studies discussed above, it is quite obvious that investigators have focused most two-phase computational efforts on relatively simple and elemental nucleate pool boiling (and very slow flow boiling) and film boiling phenomena. However, these phenomena do serve as important test cases for validation of numerical schemes and phase change models, and constitute an important foundation for addressing more complicated two-phase

phenomena. As discussed in the Introduction, most modern heat transfer applications involve far more complicated phase change phenomena, which include high flow velocities, turbulence, and many discrete moving interfaces.

Flow boiling is characterized by liquid-to-vapor phase change along a heated wall where flow velocity plays a crucial role in maintaining heat flux above incipient boiling, but safely below CHF. There is also a gradual axial increase in vapor production, which increases void fraction and results in several transitions between two-phase flow patterns. For example, vertical upflow in a long heated circular tube with subcooled inlet produces a succession of flow patterns, including pure liquid, bubbly, slug, annular, mist, and pure vapor. However, changes in any of the system parameters, such as inlet pressure, inlet quality, mass velocity, heat flux, tube diameter, or orientation relative to gravity, can have a drastic influence on transport behavior within each flow pattern, as well as transitions between patterns, hence on pressure drop, heat transfer coefficient, and CHF.

By examining the progress made with direct numerical simulations of nucleate boiling and film boiling, it is evident that their adaptability to flow boiling scenarios of practical interest requires extremely high grid resolution, rendering computations practically impossible. This is why investigators attempting full-scale simulation of flow boiling, such as in micro-channels, usually rely on simple models with coarser grid. Reviewed below are these flow boiling simulation efforts. Table A.4 provides a useful summary of these studies.

Mukherjee and Kandlikar [259] studied vapor bubble growth in water along a micro-channel using the LS method in 3-D domain, with phase change based on energy jump

Table A.4: Summary of computational studies on flow boiling.

Author(s)	Two-phase System	Test Fluid	Multiphase Scheme	Mesh[a]	Mass Source Terms[b]	Remarks
				LS Method		
Mukherjee and Kandlikar (2005) [259]	Single bubble growth in rectangular micro-channel during flow boiling	Water	LS in 3-D domain	Domain: $4.95l_s \times 0.99l_s \times 0.99l_s$ $l_s = 200$ μm Mesh: $480 \times 96 \times 48$ (half domain with symmetry wall)	$$\dot{m}_g = \frac{k_f \cdot \nabla T}{h_{fg}}$$ where $k^{-1} = k_f^{-1} H$	− Studied single bubble growth in superheated liquid placed at the center of the cross-section of a microchannel during flow boiling − Initial growth rate was constant but once it filled the cross-section the growth rate increased rapidly due to high evaporation rate caused by the thin layer of liquid between the bubble and the wall − Bubble growth rate increases with increase in superheat and decrease in Reynolds number − Gravity played an insignificant role on bubble growth − Bubble behavior qualitatively similar to experimental observations
Lee and Son (2008) [260]	Single bubble dynamics in rectangular micro-channel during flow boiling	Water	LS in 3-D domain	Domain 1: 0.4 mm × 0.4 mm × 10 mm Mesh: 0.0125 mm cell size Domain 2: 3 mm × 3 mm× 10 mm Mesh: 0.094 mm cell size	$$\dot{m}_g = \frac{k \cdot \nabla T}{h_{fg}}$$ where $k^{-1} = k_f^{-1} H$	− Studied bubble dynamics during flow boiling in microchannel using a simplified model for microlayer evaporation − Bubble growth rate and heat transfer increased significantly when channel size was smaller than departure diameter − Contact angle affected the heat transfer in the thin liquid layer between the bubble and the wall − Obtained good agreement of bubble growth rate with experiments from literature
Suh *et al.* (2008) [261]	Flow boiling in multiple parallel rectangular micro-channels	Water	LS in 3-D domain	Domain: 0.2 mm × 0.4 mm× 10 mm Mesh: 0.0125 mm cell size	$$\dot{m}_g = \frac{k \cdot \nabla T}{h_{fg}}$$ where $k^{-1} = k_f^{-1} H$	− Studied flow boiling in parallel microchannels using method similar to [260] including the effect of immersed solid − When bubble formation is not simultaneous in parallel channels, backward bubble expansion causing reverse flow was observed − More reverse flow was observed for smaller contact angle and higher wall superheat − There was an overall reduction in average heat transfer with backward flow when compared with single microchannel with no backward flow

Mukherjee (2009) [262]	Single bubble growth on heated wall in rectangular micro-channel during flow boiling	Water	LS in 3-D domain	Domain: $4.95l_s \times 0.99l_s \times 0.99l_s$ $l_s = 200$ μm Mesh: $320 \times 80 \times 40$ (half domain with symmetry wall)	$$\dot{m}_g = \frac{k_f \cdot \nabla T}{h_{fg}}$$ where $k^{-1} = k_f^{-1} H$	− Studied bubble growth in flow boiling and compared with pool boiling − Increase in contact angle increased heat transfer in nucleate boiling but not so much in flow boiling − The receding bubble interface performed better than advancing bubble interface in term of heat transfer − Thin-film evaporation was observed to be the primary heat transfer mechanism
Mukherjee and Kandlikar (2009) [263]	Single bubble growth on heated wall with restriction at inlet in rectangular micro-channel during flow boiling	Water	LS in 3-D domain	Domain: $3.96l_s \times 0.99l_s \times 0.99l_s$ $l_s = 200$ μm Mesh: $512 \times 128 \times 64$ (half domain with symmetry wall)	$$\dot{m}_g = \frac{k_f \cdot \nabla T}{h_{fg}}$$ where $k^{-1} = k_f^{-1} H$	− Studied single bubble growth in flow boiling with constrained inlet − The heat transfer performance was seen to reduce significantly only when they reached a restriction where only 4% inlet area was open − Results were consistent with experiments
Mukherjee et al. (2011) [264]	Single bubble growth on heated wall in rectangular micro-channel during flow boiling	Water	LS in 3-D domain	Domain: $3.96l_s \times 0.99l_s \times 0.99l_s$ $l_s = 200$ μm Mesh: $320 \times 80 \times 40$ (half domain with symmetry wall)	$$\dot{m}_f = -\frac{k_f \cdot \nabla T}{h_{fg}}$$ where $k^{-1} = k_f^{-1} H$	− Performed a parametric study to understand effects on single bubble growth during flow boiling − Bubble growth rate and shape compared well with experimental observations − Wall heat transfer increased with superheat but did not change with flow rate − Surface tension did not affect bubble growth − Bubble with the lowest contact angle showed highest growth rate and wall heat transfer − Wall heat transfer increased significantly due to movement of liquid-vapor interface
Zhou et al. (2013) [265]	Flow boiling in micro-channel	Water	LS in 2-D domain (using COMSOL)	Domain: 107 μm $\times 40$ mm Mesh: 250,000 cells	$$S_g = r_c \rho_f \frac{(T - T_{sat})}{T_{sat}}$$ where r_c is mobility factor, which is proportionally increased depending on interface temperature deviation from T_{sat} $$Q = -S_g h_{fg} \delta_s$$	− Studied flow boiling in a microchannel − Boiling regimes were identified and validated with analytical model and experimental data − CHF was said to occur when liquid layer at the wall diminishes completely − Effect of reentrant cavities was included and it was observed to enhance CHF − Investigated non-uniform heating configurations and CHF was observed to be higher for microchannel with upstream heating

Table A.4: Continued

				VOF Method		
Yang *et al.* (2008) [266]	Horizontal flow boiling in coiled tube with circular cross-section	R141b	VOF in 3-D domain (using Fluent) Turbulence: Realizable *k-ε* model	Domain: $D = 6$ mm, coil length = 70 mm, bend radius = 28 mm Mesh: 118,800 cells	$S_g = -S_f = r_i \alpha_g \rho_g \dfrac{\left(T - T_{sat}\right)}{T_{sat}}$ for condensation ($T < T_{sat}$) $S_g = -S_f = r_i \alpha_f \rho_f \dfrac{\left(T - T_{sat}\right)}{T_{sat}}$ for evaporation ($T > T_{sat}$) $r_i = 100$ s^{-1} $Q = S_f h_{fg}$	− Studied flow boiling in a horizontal coiled tube − Phase distribution agreed with experimental observations − Flow velocities behaved as expected with bubbly flow showing similar velocities in both phases, while stratified flow showing strong differences between velocity of phases.
De Schepper *et al.* (2009) [165]	Flow boiling in convection section of steam cracker with circular cross-section	Gasoil	VOF in 3-D domain (using Fluent) Turbulence: Standard *k-ε* model	Domain: $D = 0.0525$ m, each tube has 4 passes with 11.3 m length each Mesh: 1,993,648 cells	$S_g = -S_f = r_i \alpha_g \rho_g \dfrac{\left(T - T_{sat}\right)}{T_{sat}}$ for condensation ($T < T_{sat}$) $S_g = -S_f = r_i \alpha_f \rho_f \dfrac{\left(T - T_{sat}\right)}{T_{sat}}$ for evaporation ($T > T_{sat}$) $r_i = 0.1$ s^{-1} $Q = S_f h_{fg}$	− Studied flow boiling in a convection section of a steam cracker − Various flow boiling regimes like bubbly, slug, wavy and stratified were captured in the simulations
Fang *et al.* (2010) [267]	Flow boiling in vapor-venting rectangular micro-channel	Water	VOF in 3-D domain (using Fluent)	Domain: Fluid: 5 mm × 150 μm × 300 μm Mesh: 330 × 20 × 25 Membrane: 5 mm × 150 μm × 50 μm Mesh: 330 × 20 × 4	$S_g = -S_f = r_i \alpha_g \rho_g \dfrac{\left(T - T_{sat}\right)}{T_{sat}}$ for condensation ($T < T_{sat}$) $S_g = -S_f = r_i \alpha_f \rho_f \dfrac{\left(T - T_{sat}\right)}{T_{sat}}$ for evaporation ($T > T_{sat}$) $r_i = 100$ s^{-1} $Q = S_f h_{fg}$	− Studied flow boiling in microchannel with vapor-venting capability − Vapor-venting channel gave much lower pressure drop in comparison to conventional channel − Vapor venting significantly inhibited liquid film rupture and local dryout − Superhydrophobic membrane increased vapor-venting efficiency but some condensation on the membrane compromised part of the performance

Zhuan and Wang (2010) [167]	Flow boiling in rectangular micro-channel	Water	VOF in 3-D domain	Domain: 275 μm × 636 μm × 25,400 μm Mesh: 2,593,674 cells Uniform and non-uniform grids	For first stage: $q_i'' = \dot{m}_g h_{fg}$ q_i'' based on Marangoni heat flux correlation [168,169] For second stage: $\dot{m}_g = f(R)$ is related to the growth rate and R defined in [170,171] $q_i'' = h_{fg}\dfrac{d\dot{m}_g}{dt}\Delta t$	– Studied flow boiling in microchannel – Correlations were uses to calculate heat flux and corresponding interfacial mass flux – Bubble generation, growth, departure, combining and shrinking was displayed in numerical results – Results showed qualitative agreement with prior experimental data
Wei *et al.* (2011) [268]	Subcooled vertical upflow boiling in rectangular channel under swing motion	Water	VOF in 3-D domain	Domain: 2 mm × 20 mm × 5 mm Mesh: 675,000 cells	$S_g = -S_f = r_i\alpha_g\rho_g\dfrac{\left(T-T_{sat}\right)}{T_{sat}}$ for condensation ($T < T_{sat}$) $S_g = -S_f = r_i\alpha_f\rho_f\dfrac{\left(T-T_{sat}\right)}{T_{sat}}$ for evaporation ($T > T_{sat}$) $r_i = 100$ s^{-1} $Q = S_f h_{fg}$	– Studied flow boiling in a vertical channel with additional inertial forces induced by swing motion – Bubble sliding along the wall, growth of bubbles and multiple bubbles mergers were observed – Smaller bubbles with higher pressure were sucked into the bigger bubble with lower pressure – Growth curves for bubbles and wall temperatures near ONB agreed well with correlations – Swing motion effected bubble sliding, bubble detachment, pressure drop, and heat transfer
Zhuan and Wang (2011) [269]	Subcooled flow boiling in rectangular micro-channel	HFE-7100	VOF in 3-D domain	Domain: 235.2 μm × 578.8 μm × 1 cm Mesh: 1,367,834, 452,866 cells	Bubble growth in wall superheated region: $\dot{m}_v = f(R)$ related to growth rate and R defined in [170,171] $q_i'' = h_{fg}\dfrac{d\dot{m}_g}{dt}\Delta t$ Bubble condensation in subcooled liquid: $q_i'' = h_i\left(T_g - T_f\right)$ h_i is heat transfer coefficient from correlation [270]	– Studied bubble growth, condensation, and collapse in subcooled microchannel flow boiling – Bubbles grew at the superheated region close to the wall, departed from the wall, and then started condensing in the subcooled flow – This condensing behavior is different from what is observed in saturated boiling where the bubble will continue to grow or transition to slug flow – At high subcooling, surface tension was shown to effect evolution of subcooled boiling behavior – Flow patterns compared well with experiments

Zu *et al.* (2011) [176]	Single bubble growth in rectangular mini/micro-channel during flow boiling	Water	VOF in 3-D domain Turbulence: Standard *k-ε* model	Domain: 40 mm × 1.6 mm × 0.38 mm Mesh: 225 × 50 × 20	Pseudo nucleation used to inject vapor from wall to simulate mass transfer	− Studied bubble growth in a mini/micro-channel using a simplified model for mass transfer − Experimental observation was used to define growth rate − Results reproduced experimental observation of bubble distortion and its trajectory
Jeon *et al.* (2011) [172]	Subcooled vertical upflow boiling in rectangular channel to study single condensing bubble	Water	VOF in 3-D domain (using Fluent)	Domain: 15 mm × 15 mm × 30 mm Mesh: cell size at interface = 1/16th initial bubble diameter	$S_f = -S_g = \dfrac{h_i}{h_{fg}} \dfrac{(T_{sat}-T_{i,j})A_b\alpha_{g,j}}{\Sigma_j \alpha_{g,j} V_j}$ *j* is interfacial cell and h_i interfacial heat transfer coefficient from [173]. $Q_i = S_f h_{fg}$	− Studied single condensing bubble during subcooled flow boiling in vertical upflow configuration − Predicted bubble volume compared well with experimental volume which was analyzed using technique in [271] − Results showed condensation increases the bubble velocity but decreases the rise distance due to a shorter lifespan − Velocity gradient in the flow accelerated the bubble lateral motion
Zhuan and Wang (2012) [272]	Flow boiling in circular micro-channel	R134a, R22	VOF in 3-D domain	Domain: D = 0.5 mm, L = 70.7 mm Mesh: 1,436,298 cells, 20 μm cell size	$\dot{m}_g = f(R)$ related to growth rate, R defined in [170,171] $q_i'' = h_{fg} \dfrac{d\dot{m}_g}{dt}\Delta t$	− Studied flow regimes and flow regime transitions in a circular microchannel − Effects of heat flux, saturated temperature, and mass velocity on bubble growth, coalescence, incipience point, and flow regime transition was captured − Predicted flow patterns and bubble distribution at the end of the channel agreed well with experiments
Pan *et al.* (2012) [273]	Subcooled vertical upflow boiling in rectangular channel to study single condensing bubble	Water	VOF in 3-D domain (using Fluent)	Domain 1: 2 mm × 10 mm × 5 mm Mesh: 457,413 cells Domain 2: 15 mm × 30 mm × 15 mm Mesh: 432,000 cells	$S_f = -S_g = \dfrac{h_i}{h_{fg}} \dfrac{(T_{sat}-T_{i,j})A_b\alpha_{g,j}}{\Sigma_j \alpha_{g,j} V_j}$ *j* is interfacial cell and h_i given by $h_i = \dfrac{k_f Nu_b}{D_b}$ where $Nu_b = f(\mathrm{Re}_b, \mathrm{Pr}_f, Ja, Fo_{bi})$, *bi* denotes initial bubble diameter $Q = S_f h_{fg}$	− Studied single condensing bubble during subcooled flow boiling in vertical upflow configuration in two separate channels − The bubble lifetime and bubble size history agreed well with prior experiments − Results of bubble deformations agreed with experiments. − Initial bubble size, liquid subcooling and system pressure significantly influenced bubble deformation

Magnini *et al.* (2013) [89]	Flow boiling of single elongated bubble in circular micro-channel	R113, R245f, R134a	VOF in 2-D axisymmetric domain, modified with height function reconstruction algorithm (using Fluent)	Domain: $D = 0.5$ mm, adiabatic length = $8D$ to $16D$, heated length = $12D$ to $56D$ Mesh: $D/300$ minimum cell size	$\dot{m}_g = \dfrac{2\gamma}{2-\gamma}\sqrt{\dfrac{M}{2\pi R}}\dfrac{\rho_g h_{fg}\left(T - T_{sat}\right)}{T_{sat}^{3/2}}$ where $\gamma = 1$ $S_g = -S_f = \dot{m}_g\left|\nabla\alpha_g\right|$ $Q = -S_g\left(h_{fg} - T\left(c_{pg} - c_{pf}\right)\right)$ Procedure to smear mass source term is similar to that of Hardt and Wondra [88]	− Studied flow boiling of elongated bubble as they move in the heated microchannel during flow boiling − In heated section, bubble nose was observed to accelerate following an exponential time law which agreed with theoretical models − Film evaporation was the primary heat transfer mechanics, but heat transfer enhancement was also observed in the wake region
Magnini *et al.* (2013) [274]	Flow boiling of back-to-back elongated bubbles in circular micro-channel	R113, R245fa	VOF in 2-D axisymmetric domain, modified with height function reconstruction algorithm (using Fluent)	Domain: $D = 0.5$ mm, adiabatic length = $8D$ to $50D$, heated length = $12D$ to $22D$ Mesh: $D/300$ minimum cell size	$\dot{m}_g = \dfrac{2\gamma}{2-\gamma}\sqrt{\dfrac{M}{2\pi R}}\dfrac{\rho_g h_{fg}\left(T - T_{sat}\right)}{T_{sat}^{3/2}}$ where $\gamma = 1$ $S_g = -S_f = \dot{m}_g\left|\nabla\alpha_g\right|$ $Q = -S_g\left(h_{fg} - T\left(c_{p,g} - c_{p,f}\right)\right)$ Procedure to smear mass source term is similar to that of Hardt and Wondra [88]	− Studied flow boiling of back to back elongated bubble in the heated microchannel − Trailing bubble in the heated section exhibited different behavior than the leading bubble because of the long thermal disturbance behind the first bubble − Overlap of effects of two bubbles increased average heat transfer in comparison to the case with single bubble
Bahreini *et al.* (2015) [164]	Subcooled flow boiling to study single condensing bubble	Water	VOF in 2-D domain (using OpenFOAM)	Domain: 10 mm × 20 mm Mesh: 200 × 400	$S_g = r_i\alpha_f\rho_f\dfrac{\left(T_{in} - T_{sat}\right)}{T_{sat}}$ where $r_i = 100$ s^{-1} $Q = -S_g h_{fg}$	− Studied condensing bubble in subcooled flow boiling − Predicted condensing behavior compared well with experiments − Results showed condensation increased the bubble velocity and the bubble covers longer path than an adiabatic bubble − Increase in subcooling reduced bubble life span − Velocity gradient in the flow accelerated the bubble lateral motion towards higher velocity flow

Lorenzini and Joshi (2015) [275]	High heat flux flow boiling in rectangular micro-channel	Water	VOF in 3-D domain (using Fluent)	Domain: 300 μm × 150 μm, adiabatic length = 0.5 mm, heated length = 4.5 mm. Mesh: 267,900 cells	$S_g = -S_f = r_i \alpha_g \rho_g \dfrac{(T - T_{sat})}{T_{sat}}$ for condensation ($T < T_{sat}$) $S_g = -S_f = r_i \alpha_f \rho_f \dfrac{(T - T_{sat})}{T_{sat}}$ for evaporation ($T > T_{sat}$) $r_i = 0.1 \text{ s}^{-1}$ $Q = S_f h_{fg}$	− Studied flow boiling in a rectangular microchannels − Effect of non-uniform heat flux was compared to uniform heat flux − For cases with more heat rejection downstream, large temperature gradients were observed due to accumulation of vapor in that region
Lee *et al.* (2016) [276]	Flow boiling in micro-channel specially designed for extreme heat fluxes	Methanol	VOF in 3-D domain (using Fluent) Turbulence: Standard *k-ε* model	Domain: fluid between fins: 10 μm × 90 μm, separate inlet and outlet sections Mesh: 2,301,160 cells, 1 μm minimum cell size	$S_g = -S_f = r_i \alpha_g \rho_g \dfrac{(T - T_{sat})}{T_{sat}}$ for condensation ($T < T_{sat}$) $S_g = -S_f = r_i \alpha_f \rho_f \dfrac{(T - T_{sat})}{T_{sat}}$ for evaporation ($T > T_{sat}$) $r_i = 10{,}000 - 50{,}000 \text{ s}^{-1}$ $Q = S_f h_{fg}$	− Studied flow boiling in extreme heat flux microchannels − Void fraction contours as well as pressure and temperatures of the wall were investigated
Pan *et al.* (2016) [277]	Single bubble growth during flow boiling in circular and square micro-channels	R113	VOF in 2-D axisymmetric and 3-D domains (using Fluent)	Domain: For 2-D: $D = 0.5$ mm, adiabatic length = $8D$, heated length = $14D$ Mesh: 68,780 cells For 3-D: $W = 0.5$ mm, adiabatic length = $6W$, heated length = $10W$ Mesh: 634,260 cells	$Q = \dfrac{\alpha_g \rho_g c_{p.g} (T_{sat} - T) + \alpha_f \rho_f c_{p.f} (T_{sat} - T)}{\Delta t}$ $S_g = -S_f = -Q / h_{fg}$ Using non-iterative time advancement (NITA) scheme in Fluent, energy source term isiteratively set to T_{sat} after every time step	− Studied flow boiling in circular and square microchannel − Excellent quantitative agreement is observed for bubble motion, bubble growth rate, liquid film thickness and heat transfer coefficient with literature in the 2-D case

Table A.4: Continued

Magnini and Thome (2016) [278]	Slug flow during flow boiling in circular micro-channel	R245fa	VOF in 2-D axisymmetric domain (using Fluent)	Domain: $D = 0.5$ mm, adiabatic length = $8D$, heated length = $22D$ Mesh: 1.65 µm cell size	$\dot{m}_g = \frac{2\gamma}{2-\gamma}\sqrt{\frac{M}{2\pi R}}\frac{\rho_g h_{fg}\left(T - T_{sat}\right)}{T_{sat}^{3/2}}$ $\gamma = 1$ $S_g = -S_f = \dot{m}_g \left\|\nabla\alpha_g\right\|$ $Q = -S_g\left(h_{fg} - T\left(c_{p,g} - c_{p,f}\right)\right)$ Procedure to smear mass source term is similar to that of Hardt and Wondra [88]	– Studied slug flow in a circular microchannel – Vapor bubbles were patched in the inlet region with a constant generation frequency – Behavior of multiple bubbles was seen to be significantly different from single bubble – Behaviors like recirculating flow in liquid slug and interfacial waviness at the vapor bubble tail were captured – Results were used to advance theoretical model developed to predict bubble velocity and film thickness
Other Methods						
Wu *et al.* (2007) [279]	Horizontal flow boiling in serpentine tube with circular cross-section	R141b	Eulerian multiphase flow model in 3-D domain (using Fluent) Turbulence: Realizable k-ε model	Domain: $D = 10$ mm, 4 heated sections 80 mm long, with unheated straight and round sections	$S_g = -S_f = r_i\alpha_g\rho_g\frac{\left(T - T_{sat}\right)}{T_{sat}}$ for condensation ($T < T_{sat}$) $S_g = -S_f = r_i\alpha_f\rho_f\frac{\left(T - T_{sat}\right)}{T_{sat}}$ for evaporation ($T > T_{sat}$) $r_i = 0.1$ s^{-1} $Q = S_f h_{fg}$	– Studied flow boiling in serpentine tube – Experimental observations and numerical predictions were consistent with each other – Horizontal channel showed stratification of phases pointing to gravity dominance. Bends showed redistribution of phases causing vapor to go towards the inside part of the tube.
Nichita and Thome (2010) [155]	Single bubble growth during flow boiling in rectangular micro-channel	Water, R134a	CLSVOF in 3-D domain (using Fluent)	Domain: 800 µm × 200 µm × 200 µm Mesh: 320 × 80 × 80	$S_g = -S_f = \frac{k\left(\nabla T \cdot \nabla\alpha_f\right)}{h_{fg}}$ $k = \alpha_g k_g + (1-\alpha_g)k_f$ $Q = S_f h_{fg}$	– Studied bubble growth during flow boiling in microchannel – Simplified source terms were used

a   Indicated mesh sizes are optimum sizes chosen by original authors in simulations

b   (1) Positive and negative signs of mass source term may differ from those used by original authors due to differences in definition used. (2) Some variations in mass source terms are expected due to scalar versus vector definitions. (3) Only source term formulations are described in this table; exact usage in continuity equations should be obtained from original sources. (4) Micro-layer formulation is not included in description of source term in this table.

condition. A spherical vapor bubble was initiated at the center of a square 200-μm micro-channel with superheated liquid flowing around it. Using a constant contact angle, they found that bubble growth rate increases with increasing superheat and decreases with increasing flow rate. Figure A.11 depicts bubble growth for $T_{in} = 102°C$ and wall superheat of $\Delta T_w = 7°C$. The initial bubble maintains spherical shape while growing until it reaches the size of the channel's cross-section, following which it begins to grow axially into oblong shape, a behavior that is qualitatively consistent with experimental observations. Mukherjee [262] extended this model to bubble growth in flow boiling of along the wall of a micro-channel. His simulations suggest the effect of contact angle on a moving meniscus in flow boiling is far less significant than in nucleate pool boiling. Mukherjee and Kandlikar [263] extended this model further to flow boiling in a micro-channel with inlet flow constriction, and showed that the restriction decreases bubble growth and increases flow reversal. Mukherjee *et al*. [264] also examined wall heat flux during vapor bubble growth along a micro-channel. Their simulations yielded good agreement of bubble growth rate with experiments, and wall heat flux was shown to increase with increasing superheat, unaffected by changes in flow rate.

Magnini *et al*. [89] incorporated the height function interface reconstruction method in the VOF scheme, with phase change according to Tanasawa's model, to simulate growth of a Taylor bubble during flow boiling in micro-channel. The model was solved in Fluent using 2-D domain for three different fluids, R113, R134a, and R245fa. Fig. A.12(a) shows axial growth of an R113 bubble for $G = 600$ kg/m²s and $q_w" = 9$ kW/m². Fig. A.12(b) shows velocity contours along with variations of axial and radial velocities, and Fig. A.12(c) temperature contours and corresponding heat transfer coefficient variations as
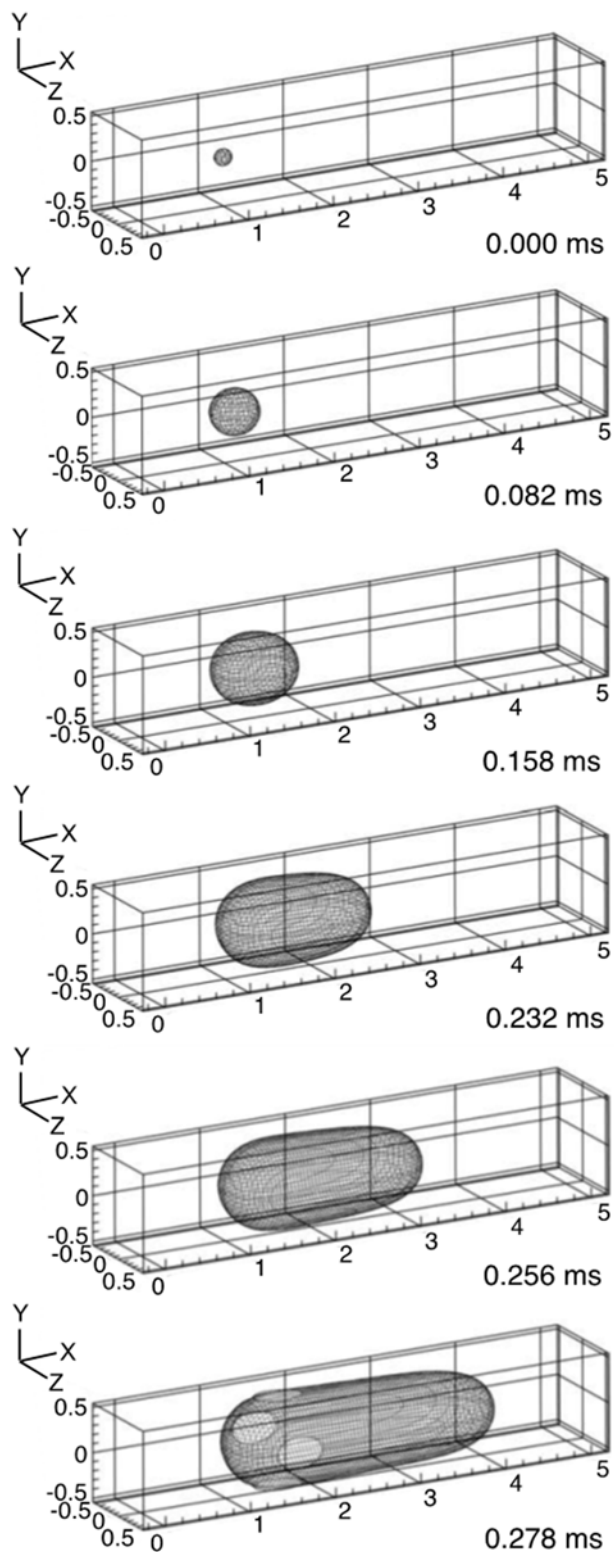
Fig. A.11: Simulation results for vapor bubble growth in water flow boiling along a 200-μm micro-channel using LS scheme in 3-D domain with energy jump condition for T_{in} = 102°C, ΔT_w = 7°C, Re = 100, and g = 0. Adapted from Mukherjee and Kandlikar [259].
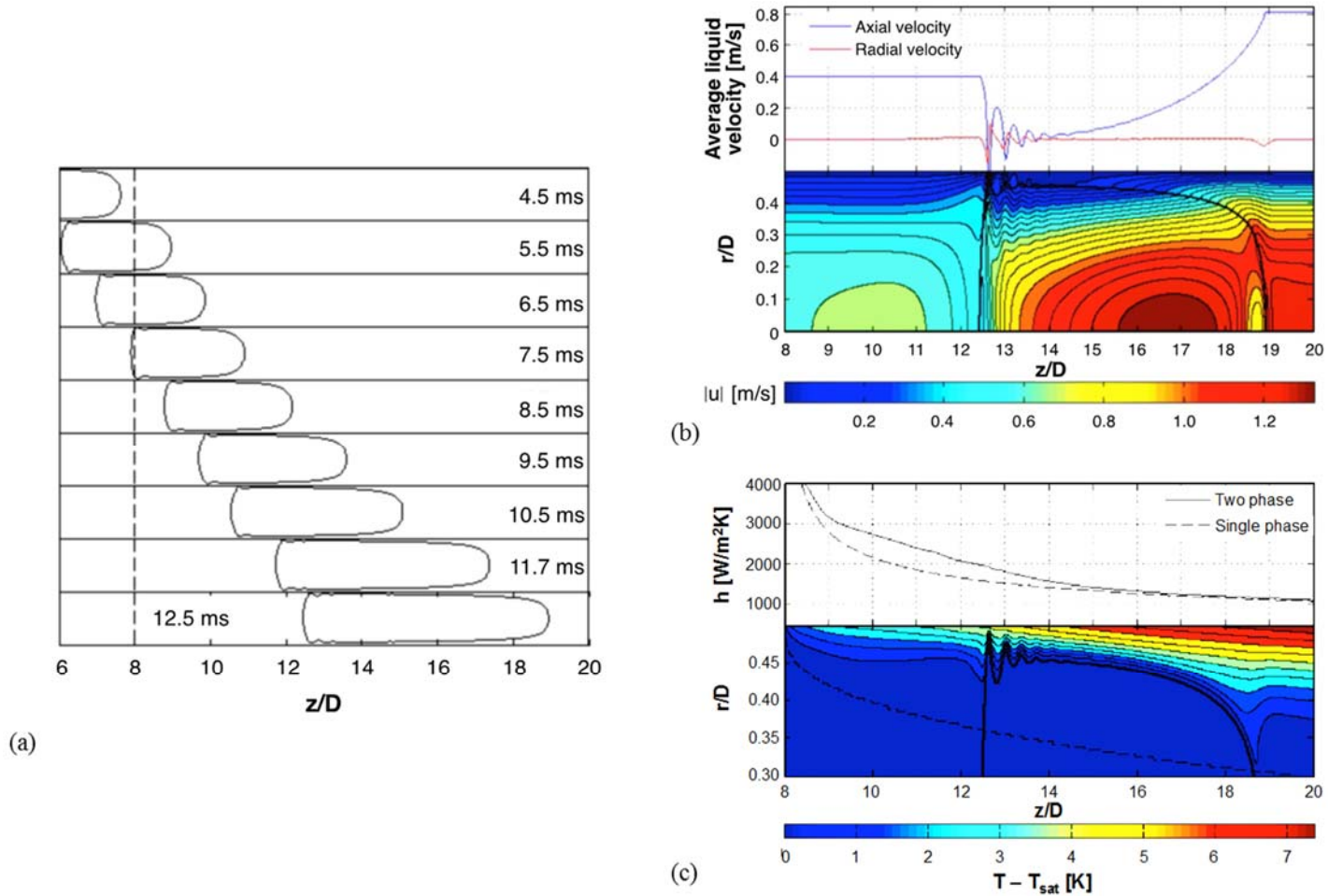
Fig. A.12: (a) Simulation results for bubble growth in flow boiling of R113 along a 0.5-mm channel at $G = 600$ kg/m^{2}s using VOF scheme in 2-D axisymmetric domain with Tanasawa phase change model (dashed line marks entrance to heated region). (b) Average liquid axial and radial velocities (above) and velocity contours (below); the thick solid black line indicates bubble interface. (c) Heat transfer coefficient (above) and temperature contours (below). Adapted from Magnini *et al.* [89].

compared to single-phase flow. Magnini *et al*. performed single-phase computations separately with single-phase liquid domain. Based on the computed flow and temperature field variations around the bubble, they identified four separate heat transfer regions: wake region downstream from the bubble (z/D = 8-10), wake region near the bubble (z/D = 10-12.5), liquid film region (z/D = 12.5-19), and liquid region upstream of the bubble (z/D > 19). Magnini *et al*. [274] extended this work to two elongated Taylor bubbles, and showed how bubble overlap improves heat transfer compared to a single bubble. In another study, Magnini and Thome [278] investigated back-to-back vapor bubbles that are generated at fixed frequency.

Lee and Son [260] studied flow boiling of water in a micro-channel using the LS method in 3-D domain, with phase change based on energy jump condition, by incorporating a simplified model for micro-layer evaporation as in [183], and achieved good agreement of predicted bubble growth rate with experiments. They showed that both bubble growth rate and wall heat transfer rate increase when channel size is smaller than bubble departure diameter. Suh *et al*. [261] extended the same model to parallel micro-channels, accounting also for the solid wall. They captured the backward bubble expansion responsible for flow reversal that occurs when bubbles do not form concurrently in the separate channels. They also showed that the backward bubble growth reduces wall heat transfer rate in multiple micro-channels compared to a single micro-channel.

Zu *et al*. [176] studied flow boiling of water in a micro-channel using the VOF method in 3-D domain by approximating phase change using a method they termed "pseudo-boiling". They injected vapor artificially through a small hole on the wall to simulate nucleation. Then bubble growth was defined by a fixed rate of vapor generation at the

contact area between the bubble and the superheated wall; the vapor injection and generation rate were based on experimental observations [177]. This method was shown to reproduce experimental observations of bubble distortion and trajectory. Zhuan and Wang [167] studied nucleate boiling of water in a micro-channel using the VOF method in 3-D domain, along with correlations to define interfacial mass and energy transfer for different stages of boiling, and achieved qualitative agreement with prior experiments. Zhuan and Wang [272] extended this model to flow boiling of R134a and R22 in a micro-channel with mass velocities ranging from 350-2000 kg/m^{2}s, and demonstrated good agreement of predicted flow patterns and flow pattern transitions with experimental data.

Bubble growth in subcooled flow boiling is undoubtedly more complicated that in saturated flow boiling. Here, superheated liquid is present close to the heated wall, and subcooled liquid in the central core, causing bubbles departing from the wall to incur condensation in the core. Zhuan and Wang [269] studied the effects of subcooled boiling of water on bubble growth, condensation and collapse using the VOF model with bubble condensation rate based on a heat transfer coefficient correlation by Warrier *et al*. [270]. The predicted flow patterns corresponded well with experimental observations, but heat transfer coefficient predictions were less accurate. Jeon *et al*. [172] investigated condensation of a bubble in subcooled water in a channel with rectangular cross section in vertical upflow using the VOF method in 3-D domain, with phase change based on an interfacial heat transfer correlation from [173]. Figure A.13(a) compares predicted temporal variations of bubble shape alongside actual bubble images. Since initial conditions affect bubble shape, they were not able to compare exact bubble shape with
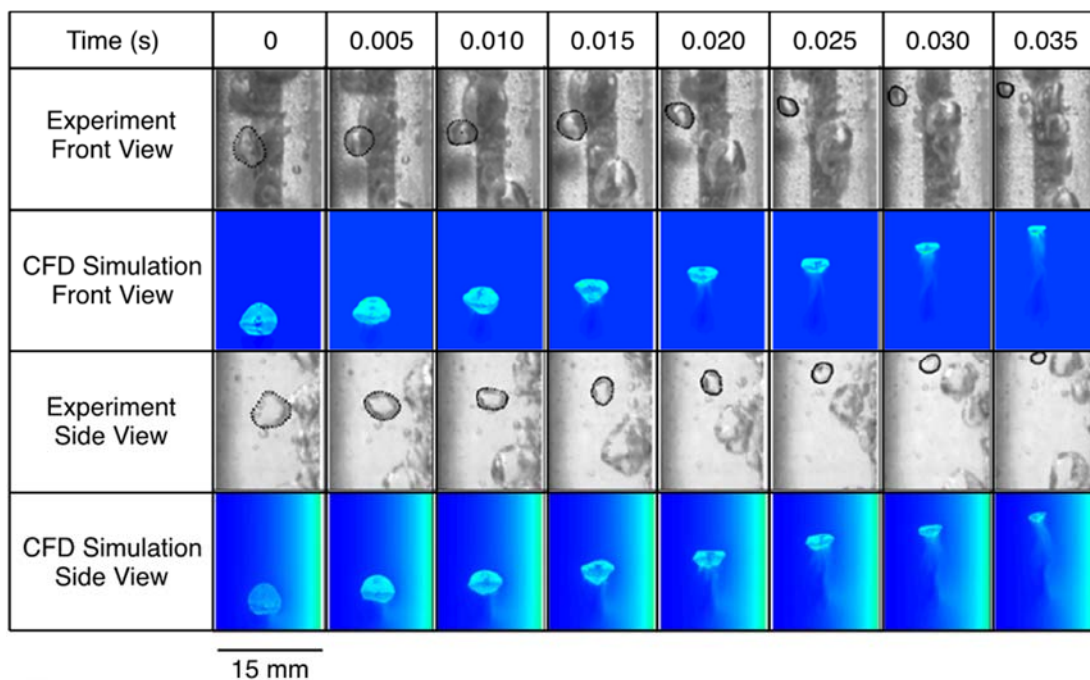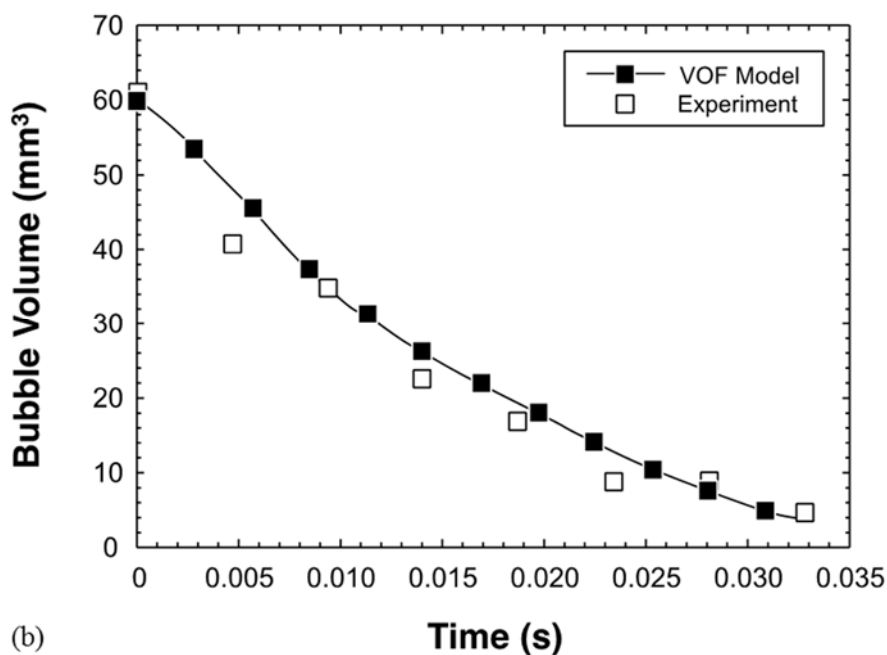
Fig. A.13: (a) CFD simulations of void fraction for condensation in subcooled water flow using VOF scheme in 3-D domain with phase change based on heat transfer correlation, compared to experimentally captured images. (b) Comparison of temporal variations of predicted and experimental bubble volume. Adapted from Jeon *et al.* [172].

experiments. However, as shown in Fig. A.13(b), bubble volume agrees well with experimental data, an indication of the effectiveness of the model in capturing mass transfer rate. Pan *et al*. [273] also studied condensation of water bubbles in a vertical channel using the VOF scheme in 3-D domain, and formulated phase change based on heat transfer coefficient $h_i = k_f \, Nu_b \, / \, D$, where $Nu_b = f(\text{Re}_b, \text{Pr}_f, Ja, Fo_{b_i})$, and Re_b, Pr_f, Ja, and Fo_{bi} are, respectively, the bubble Reynolds number, liquid Prandtl number, Jacob number, and Fourier number evaluated using initial bubble diameter. Their predictions of bubble size, deformation and lifetime compare well with prior experiments. Bahreini *et al*. [164] studied bubble condensation in subcooled water flow using the VOF scheme in 2-D domain with phase change based on the Lee model [73], and their predictions show consistency with prior experimental observations.

Several researcher teams [165,266-268,275,276,279] have relied on the Lee model [73] to simulate phase change during flow boiling using 3-D domain. Wu *et al*. [279] used the Eulerian multiphase phase model in Fluent. Unlike the VOF model, this model solves continuity and momentum equations separately for the two phases, and coupling at the interface is achieved through pressure and interphase exchange coefficients. Wu *et al*. studied flow boiling of R141b in a horizontal serpentine tube with heating along only the straight sections, where flow enters the tube 3°C subcooled and exits saturated. They accounted for turbulence using Realizable *k-ε* model, and showed good agreement of predictions with experiments. Yang *et al*. [266] simulated flow boiling of R141b in heated coiled tube with circular cross section, with the flow entering the tube 8.5-10.5°C subcooled. They used the VOF scheme in Fluent using 3-D domain and, like Wu *et al*., used Realizable *k-ε* model for turbulence. They captured experimentally observed flow

regimes, including bubbly, churn, slug, stratified, and wavy, in order of increasing flow quality. As shown in Fig. A.14, both simulations and experiments show increasing flow rate for fixed heat flux delays transition to higher quality flow regimes, while increasing heat flux for fixed flow rate promotes earlier transition to high quality regimes. De Schepper *et al*. [165] simulated hydrocarbon feedstock of the convection section of a steam cracker in 3-D domain using standard *k-ε* model for turbulence, and were able to capture flow regimes from earlier literature. Fang *et al*. [267] simulated flow boiling of water in a vapor venting micro-channel with 3°C inlet subcooling using VOF model in Fluent, and assumed laminar flow because of low Reynolds numbers. They showed that the vapor venting micro-channel produces lower pressure drop than a micro-channel without venting for the entire range of heat fluxes below critical value, which defines when vapor generation rate exceeds vapor venting capacity of the channel, but pressure drops are similar above this value. Wei *et al*. [268] simulated subcooled flow boiling of water in a vertical rectangular channel with single-sided heating using the VOF scheme, and achieved good agreement with correlations from literature. They also induced inertia by swing motion and, as expected, found pressure to increase in comparison to motionless conditions. Lee *et al*. [276] investigated void fraction patterns, temperature, and pressure in specially designed micro-channels for GaN-on-SiC semiconductor devices. Lorenzini and Joshi [275] studied the effects of non-uniform heating on high-flux micro-channel flow boiling.

Other noteworthy simulations of micro-channel boiling flow include a study by Nichita and Thome [155], who used CLSVOF with a simplified source term based on energy jump condition to study bubble growth and departure in a micro-channel. Using the Level Set
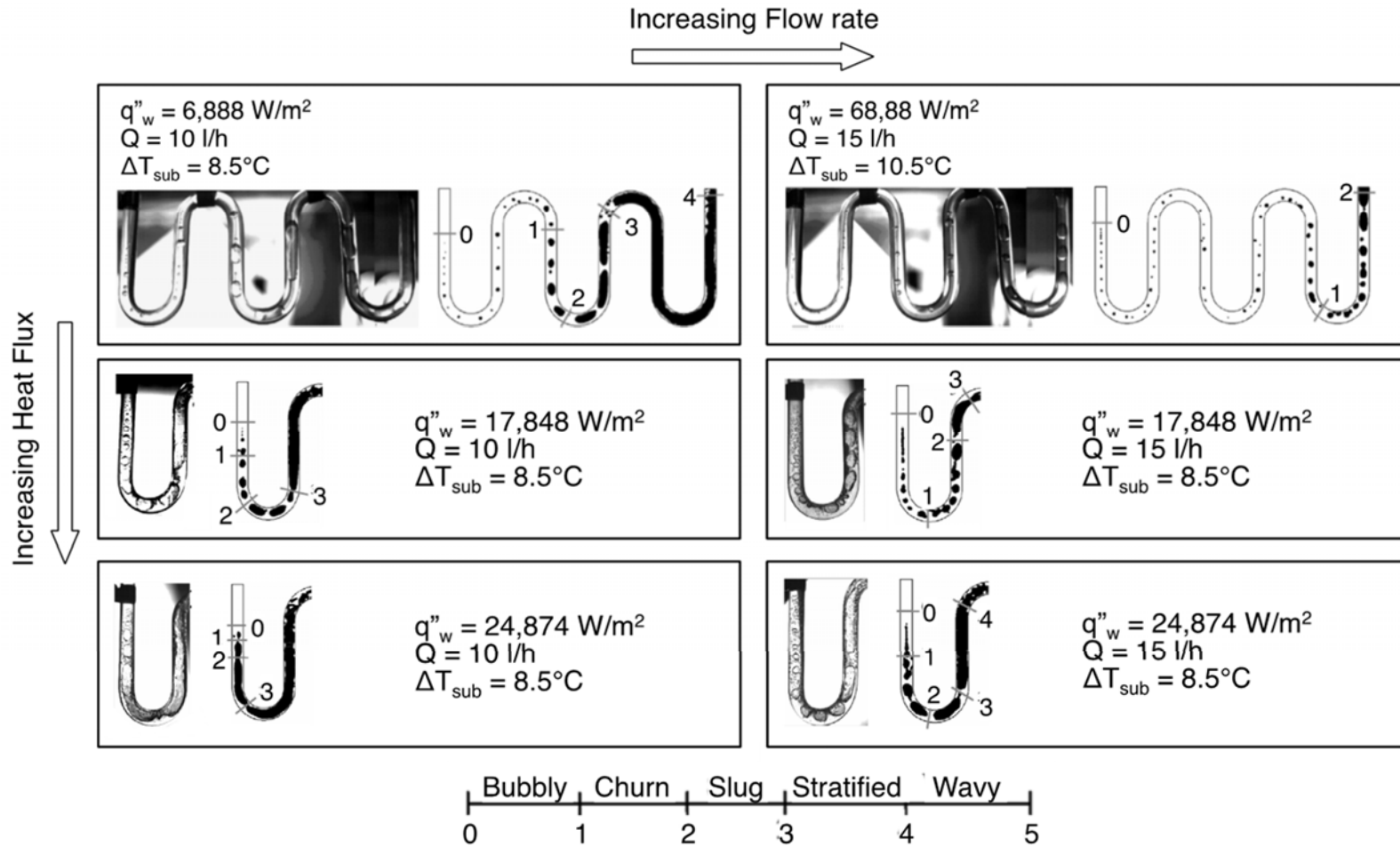
Fig. A.14: Comparison of simulation predictions and experimental results for axial variations of flow regimes and void fraction for horizontal flow boiling of R141b along a 6-mm diameter serpentine tube. Simulations are based on VOF scheme in 3-D domain and Lee phase change model. The tube has a centerline length of 70 mm and 28 mm pitch. Dark color in simulation results represents vapor-liquid interface and not vapor phase. Adapted from Yang *et al.* [266].

Two-Phase Flow Mode available in Chemical Engineering Module in the commercial finite element analysis software COMSOL, Zhou *et al.* [265] performed both steady state and transient computations of flow boiling to explore both bubble flow patterns and flow transitions. They also showed how reentrant cavities increase dryout heat flux. Pan *et al.* [277] defined a new source term for phase change based on energy required for the cell containing the interface to achieve saturation conditions. They defined the energy and mass source terms as

$$Q = \frac{\alpha_g \rho_g c_{p,g} (T_{sat} - T) + \alpha_f \rho_f c_{p,f} (T_{sat} - T)}{\Delta t} \qquad \text{(A.47)}$$

and
$$S_g = -S_f = -Q/h_{fg}. \qquad \text{(A.48)}$$

They tested this method with saturated flow boiling in circular and square micro-channels using 2-D and 3-D domains, respectively. They used the non-iterative time advancement (NITA) scheme in Fluent and iteratively solved the energy equation to set interfacial temperature to T_{sat}, and showed good agreement with prior findings.

As an example of other simulation approaches, Krepper *et al.* [174] studied subcooled flow boiling in a channel of a nuclear fuel assembly in commercial software CFX using a two-fluid Eulerian approach. This approach requires validation and improvement in interfacial source/sink terms and results are very application specific. Krepper *et al.* adopted the wall boiling model by Kurul and Podowski [280] and compared predictions to experimental data by Bartolomej and Chanturiya [281] and Bartolomej *et al.* [282] for preliminary model validation. Krepper and Rzehak [283] and Krepper *et al.* [284] further improved this model for vertical upflow boiling of R12 in a heated circular pipe.

A.5.2 <u>Condensation</u>

Condensation is commonly encountered in heat exchange devices tasked with rejecting heat from a closed two-phase loop, and is associated with conversion of vapor to liquid. Common condensation configurations include film condensation with and without flow, dropwise condensation, and internal flow condensation. Film condensation involves formation of a liquid on a wall whose temperature is below saturation, and the film increases in thickness and flow rate in the direction of gravity in the absence of vapor flow, or in the flow direction in the presence of high vapor shear. This form of condensation is encountered mostly on tubes or vertical walls. Dropwise condensation is characterized by droplets covering the wall, which range in thickness from a few micrometers to larger, more visible liquid masses. Flow condensation occurs within a tube and involves a succession of flow patterns including pure vapor, annular, slug, bubbly and pure liquid [285] in order of decreasing quality. In the literature, numerical simulations have been focused on film condensation and internal flow condensation. This is why the review below will be focused on these configurations, with relevant works summarized in Table A.5.

Early simulations of flow condensation were performed by Zhang *et al*. [178] in an investigation of capillary blockage in mini-channel. Using the VOF scheme in 2-D domain, they applied an artificial source term to force the interface to T_{sat}, then calculated an energy source term and corresponding mass source term using the newly updated temperature field. Their results show that increasing flow velocity increases the length required to achieve full condensation, and higher flow rates increase interfacial waviness.

Table A.5: Summary of computational studies on condensation.

Author(s)	Two-phase System	Test Fluid	Multiphase Scheme	Mesh[a]	Mass Source Terms	Remarks
				VOF Method		
Zhang *et al.* (2001) [178]	Horizontal flow condensation in miniature circular channel and between parallel plates	Water	VOF in 2-D domain	Domain: *(R or H)* × *L* = 1.5 mm × 1 cm Mesh: 32 × 42	Artificially large source term used to set temperature of interface to T_{sat}, Q based on newly updated temperature field from energy equation $$S_f = \frac{Q}{h_{fg}}$$	− Studied flow condensation to understand capillary blocking − Predicts condensation length increases with increasing velocity; change in saturation temperature for same velocity does not have significant influence on condensation length − Predicts film thickness and condensation length decease with decreasing hydraulic diameter or distance between plates − Predicts higher velocities produce waviness at liquid film interface
Yuan *et al.* (2006) [286]	Vertical downflow condensation between parallel plates	Water	Derivative of VOF model in 2-D domain, where fluid fraction is defined in terms of total enthalpy	Domain: *W* × *L* = 4 cm × 20 cm (half domain of 2 cm × 20 cm used) Mesh: 18 × 70 for half domain	Artificially large source term used to set temperature of interface to T_{sat}, Q_f based on liquid water fraction factor f defined in terms of total enthalpy $$S_f = \frac{\rho_f}{\rho_g}\frac{Q_f}{h_{fg}}$$	− Studied vertical downflow film condensation between parallel plates − Surface tension effects not included in simulations − Predicts velocity strongly influences interfacial behavior
Da Riva and Del Col (2010) [287]	Flow condensation in circular mini-channel in multiple orientations	R134a	VOF in 2-D axisymmetric and 3-D domains (using Fluent) Turbulence: k-ω SST model	Domain: *D* = 1 mm, *L* = 1 m For 2-D domain: Mesh: 25,000 cells For 3-D domain: Mesh: 1,150,000 cells	$$S_g = -S_f = r_i\alpha_g\rho_g\frac{\left(T-T_{sat}\right)}{T_{sat}}$$ for condensation ($T < T_{sat}$) $$S_g = -S_f = r_i\alpha_f\rho_f\frac{\left(T-T_{sat}\right)}{T_{sat}}$$ for evaporation ($T > T_{sat}$) r_i = 7.5×10^5 - 10^7 s^{-1} $$Q = S_f h_{fg}$$	− Studied flow condensation in circular mini-channel in horizontal flow, vertical downflow, and in microgravity − Predicts flow is gravity dominated at low mass velocity of G = 100 kg/m²s, resulting in large variations among three flow configurations − Predicts flow is inertia dominated at high mass velocity of G = 800 kg/m²s due to strong interfacial shear, resulting in similar behavior among three flow configurations

Alizadehdakhel et al. (2010) [288]	Simultaneous evaporation and condensation in vertical thermosyphon	Water	VOF in 2-D domain (using Fluent)	Domain: bottom evaporator length = 40 cm, adiabatic length = 20 cm, top condenser length = 40 cm, D = 1.75 cm for fluid domain, with 1.9 cm outer diameter solid shell domain Mesh: 47,124 cells in inner fluid domain, 14,361 in outer solid domain	$S_g = -S_f = r_i x_{water} \alpha_g \rho_g \dfrac{(T-T_{sat})}{T_{sat}}$ for condensation ($T < T_{sat}$), x_{water} is mole fraction of water in gas phase $S_g = -S_f = r_i \alpha_f \rho_f \dfrac{(T-T_{sat})}{T_{sat}}$ for evaporation ($T > T_{sat}$) $r_i = 0.1$ s^{-1} $Q = S_f h_{fg}$	– Studied evaporation and condensation in vertical thermosyphon – Temperature profiles predicted for entire length compare well with experiments – Liquid and vapor void fraction contours accurately captured in both condensation and evaporation sections
Liu et al. (2012) [166]	Vertical downflow condensation between parallel plates	Water	VOF in 2-D domain	Domain: $W \times L$ = 4 cm × 40 cm (half domain of 2 cm × 40 cm used) Mesh: 500,000 cells for half domain	$S_g = -S_f = r_i \alpha_g \rho_g \dfrac{(T-T_{sat})}{T_{sat}}$ $r_i = 5000$ s^{-1} $Q = S_f h_{fg}$	– Studied vertical downflow film condensation between parallel plates – Predicts film starts laminar upstream and turns wavy laminar downstream – Predicts heat transfer is enhanced with increasing difference between wall temperature and inlet vapor temperature
Ganapathy et al. (2013) [156]	Flow condensation in rectangular micro-channel	R134a	VOF in 2-D domain (using Fluent)	Domain: H = 100 µm, L = 0.03 m Mesh: cell size = 2 µm	$S_g = -S_f = \dfrac{k(\nabla T \cdot \nabla \alpha_g)}{h_{fg}}$ k is effective thermal conductivity $Q = S_f h_{fg}$	– Studied flow condensation in micro-channel – Good agreement achieved between predicted two-phase frictional pressure drop and Nusselt number, and correlations from the literature – Good qualitative agreement achieved between predicted and experimental flow regimes
Chen et al. (2014) [163]	Horizontal flow condensation in rectangular micro-channel	FC-72	VOF in 3-D domain (using Fluent) Turbulence: Realizable k-ε model	Domain: square, W = 1 mm, L = 30 cm Mesh: 200,000 cells	$S_g = -S_f = r_{i,m} \alpha_g \rho_g (T-T_{sat})$ for condensation ($T < T_{sat}$) $S_g = -S_f = r_{i,mi} \alpha_f \rho_f (T-T_{sat})$ for evaporation ($T > T_{sat}$) $r_{i,m} = 100$ s^{-1} $Q = S_f h_{fg}$	– Studied flow condensation in micro-channel in horizontal orientation – Simulations capture bubbly, slug, transition, wavy annular, and smooth annular flow regimes – Predicted flow regimes agree well with prior experimental data

Yin *et al.* (2014) [289]	Horizontal flow condensation in circular mini-channel	Water	VOF in 3-D domain (using Fluent)	Domain: $D = 1$ mm, $L = 50$ mm Mesh: 1.54×10^6 cells	$S_g = -S_f = r_i \alpha_g \rho_g \dfrac{\left(T - T_{sat}\right)}{T_{sat}}$ for condensation ($T < T_{sat}$) $S_g = -S_f = r_i \alpha_f \rho_f \dfrac{\left(T - T_{sat}\right)}{T_{sat}}$ for evaporation ($T > T_{sat}$) $r_i = 5 \times 10^4$ s^{-1} $Q = S_f h_{fg}$	– Studied flow condensation in horizontal orientation with and without non-condensable gases – Predicts heat transfer coefficient is not affected by degree of superheat or flow rate – Predicts annular flow is prevalent with vapor fraction decreasing along channel – Predicts significant reduction in heat transfer coefficient when non-condensable gases are present, as gas layer is generated between vapor and liquid
Qiu *et al.* (2014) [290]	Vertical upflow condensation in circular channel	Water	VOF in 3-D domain (using Fluent) Turbulence: Reynolds Stress model	Domain: developing length = 1.8 m, test section length = 0.2 m, $D = 12$ mm Mesh: 630,000, 980,000 cells	$S_g = -S_f = r_i \alpha_g \rho_g \dfrac{\left(T - T_{sat}\right)}{T_{sat}}$ for condensation ($T < T_{sat}$) $S_g = -S_f = r_i \alpha_f \rho_f \dfrac{\left(T - T_{sat}\right)}{T_{sat}}$ for evaporation ($T > T_{sat}$) $r_i = 10^4$ s^{-1} $Q = S_f h_{fg}$	– Studied flow condensation in circular tube in vertical upflow – Predictions of frictional pressure drop and heat transfer compare well with correlations – Predicts bubbly, slug, churn, whispy annular, and annular flow regimes, which match flow regime map from the literature – Predicts eddy behavior in slug and churn flow regimes
Lee *et al.* (2015) [100]	Vertical downflow condensation in circular channel	FC-72	VOF in 2-D axisymmetric domain (using Fluent) Turbulence: k-ω SST model	Domain: $L = 0.8$ m, $D = 11.89$ mm Mesh: minimum cell size = 1.3 μm	$S_g = -S_f = r_i \alpha_g \rho_g \dfrac{\left(T - T_{sat}\right)}{T_{sat}}$ for condensation ($T < T_{sat}$) $S_g = -S_f = r_i \alpha_f \rho_f \dfrac{\left(T - T_{sat}\right)}{T_{sat}}$ for evaporation ($T > T_{sat}$) $r_i = 10^4$ s^{-1} $Q = S_f h_{fg}$	– Studied flow condensation in circular tube in vertical downflow – Predictions of heat transfer coefficient agree well with experiments – Predicts significant dampening of eddy diffusivity and steep temperature gradient at interface – Predicts wavelength and amplitude of interfacial disturbances increase along the channel

Qiu *et al.* (2015) [291]	Flow condensation in upright spiral tube	Propane	VOF in 3-D domain (using Fluent) Turbulence: Reynolds Stress model	Domain: hydraulic developing length = 1.4 m, thermal developing length = 0.4, test section length = 0.2 m, D = 14 mm, curvature diameter of tube = 2 m, inclination angle = 10°. Mesh: 980,000 cells	$S_g = -S_f = r_i \alpha_g \rho_g \dfrac{\left(T - T_{sat}\right)}{T_{sat}}$ for condensation ($T < T_{sat}$) $S_g = -S_f = r_i \alpha_f \rho_f \dfrac{\left(T - T_{sat}\right)}{T_{sat}}$ for evaporation ($T > T_{sat}$) $r_i = 10^4$ s^{-1} $Q = S_f h_{fg}$	– Studied flow condensation in upright spiral tube – Predicts stratified, annular, and mist flow regimes, which agree with experiments – Predicts heat transfer coefficient and frictional pressure drop increase with increasing flow rate and/or vapor quality – Predictions agreed well with experimental results and prior correlations
Zhang *et al.* (2016) [292]	Horizontal flow condensation in circular mini/micro-channel	R410a	VOF in 3-D domain (using Fluent) Turbulence: k-ω SST model	Domain: D = 0.25 – 4 mm, L = 100D Mesh: 1,340,000 cells for half-domain	$S_g = -S_f = r_i \alpha_g \rho_g \dfrac{\left(T - T_{sat}\right)}{T_{sat}}$ for condensation ($T < T_{sat}$) $S_g = -S_f = r_i \alpha_f \rho_f \dfrac{\left(T - T_{sat}\right)}{T_{sat}}$ for evaporation ($T > T_{sat}$) $r_i = 1.5 \times 10^6$ s^{-1} $Q = S_f h_{fg}$	– Studied flow condensation in mini/micro circular tube in horizontal orientation – Predicts heat transfer is enhanced with increasing mass velocity and/or vapor quality, and decreasing tube diameter and/or saturation temperature – Predicts liquid film thickness increases with increasing saturation temperature due to reduction in surface tension – Predictions of heat transfer coefficient and pressure gradient compare well with empirical correlations

Table A.5: Continued

Kharangate [Chapter 8, current work]	Vertical upflow condensation in circular channel	FC-72	VOF on 2-D axisymmetric domain (using Fluent) Turbulence: k-ω SST model with turbulence dampening of 10	Domain: $L = 0.8$ m, $D = 11.89$ mm Minimum cell size = 2 μm	$S_g = -S_f = r_i \alpha_g \rho_g \dfrac{\left(T - T_{sat}\right)}{T_{sat}}$ for condensation $(T < T_{sat})$ $S_g = -S_f = r_i \alpha_f \rho_f \dfrac{\left(T - T_{sat}\right)}{T_{sat}}$ for evaporation $(T > T_{sat})$ $r_i = 10^4$ s^{-1} $Q = S_f h_{fg}$	– Studied flow condensation in circular tube in vertical upflow – Predicts complex interfacial behavior corresponding to climbing film and flooding regimes – Local heat transfer coefficients are underpredicted upstream and overpredicted downstream – Predictions of average heat transfer coefficient and average wall temperature compare well with experimental data – Predicts sharp gradient in film temperature at interface due to dampening of eddy diffusivity

a   Indicated mesh sizes are optimum sizes chosen by original authors in simulations

Yuan *et al*. [286] studied film condensation between parallel plates in vertical downflow in 2-D domain using an approach to achieve T_{sat} at the interface similar to that of Zhang *et al*., along with the traditional VOF scheme, but defined fluid fraction in terms of total enthalpy. Liu *et al*. [166] also studied vertical downflow film condensation between parallel plates using the VOF method in 2-D domain, but with phase change based on the Lee model [73]. They showed the condensing film is initiated in smooth laminar state and becomes wavy laminar downstream due to increases in both Reynolds number and film thickness as depicted shown in Fig A.15.

Da Riva and Del Col [287] used the VOF scheme with phase change based on the Lee model [73] to study flow condensation of R134a in a circular micro-channel at different orientations relative to gravity and in microgravity. Gravity dominance was observed at low mass velocity of $G = 100$ kg/m^{2}s, with large differences in flow and heat transfer behaviors corresponding to different orientations. Differences were significantly reduced as mass velocity was increased to $G = 800$ kg/m^{2}s, where inertia began to dominate gravity. Ganapathy *et al*. [156] studied flow condensation of R134a in a micro-channel using the VOF scheme with phase change based on a simplified form of energy jump condition, and achieved qualitative agreement with flow patterns captured in prior experiments as shown in Fig A.16. They also achieved good agreement of two-phase frictional pressure drop and Nusselt number predictions with prior correlations from the literature. In another study, Chen *et al*. [163] used the VOF scheme to simulate flow condensation of FC-72 in a micro-channel, and their predictions of two-phase flow patterns agreed quite well with prior experiments. Yin *et al*. [289] and Zhang *et al*. [292] studied flow condensation in horizontal tubes. Yin *et al*. [289] studied the effect of non-condensable gases on flow
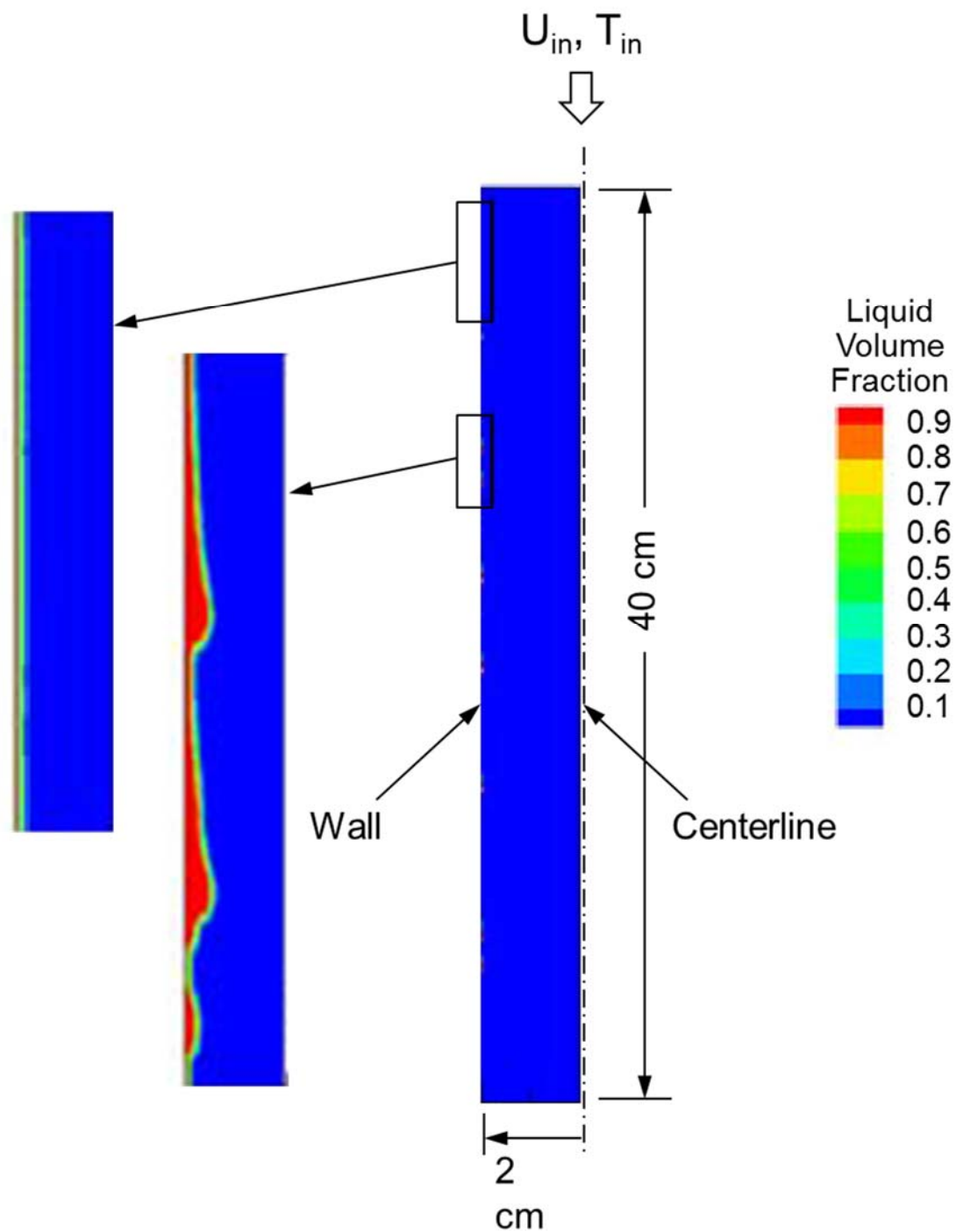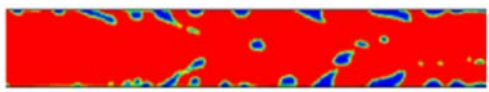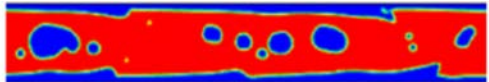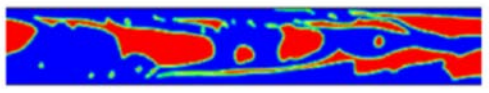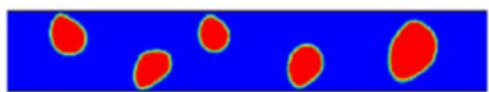
Fig. A.15: Void fraction predictions for film condensation of water during vertical downflow between parallel plates using VOF scheme in 2-D domain and Lee phase change model. Adapted from Liu *et al.* [166].

Fig. A.16: Comparison of numerically predicted condensation flow regimes for R134a along a 100-μm wide micro-channel using VOF scheme in 2-D domain and Lee phase change model, and experimental images from the literature. Adapted from Ganapathy *et al.* [156].

condensation in horizontal micro-tubes using the VOF scheme and showed how heat transfer is significantly compromised in the presence of air. Zhang *et al*. [292] investigated flow condensation of R410a in horizontal tubes ranging in diameter from 0.25 to 4 mm. Using the VOF scheme, they achieved good agreement of predicted heat transfer coefficients and pressure drops with empirical correlations.

Internal flow condensation studies at the macro scale include vertical downflow by Lee *et al*. [100] and vertical upflow by Qiu *et al*. [290] and by me in Chapter 8 of current work; all of whom used the VOF scheme with phase change based on the Lee model [73]. In Chapter 8, I investigated high heat flux vertical upflow condensation of FC-72 by rejecting heat to water flowing in counter-flow through an outer annulus. I used the k-ω model with Shear Stress Transport (SST) and a turbulence dampening factor of 10 as defined in the ANSYS Guide [86] to account for turbulence across the annular liquid film and the vapor core. The simulations yielded predictions of axial variations of void fraction, radial temperature profile, and heat transfer coefficient. Figure A.17(a) compares predicted and measured annular film flows corresponding to the climbing (upward moving) film regime. They both show interfacial ripples along the liquid film's interface, and liquid droplets entrained in the vapor core. Figure A.17(b) shows good agreement between predicted and measured average heat transfer coefficient for a broad range of mass velocities. Another important aspect of their study is the temperature distribution across the liquid film and influence of interfacial dampening of eddy diffusivity at the interface due to surface tension, as shown in Fig. A.17(c). This important interfacial dampening phenomenon will
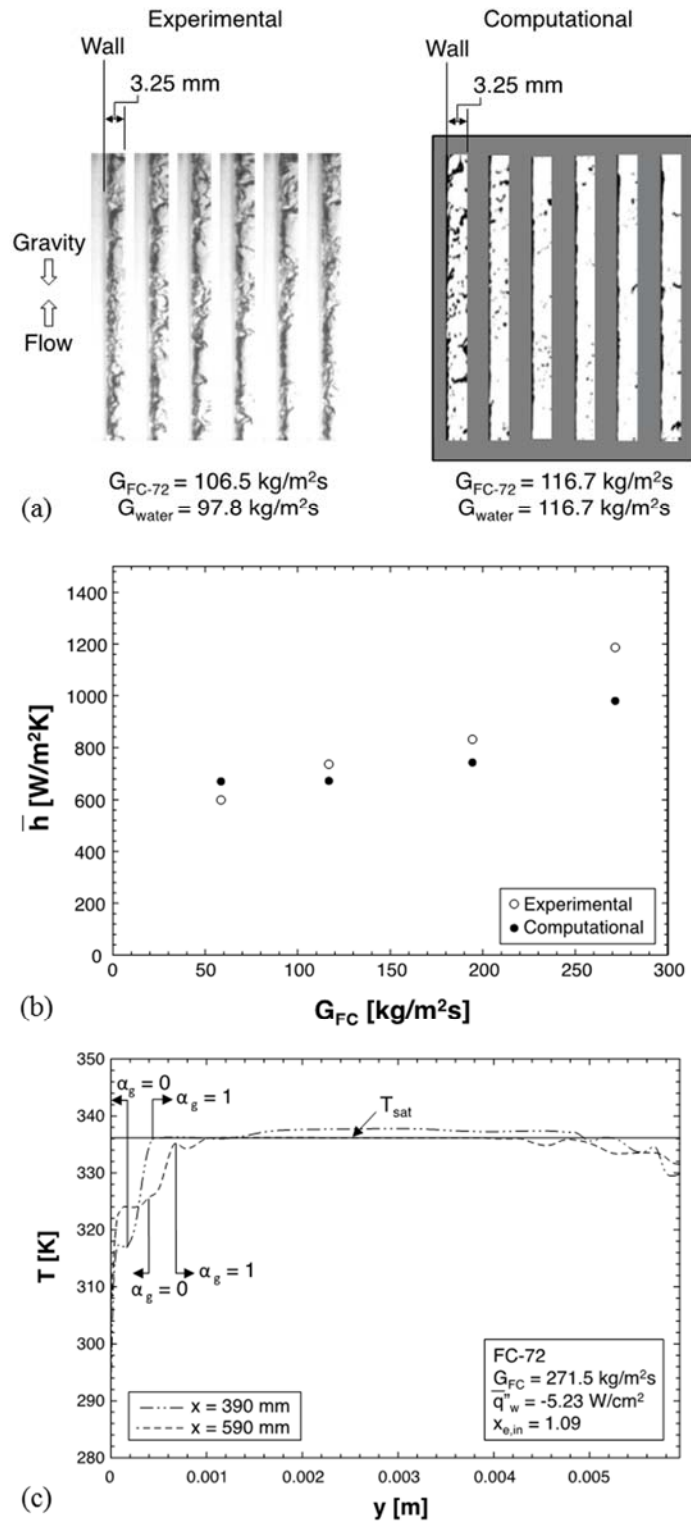
Fig. A.17: (a) Void fraction predictions using VOF scheme in 2-D axisymmetric domain and Lee phase change model of climbing film regime during vertical upflow condensation of FC-72, and experimental images. (b) Comparison of experimental and computed spatially averaged condensation heat transfer coefficient versus mass velocity. (c) Variation of computed fluid temperature with radial distance from the wall at two axial locations for $G_{FC} = 271.5$ kg/m^{2}s. Adapted from Chapter 8 of current work.

be addressed in more detail later in this paper. In another study, Qiu *et al*. [291] used the VOF scheme to study flow condensation of propane in an upright spiral tube. Alizadehdakhel *et al*. [288] used the VOF scheme in 2-D domain, with phase change based on the Lee model, to investigate simultaneous evaporation and condensation of water in a thermosyphon. Figure A.18(a) shows predicted wall temperature along the evaporation, adiabatic, and condensation sections of the thermosyphon, alongside closely matched experimental data. Figure A.18(b) shows the computational domain and vapor void fraction contours captured in the three sections.

Other noteworthy investigations are two simulation studies by Liu and Cheng [293,294], who used the LB method to model both film and dropwise condensation.

A.6 Future Needs and Recommendation

A.6.1 Overriding Needs

Clearly, investigators have achieved many noteworthy breakthroughs in simulating boiling and condensation systems. However, there is broad diversity in the methods used, and computations are presently limited to rather simple configurations, unlike the many diverse configurations found in systems of practical interest as discussed in the Introduction. Looking forward, it is universally acknowledged that computational tools will play a vital role in two-phase flow and heat transfer research, in departure from the present practice of relying on empirical correlations and costly experimental work. However, several important tasks must be undertaken before investigators can achieve the long-term objective of developing a more unified, physically based, accurate, and computationally efficient methodology. Key among these tasks are:
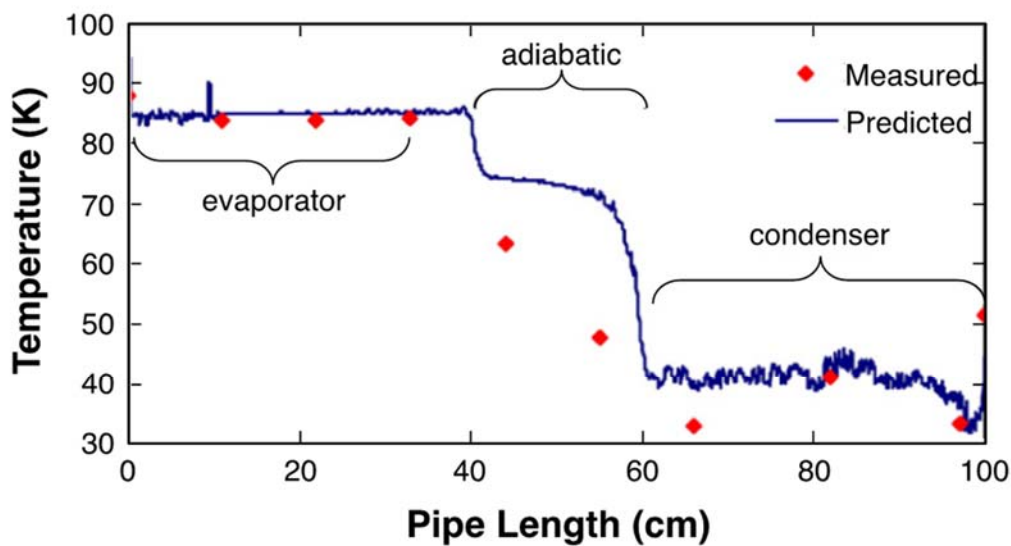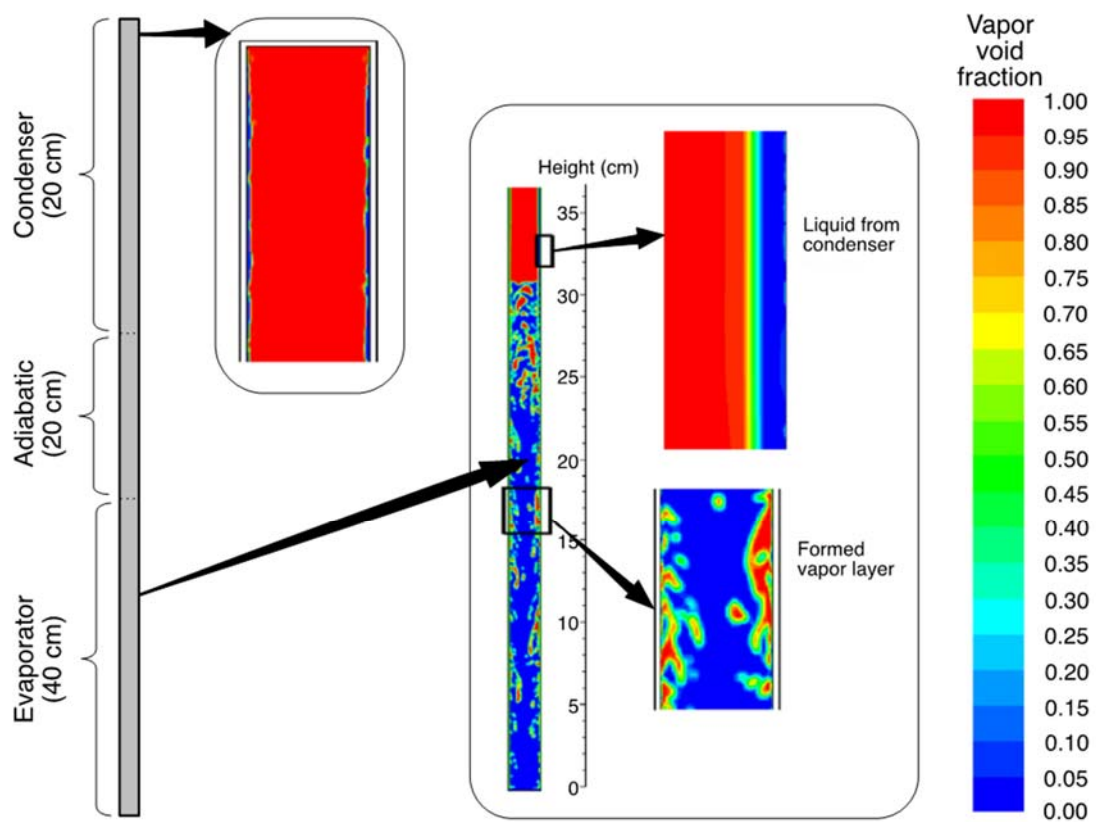
Fig. A.18: Simulation results for water thermosyphon using VOF scheme in 2-D domain and Lee phase change model. (a) Comparison of predicted and measured wall temperatures. (b) Void fraction predictions. Adapted from Alizadehdakhel *et al.* [288].

(1) New experiments designed specifically for validation of simulation models of boiling and condensation, and involving simultaneous use of state-of-the-art diagnostics tools.

(2) New or improved interface tracking schemes that conserve mass and accurately capture complex interface topologies.

(3) New or improved mass transfer models that capture the true physics of mass and energy transfer at the interface.

(4) New or improved turbulence models that accurately account for dampening of eddies across the liquid-vapor interface.

(5) More aggressive computational modeling of complicated phase-change configurations prevalent in modern applications.

A.6.2 <u>Validation Experiments and Better Diagnostics Tools</u>

Like experiments that have already been used to validate prior simulation work, future experiments must be carefully designed for the specific purpose of validating future simulations. Use of state-of-art diagnostic tools will play a vital role in these experiments. Aside from maximizing the use of conventional pressure, temperature, and flow rate measurement instrumentation, phase change experiments intended for validation of simulation models will require implementation of sophisticated diagnostic tools to measure volume fraction as well as both velocity and temperature contours. It is obvious from studies reviewed earlier that investigators have relied heavily on high-speed video imaging of the interface as a means of assessing the validity of two-phase schemes. This non-intrusive method of image capture and analysis has been used to determine interface shape

and in many cases used to infer void fraction. But, while high-speed video will continue to play a vital role in most phase change experiments, investigators often face difficulty resolving accurate void fraction information in situations involving multiple overlapping interfaces or reflection from the heated wall. Some researchers [295,296] have employed a 'total reflection method' to mitigate reflection problems, by visualizing the boiling process from behind a completely transparent heated wall, with a silicon oil layer used beneath the wall. However, a key drawback of this approach is it precludes testing realistic metallic surfaces when performing boiling experiments, given that lateral conduction plays a key role in all boiling situations. Temperature measurements can be made with probes embedded directly in the heated wall and in the flow. But most temperature measurements suffer from spatial resolution issues and relatively slow response time. Temperature sensors with fast response and higher spatial resolution have been developed by Heng *et al*. [297] and Moghaddam and Kiger [298], respectively. Multi-sensor conductivity and optical probes by Barrau *et al*. [299] and Kim *et al*. [300], and wire mesh probes by Prasser *et al*. [301] have been used to measure bubble diameter and velocity in pool boiling. Lyu and Mudawar [75,302,303] used a thin blade fitted with an array of micro-thermocouples to measure instantaneous temperature profile across a wavy, free-falling water film, simultaneously with measurements of film thickness and wave speed using thermal conductance sensors. Mudawar and Houpt [304,305] used laser Doppler velocimetry (LDV) to measure velocity profile (including turbulent fluctuations) across a free-falling film simultaneously with film thickness, the latter using an electrical conductance probe. This technique facilitated detailed mapping of liquid velocity streamlines relative to interfacial waves. A key limitation of many of the instruments just mentioned is their

intrusive nature. A very promising tool for velocity measurements is micro-particle image velocimetry (μ-PIV), which was used by Qu *et al*. [74] to measure liquid velocity profile in a micro-channel, and infrared (IR) thermography, used by Theofanous *et al*. [306,307] to capture thermal patterns on a heated wall. Khodaparast *et al*. [308] employed another type of μ-PIV called micro-particle shadow velocimetry (μ-PSV) to measure micro-channel flows. Further improvements in velocity measurements for boiling and condensing flows are possible with 3D PIV [309,310]. For micro-channel measurements, two noteworthy examples of studies involving simultaneous use of multiple diagnostic tools are experiments by Gerardi *et al*. [311] and Duan *et al*. [312]. These recent studies are good examples of the type of experiments and diagnostics tools that are needed for validation of future simulations of boiling and condensation.

A.6.3 <u>Improving Interface Tracking Methods</u>

Reviewed earlier in this article were several methods of interface tracking along with their advantages and disadvantages. Overall, it is crucial for numerical schemes to accurately conserve mass as well as capture interface topologies accurately. Even though several advances have been made towards accomplishing these goals, further improvements are necessary to tackle complex phase change scenarios. One aspect of interface tracking is the treatment of interface thickness. Some models use zero thickness [179], but are numerically difficult to solve, while others use an artificial thickness to smooth properties across multiple cells [88,135].

While different methods are available to account for surface tension, spurious currents must be avoided. Phase-field methods [146] take into account physical interactions at the

molecular level better than VOF, LS, and FT methods, hence improvements in those methods may be needed to better capture interfacial physics and surface tension effects.

Computing requirements are perhaps the biggest obstacle in computational modeling of phase change processes, and are the main impetus for preferring 2-D over 3-D simulations. However, two-phase flows are inherently highly three-dimensional and involve complex interface topologies that cannot be accurately resolved with 2-D simulations. Limitations of 2-D simulations have spurred the development of methods that combine multiscale (adaptive) meshes [135,313], where, to reduce computing requirements, analytical models are employed in certain regions of the grid where computations would have otherwise demanded very fine mesh. Overall, while researchers continue to develop new or improved methods for interface capturing, further validation of these methods is required using simulations of more complex phase change processes.

A.6.4 <u>Improving Mass Transfer Models</u>

The different phase change models that have been developed and/or adopted thus far fall short in both accuracy and ability to capture the true physics of mass and energy transfer at the interface. Simplifying assumptions such as constant temperature in the entire saturated phase, interface maintaining saturation temperature, and zero conductivity of one of the phases, preclude model closure and jeopardize predictive accuracy. In the short term, new or improved adaptive phase change schemes are needed that can accurately maintain interfacial temperature depending on local temperature deviation of the interface cell. The empirical coefficients in models like those of Tanasawa [72] and Lee [73] could be adjusted locally and not kept constant in simulations. In the long term, new or improved

phase change models are needed that can more accurately estimate both mass and energy transfer at the interface, which is lacking is current models.

A.6.5 <u>Better Account of Turbulence Effects</u>

Turbulence is prevalent in most practical two-phase flow and heat transfer processes. Moreover, two-phase flow generally promotes transition to turbulent flow at much lower Reynolds numbers than single-phase flow. Even though Direct Numerical Simulations (DNS) provide the highest accuracy, computing requirements are a major obstacle to implementing this method for full-scale phase change simulations. Many of the phase change studies involving turbulent modeling that were discussed earlier in this article employ Reynolds-averaged Navier-Stokes (RANS) models like the 2-equation, k-ε and k-ω models. While standard k-ε model is the most widely used turbulent model, it cannot accurately resolve momentum and thermal boundary layers in the vicinity of the wall, which is why low Reynolds number k-ε model is used in those locations. The standard k-ω model and k-ω model with Shear Stress Transport (SST) are also good models for momentum and thermal boundary layers. Using either low Reynolds number k-ε model or k-ω models in simulations requires high resolution mesh in locations like the wall or near a liquid-vapor interface.

An important aspect of turbulence in two-phase flows is dampening of turbulent fluctuations at the liquid-vapor interface by surface tension force: [100], Chapter 7 and Chapter 8 of current work. This phenomenon is illustrated in Fig. A.19(a) for a thin, free-falling film undergoing interfacial evaporation. As discussed in Chapter 7, turbulence intensity is reflected in the magnitude of eddy momentum diffusivity, ε_m. Near the wall,

$\varepsilon_m \to 0$, which, in the presence of a fairly constant heat flux across the thin film, produces large temperature gradient near the wall. A large increase in ε_m in the middle region of the film greatly decreases temperature gradient, resulting in fairly constant liquid temperature in the middle region. However, turbulent eddies are suppressed at the liquid-vapor interface by surface tension, and with $\varepsilon_m \to 0$ at the interface, a second large temperature gradient is produced near the interface. Figure A.19(b) shows temperature profiles across the film at different axial locations predicted using VOF scheme in 2-D axisymmetric domain and Tanasawa's phase change model. To generate the temperature profiles in Fig. A.19(b), I used the k-ω model with Shear Stress Transport (SST), with a turbulence dampening factor of 10. The large interfacial temperature gradient is clearly captured for downstream locations. A similarly large interfacial temperature gradient is captured in annular condensing films [Chapter 8 of current work] as was shown earlier in Fig. A.17(c). As discussed in Chapter 7 of current work, the large interfacial gradient can in fact be used to assess the accuracy of phase change models used.

Moving forward, a shift to higher accuracy simulations like Large Eddy Simulations (LES) would constitute an important step towards improving predictive accuracy of computational models involving turbulent boiling and condensing flows.

A.6.6 <u>Simulating more Complex Phase-Change Configurations Prevalent in Modern Applications</u>

It is obvious from the studies reviewed in this article that phase change simulation efforts have been focused on rather simple pool boiling, film boiling, flow boiling and flow
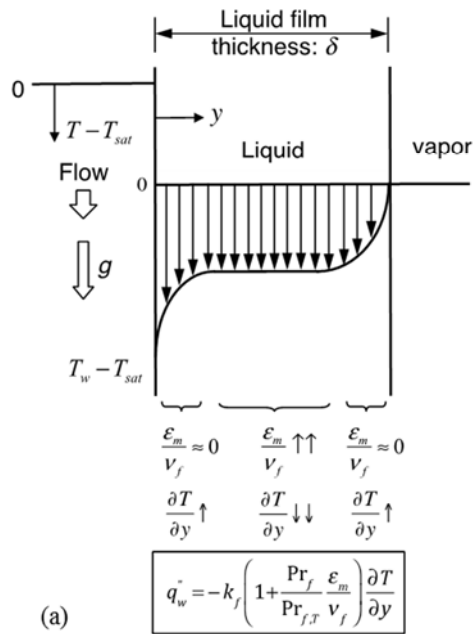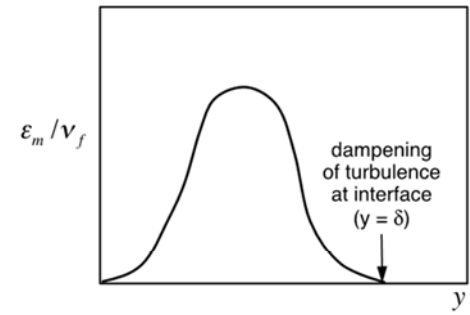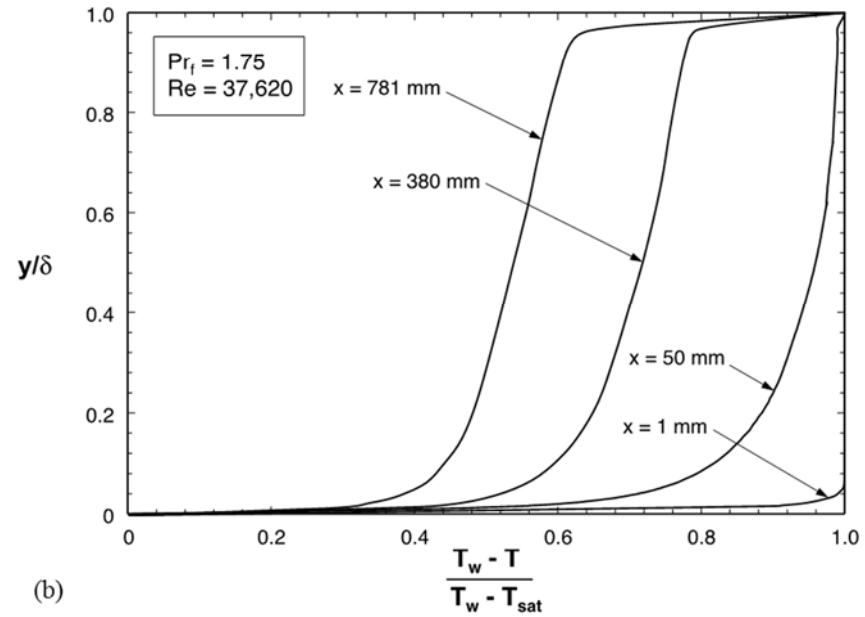
Fig. A.19: (a) Schematic representations of eddy momentum diffusivity profile across free-falling evaporating water film, and influence of interfacial dampening of eddy momentum diffusivity on temperature profile. (b) Temperature profiles across evaporating film at different axial locations predicted using VOF scheme in 2-D axisymmetric domain with Tanasawa phase change model. Adapted from Chapter 7 of current work.

condensation configurations. While some attempts have been made to address more complex phase change problems, including falling films [160, Chapter 7 of current work], heat pipes [314], jet impingement [315] and cryogenics [91,316], there is now a need to undertake more aggressive steps to tackle several important phenomena that have received significant attention in experimental studies and/or are crucial to design of modern phase change devices and systems. Following is a summary of such phenomena:

(1) As shown in Fig. A.20(a), two distinct mechanisms have been proposed as dominating flow boiling heat transfer in micro-channel heat sinks: nucleate boiling and convective boiling. And recommendations have been made in numerous, mostly experimental studies regarding operating conditions that render dominant one mechanism versus the other [317,318]. Clearly, computational models might play a crucial role in capturing detailed interfacial behavior associated with each.

(2) Flow boiling CHF is one of the most important design parameters for heat-flux-controlled two-phase cooling systems. For the most common configuration of flow boiling in a tube, experimental evidence points to formation of a wavy insulating vapor layer prior to CHF, with cooling provided only in 'wetting fronts' correspond to the wave troughs, Fig. A.20(b), with CHF triggered by lift-off of the troughs from the wall [45]. This depiction of interfacial behavior lends itself well to computational modeling.

(3) Two-phase micro-channel heat sinks are susceptible to different types of instabilities, including severe pressure drop oscillations and mild parallel channel
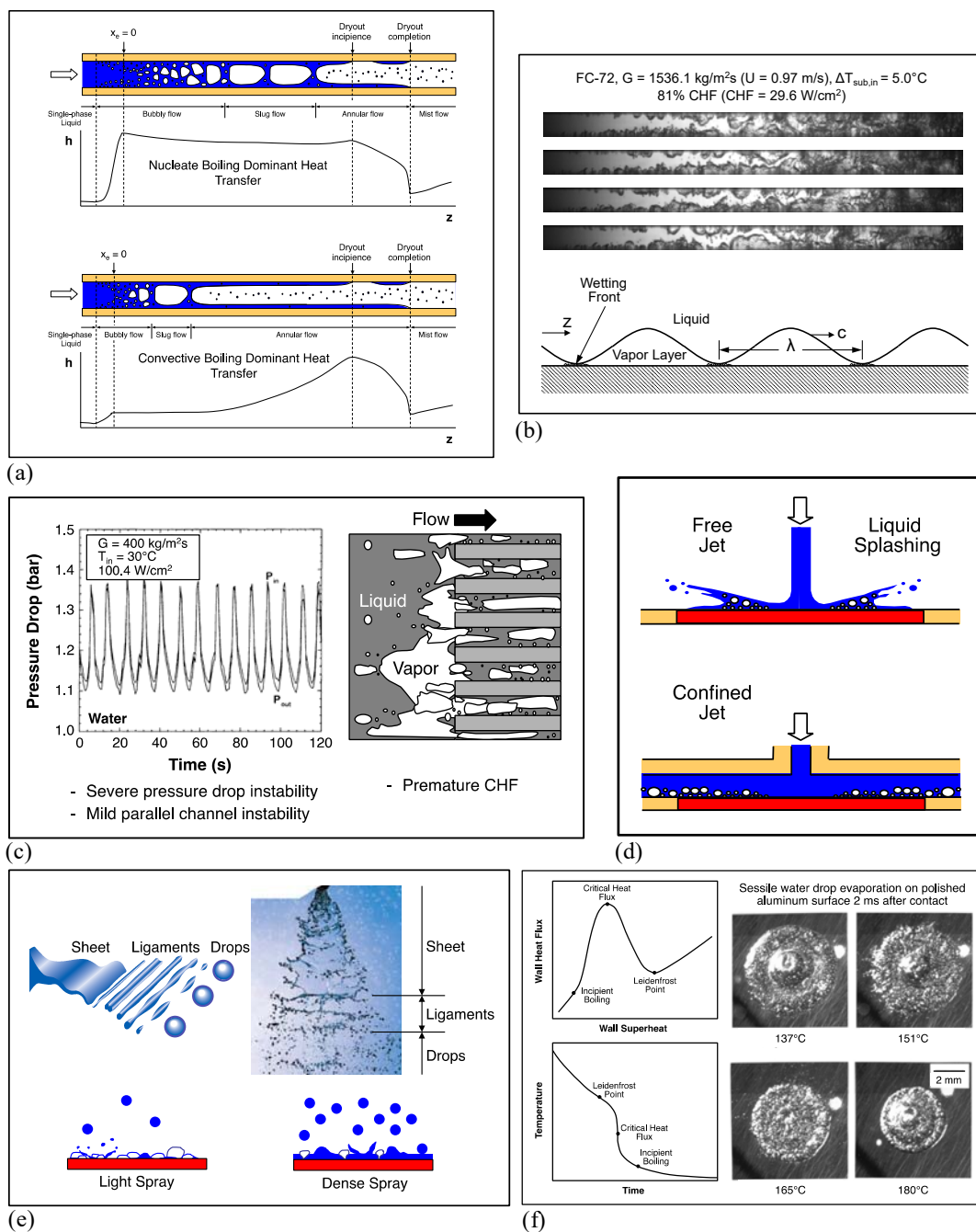
Fig. A.20: Examples of phase change phenomena that are crucial to design of modern devices and systems, and which can benefit greatly from computational modeling. (a) Dominant flow boiling heat transfer mechanisms in micro-channels [317,318]. (b) Flow boiling CHF in tubes [45]. (c) Instabilities and premature CHF in micro-channels [1]. (d) Liquid splashing and dryout in free jet impingement [319]. (e) spray cooling and liquid film buildup [106,320]. (f) Leidenfrost phenomenon [321].

oscillations, and these instabilities have been shown to trigger pre-mature CHF [1], as shown in Fig. A.20(c). While, as discussed earlier, some investigators have simulated the problem of bubble backflow in micro-channels, more aggressive computational efforts are needed to address these important phenomena.

(4) While jet impingement has been the target of a few computational efforts, important phenomena such as splashing of liquid away from the heated wall and ensuing wall dryout [319], Fig. A.20(d), warrant more aggressive computational modeling efforts.

(5) Impact of individual droplets with dry or wet surfaces has been the subject of a substantial number of computational efforts. However, a very important application of droplet impact is spray cooling, where liquid supplied through a nozzle undergoes breakup into a large number of droplets with broad range of trajectories as shown in Fig. A.20(e) [106,320]. Admittedly, computational modeling of spray cooling is a formidable task, given its flow complexity and large number of discrete interfaces. Nonetheless, computational efforts might shed light on crucial mechanisms associated with liquid film buildup on the heated wall, and its impact on spray cooling.

(6) The Leidenfrost point is one of the most important phenomena in the production of metal alloys, which is encountered during the quench phase of heat treating [321]. As the metal alloy part is cooled from very high temperature, this point marks a transition from slow cooling in the film boiling regime to fast cooling, as the surface enters the transition boiling regime. This behavior, which is depicted in Fig. A.20(f), has a strong bearing on alloy microstructure and hence mechanical properties of the part produced. Accurate computational modeling of the Leidenfrost point will therefore have a profound practical impact on the entire heat treating industry.

A.7 <u>Concluding Remarks</u>

This article reviewed published papers concerning computational fluid dynamics simulations of boiling and condensation. Two-phase schemes and surface tension models adopted by different research teams were discussed, followed by thorough discussion on implementation of mass transfer across the two-phase interface. Also included was a comprehensive review of articles covering a variety of boiling and condensation configurations, along with the computational methods used, examples of their predictions, and comparisons with experimental data. The article was concluded with identification of future research needs to improve predictive capabilities, as well as crucial phase change phenomena that warrant significant attention in future computational studies.

VITA

VITA

<u>EDUCATION</u>

Purdue University, West Lafayette, IN   2013-expected August 2016
Doctor of Philosophy
GPA 3.86/4

Purdue University, West Lafayette, IN   2009-2011
Master of Science in Mechanical Engineering (Thesis)
GPA 3.86/4

National Institute of Technology - Allahabad, India   2005-2009
Bachelor of Technology (Mechanical Engineering)
GPA 9.46/10

<u>FIELDS OF INTEREST</u>
- Heat and Mass Transfer
- Computational Fluid Dynamics
- Two-Phase Flows

<u>AWARDS AND HONORS</u>
- **2016: College of Engineering Outstanding Graduate Student Research Award, Purdue University**
  Awarded to outstanding PhD candidates who have demonstrated excellence in research
- **2015: Drs. Helen and Marvin Adelberg Fellowship, Purdue University**
  Awarded to outstanding PhD students in their final year of degree
- **2009: J. N. Tata Endowment Scholarship, India**
  Awarded to top undergraduate students from India for pursuing higher education outside India
- **2007 and 2008: Merit Scholarship, NIT Allahabad, India**
  Awarded to top performing students at the University

INDUSTRIAL EXPERIENCE

Electrification Mechanical Engineer - I (Aug 2011 – April 2013), Advanced Engineering
Electrification Mechanical Engineer - II (May 2013 – July 2013), Advanced & Production Engineering
Delphi Electronics & Safety, Kokomo, IN

- Design and testing of thermal management systems used in various power electronics applications for HEVs and PHEVs: Inverters, Converters and Battery Packs.
- Numerical analysis using different CFD/thermal analysis tools for validation and design of cooling components. Software Packages used: Fluent, Icepak, ANSYS Mechanical, FloEFD. Some work with structural and vibration analysis.
- Led a technology development project to direct cool discrete semiconductor power devices used in HEVs with multiple direct attach methods for enhancing thermal performance. Technologies were identified and evaluated based on coefficient of thermal expansion, heat transfer performance, pressure drop and cost of the product. For certain technologies a reduction in thermal resistance of 30% was successfully demonstrated.

TEACHING EXPERIENCE

*Teaching Assistant, Purdue University (***Spring 2011:** *January 2011-May 2011)*

- TA for Heat and Mass Transfer (ME315) for two sections with 12 students each.
- Duties included conducting laboratory sessions, guiding students with projects and helping them with technical problems.

*Teaching Assistant, Purdue University (***Fall 2010:** *August 2010-December 2010)*

- TA for Intermediate Heat Transfer (ME505) graduate level course for on-campus and distance learning. Total students: 105.
- Duties included setting up and grading homeworks/exams and helping students with technical problems. Taught videotaped lectures in absence of the Teacher.

RESEARCH EXPERIENCE

Experimental, Theoretical and Computational Modeling of Flow Boiling, Flow Condensation and Evaporating Falling Films (PhD Thesis), Position: Graduate Research Assistant (**August 2013-present**), Adelberg Fellow (**August 2015-July 2016**)
Purdue University, West Lafayette, IN

- Study aimed at future implementation of two-phase thermal management systems in space applications. Worked on a project to design a flow boiling and condensation experimental facility to be tested on the **International Space Station** in the year 2018.
- Experimental study and theoretical modeling of flow boiling heat transfer and critical heat flux in channel flows for Earth gravity and microgravity.

- FLUENT based computational modeling of annular flow condensation and evaporating falling films.

Photographic Study and Modeling of Critical Heat Flux in Horizontal Flow and Vertical Upflow with Inlet Vapor Void (Master's thesis), *Position: Graduate Research Assistant (**May 2010-July 2011**)*
Purdue University, West Lafayette, IN
- Experimental work involved flow visualization to study the flow behavior before and during transient CHF.
- A completely theoretical model was developed for flow behavior and critical heat flux predictions.
- Work part of a project to study flow boiling in microgravity on the **International Space Station.**

Design of a Vapor-compression cum Evaporative-cooling System (Senior Year Thesis, July 2008- May 2009)
National Institute of Technology-Allahabad, India
- Central air-conditioning system was designed for a four-story building incorporating vapor-compression and evaporative-cooling cycles.
- Concept of Y-ducting was successfully implemented on the duct architecture of the building.
- System proved to be highly economical when compared to a traditional central air-conditioning system.

Using Delta Wing Inserts for Heat Transfer Enhancement in Tubular Flows, *Position: Undergraduate Researcher (**May-July 2008**)*
Indian Institute of Technology-Bombay, India
- Simple delta Vortex Generators were modified into curved geometries and tested for turbulent flows.
- Nusselt number enhancement was tested at constant Reynolds number and constant Pumping power.
- Heat transfer values were comparable to conventional inserts making this an alternative for many applications.

Heat Transfer Enhancement in Laminar Channel Flows, *Position: Undergraduate Researcher (**May-July 2007**)*
Indian Institute of Technology-Bombay, India
- Sponsored by **Intel Corp.,** project involved improving the efficiency of laptop chips.
- Involved use of delta vortex generators to improve heat transfer in heated rectangular channels, simulating conditions similar to laptops.

JOURNAL PUBLICATIONS

1. **Kharangate, C.**, Lee, H., Park, I., Mudawar, I., "Experimental and computational investigation of vertical upflow condensation in a circular tube," *International Journal of Heat and Mass Transfer,* Vol. 95, pp. 249-263, 2016.

2. **Kharangate, C.**, Konishi, C., Mudawar, I., "Consolidated methodology to predicting flow boiling critical heat flux for inclined channels in Earth gravity and for microgravity," *International Journal of Heat and Mass Transfer,* Vol. 92, pp. 467-482, 2016.

3. **Kharangate, C.**, O'Neill, L., Mudawar, I., Hasan, M., Nahra, H., Balasubramaniam, R., Hall, N., Macner, A., Mackey, J., "Effect of subcooling and two-phase inlet on flow boiling heat transfer and critical heat flux in a horizontal channel with one-sided and double-sided heating," *International Journal of Heat and Mass Transfer,* Vol. 91, pp. 1187-1205, 2015.

4. **Kharangate, C.**, O'Neill, L., Mudawar, I., Hasan, M., Nahra, H., Balasubramaniam, R., Hall, N., Macner, A., Mackey, J., "Flow boiling and critical heat flux in horizontal channel with one-sided and double-sided heating," *International Journal of Heat and Mass Transfer,* Vol. 90, pp. 323-338, 2015.

5. Lee, H., **Kharangate, C.**, Mascharehnas, N., Park, I., Mudawar, I., "Experimental and computational investigation of vertical downflow condensation," *International Journal of Heat and Mass Transfer,* Vol. 85, pp. 865-879, 2015.

6. **Kharangate, C.**, Lee, H., Mudawar, I., "Computational modeling of turbulent evaporating falling films," *International Journal of Heat and Mass Transfer,* Vol. 81, pp. 52-62, 2015.

7. **Kharangate, C.**, Mudawar, I., Hasan, M., "Experimental and theoretical study of critical heat flux in vertical upflow with inlet vapor void," *International Journal of Heat and Mass Transfer,* Vol. 55, pp. 360-374, 2012.

8. **Kharangate, C.**, Mudawar, I., Hasan, M., "Photographic study and modeling of critical heat flux in horizontal flow boiling with inlet vapor void," *International Journal of Heat and Mass Transfer*, Vol. 55, pp. 4154-4168, 2012.

9. **Kharangate, C.**, O'Neill, L., Mudawar, I., "Effects of two-phase inlet quality, mass velocity, flow orientation, and heating perimeter on flow boiling in a rectangular channel: Part 1 – Two-phase flow and heat transfer results," *International Journal of Heat and Mass Transfer,* in press.

10. **Kharangate, C.**, O'Neill, L., Mudawar, I., "Effects of two-phase inlet quality, mass velocity, flow orientation, and heating perimeter on flow boiling in a rectangular channel: Part 2 – CHF experimental results and model," *International Journal of Heat and Mass Transfer,* in press.

11. Park, I., O'Neill, L., **Kharangate, C.**, Mudawar, I., "Assessment of body force effects in flow condensation, part I: Experimental investigation of liquid film behavior for different orientations," *International Journal of Heat and Mass Transfer,* in press.

12. O'Neill, L., Park, I., **Kharangate, C.**, Devahdhanush, V., Ganesan, V., Mudawar, I., "Assessment of body force effects in flow condensation, part II: Criteria for negating influence of gravity," *International Journal of Heat and Mass Transfer,* in press.

13. O'Neill, L., **Kharangate, C.**, Mudawar, I., "Time-averaged and transient pressure drop for flow boiling with saturated inlet conditions," *International Journal of Heat and Mass Transfer,* in press.

14. **Kharangate, C.**, Mudawar, I., "Review of computational studies on boiling and condensation," *International Journal of Heat and Mass Transfer,* in review.

CONFERENCE PUBLICATIONS/PRESENTATIONS

1. **Kharangate, C.**, O'Neill, L., Konishi, C., Mudawar, I., Hasan, M., Nahra, H., Hall, N., Balasubramaniam, R., Mackey, J., "Flow Boiling and Condensation Experiment for the International Space Station," *31ˢᵗ Annual Meeting of American Society for Gravitational and Space Research*, Alexandria, VA, November 2015.

2. Nahra, H., Hasan, M., Balasubramaniam, R. Patania, M., Hall, N. Wagner, J., Mackey, J., Frankenfield, B., Hauser, D., Harpster, G. Nawrocki, D., Clapper, R.Kolacz, J., Butcher, R.,May, R., Chao, D., Mudawar, I., **Kharangate, C.**, O'Neill, L., "Development and Capabilities of ISS Flow Boiling and Condensation Experiment," *31ˢᵗ Annual Meeting of American Society for Gravitational and Space Research*, Alexandria, VA, November 2015.

3. Sawarkar, P., **Kharangate, C.**, Gokhale, O., Vedula, R., "Use of modified delta wing inserts for heat transfer augmentation in tubular flows," *35ᵗʰ National Conference of Fluid Mechanics and Fluid Power*, India, December 2008.

ACADEMIC PROJECTS

- *Simulation of Turbulent Flow Condensation using ANSYS-Fluent, AAE 626 Project (Spring 2015),* Purdue University, West Lafayette, IN

- ***Modelling of Two-Phase Annular Flow, ME 506 Project (Spring 2014),*** Purdue University, West Lafayette, IN
- ***Waste Heat Recovery Using Organic Rankine Cycle for Semi-Truck Automotive Applications, ME 518 Project (Fall 2013),*** Purdue University, West Lafayette, IN
- ***Algebraic Multigrid Solver for Structured Meshes, ME 608 Project (Spring 2011),*** Purdue University, West Lafayette, IN
- ***Slip Flow Model to Predict Dryout, ME 697 Project (Spring 2010),*** Purdue University, West Lafayette, IN

CERTIFICATIONS

Certified LabVIEW Associate Developer (CLAD), Serial Number: 100-311-2233

SOFTWARE SKILLS

- ➢ CFD: Fluent, Icepak, FloEFD
- ➢ ANSYS Workbench
- ➢ NX Unigraphics, PRO/E
- ➢ LabVIEW, MATLAB/Simulink
- ➢ C, C++

LANGUAGE SKILLS

- ➢ English (Full Professional Proficiency)
- ➢ German (Limited Working Proficiency)
- ➢ Hindi (Full Professional Proficiency)

PROFESSIONAL MEMBERSHIPS

- ➢ American Society of Mechanical Engineers (**ASME**)
- ➢ American Society for Gravitational and Space Research (**ASGSR**)

SERVICE AND ACTIVITIES

- ➢ Completed a 2 credit course on preparing for an academic career: **Preparing Future Faculty (GRAD 590)**
- ➢ Regularly review papers for journal: **International Journal of Heat and Mass Transfer**
- ➢ Served as a reviewer for the 15th IEEE Intersociety Conference on Thermal and Thermomechanical Phenomena in Electronic Systems (**ITHERM 2016**)
- ➢ Mentored new incoming ME PhD students in Fall 2014 and Fall 2015 as part of the peer mentoring program "eMentoring" at Purdue University
- ➢ Tutored students in Fall 2013 and Fall 2014 for Undergraduate Heat and Mass Transfer (ME 315)

➢ Actively participated in multiple community development activities organized by United Way of Howard County, IN (2011-2013)

➢ Member of Kokomo Young Professionals Group (2011-2013)

PUBLICATIONS

PUBLICATIONS

JOURNAL PUBLICATIONS

1. Kharangate, C., Lee, H., Park, I., Mudawar, I., "Experimental and computational investigation of vertical upflow condensation in a circular tube," *International Journal of Heat and Mass Transfer,* Vol. 95, pp. 249-263, 2016.

2. Kharangate, C., Konishi, C., Mudawar, I., "Consolidated methodology to predicting flow boiling critical heat flux for inclined channels in Earth gravity and for microgravity," *International Journal of Heat and Mass Transfer,* Vol. 92, pp. 467-482, 2016.

3. Kharangate, C., O'Neill, L., Mudawar, I., Hasan, M., Nahra, H., Balasubramaniam, R., Hall, N., Macner, A., Mackey, J., "Effect of subcooling and two-phase inlet on flow boiling heat transfer and critical heat flux in a horizontal channel with one-sided and double-sided heating," *International Journal of Heat and Mass Transfer,* Vol. 91, pp. 1187-1205, 2015.

4. Kharangate, C., O'Neill, L., Mudawar, I., Hasan, M., Nahra, H., Balasubramaniam, R., Hall, N., Macner, A., Mackey, J., "Flow boiling and critical heat flux in horizontal channel with one-sided and double-sided heating," *International Journal of Heat and Mass Transfer,* Vol. 90, pp. 323-338, 2015.

5. Lee, H., Kharangate, C., Mascharehnas, N., Park, I., Mudawar, I., "Experimental and computational investigation of vertical downflow condensation," *International Journal of Heat and Mass Transfer,* Vol. 85, pp. 865-879, 2015.

6. Kharangate, C., Lee, H., Mudawar, I., "Computational modeling of turbulent evaporating falling films," *International Journal of Heat and Mass Transfer,* Vol. 81, pp. 52-62, 2015.

7. Kharangate, C., Mudawar, I., Hasan, M., "Experimental and theoretical study of critical heat flux in vertical upflow with inlet vapor void," *International Journal of Heat and Mass Transfer,* Vol. 55, pp. 360-374, 2012.

8. Kharangate, C., Mudawar, I., Hasan, M., "Photographic study and modeling of critical heat flux in horizontal flow boiling with inlet vapor void," *International Journal of Heat and Mass Transfer*, Vol. 55, pp. 4154-4168, 2012.

9. Kharangate, C., O'Neill, L., Mudawar, I., "Effects of two-phase inlet quality, mass velocity, flow orientation, and heating perimeter on flow boiling in a rectangular channel: Part 1 – Two-phase flow and heat transfer results," *International Journal of Heat and Mass Transfer*, in press.

10. Kharangate, C., O'Neill, L., Mudawar, I., "Effects of two-phase inlet quality, mass velocity, flow orientation, and heating perimeter on flow boiling in a rectangular channel: Part 2 – CHF experimental results and model," *International Journal of Heat and Mass Transfer,* in press.

11. Park, I., O'Neill, L., Kharangate, C., Mudawar, I., "Assessment of body force effects in flow condensation, part I: Experimental investigation of liquid film behavior for different orientations," *International Journal of Heat and Mass Transfer,* in press.

12. O'Neill, L., Park, I., Kharangate, C., Devahdhanush, V., Ganesan, V., Mudawar, I., "Assessment of body force effects in flow condensation, part II: Criteria for negating influence of gravity," *International Journal of Heat and Mass Transfer,* in press.

13. O'Neill, L., Kharangate, C., Mudawar, I., "Time-averaged and transient pressure drop for flow boiling with saturated inlet conditions," *International Journal of Heat and Mass Transfer,* in press.

14. Kharangate, C., Mudawar, I., "Review of computational studies on boiling and condensation," *International Journal of Heat and Mass Transfer,* in review.

CONFERENCE PUBLICATIONS/PRESENTATIONS

1. Kharangate, C., O'Neill, L., Konishi, C., Mudawar, I., Hasan, M., Nahra, H., Hall, N., Balasubramaniam, R., Mackey, J., "Flow Boiling and Condensation Experiment for the International Space Station," *31st Annual Meeting of American Society for Gravitational and Space Research*, Alexandria, VA, November 2015.

2. Nahra, H., Hasan, M., Balasubramaniam, R. Patania, M., Hall, N. Wagner, J., Mackey, J., Frankenfield, B., Hauser, D., Harpster, G. Nawrocki, D., Clapper, R.Kolacz, J., Butcher, R.,May, R., Chao, D., Mudawar, I., Kharangate, C., O'Neill, L., "Development and Capabilities of ISS Flow Boiling and Condensation Experiment," *31st Annual Meeting of American Society for Gravitational and Space Research*, Alexandria, VA, November 2015.

3. Sawarkar, P., Kharangate, C., Gokhale, O., Vedula, R., "Use of modified delta wing inserts for heat transfer augmentation in tubular flows," *35th National Conference of Fluid Mechanics and Fluid Power*, India, December 2008.